NUMERICAL SIMULATIONS OF ASTROPHYSICAL JETS FROM KEPLERIAN ACCRETION DISKS

By

RACHID OUYED, D.E.A., M.SC.

A Thesis

Submitted to the School of Graduate Studies

in Partial Fulfilment of the Requirements for the Degree

Doctor of Philosophy

McMaster University

December 1996

NUMERICAL SIMULATIONS OF ASTROPHYSICAL JETS FROM KEPLERIAN ACCRETION DISKS

DOCTOR OF PHILOSOPHY (1996) (ASTROPHYSICS)

McMASTER UNIVERSITY
Department of Physics and Astronomy
Hamilton, Ontario

TITLE: Numerical Simulations of Astrophysical Jets from Keplerian Accretion Disks

AUTHOR: Rachid OUYED
D.E.A. (Université de Paris-VII)
M.Sc. (McMaster University)

ADVISOR: Professor Ralph E. PUDRITZ

PAGES: xvii, 271

Abstract

This thesis presents a series of magnetohydrodynamic (MHD) simulations which were designed to study the origin and evolution of astrophysical jets (galactic and extra-galactic). We developed and extended a version of the ZEUS-2D code which served as the numerical basis of our simulations and attached to it a complete analysis package that was developed in order to make contact with theory and observations of jets.

With our version of the code, we managed to establish an initial state which consists of an accretion disk and its cold corona in stable equilibrium around a central object. No softening parameter was used to model the Newtonian gravitational potential of the central object. The corona and accretion disk are initially in pressure balance with one another. These initial states were constructed so as to be numerically stable. The corona is magnetized with the magnetic field lines extending smoothly into the disk without kinks or discontinuities, avoiding, in this way, any undesired currents in the initial set up. The disk is set in Kepler rotation and gas is continuously injected into the corona above at the very small speed of 10^{-3} times the Kepler velocity.

In this thesis, we only considered magnetic configurations for which the Lorentz force is initially zero ($\mathbf{J} \times \mathbf{B} = 0$). In particular initial $\mathbf{J} = 0$ configurations are studied. We carefully set the boundary conditions to be open conditions so as to

avoid any collimation due to grid reflection effects.

To test the theory of winds centrifugally driven from the surface of Keplerian accretion disks, we started with an open magnetic field line configuration. The magnetic field lines have opening angles (with respect to the disk surface) less than the critical angle ($\simeq 60°$), as required for a centrifugally driven wind to start. We found that a steady jet is quickly established, allowing direct comparison with the theory. We find the gas to be centrifugally accelerated through the Alfvén and the fast magnetosonic surfaces and collimated into cylinders parallel to the disk's axis. The collimation is due to the pinch force exerted by the dominant toroidal magnetic field generated by the outflow itself. The velocities achieved in our simulations are of the order of 250 km/s for our standard young stellar object (a 0.5 $M_\odot$ proto-star) and of the order or 10^5 km/s for our standard active galactic nuclei (a $10^8 M_\odot$ black hole). Our jet solutions are very efficient in magnetically extracting angular momentum and energy from the disk.

The second magnetic configuration we have studied consists of a uniform vertical structure wherein the magnetic field lines are parallel to the disk's axis. Here, the rotation of the disk twists the magnetic field lines and generates a toroidal field component. Because of the Keplerian scaling of the rotational velocity with the disk radius, the twisting of the field lines is higher in the inner parts of the disk. The strong magnetic gradient thus generated opens up the initial magnetic configuration in a narrow region located at $1r_i < r < 8r_i$, with r_i being the innermost radius of

the disk. Within this narrow region, a wind is ejected from the field lines that have opened to less than the critical angle ($\simeq 60^o$), as expected from the centrifugally driven wind theory. Our simulations show that the strong toroidal magnetic field generated recollimates the flow towards the disk's axis and, through MHD shocks, produces knots. The knot generation mechanism occurs at a distance of about $z \simeq 8r_i$ from the surface of the disk.

We have discovered that *no special initial magnetic field structure* is required in order to launch episodic outflows in our simulations. Rather, conditions favorable for the formation of an outflow set themselves up automatically through the production of a toroidal magnetic field whose pressure readjusts the structure of the field above the disk. The knot generator is episodic, and is inherent to the jet. Thus, jets are apparently capable of producing the variability that leads to episodic events, independently of the underlying source.

Acknowledgments

I would like to express my gratitude to the following people, who have helped me in carrying out this work:

- My supervisor Ralph E. Pudritz, whose trust, understanding, caring and, most importantly, ideas not only allowed me to carry out this exciting work with great interest, but taught me the meaning of being a scientist. With Ralph, research is more than just fun, it is learning at its best. Many thanks Ralph!

- Jim Stone and David Clarke, for the very fruitful and interesting discussions concerning this work.

- Patricia Monger, for all the help and hints she provided me with during the problems related to the numerical aspect of this work.

- The members of the advisory committee, Peter Sutherland, Mike Fich, Randy Dumas, David Goodings and David Clarke for the very helpful comments on how to improve the overall presentation of the thesis.

- The faculty and staff of the Physics and Astronomy Department, for making our working environment a very encouraging one. Thanks to Wendy, Rosemary, Jackie, Cheryl and Margaret. You are the best!

- The Ontario Government, for their financial support through the ODFW and the Department of Physics and Astronomy of McMaster University for the fellowship and the assistantship financial support that made this work possible.

- I would also like to thank, A^2, Steve Arnold, Bill Atkinson, Dwayne Branch, Charles Curry, Chris O'Donovan, Pat Durell, Guillaume Gervais, Hamish Johnston, Andéa and Denis Litva, Peter Mason, Brenda Mathews, Bill Minor, Vicky Smallman, Kaori Tanaka, and others, who made my stay at the department of Physics and Astronomy and/or at McMaster University very enjoyable. Thanks Guys !

Special thanks to:

- Greg Cripps and his wife Julia Steegmann who showed me what friendship is all about.

- My Sensei, Phil McColl, for teaching me how to be a Martial Artist both in the Dojo and in Life.

Finally, I reserve a special section of these acknowledgements to show my appreciation and thanks to my family:

- My parents, VAVA d YEMA, for their love, their kindness and their patience. Because you let me fly on my own, because you believed in me, because you understood me, because you knew how to encourage me, this work is for you!!

- To my brothers and sisters, in Algeria and in France.

- To my family in Toronto, Ali, Christine and Sami OUYED, for their much appreciated moral support when needed.

- To my family in Mexico, Mekhlouf, Emalda, Emir, Juanito, Cecilia and Hakim OUYED, for making me feel so close from home while this far away.

" *This work is dedicated to all the innocent people that died in Algeria, victims of military oppression or of blind Islamic fundamentalism.*"

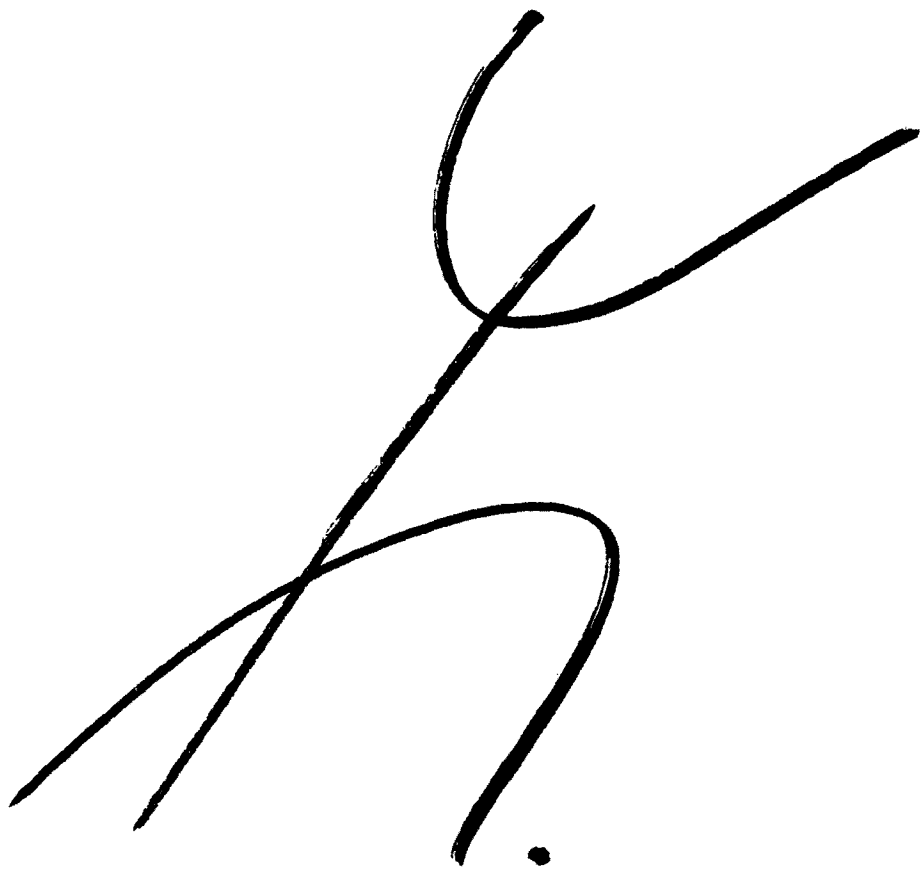

I Vava d Yema

Contents

List of Figures

List of Tables

Chapter 1

Introduction

In this chapter, we introduce the reader to the topic of astrophysical jets. We describe the most recent observational evidence for the importance of jets in the process of star formation and the physics of galactic nuclei, as well as the constraints these observations put on models of jets. The necessity of a numerical approach to the study of these phenomena is illustrated.

1. Astrophysical Jets

Jets are observed on a wide variety of length scales. They are seen on a parsec scale emerging from young stellar objects (YSOs) and on the scale of many kiloparsecs emerging from active galactic nuclei (AGNs)[1]. Although the scales at which jets have been observed vary widely it seems likely that the underlying nature of their sources might be similar. In each case, there is good evidence that matter is accreting onto a central object: in the case of a YSO it is a newly formed star, and in that of the AGN it is probably a massive black hole.

In a description of an optical image of M87 (the prototype of extra-galactic jets, Figure 1), Baade & Minkowski (1954) used the term 'jet' to describe a feature which seemed to be associated with the ejection of material from the innermost region of the galaxy, although the concept of a continuous flow was not then envisaged. Figure 2 shows another kiloparsec scale jet (the Hydra A jet). Many more jets (at kpc scales) have since been observed with the VLA which show many similarities to M87. Modern VLBI maps of the cores of jet sources revealed that extra-galactic jets also exist at the pc-scale. These maps show that the knots associated with these jets move at relativistic speeds (see Leahy, 1993 for details on this topic). These inner jets are always correlated with the large kpc-scale jets (like the Hydra jet which possess a pc-scale relativistic jet). In this thesis, we only simulate the non-relativistic jets but

[1]These are nuclei of active galaxies. The activity, not related to ordinary stellar processes, is centered in a small nuclear region and associated with strong emission lines.

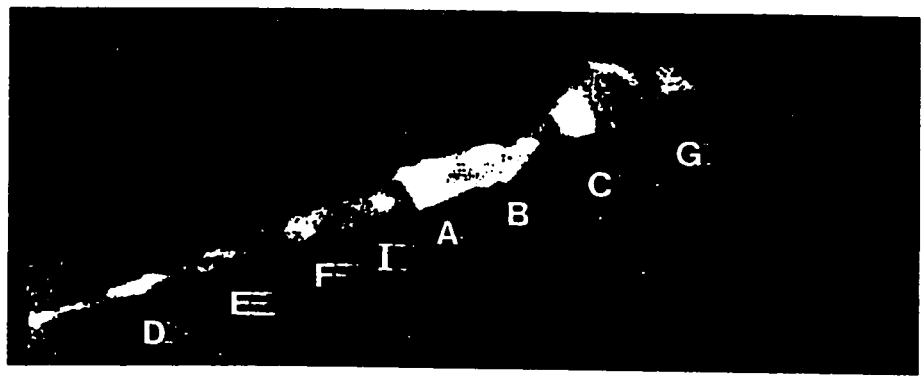

Figure 1. - M 87 jet seen at 15 GHz with the VLA. Prominent knots are seen. The total extent of the jet is about 6 kpc (75") from the nucleus which is to the far left and is the brightest region (from Owen, Hardee, & Cornwell 1989).

we will keep this relativistic component of jets in AGNs in mind.

The first time the phrase 'jet' was used in the context of observed outflows from YSOs was by Mundt & Fried (1983) when they announced the discovery of jets from DG Tau. Many more jets have since been observed, among the most striking being the HH34 jet (Figure 3) that shows the knotty structure.

The HH30 jet observed by HST (Figure 4) shows details of how jets might be linked to the central source or system that they emerge from. The jet emanates from the center of a dark disk of dust which encircles the star and hides it from view.

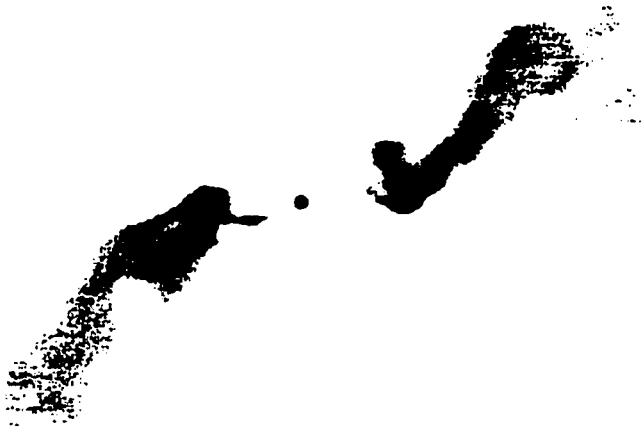

Figure 2. - The radio source Hydra A showing symmetrical jets emanating from the core. This map was obtained at 6 cm with the VLA (from Taylor et al., 1990).

Among the many features that one notices about these jets are their knotty structure and the fact that they are highly collimated. The high degree of jet collimation and knottiness motivated many observational and theoretical investigations designed to understand the physics responsible for such features. Here is a brief summary of the outcome:

Collimation:

Simply put, most of the observed jets (galactic and extra-galactic) have an internal gas pressure (p_j) that exceeds the pressure in the external medium p_e (Bridle, 1985; Königl, 1985). One then should expect the jet to spread with a constant lateral

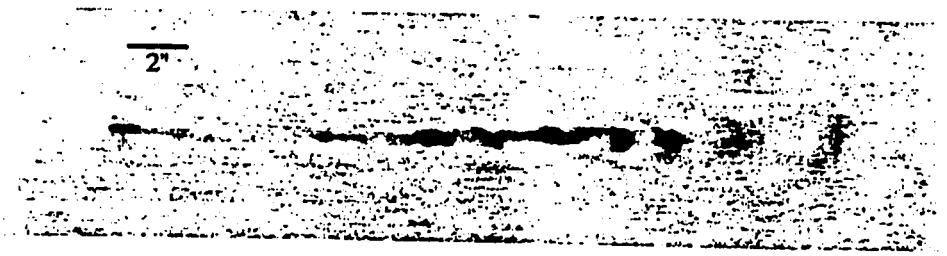

Figure 3. - The HH 34 jet in [SII]$\lambda\lambda$6716,6731 as observed by the HST with the Wide-Field Planetary Camera-2 (WFPC2). Notice that the knots become more bow-like with distance from the source. The source is to the far left. The resolution is $1'' \equiv 140$ AU (from Ray, 1996).

velocity equals to its sound speed. Its radius would, therefore, grow with distance from the source. This is not observed, leading to models of jet confinement.

Purely hydrodynamic models were first introduced to explain jet collimation. Even if the wind is initially isotropic (e.g, a radiatively accelerated wind from a YSO), it could still be collimated if the pressure and density distribution in the confining external medium is anisotropic (Barral et al., 1981). Furthermore, if the wind is of sufficiently high velocity (so that it does not cool too rapidly after being shocked), then it is, in principle, possible to achieve collimation. This may be done by means of the Laval nozzle mechanism, first proposed in the context of AGN jets (Blandford et al., 1974). However, measurements of magnetic field strength in these jets lead us to believe that magnetic fields might play an important role in jets.

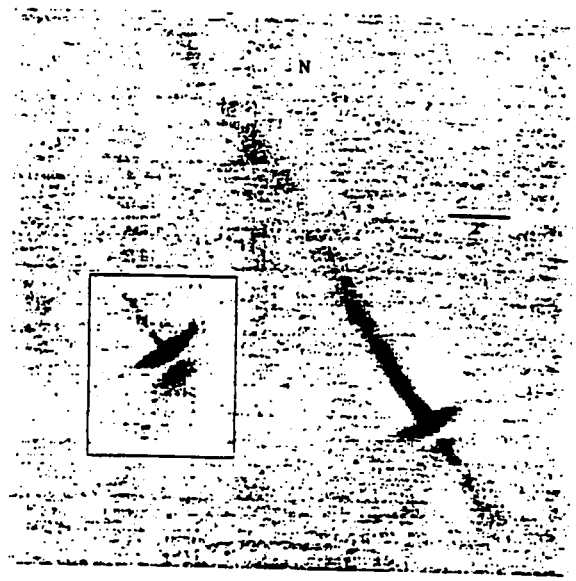

Figure 4a. - The HH 30 jet in [SII]$\lambda\lambda$6716,6731 as observed by the HST with the WFPC2 (minus the continuum). The resolution is 1" $\equiv$ 140 AU (from Ray, 1996).

Figure 4b. - The HH 30 jet (Stapelfeldt, 1996). See the color image at the end of this introductory chapter (donated to us by Dr. Stapelfeldt).

For example, in extended regions of some observed AGNs jets, the *minimum* internal pressure deduced from synchrotron radiation theory appears to exceed the *maximum* internal gas pressure as deduced from X-ray observations (Wardle & Potash, 1982). We will show in §3 that there exists even stronger observational evidence for the importance of magnetic fields in collimating these jets, and they should, therefore, be included in the physics.

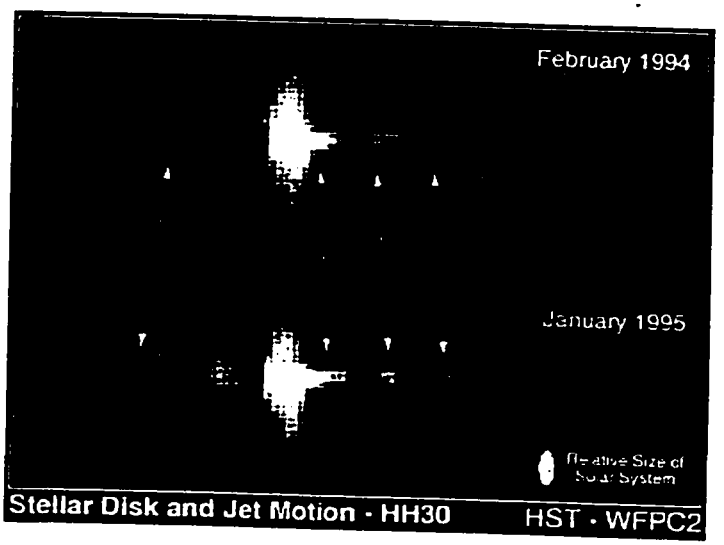

Figure 5. - This NASA Hubble Space Telescope image reveals unprecedented details in HH 30. Besides the high collimation, this image demonstrates the non-stationarity of the knots (from "http://www.ast.cam.ac.uk/HST/press/jetdisk.html").

The Knots:

The knots in astrophysical jets have been studied observationally, theoretically and numerically. The general agreement is that the knot emission is shock excited[2]. In stellar jets this is readily determined by analyzing the optical emission lines (Mundt & Fried 1983) whose spectra are consistent with theoretical models of line formation behind radiative shock waves (Dopita 1978). In extra-galactic jets, the most compelling evidence that shock waves excite knot emission is seen in the 15 GHZ intensity VLA maps of the M87 jet which show sharp intensity jumps on the upstream sides of the knots (Biretta, Owen & Hardee, 1983). The knots are often regularly-spaced

[2]This is a recent discovery which showed that the knots are non-stationary (Eïsloffel & Mundt 1994). Knots move at velocities less than or equal to typical jet velocities. This discovery is important since it automatically rules out models of jets with stationary shocks. Figure 5 shows that indeed the knots move in time.

Table 1. Jet Parameters

Parameters*		
	YSOs	AGNs
Temperature (K)	$5 \times 10^3 - 10^4$	$10^7 - 10^8$
Velocity (km/s)	$50.0 - 300$	$10^4 - 10^5$
Kinetic Luminosity (erg/s)	$10^{33} - 10^{34}$	$10^{45} - 10^{46}$
Mass Flux $(M_\odot/yr)$	$10^{-8} - 10^{-6}$	$0.1 - 1.0$

* The range in the above numbers is largely due to the range in the mass of the central object (Briddle, 1985; Lada, 1985; Padman et al., 1991; Muxlow et al., 1991; Mundt et al., 1994; Ray et al., 1996).

with separations of the order of the beam diameter.

Typical parameters that characterize jets in YSOs and AGNs are summarized in Table 1. The morphological aspects are summarized in Table 2.

What appears to be common to all jet sources, which is of fundamental importance for our work here, is that they show direct and/or indirect evidence for a gaseous disk rotating around the central object (§2). Moreover it would seem that such disks are actively accreting onto their central objects. Theoretical investigations tend to agree that in order to produce powerful self-collimated jets, one requires the presence of an accretion disk and a large scale magnetic field. We summarize some of the latest observational data on accretions disks and large scale magnetic fields in the environment of YSOs and of AGNs in the following sections.

Table 2. Jet Morphology

Morphology *		
	YSOs	AGNs
Size	$10^2 - 10^5$ *AU*	$0.1 - 10$ *Kpc*
Associated with Compacts Objects ?	*yes (proto − stars)*	*yes (Black holes?)*
Highly Collimated ?	*yes*	*yes*
Two Sided ?	*most cases*	*most cases*
Quasi − periodic Knots ?	*yes (HH Objects)*	*yes*
Associated with Magnetic Fields ?	*yes*	*yes*
Associated with Accretion Disks ?	*yes (direct evidence)*	*yes (indirect evidence)*

* (Briddle, 1985; Lada, 1985; Padman et al., 1991; Muxlow et al., 1991; Mundt et al., 1994; Ray et al., 1996).

2. Accretion Disks in Astrophysics

2.1 Disks around Young Stellar Objects (YSOs)

2.1.1 Direct Evidence

Ten years ago there was only circumstantial evidence for disks around young stars. Nowdays, HST observations provide us with direct evidence for the presence of disks around proto-stars. O'Dell et al. (1994) observed the Orion nebula and found several young stars surrounded by gas and dust. These are possibly proto-planetary disks. Several other HST images of proto-planetary disks have been released by McCaughrean & O'Dell(1995).

The most striking evidence of a disk is the HST image of HH30 (Figures 4 and 5) which reveals an edge on disk encircling a newly forming star. The size of the disk is several hundred AU. The disk is thick enough to fragment into a new planetary system, making HH 30 the best example of what our own Sun appeared like early in its life. It is now accepted wisdom that probably all young stars are born with circum-stellar disks.

2.1.2 Indirect Evidence

It is known that classical T Tauri stars (cTTSs)[3] emit significantly more infrared radiation than other stars of their spectral type (typically, K subgiants). In 1974, Lynden-Bell and Pringle showed that an optically thick, viscous, extended accretion disk possessing a power-law distribution of temperature $T_d \propto r^{-p}$ would exhibit a power-law infrared energy distribution $\nu F_\nu \propto \nu^n$. In their model the disk can be thought of as collection of emitting tori, each radiating as black-body. It is the sum of these blackbodies, each at different temperature, that accounts for the above infrared law.

Such energy distributions have been fitted to the spectral energy distribution of jet sources. Figure 6a shows an example of the spectral energy distribution of a typical jet source GG Tau (cTTS). The optical part of the spectrum is well-fitted by

[3]These are optically visible low-mass YSOs with ages $\leq 10^7$ years. Winds around cTTSs were first diagnosed by "P Cygni-like" profiles at H_α (Kuhi 1964). The equivalent width of the observed H_α emission line is greater than 10Å signaling the presence of strong winds.

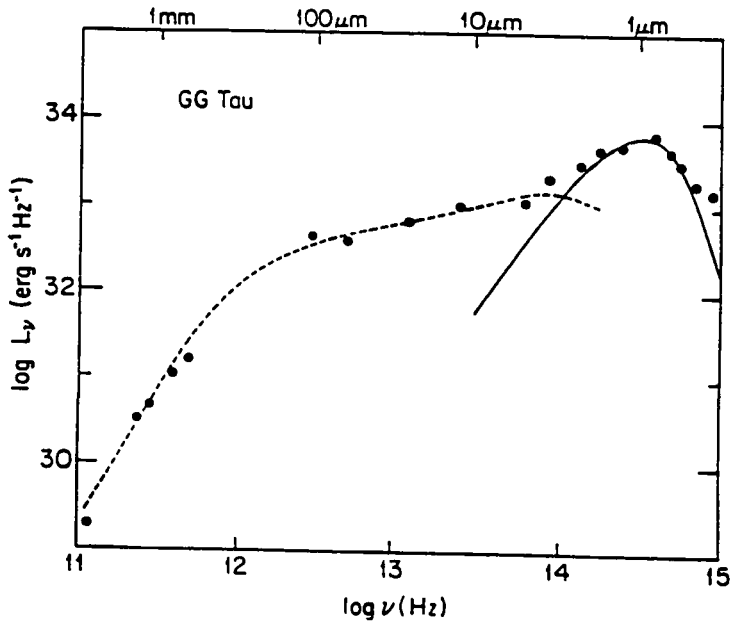

Figure 6a. - The spectral energy distribution is shown for the T Tauri star GG Tau. The solid curve shows the expected spectrum for a star alone; the dashed, for a spatially flat, but radially extended disk that locally reprocesses the starlight that falls on it (from Beckwith, 1991).

a standard blackbody-like stellar photosphere model.

Of course the spectral signature of a disk is not quite the same thing as observing it directly but it is very important when it comes to analyzing the connection between jets and accretion disks (§4). Finally, and for completeness, let us mention that these observed accretion disks might be in radial equilibrium since their rotation profile seems to be close to a Keplerian one. Figure 6b illustrates this fact which will prove important when considering the type of winds we will study in this thesis.

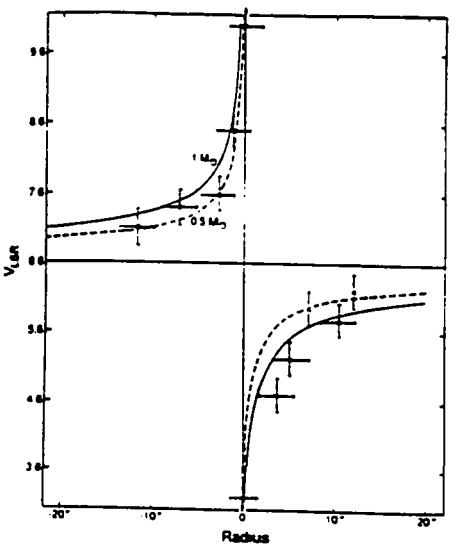

Figure 6b. - The measured velocities of the CO^{13} emission as a function of distance from the HL Tau (from Beckwith & Sargeant, 1995). The solid and dashed lines are the expected Keplerian orbital velocities.

2.2 Disks around Active Galactic Nuclei (AGNs)

Direct information about the nature of central objects in AGNs is very hard to obtain. In fact, even after decades of observational study of these objects, little is known about the mechanisms that produce the generally featureless continua observed in the UV, optical and infrared spectral regions (Figure 7). By a process more of elimination than by direct evidence, it has become accepted that the ultimate source of energy is accretion of material by a massive compact object, presumably a black hole.

In an attempt to find evidence for disks, a considerable amount of effort has been devoted to a study of the thermal emission that could be produced by the accretion disk itself. Even though the results in some cases show excellent agreement

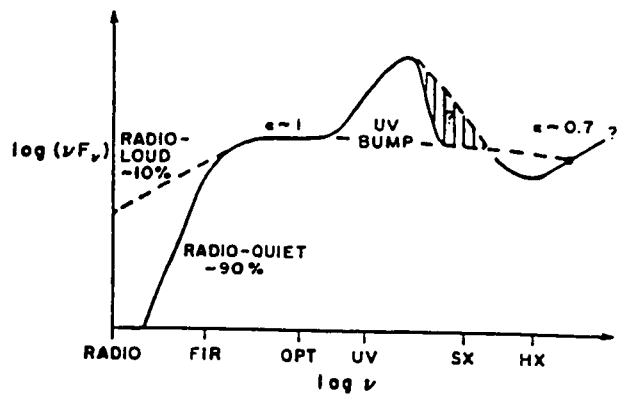

Figure 7. - A typical AGN continuum. The optical-UV feature is referred to as the "big blue bump", which in many sources contains a significant fraction of the bolometric luminosity (from Begelman, 1989)

between the model continua and what is observed (Figure 8), these have not been so compelling[4] as to provide universal acceptance that thermal emission from disks is responsible for the UV-optical continuum (Wallinder, 1991). However, recent measurements of optical polarization of dust grains also seem to favor the presence of a disk-like structure around AGNs (Netzer, 1991). To carry on with our investigation we will assume that an accretion disk around a massive black hole is indeed a vital component in AGNs.

[4]The optical-UV feature in Fig.7 is referred to as the 'big blue bump", which in many sources contains a significant fraction of the bolometric luminosity. One possible origin is the thermal emission from an accretion disk. However, a part of the UV bump may arise from reprocessing of radiation from the central hard X-ray source, which seems indicated by the similar variability patterns seen in UV, optical and X-rays (see Wallinder 1991).

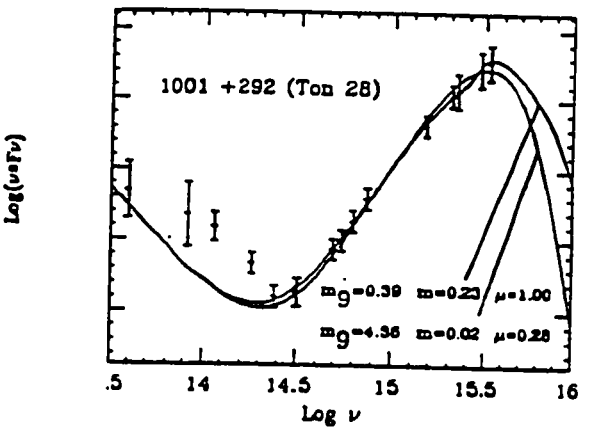

Figure 8. - Fits of accretion disk models (solid lines) to the "big blue bump" of the spectrum of a quasar (Ton 28). Note that equally good fits to the spectrum are obtained with very different values of the physical parameters of the disk (from Netzer, 1991).

3. Large Scale Magnetic Fields

3.1 Magnetic Fields around YSOs

There is now considerable observational evidence that magnetic fields are tightly related to astrophysical jets. For instance, measurements of the magnetic field strengths in regions near outflows reveal that these are strong enough to play an important role in the dynamics of the regions (Reipurth, 1989). Perhaps the most compelling piece of evidence, however, is the observation that more than 70% of the outflows are aligned to within 30% of the ambient magnetic field direction as determined by optical polarization studies (Strom & Strom, 1987, see Figure 9a).

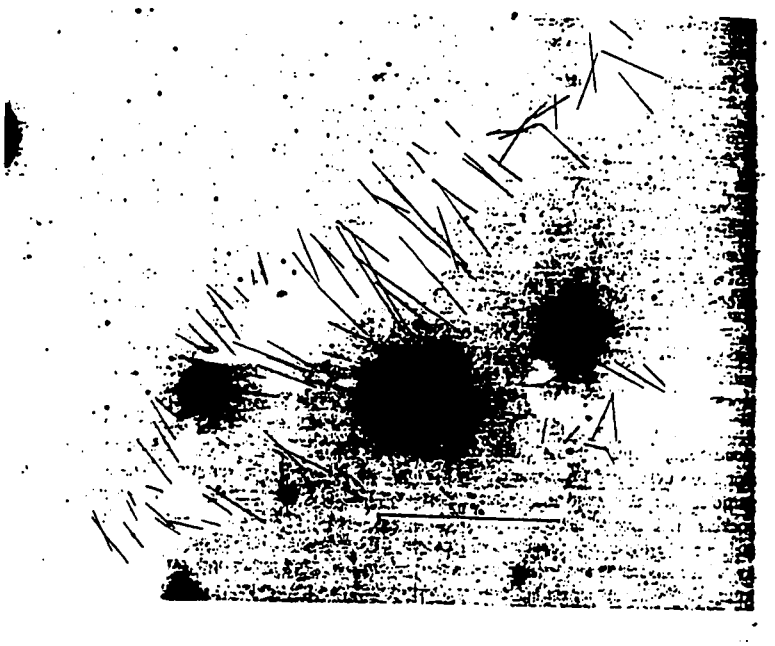

Figure 9a. - The observed polarization vectors (**B**) for the Lupus 1 cloud (white background) superposed on an R-band photograph. This image shows that the cloud has probably been constrained to collapse along the magnetic field lines and that the magnetic field plays a major role in star formation processes (from Strom & Strom 1987).

However, one of the most readily observable phenomena arising from the presence of magnetic fields is the linear polarization of starlight, attributed to extinction by partially aligned, aspherical grains[5]. Figure 9b shows the distribution of infrared polarization vectors in the Chameleon I cloud (this cloud contains one of the closest regions of recent star formation, situated at about 140 pc from the Solar system). There is considerable uniformity in the plot, consistent with the presence of a large

[5]The standard interpretation of interstellar polarization is that the long axes of interstellar grains are oriented perpendicular to the magnetic field. The distribution of polarization vectors on the sky thus provides a two-dimensional representation of the local magnetic field.

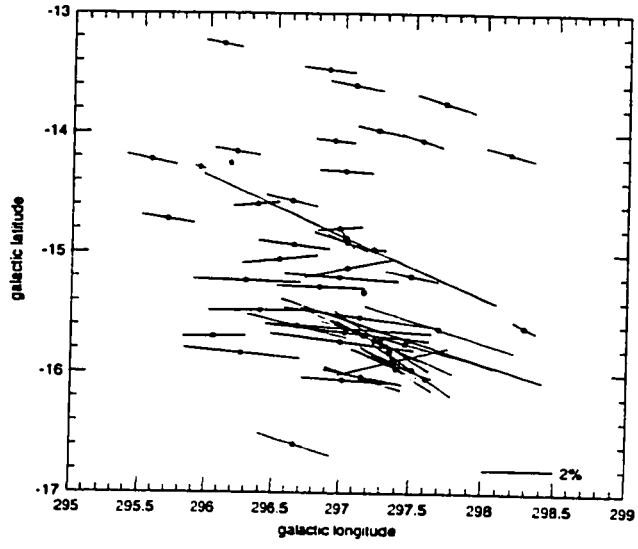

Figure 9b. - Map of infrared polarization vectors in Cha I (from Whittet et al., 1994).

scale magnetic field in the cloud (Whittet et al., 1994). The general orientation of the field is in a direction roughly perpendicular to the long axis of the cloud. Here again, the shape of the cloud is consistent with collapse preferentially along magnetic field lines, with magnetic pressure continuing to support the cloud in its long dimension.

Moreover, when disks are resolved, their axis are usually aligned with the local magnetic field direction. It is probable that the large scale magnetic field determines the orientation of the disks (through magnetic braking effects, Mouschovias & Paleologou, 1980) and the direction of the subsequent outflow.

Even more striking are the recent VLA Zeeman observations of star forming cores (Roberts et al., 1993). The Zeeman effect is observed in the 1420 MHz line of HI.

An example is the W3 core in the W3 complex[6] which shows the morphology of the magnetic structure during core collapse. The observed magnetic field around the core (Figure 9c.) is in excellent agreement with current theoretical ideas on self-initiated star formation (see McKee et al. 1992) where the collapse begins with an initially uniform field frozen into the gas. Gravitational contraction forms a flattened dense cloud supported by the field and the final magnetic configuration is an hourglass shape, as shown in Figure 9d. The theoretical model is superimposed as white contours on the observed field.

3.2 Magnetic Fields around AGNs

Figure 10 is a superposition of radio and optical polarization (**B** vectors) in the M87 jet. The correspondence between the flow and the magnetic field is striking, the magnetic field is predominantly parallel to the jet axis in the inner jet (out to the first knot, 10″ (i.e. 800 pc) from the core). The magnetic field is *perpendicular* to the jet around the knots. Note that in-between knots a rather abrupt change back to **B** *parallel* to the jet occurs[7]. These features have been observed in many extra-galactic jets indicating the importance of magnetic fields on these scales (Biretta et al., 1993).

[6]W3 complex is a region of star formation in the Perseus arm ($l = 134^o$, $b = 1^o$) containing interstellar gas, stars, and several HII regions at various stages of evolution. The youngest and brightest core is the W3 core.

[7]Further maps of how closely the magnetic field in M87 matches the radio structures is given by the deconvolved HST images in Boksenberg et al. (1992).

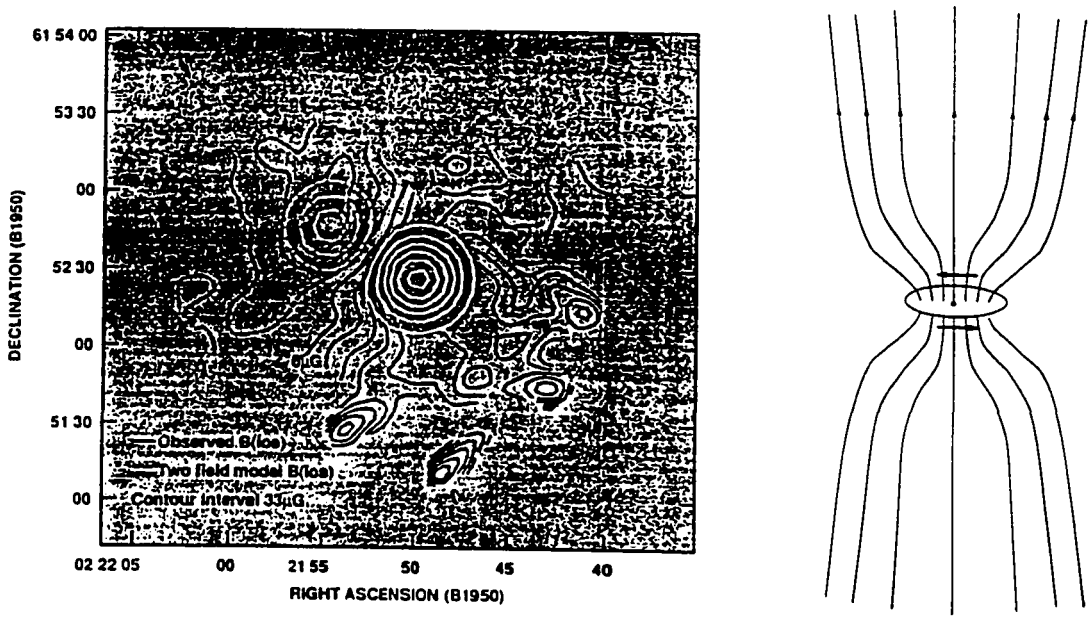

Figure 9c. - A contour presentation of the measured magnetic field strength in the W3 core. The theoretical magnetic field is superimposed as white contours (from Roberts et al., 1993). Figure 9d. - A theoretical model for magnetic field geometry during core collapse. The final magnetic structure is consistent with an originally uniform field that has been pinched into an hourglass shape (right figure) near the core.

4. Disk-Jet Connection

Cabrit et al. (1990) found that the luminosity of the forbidden lines (jets signatures, like $[OI]\lambda 6300$), observed in cTTSs, is better correlated with the excess infrared luminosity (disk signature) than with the photospheric luminosity (Figure 11a,b). This suggests that it is the disk, not the star, that primarily determines the strength of the lines in cTTSs. Probably the best argument for the connection between accretion disks and jets is that no known jets have ever been found to be

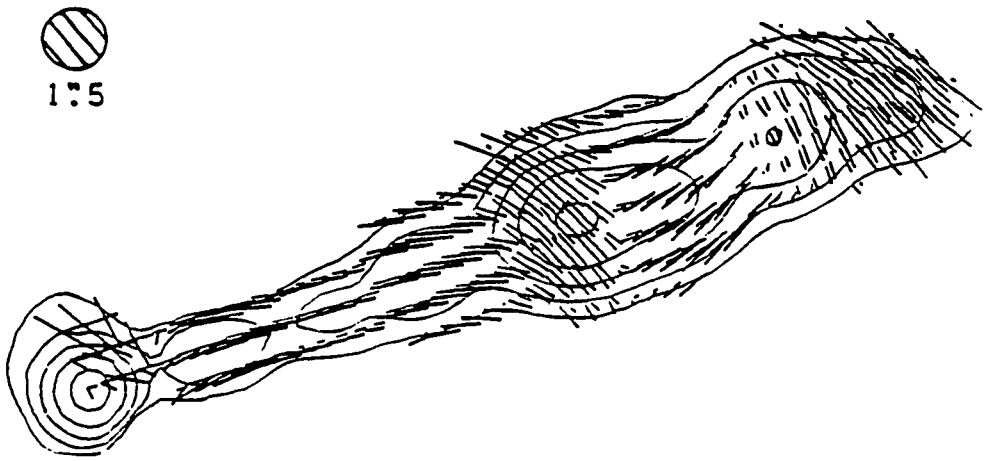

Figure 10. - Comparison of radio (2 cm) and optical (0.65 μm) polarization (**B** vectors) in the jet of M87 at a common resolution of 1".5 $\equiv$ 120 pc (from Biretta et al., 1993).

associated with the weak-line T Tauri stars (wTTSs)[8]. If the jet formation process depended solely on the star itself, one would expect to see them in the case of the wTTSs.

For completeness, we note that the possibility that jets are standard stellar winds (Cantó 1980; Hartmann et al. 1982) has been ruled out. Both the mass and momentum fluxes of the observed jets are much higher than could be provided by the proto-star luminosity, so that the standard thermally and radiation pressure driven stellar wind model cannot explain the observations (DeCampli, 1981; Königl, 1986).

[8]These are T Tauri stars which in most respects resemble the cTTSs with the difference that their spectral energy distributions do not show any evidence for a disk (Osterloh & Beckwith, 1994).

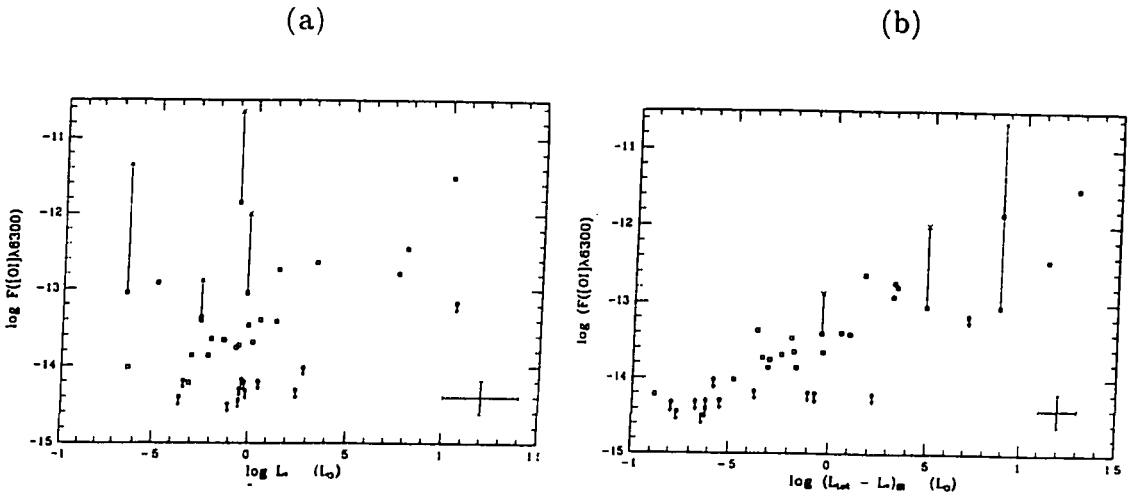

Figure 11. - (a) Relationships between $[OI]\lambda 6300$ and the photospheric luminosity (the open circles represent stars for which no $[SII]$ has been observed). (b) Same as in (a) for the relationships between the $[OI]\lambda 6300$ luminosity and the infrared excess for the TTs studied by Cabrit et al. (1990). There is a clear correlation between the two quantities in (b), not seen in (a).

5. Theoretical Models of Jets

In view of the observational facts presented above and of the existence of a detailed body of analytical work on winds emanating from accretion disks, this thesis concentrates on magnetic outflows emanating directly from accretion disks.

Accretion disks have been proposed to help solve the "angular momentum problem". In star formation theory for example, one of the most critical problems is that the galactic gas from which stars form has an angular momentum per unit mass that

is $10^5 - 10^6$ times larger than that of a star (Pudritz, 1985). It is therefore natural, in view of the observational facts above, to suppose that this angular momentum is shed through the disk. We briefly describe the theory of accretion disks and how, and why, jets come to play an important role in angular momentum transport.

A Keplerian accretion disk with an accretion rate $\dot{m}_a$ releases a known amount of gravitational binding energy of gas as it slowly spirals inward toward the central object. The classical theory of viscous, Keplerian disks (Shakura & Sunyaev, 1973; Lynden-Bell & Pringle, 1974) assumes that the viscous stress in the disk plays the central role in this process. In this case, the gravitational binding energy must all go into the heating of the disk, and the angular momentum is transported radially outward through the disk by turbulent stresses. *There is nothing in this viscous disk theory, however, that compels one to suppose that bipolar flows would arise.* The evidence for the presence of magnetic fields associated with astrophysical jets gives rise to a completely new possibility. The gravitational binding energy that must be released in the accretion process could be converted efficiently into mechanical energy of a disk wind. In addition, the angular momentum that must be transported is very efficiently carried off by the wind through the disk surfaces. We divide the extant models up into two groups, according to whether the wind originate in the disk-core boundary layer or directly from the accretion disk.

5.1 The Steady X-wind model

Imagine with Shu et al. (1994) an infinitely conducting, non-magnetized, thin accretion disk placed in the equatorial plane of a stellar magneton (a star with a pure dipole magnetic field if it existed in a vacuum). The magnetic field tries everywhere to thread vertically through the disk, but the diamagnetic properties of the spiraling disk plasma prevent such penetration and pushes the magnetic field lines towards the star's surface. Eventually the magnetic energy density becomes strong enough to take over, *truncating the disk* at R_t (Figure 12). Interior to R_t particles eventually climb into the closed field lines and are funneled at near free-fall speeds onto the the star.

Slightly exterior to R_t, where the magnetic energy density is lower, the magnetic field lines are bent outwards. When these field lines are tilted radially outward, by more than 30^o from the vertical above the midplane, they launch a centrifugal flow (refer to Shu et al., 1988; Shu et al., 1994, for more details) which is the so-called X-wind. In this model the excess angular momentum brought in through the disk is extracted by the X-wind which flows along the open magnetic field lines.

Despite the necessity of taking this model into consideration (one needs to worry about the inner disk boundary!), we still have few concerns:

i) To avoid any wrapping up of the magnetic field lines (due to the differential rotation), Shu et al. had to assume that interior to R_t the magnetic configuration co-rotates with the star (the magnetic field retains a fixed pattern in a frame that

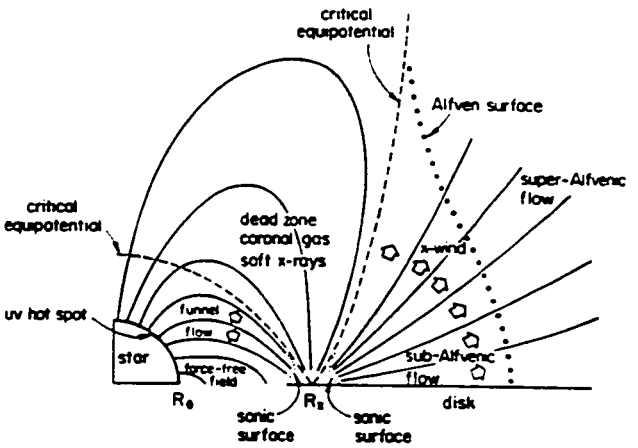

Figure 12. - Shu's et al. (1994) picture for the generation of an X-wind from a proto-star. Open magnetic field lines originating from the X-point drive a magneto-centrifugal wind, which removes angular momentum from the proto-star and permits further accretion. Note that the co-rotation radius is defined here as $R_x = R_t = R_c$.

rotates with the star); that is, $R_t = R_c$ where R_c is the co-rotation radius. Whether or not such an assumption is plausible remains to be carefully worked out before further analysis of the X-winds[9].

ii) The X-wind only exists *if the field lines that would originally close by bending at very large distance back to the star can be opened by the ram pressure*[10] *of the outflowing gas.*

[9]To deal with this problem, Ghosh & Lamb (1978) introduced diffusive instabilities to reconnect the field continually. While this may well happen, the uncertainty introduced in the theoretical calculations vitiates detailed predictions.

[10]Although recent 2-D numerical investigation by Hayashi (1996) have shown that the closed field lines become *partially* open through magnetic reconnection, leading to the ejection of a cold wind, it is important to emphasize that Hayashi neglected the rotation of the star in his work. Furthermore, he needs to run the simulation until a steady state is reached for a more reliable comparison of his results with the steady X-wind model.

iii) Finally, while the scenario in this model may be plausible for the case of proto-stars, it is hard to see how it could be relevant for jets from accreting black holes.

Disk wind models, on the other hand, have the great appeal that they may be applicable to both YSOs and AGNs. Furthermore, they provide a very simple and direct method for transferring angular momentum out of the system, without having to invoke poorly understood *physics at the inner edge of the disk*. Thus without ruling out X-wind models, we now go on to discuss pure disk winds in more details.

5.2 Disk winds

Disk winds can be divided into two categories:

(1) winds driven by magnetic pressure:

Uchida & Shibata (1985) envisaged that a frozen-in field parallel to the disk axis is wrapped up by rotation[11], establishing a large toroidal field. The magnetic stress ∇B_ϕ^2 is then essentially directed parallel to the rotation axis, and drives a wind off the disk surface (Figure 13a). This is the so-called "coiled spring" which propagates away from the disk as a transient, non-linear torsional Alfvén wave and an associated burst of matter.

(2) winds driven by centrifugal forces:

[11] the disk is supposed to be in radial free fall. See §7 for details.

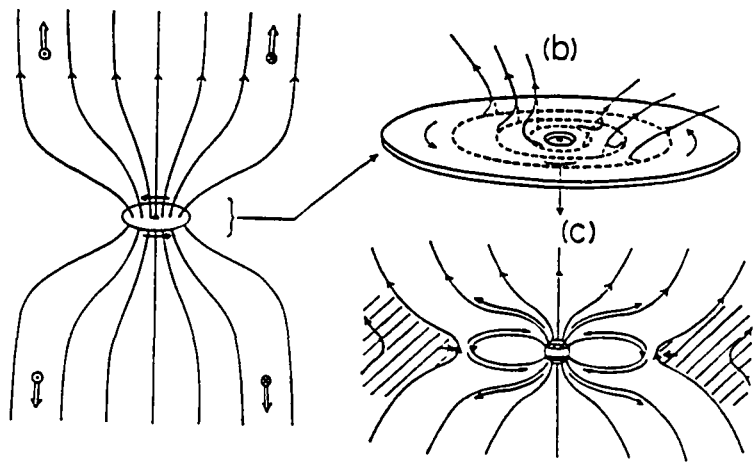

Figure 13a. - A schematic picture of the magnetic pressure driven wind model (from Uchida & Shibata, 1985).

Here, one can picture a particle which is attached to a magnetic field line that is co-rotating with the disk (Figure 14b). In the case of a cold flow, one can show that the centrifugal force will be able to overcome gravity if the inclination angle of the field line with respect to the surface of the disk is less than 60^o (details in the next section).

Both for winds driven centrifugally and for those driven by magnetic pressure gradients, the energy to power the flow comes directly from the gravitational binding energy released by material in the disk as it spirals in towards the central object. The terminal velocity reflects the gravitational potential (or the Keplerian velocity) at the

point of origin. The central object, being formed in the center of the disk, is assumed to derive a significant fraction of its luminosity from accretion. This predicts that there ought to be a direct relationship between the luminosity of the central object and the total energy and the momentum flux of the outflow[12].

The centrifugal wind models are simple in that there is no need to invoke *sub-Keplerian accretion disks* (disks out of radial equilibrium) whose physics still needs to be carefully worked out. *There is further indication (Figure 6b.) that accretion disks are indeed in Kepler rotation.* Thus without ruling out winds driven by magnetic pressure pressure at this stage, we now discuss the simpler case of centrifugally driven winds in more detail.

6. Centrifugally Driven Winds

Figure 13c illustrates the geometry of a magnetic field line, in cylindrical coordinates (r, ϕ, z), as it penetrates through the disk at radius r_o (called the *foot-point*). For a sufficiently cold disk atmosphere, the only forces acting on a parcel of gas attached to the field lines are the gravity of the central star $\mathbf{F_g}$ (if the disk is self gravitating, this of course also contributes) and the centrifugal force due to the Keplerian rotation of the particle $\mathbf{F_c}$.

[12]This statement is only true for the case of black holes and low-mass YSOs ($< 2M_\odot$). High mass stars (Herbig Ae and Be stars) are known to turn on an intense radiation field while still accreting. However, it is still possible for these objects to launch a disk wind early in their evolution, before the radiation dominated era.

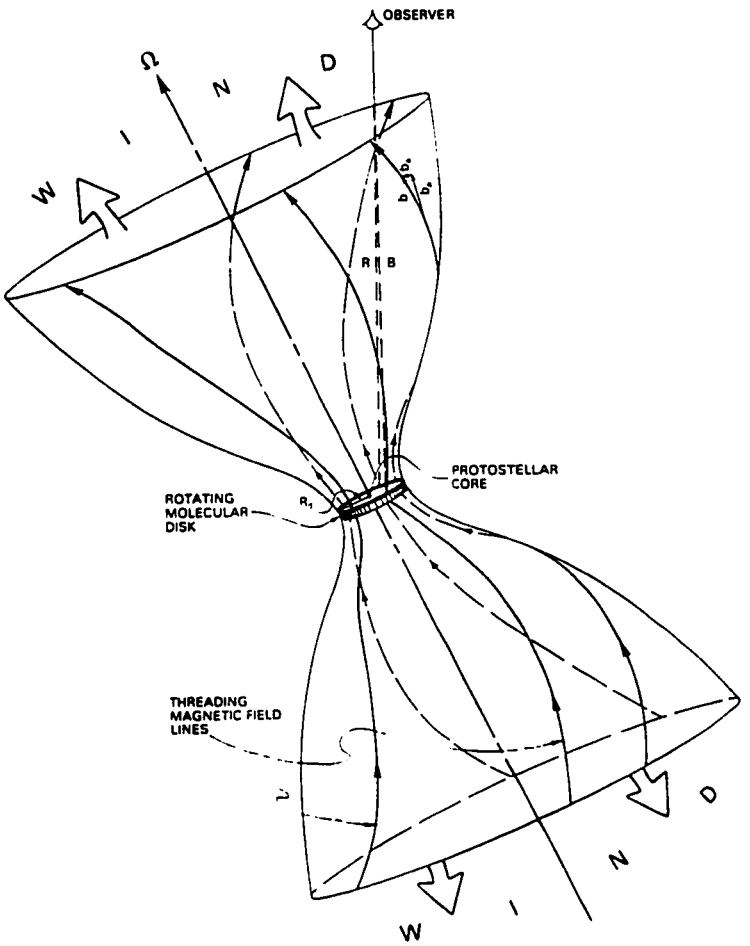

Figure 13b. - Pudritz's (1985) picture for the generation of bipolar wind from a rapidly rotating disk surrounding a central object (a proto-star or a black hole). Accretion at the midplane of the dense disk pinches the magnetic field lines radially, which then drives a strong magnetocentrifugal wind from the disk surface.

By decomposing these forces into components parallel and perpendicular to the magnetic line, one sees that if one goes out along the field line far enough, the effective gravity on the particle vanishes. From that point onwards, the gas will be centrifugally accelerated to form a wind. At larger distances from the disk, the inertia of the gas will cause the magnetic field to become increasingly toroidal (Achterberg et al., 1983). This introduces a magnetic 'hoop' stress which causes the collimation. The reader can

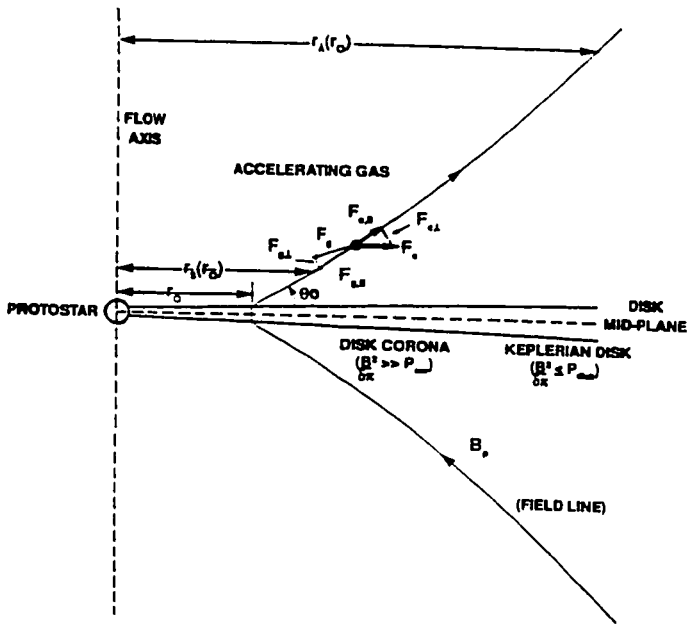

Figure 13c. - Details of the centrifugally driven wind. When one goes out along the field line far enough, the effective gravity on the particle vanishes. From that point onwards, the gas will be centrifugally accelerated to form a wind (from Pelletier & Pudritz, 1992).

think of a bead on a "wire" co-rotating with the Keplerian angular velocity ($\sqrt{\frac{GM}{r_o^3}}$) at the foot-point , which is released from rest at r_o under the assumption of cold gas in the disk atmosphere (it is important to understand that as far as the MHD analysis is concerned, it is possible for flow injected from rest and cold to pass smoothly through a sonic point).

Because of the co-rotation of the magnetic field lines with the disk, the energy and angular momentum is extracted by magnetic torques upon the disk, before transferring it into the centrifugally driven winds described above. Indeed, MHD wind torques

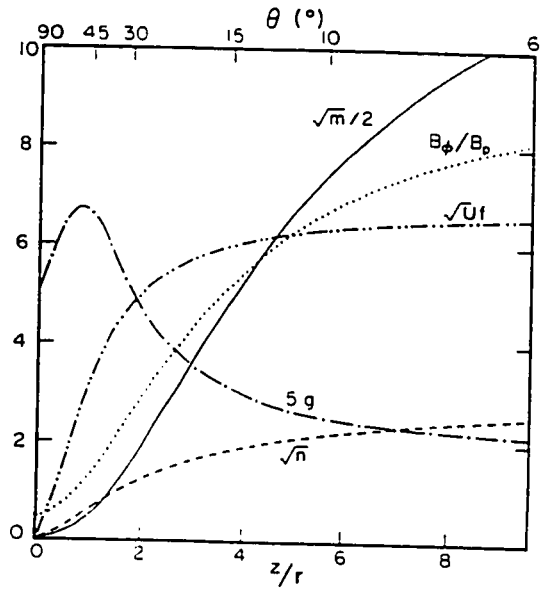

Figure 14. - Here we illustrate the variation of, the Alfvén Mach number $m^{1/2}$, the fast magnetosonic number $n^{1/2}$, the poloidal velocity $U^{1/2}f$, the toroidal velocity g, and the ratio of the toroidal field strength to the poloidal field strength along a single streamline (from Blandford & Payne 1982).

are distinguished from all others (such as viscous torques for example; Shakura & Sunayev 1973, for e.g.) in the sense that angular momentum flows primarily vertically out of the disk surfaces rather than radially through the body of the disk. That is, magnetized disks must essentially rid themselves of their angular momentum by transporting it vertically outwards in a wind. Thus, mass accretion and disk wind mass loss are fundamentally linked with one another. Figure 15 (from Blandford and Payne 1982) displays the evolution of physical quantities along a magnetic field line. Note especially the increase of the toroidal magnetic field which ultimately dominates the dynamics and collimates the flow. Further details and numbers will be given when necessary, in chapter 3.

7. Numerical Simulations of Astrophysical Jets

Numerical simulations are beginning to play a major role in modeling global aspects of astrophysical jets whose time evolution is very difficult to investigate experimentally or theoretically because of the complex physical effects and regimes that exist in these jets (see above).

The early simulations that have been carried out provided us with a wealth of information on the role and the importance of the magnetic field lines in collimating and stabilizing jets (we refer the reader to Norman et al., 1985; Clarke & Norman, 1986; Lind et al., 1989 and Kössl et al., 1990 for more details on the subject). As an example, Figure 15 compares a simulated MHD jet to an HD jet for the same set of parameters except for the absence of the magnetic field in the HD case. It is immediately seen that the essential difference is that shocked jet gas, in MHD, accumulates in a forward "nose-cone" rather than flowing back into the cocoon. Consequently, the cocoons of magnetically confined jets are insubstantial. This is simply explained as follows: at the leading bow shock, the current density is directed radially (perpendicular to the jet axis), and the $\mathbf{J} \times \mathbf{B}$ force points toward the right. This drives the head of the jet forward and explains why the magnetic jet progresses faster into the ambient medium than the HD jet. This lobeless structure turned out to be very different from that of most observed jets (we refer the reader to Leahy, 1993, for informations on the different type of observed jets).

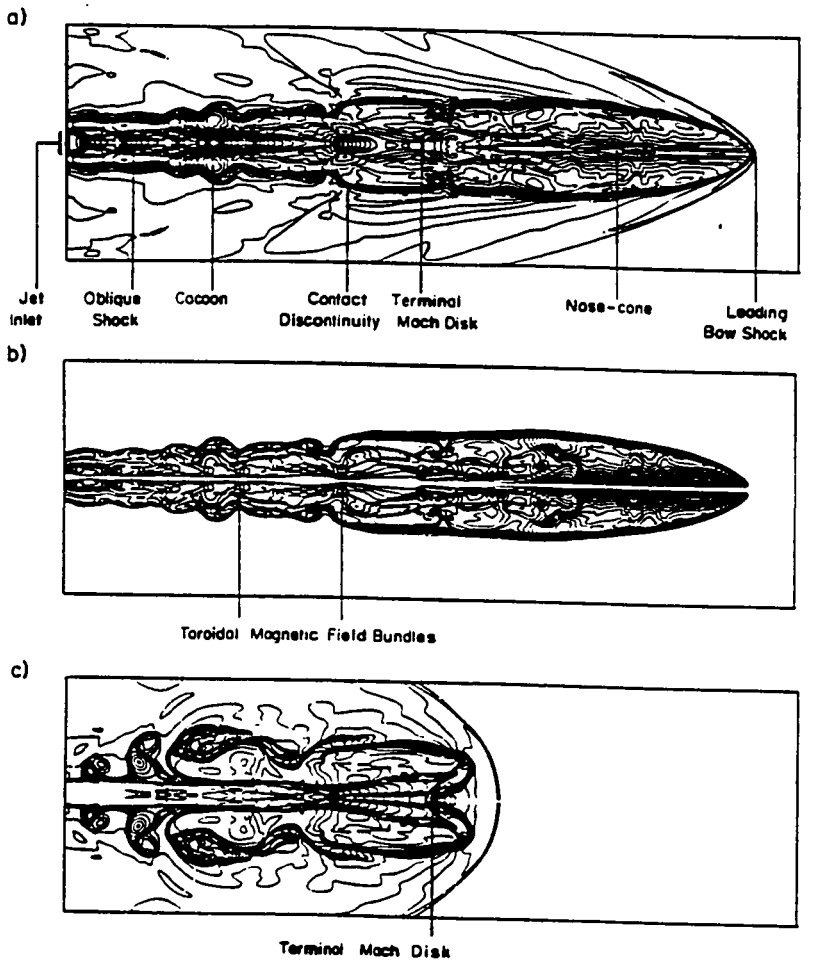

Figure 15. - Comparison between simulations of an MHD jet (the two upper panels) and a HD jet. The head of the MHD jet has a shape of a "nose-cone" due to the confining effect of the toroidal magnetic field (from Clarke et al., 1986).

While these types of numerical investigations help us test some basic ideas, such as the apparent stability of astrophysical jets (as compared to jet in laboratories, see Birkinshaw, 1991) due to the presence of magnetic fields, they still don't inform us about the physics behind the origin of the jets and their acceleration mechanism[13]. Such physics occurs very deep in the gravitational well where sophisticated codes (like

[13]In fact, most of the early simulations of astrophysical jets neglected gravity and assumed a uniform external medium.

ZEUS-2D) seem to have numerical (or technical) difficulties. We will come back to this point in chapter 2.

Because of the many free parameters present in the simulations of jets, among the important ones being the density distribution and the magnetic structure of the "engine", one cannot make final conclusions. Hence, we have decided to only consider simulations where accretion disks threaded by magnetic fields are in play. A few such simulations (of axisymmetric magnetized flows *from an accretion disk*) have been computed, and here we summarize the main physics that came out of the two "classes" of simulations.

In the first class, the internal dynamics of the disk is followed self-consistently. For 2-D models in which the accretion disk has sub-Keplerian rotation rates (Ushida & Shibata, 1985 and Bell & Lucek, 1995), or in which the Balbus & Hawley instability[14] is present (Stone & Norman, 1994), the disk undergoes rapid radial collapse which generates a strong toroidal twist of the threading magnetic field. This generates a burst of matter from the disk surface (refer to Figure 13a). This is simply the numerical aspect of what we have referred to as the "coiled spring" (§5.2). These models have not been run long enough to establish whether or not a steady state ensues, or whether such outbursts would continue over the time-scales demanded by the observations. In the second class of models, one treats the disk as a boundary

[14]This instability is due to the interaction between the disk's magnetic field and the Keplerian fluid shear (see Balbus & Hawley, 1991).

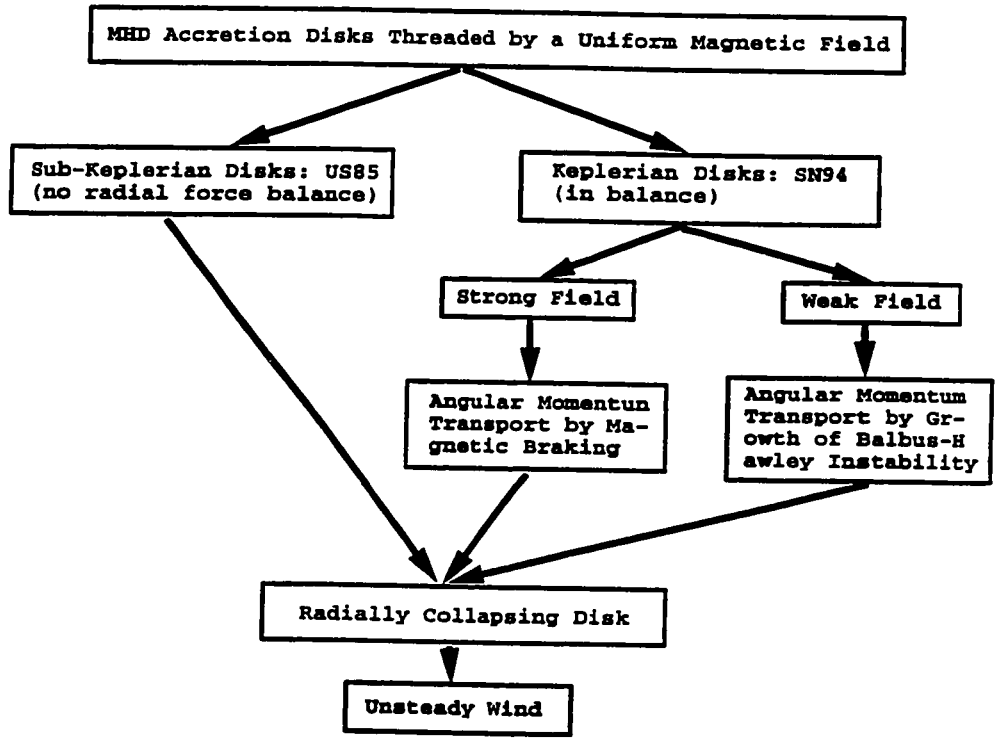

Figure 16. - A schematic flow chart showing the possible paths of evolution of a magnetic accretion disk as observed is the simulations. Regardless of the initial conditions, all the simulations lead to radial collapse of the disk. This then generates the strong ∇B_ϕ^2 pressure that drives the wind.

condition at the base of the wind without following its internal dynamics and assuming that it is in Keplerian equilibrium. This allows one to isolate the physics of the formation of the jet for a well defined set of conditions imposed at the base of the wind (Ustyugova et al., 1995). The main results are more or less similar in this case: the rotation of the disk twists the initial poloidal magnetic field, and this twist propagates into the corona collimating matter into jetlike cylindrical outflow. The flow usually accelerates through the critical points and becomes collimated by the pinching force of the toroidal magnetic field.

There are however many points of concern that we summarize as follows:

Softened Gravitational Potential: To allow for a relatively stable initial state, many authors use a softened gravitational potential (Lovelace et al., 1994; Bell & Lucek, 1995 to cite only few). First of all, softening the potential means that one cannot investigate outflow deep within the gravitational potential well where most of the interesting physics seems to be occurring. Secondly, we found that the softening parameter strongly affects the results. A slight variation in the value of the softening parameter changes the solution dramatically (chapter 3).

The Magnetic Structure: The initial magnetic field configuration usually considered is a split magnetic monopole (Lovelace et al., 1994 and Bell & Lucek, 1995). One needs a more realistic configuration such as expected from MHD collapse calculations (Stepinski et al., 1991 and Lubow et al., 1990). Furthermore, it is not clear how the above simulations deal with the field at the disk-corona interface. Any kink introduced in the initial configuration induces currents (hence forces) into the dynamics making the simulations unreliable. One would hope to reduce the undesired numerical effects as much as possible and reduce the number of free parameters in the problem (chapter 3).

The Diagnostic Routines: Finally, the physics behind the initiation, acceleration and collimation of the jets is still not understood. This is due to a lack of analysis routines that might give us a direct comparison with both observations and theory. This is the reason why jet simulations are sometimes referred to as "Numerical Ob-

servations" of jets. One runs the simulations and tries to summarize the features (morphology, confinement, etc..) observed.

That said, we now go on to present our plan of work, and how we deal with the above points. We remind the reader that, in this thesis, *we do not attempt to model the accretion disks*; rather, they are used as a fixed platform[15] (fixed boundary condition) for the outflow problem.

8. Purpose and Outline of this Thesis

In view of what we have presented above, jets seem to be naturally linked to the global accretion process around proto-stars and black holes. The truth is, we still do not quite understand the exact role played by jets in the process of star and galaxy formation. It is true that jets might rid the source of its angular momentum inducing further accretion, but one still needs to understand why these sources use jets to do the job.

A first step towards such an understanding would be to answer fundamental questions such as: how are these jets (i) generated: (ii) accelerated; and (iii) collimated?

These three points remain extremely difficult to discuss in a detailed and convincing manner. There are two main reasons for this. The first is a lack of unequivocal observations. The phenomena that govern the production of jets almost certainly occur on scales at least two to three orders of magnitude smaller than what instru-

[15]We discuss in chapter 3 the consequences of such an assumption.

ments can currently resolve. The second generic difficulty has to do with the certainty that the physical processes involved in reproducing jets are extraordinarily complex. Indeed, hydrodynamics, plasma physics and radiation physics all play an important role in these phenomena, and on the basis of current observations and theoretical models (see previous sections), choosing which physical processes to emphasize is a hard problem.

It is the goal of this thesis to address the questions above by using a numerical approach. Aside from detailed modeling, we have used our simulations to test the validity of proposed jets mechanisms, to elucidate the behavior and effects of these mechanisms in the non-linear and time-dependent regime, to search for systematic behavior, to act as a bridge between experiment and analytical theory, and finally to serve as a laboratory for discovering new mechanisms. The real challenge lies in tackling such a problem in a simple and understandable manner so as to make it accessible to any scientist. Our plan of work is described below.

We start in Chapter 2 by introducing the reader to the physics of magnetohydrodynamics (MHD) and why it is necessary to use advanced codes such as ZEUS-2D to solve for the equations involved in our problem. Chapter 2 explains the importance of carefully defining one's problem when it comes to numerical simulations. In our case, our initial set up is such that the ZEUS-2D code had to be extended. Furthermore, we have attached an analysis package to the extended version of the code so that future contact might be made between theoretical results and observational data.

Chapter 3 is a preprint of the paper:

"NUMERICAL SIMULATIONS OF ASTROPHYSICAL JETS FROM KEPLERIAN DISKS I: Stationary Models"

Ouyed, R. & Pudritz, E. R. 1997, accepted for publication in the "Astrophysical Journal".

In this paper, we verify some of the basic results of stationary MHD winds. This is the first time such a study is done, where numerical simulations (that is full treatment of MHD winds) are used to test the predictions of steady state theory. This paper has been included here in manuscript form. Because of the first two chapters in this thesis, I have modified this paper as to avoid as many repetitions as possible.

Chapter 4 is a preprint of the paper:

"NUMERICAL SIMULATIONS OF ASTROPHYSICAL JETS FROM KEPLERIAN DISKS II: Episodic Outflows"

Ouyed, R. & Pudritz, E. R. 1997, accepted for publication in the "Astrophysical Journal".

Similarly, this paper has been included here in manuscript form and slightly altered to fit the overall presentation of the thesis. In this paper, we elucidate a simple and robust explanation of why episodic jets might be a natural outcome of accretion via a Keplerian disk. We have shown that knots might be a generic feature of astrophysical jets and are indeed formed as shocks.

Chapter 5 is a preprint of the paper:

"Episodic Jets from Black Holes and Proto-stars"

Ouyed, R., Pudritz, E. R.& Stone, M. J. 1997, accepted for publication in the "Nature" journal.

This paper is complementary to the two papers above. It places our work in the wider context of theoretical and numerical investigations of astrophysical jets. Because of the particular style required by *Nature* publications, I have simply attached it to the thesis.

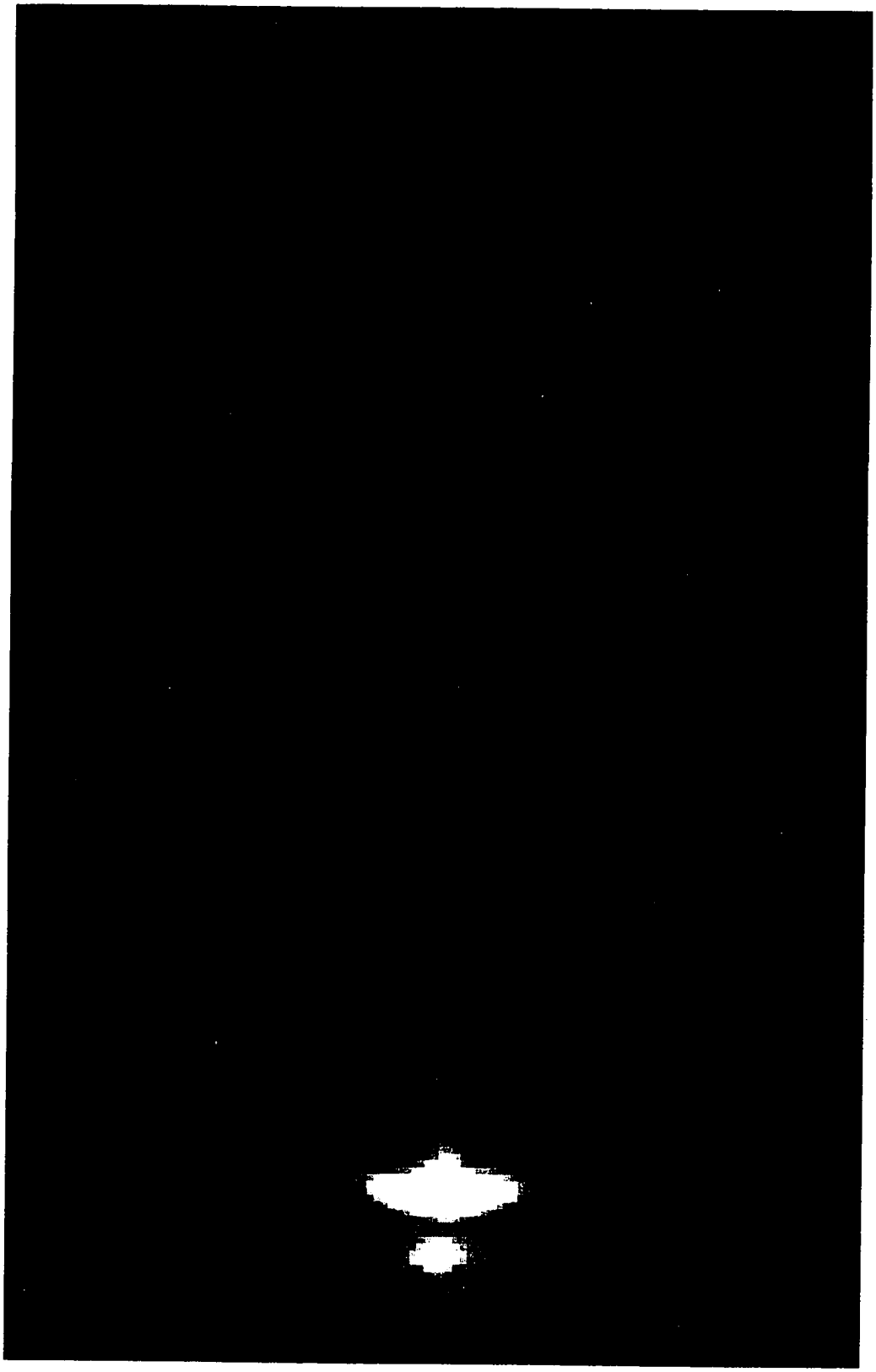

Chapter 2

The Magneto-Hydrodynamics Code

In this chapter, we present the equations describing our jets as well as the philosophy of the numerical code we use to solve them. We show that a numerical simulation can be tractable only if one defines a physically acceptable and realistic initial state. The difficulty in properly coding our problem is outlined as well as the extensions and changes added to the code, which were needed to carry out our investigation. Finally, we emphasize the importance of a good analysis package in analyzing any simulations, if one wants to make contact with theory and observations. We thus describe, and attach to the code, our own analysis package.

1. The equations of Magnetohydrodynamics

Whenever inter-particle collisions are very frequent (at least so frequent that the mean free path of a particle is much smaller than a scale length in the system), then one can use a simple, statistical description of a plasma involving only macroscopic quantities. MHD is the simplest single-fluid model for determining the macroscopic equilibrium and stability properties of a plasma, such as the small scale laboratory plasma in experiments for magnetic fusion, or, the large scale plasma in astrophysics. Specifics are outlined below.

Assuming that the Debye length l_D (determining the shielding distance between charges), the cyclotron radius r_c and the mean free path λ are small compared to the characteristic scale r of a system, $r >> \lambda >> r_c >> l_D$, the plasma may be treated as a single fluid. Intuitively speaking, in the limit of large-wavelength MHD disturbances (large dimensions involved in astrophysics), electrons collide many times with ions and neutrals in the time of the disturbance. This assures us that charge neutrality is a good approximation and that therefore, collective plasma effects can be neglected. Furthermore, because of the low density of such media, collision frequencies between electrons and ions and between ions and neutrals are much smaller than the gyro-frequencies. Hence, the diffusion across the magnetic field lines is neglected since the charged particles make many gyrations around these lines in a collision time. This approximation implies that we can treat the flow as that of a conducting fluid in a

magnetic field.

Mathematically, let us start at the microscopic level. At any instant of time, the state of the system can be completely described by specifying the distribution function, $f(\mathbf{x}, \mathbf{v}, t)$ (phase space density). The time evolution of the system is then given by evolving this distribution function using the Vlasov equation (Landau & Lifshitz, 1960; Spitzer, 1962):

$$0 = \frac{df}{dt} = \frac{\partial f}{\partial t} + \mathbf{v}.\nabla f + \frac{q}{m}(\mathbf{E} + \frac{\mathbf{v}}{c} \times \mathbf{B}).\frac{\partial f}{\partial \mathbf{v}}, \tag{2.1}$$

where q and m are the electric charge and the mass of the particles in question. If we have collisions, then $\frac{df}{dt} = (\frac{\partial f}{\partial t})_{coll}$. The velocity moment is now defined as

$$\bar{Q} = \int d\mathbf{v} Q(\mathbf{v}) f(\mathbf{x}, \mathbf{v}, t). \tag{2.2}$$

For example, when $Q(\mathbf{v})$ takes specific forms, the moment corresponds to well-known macroscopic quantities such as the *density* ($Q(\mathbf{v}) = 1$), *momentum* (($Q(\mathbf{v}) = \mathbf{v}$) and *energy* ($Q(\mathbf{v}) = \mathbf{v}^2$). By taking succesively higher order moments of equation (2.1) coupled with the Maxwell equations, one obtains the equations of MHD (Jackson 1975)

$$\frac{\partial \rho}{\partial t} + \nabla.(\rho \mathbf{v}) = 0, \tag{2.3}$$

$$\rho\left(\frac{\partial \mathbf{v}}{\partial t} + (\mathbf{v}.\nabla)\mathbf{v}\right) = -\nabla p + \mathbf{j} \times \mathbf{B} + \mathbf{F}, \tag{2.4}$$

$$\rho\left(\frac{\partial \epsilon}{\partial t} + (\mathbf{v}.\nabla)e\right) = -p\nabla.\mathbf{v}, \tag{2.5}$$

$$\frac{\partial \mathbf{B}}{\partial t} = \nabla \times (\mathbf{v} \times \mathbf{B}) + \nu_m \nabla^2 \mathbf{B}, \tag{2.6}$$

$$\nabla . \mathbf{B} = 0, \tag{2.7}$$

where the dependent variables are the mass density ρ, the vector velocity $\mathbf{v}$, and the internal energy density e. The quantity $\nu_m = 1/(\mu\sigma)$, is the magnetic diffusivity of the gas which is defined in terms of σ, the electric conductivity of the gas (μ is the magnetic permeability of the media). $\mathbf{F}$ is any external force affecting the dynamics of the plasma.

Equation (2.6) is the so-called induction equation which determines the change in the magnetic field strength in space and time for a given velocity field of the gas. The ratio of the two terms on the right hand side of the induction equation is the magnetic Reynolds number (R_m). If we replace the variables by their approximate scale, we find $R_m = vr/\nu_m$. When $R_m >> 1$, the first term on the right hand side of the expression above dominates and the magnetic field is said to be "frozen-in" to the gas and moves with it. For $R_m << 1$, the diffusion term ($\nabla^2 \mathbf{B}$) is more important and the field diffuses through the charged particles of the gas. The diffusion time can be expressed from the equation $\partial B/\partial t = \nu_m \nabla^2 B$ by using the approximate scales, $t_d = r^2/\nu_m$ where t_d defines the diffusion time.

In view of the large dimensions involved in astrophysical flows on the one hand and the large conductivity of cosmic material ($\sigma >> 1$), on the other hand, the Reynolds number and the diffusion time are effectively infinite. Hence, for non-

turbulent astrophysical plasmas, we shall write the induction equation as:

$$\frac{\partial B}{\partial t} = \nabla \times (\mathbf{v} \times \mathbf{B}). \tag{2.8}$$

In physical terms, this equation states that when the plasma moves in a magnetic field, the induced electric field ($\mathbf{E}$ is given by Ohm's law, $\mathbf{E} = \frac{\mathbf{j}}{\sigma} - \mathbf{v} \times \mathbf{B}$ where j represents the current density) is produced by the motion of the conducting medium relative to the magnetic lines of force. If the electrical resistance is absent ($\sigma \rightarrow \infty$), then the induced electromotive force is zero and, consequently, the conducting fluid should not cross any magnetic field lines of force.

Analysis of the linearized time dependent equations shows that a magnetized gas supports three types of wave motion in general (Krall & Trivelpiece, 1973 and Kantrowitz & Petsheck, 1966). The phase velocity of these waves computed from the dispersion relation of such a medium can be expressed in the form

$$\frac{\omega^2}{k^2} = \frac{1}{2}[(c_S^2 + v_A^2) \pm \sqrt{(v_A^2 - c_S^2)^2 + 4c_S^2 v_A^2 sin^2(\alpha)}] \tag{2.9}$$

with $\alpha = (\mathbf{k}, \mathbf{B})$, c_S the sound speed and $v_A = B/\sqrt{4\pi\rho}$ the so-called Alfvén velocity.

It is convenient to write this as

$$\frac{\omega^2}{k^2} = \frac{v_A^2}{2}[(1 + \beta) \pm \sqrt{(1 - \beta)^2 + 4\beta sin^2(\alpha)}] \tag{2.10}$$

where we have introduced the new variable $\beta = 8\pi p/B^2$, representing the ratio of gas pressure to magnetic pressure. Since we are dealing with a non-dispersive medium,

the phase velocity is independent of wavelength.

The solutions (2.10) describe the three known modes of propagation of small amplitude waves in such media, namely the Alfvén wave ($\omega/k = v_A = B/\sqrt{4\pi\rho}$), the fast wave (+ sign) and the slow wave (- sign). *The Alfvén wave, being transverse, propagates without compression*, while the slow and the fast waves have longitudinal components and are therefore compressive.

In this thesis we will deal with winds whose bulk flow speed is non-relativistic ($\frac{v}{c} << 1$) and that have infinite electrical conductivity[1]. Since, as we have said, the corresponding length scales are much larger than the collisional mean free path: thermal conductivity, viscosity, the Hall effect, and electrical resistivity are negligible. We also neglect self-gravity and radiative transport. The resulting set of equations that describe the dynamical interaction of such fluid with magnetic fields is given by equations (2.3)-(2.7) by taking $\nu_m = 0$. The system of equations is closed with a given equation of state $p = p(\rho, e)$.

[1]Königl (1989) found that within the accretion disk, the field lines are shaped by the inward drift of material which *crosses field lines* by virtue of ambi-polar diffusion (and for more general diffusive processes, see Ferreira & Pelletier, 1955), while above the disk is matched the self-similar wind solution of Blandford & Payne (1982). According to his model, heating of the disk via ambi-polar diffusion, as well as the interaction of the proto-stellar radiation field with the wind material, can account for the optical spectral properties of YSOs. It might be then that the gas at the base of the wind is not a perfect conductor. However, Ouyed & Pudritz (1994b) have shown that one can also explain the observed forbidden-lines (optical) of YSOs as MHD shocks under infinite electrical conductivity conditions.

2. The ZEUS-2D Code

Most of the content of this section is my own summary of the fundamental concepts and basic problems related to computational MHD. This summary is based on reviews by Richtmyer & Morton (1967), Roache (1972), Shulz (1984) and Tajima (1989) to which we refer the reader for further details. The description of the ZEUS-2D code is based on the work by Stone & Norman (1992a and 1992b hereafter, SN92a & b) and Clarke (1996). When necessary, extra references are mentioned in the text.

Equations (2.3)-(2.7) are a coupled set of hyperbolic, partial differential equations (PDEs). Without making restrictive assumptions, it is generally very difficult to find analytical solutions to these equations, and one must turn to numerical methods. However, these equations are not amenable to straightforward time-integration. The main difficulties associated with the numerical approach to MHD equations can be *briefly* summarized as follow:

i) The Negative Density Difficulty: it arises because the continuity equation (2.3) does not explicitly preclude negative density *per se*. Therefore, if for some (numerical) reason the density becomes negative, eq. (2.3) behaves badly and usually leads to numerical instabilities. One usually ensures the non-negativity of density upon transporting the density by the introduction of a fictitious numerical diffusion term which stabilizes the transport, under mass conservation constraint (§2.2).

ii) The Advective Term Difficulty: this is associated with integration within Eulerian frames. Such an integration scheme is *always* numerically unstable (see appendix A), indicating that direct Eulerian algorithms cannot be utilized. One usually uses explicit time centering of variables to stabilize the integration (§2.2).

iii) The Divergence Free Constraint: Maxwell's equations require that the magnetic field satisfy the divergence free constraint ($\nabla.\mathbf{B} = 0$) at all times. *Unless this constraint is built into the numerical evolution equations, accumulation of discretization errors can ultimately lead to gross violation of the constraint equation, and this will force termination of the calculation.* This difficulty is solved in ZEUS-2D through the use of the constrained transport (CT) method first developed by Evans & Hawley (1989), (§2.3).

iv) The Alfvén Waves Transport Difficulty: MHD flows possess a family of incompressible transverse Alfvén waves modes, which tightly couple the evolution of the velocity and the magnetic field components (equations (2.4) and (2.6)). Such waves can exhibit discontinuities (rotational, transverse) at current sheets. Unlike HD shocks, these structures are not dissipative, which rules out the use of the dissipative numerical algorithms to model them. To overcome such a problem ZEUS-2D uses the Method of Characteristic to propagate the discontinuities along the Alfvén waves characteristics (§2.3).

Numerical algorithms for solving the difficulties above have been developed, and have been implemented in an abundance of computer codes (Ushida & Shibata, 1985;

Brio & Wu, 1988; Evans & Hawley 1988; Zachary & Collela, 1992; Dai & Woodward, 1994, Lovelace et al., 1994; Hayashi, 1996; to cite only the most recent). One such code, designed for solving fluid dynamical problems in astrophysics, is ZEUS-2D. In ZEUS-2D, state-of-the art hydrodynamical and MHD algorithms have been incorporated. Furthermore, a more general formalism allowing the use of any orthogonal coordinate system has been incorporated into the code (SN92). ZEUS-2D is now a two dimensional Eulerian *finite difference code* solving the equations of astrophysical fluid dynamics including the effects of magnetic fields, radiation transport, self-gravity and rotation. *We remind the reader that, in this thesis, we are neglecting radiation effects and self-gravity.*

2.1 The Finite Difference Grid

The mesh used in ZEUS-2D is unusual when compared to the standard finite difference mesh. We will see the advantages of the mesh staggering in ZEUS-2D when describing the advection algorithms (§2.2) as well as the algorithms used in propagating the Alfvén waves.

In Figure 1a, (adapted from SN92), we show the two-dimensional staggered grid used by ZEUS-2D. The, "a-grid", is defined by the co-ordinates $(x1_a(i), x2_a(j))$ while the "b-grid", co-ordinates $(x1_b(i), x2_b(j))$, define the zone centers. In such a mesh, the scalar variables (ρ, e) are "zone centered" while the vector variables $(\mathbf{v}, \mathbf{B})$ are "face-centered" (Figure 1b). Thus, gradient components of zone centered scalars are

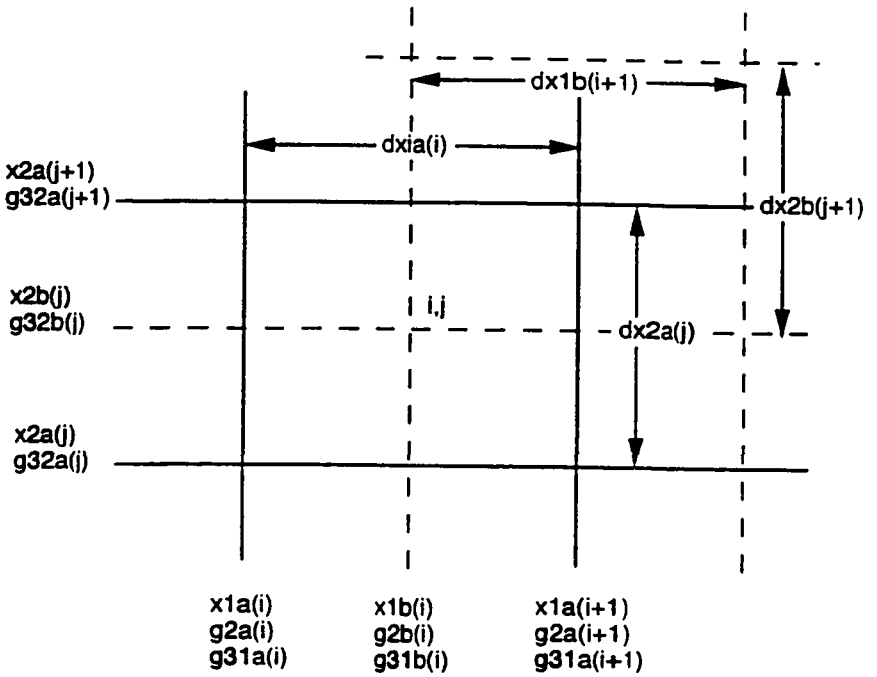

Figure 1a. - Coordinate grid definitions on the staggered grid used in ZEUS-2D: solid lines="a-mesh"; dashed lines="b-mesh" (from SN92a). g_2, g_{31} and g_{32} are the scale factor variables of the diagonal metric tensor which describes the particular orthogonal system of work (here, in cylindrical coordinates, $g_2 = 1$ and $g_{31} = g_{32} = r$).

face-centered quantities, divergences of face-centered vectors are zone-centered, and curl components of face-centered vectors (e.g., the current density $\mathbf{J} = \nabla \times \mathbf{B}$) are "edge-centered".

Note too that grid variables have specific locations attributed to them. Thus, $x1_a(i)$ is a face-centered quantity while $dx1_a(i) = x1_a(i+1) - x1_a(i)$ is a zone-centered quantity, etc.. In this scheme, the MHD equations can be differenced directly. All difference equations use the following nomenclature. The indices (i,j) denote the variable value at the (i,j)th zone located at one of the zone center, zone face, or zone

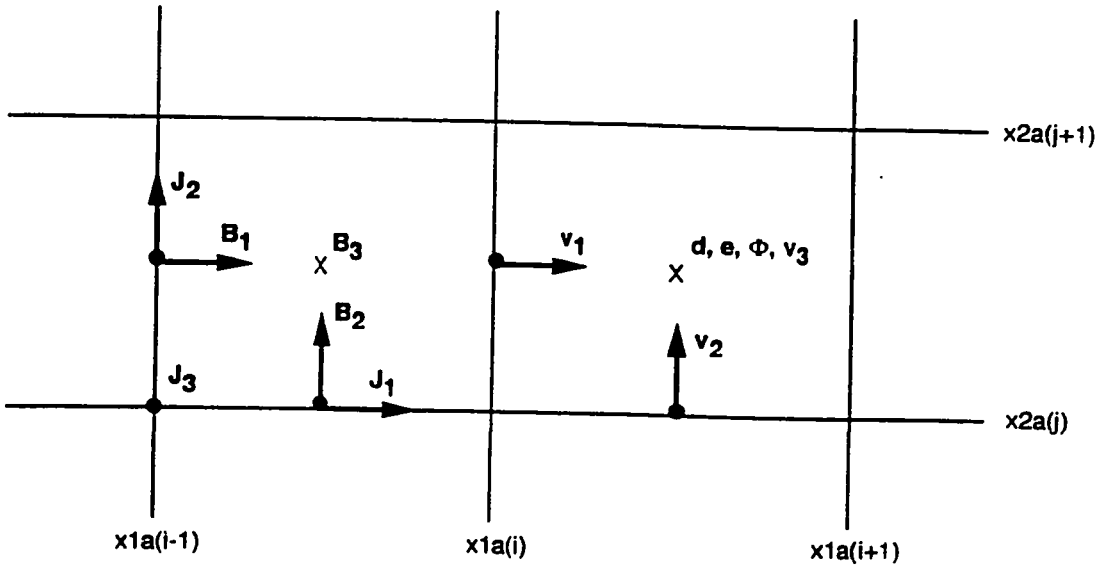

Figure 1b. - Centering of variables. $j1$,$j2$ and $j3$ are the current density components (from SN92a).

edge as discussed above. The indices is and js stand for the starting indices with $(x1a(is) = x2a(js) = 0.0)$, at the origin of the a-mesh.

2.1.1 Covariant Formalism

ZEUS-2D solves the MHD equations in covariant form for an arbitrary orthogonal coordinate system described by the metric

$$ds^2 = g_1^2 dx_1^2 + g_2^2 dx_2^2 + g_{31}^2 g_{32}^2 dx_3^2. \tag{2.11}$$

where g_2, g_{31} and g_{32} (Figure 1a) are the scale factor variables of the diagonal metric tensor which describes the particular orthogonal system of work (in cylindrical

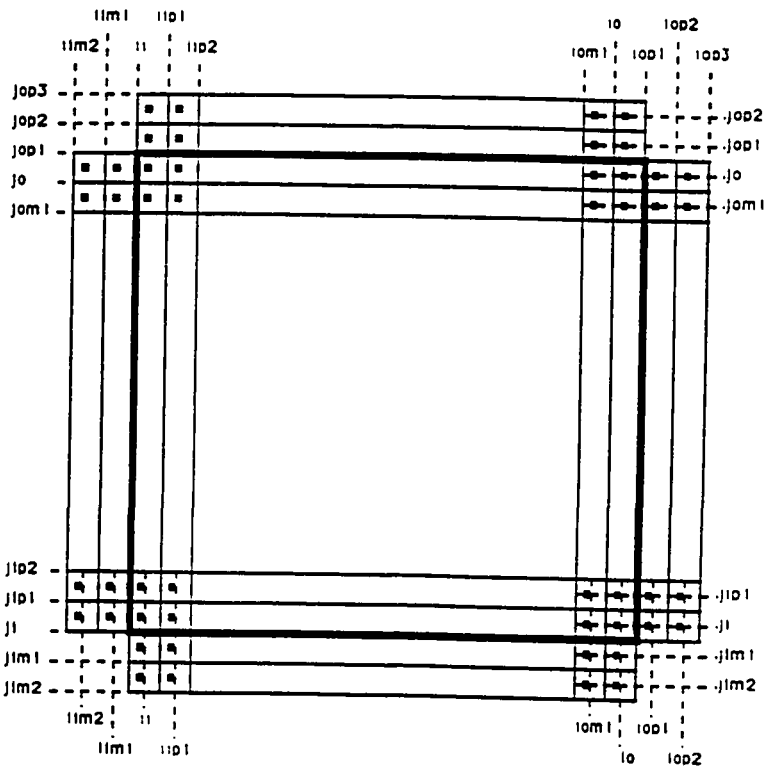

Figure 1c. - Global picture of the mesh. The computational domain, defining the active zones, is interior to the solid line. Two rows of ghost zones are added at each boundary as required by the PPA (from SN92a).

coordinates, $g_2 = 1$ and $g_{31} = g_{32} = r$).

For axisymmetric flows (our case) all spatial derivatives in the x_3 direction are set to zero, i.e $\partial/\partial x_3 \equiv 0$. Note that while this reduces the number of independent variables to two (x_1, x_2), all components of vectors and tensors are retained. *This is why such codes are referred to as 2.5 dimensional.* Currently ZEUS-2D implements Cartesian, cylindrical and spherical polar geometries.

Finally, the two rows zones beyond the computational domain are called "ghost" zones. They are defined at $(is-1), (is-2), (js-1)$ and $(js-2)$ which are added along each boundary, as required by the Piecewise Parabolic Advection (PPA) scheme

implemented in ZEUS-2D (§2.2.2). Values for the variables in the ghost zones are specified using boundary conditions appropriate to the geometry and physics of the problem being solved (Figure 1c). Thus the evolution equations are not solved in the ghost zones. However, *it is important to know that the ZEUS MHD algorithms will evolve the magnetic field components in a divergence free manner, even in the ghost zones.* This is an important point when considering the evolution of our initial magnetic configuration (chapter 3). In the "active" zones, the evolution equations are used to update the variables.

2.2 Interpolation Algorithms

ZEUS-2D solves the fluid equations using the method of finite-differences with a time explicit, multistep (*operator split*) solution procedure. An operator split method breaks the solution of the PDEs into parts, with each part representing a single term in the equations. Each part is evaluated successively using the results from the update preceding it. The individual parts in the solution procedure are grouped into two steps, called the *source* and the *transport steps*. The separation of the differentiation procedure into such terms allows one to isolate the Euler term so that it can be treated properly (see Appendix A). One can think of the source step below as the MHD equations without the Euler terms.

2.2.1 Source Step

In the *source step* one calculates the acceleration of the fluid velocity due to pressure, gravity and Lorentz forces[2], and as well as the change in the gas internal energy due to the work done by the pressure using finite-difference approximations. Thus;

$$\rho\frac{\partial \mathbf{v}}{\partial t} = -\nabla\rho - \rho\nabla\Phi - \nabla.\mathbf{Q} - \nabla(\frac{B^2}{2}) + (\nabla.\nabla)\mathbf{B} \tag{2.12}$$

$$\frac{\partial e}{\partial t} = -p\nabla.\mathbf{v} - \mathbf{Q} : \nabla\mathbf{v}, \tag{2.13}$$

where $\mathbf{Q}$ represents the artificial viscous tensor introduced in the code to treat shock waves. The artificial viscosity is adopted according to the von Neumann & Richtmyer approach (von Neumann & Richtmyer, 1950). The triumph of the von Neumann & Richtmyer approach is the realization that a nonlinear viscous pressure, sensitive only to compression, would result in the correct entropy jump across shocks and the correct shock propagation velocity, *while having negligibly small effect away from shocks.*

2.2.2 Transport Step

In the transport step (Eulerian transport), fluid and magnetic flux is transported through the computational mesh (or through cells) conservatively using finite-

[2]the longitudinal and the transverse Lorentz acceleration in equation (2.12), are treated separately for reasons that will become clear later (§2.4).

difference approximations to

$$\frac{d}{dt}\int_V \rho dV = -\int_S \rho(\mathbf{v}-\mathbf{v_g}).\mathbf{dS}, \tag{2.14}$$

$$\frac{d}{dt}\int_V \rho \mathbf{v} dV = -\int_S \rho \mathbf{v}(\mathbf{v}-\mathbf{v_g}).\mathbf{dS}, \tag{2.15}$$

$$\frac{d}{dt}\int_V e dV = -\int_S e(\mathbf{v}-\mathbf{v_g}).\mathbf{dS}, \tag{2.16}$$

$$\frac{d}{dt}\int_S \mathbf{B}.\mathbf{dS} = -\int_C (\mathbf{v}-\mathbf{v_g}) \times \mathbf{B}.\mathbf{dl}, \tag{2.17}$$

The integrations are performed over zone volumes (V), surface area (**S**), or face perimeters (**l**), where $\mathbf{v_g}$ is a grid velocity relative to an Eulerian observer.

ZEUS-2D uses the first order "donor cell" scheme as well as the second order "van Leer" scheme (1977)[3]. However, the *main* interpolation scheme used is the *piecewise parabolic advection* (PPA) method (Collela & Woodward, 1984). PPA is a third order method using parabolic interpolation within a zone to compute upwind interface values. The heart of the PPA method lies in the computation of these interface values making it a very robust method compared to the standard ones[4]. This is the one we will use in this thesis.

One key point to be made is that by using parabolic interpolation, the PPA method requires that two points be specified upwind of the interface. In general PPA uses a five-point molecule centered on the zone being updated. *Thus, at boundaries,*

[3]The order of accuracy of a scheme refers to the order of the first term dropped in the Taylor series expansion used to generate the method.

[4]Refer to SN92a & SN92b for a detailed comparison of the three schemes implemented in ZEUS-2D.

values must be specified for two ghost zones beyond the computational domain (see Figure 1c.).

Finally, note that the staggered mesh used in ZEUS-2D reduces the number of interpolations needed during the advection step. Thus, when centered on zone interfaces, the velocities naturally describe the flux of fluid into or out of a zone. However, staggered meshes often require additional averaging of variables in other parts of the calculation (for instance, the momentum equation where mass density and velocities are used together), which can ultimately limit the overall accuracy of the code. This turned out to be a major difficulty in our work as described and explained in §3.2.

2.3 Constrained transport (CT)

Note that equation (2.17) can simply be written as:

$$\frac{d\Phi_m}{dt} = \frac{d}{dt}\int_S \mathbf{B}.\mathbf{n}.dS = \int_l \epsilon.d\mathbf{l} \tag{2.18}$$

where $\epsilon = (\mathbf{v} - \mathbf{v_g}) \times \mathbf{B}$ is the EMF driving the evolution of the magnetic field and Φ_m is the magnetic flux.

Now, if we consider the magnetic flux components $\Phi 1$ and $\Phi 2$ piercing the faces of the control volume created by extending a zone in the x_3 direction (Figure 2), and $\epsilon 1$, $\epsilon 2$ and $\epsilon 3$ are the edge-centered EMF's. The magnetic flux is then expressed as

$$(\Phi 1^{n+1}_{i,j} - \Phi 1^{n}_{i,j})/\Delta t = -\epsilon 2^{n}_{i,j}\Delta x_2 - \epsilon 3^{n}_{i,j}\Delta x_3 + \epsilon 2^{n}_{i,j}\Delta x_2 + \epsilon 3^{n}_{i,j+1}\Delta x_3 \tag{2.19}$$

$$(\Phi 2_{i,j}^{n+1} - \Phi 2_{i,j}^{n})/\Delta t = -\epsilon 1_{i,j}^{n}\Delta x_1 - \epsilon 3_{i,j}^{n}\Delta x_3 + \epsilon 1_{i,j}^{n}\Delta x_1 + \epsilon 3_{i,j+1}^{n}\Delta x_3; \quad (2.20)$$

or

$$(\Phi 1_{i,j}^{n+1} - \Phi 1_{i,j}^{n})/\Delta t = +(\epsilon 3_{i,j+1}^{n} - \epsilon 3_{i,j}^{n})\Delta x_3, \quad (2.21)$$

$$(\Phi 2_{i,j}^{n+1} - \Phi 2_{i,j}^{n})/\Delta t = -(\epsilon 3_{i,j+1}^{n} - \epsilon 3_{i,j}^{n})\Delta x_3. \quad (2.22)$$

By adding the two equations together, one can calculate the new total flux through the surfaces of the control volume. Since the contribution from the EMF along each edge appears once in each equation with opposite signs, all EMFs terms will cancel in the full sum (over the whole cell) of the total flux. That is, if the old flux obeys the divergence free condition then the new flux will continue to do so. Hence,

$$\frac{d}{dt}(\nabla.\mathbf{B}) = 0 \quad (2.23)$$

will be maintained to within machine round-off errors. Thus this scheme *preserves* the initial magnetic field divergence rather than guaranteeing that it shall be zero (Evans & Halley, 1989). It is therefore left to the user to ensure that the magnetic divergence is *initialized to zero* (§3.1).

This method is a big improvement compared to the usual method of evolving the magnetic vector potential (defined via $\mathbf{B} = \nabla \times \mathbf{A}$). With the CT scheme, numerical second derivatives are not needed[5] and no anomalous current (forces) reversals are

[5]The difficulty with evolving the vector potential rather than the field components themselves is in constructing an accurate representation of the Lorentz force $(\nabla \times \mathbf{B}) \times \mathbf{B}$ in the equation of

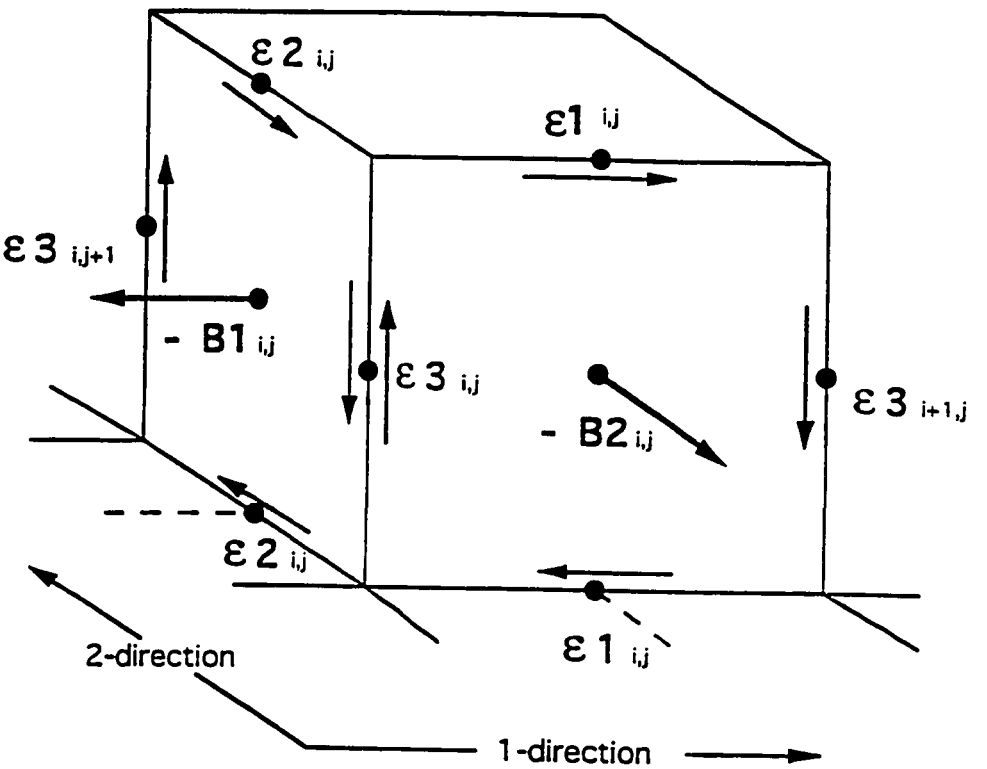

Figure 2. - When the two dimensional grid is expanded in the 3-direction (plotted vertically in this figure), the closed contours around which the EMF is integrated (to evolve the components of the magnetic flux using the integral form of Faraday's law) become evident. Arrows indicate the direction of the path integral around the edges. Note the magnetic field components are shown pointing in the opposite direction of the coordinates unit vectors (from SN92b).

introduced in the vicinity of sharp features (such as shocks and discontinuities) in the magnetic field (Clarke, private communications).

In essence, CT is a formalism for conservative differencing of the integral term of the induction equation (which is simply part of the transport step). By guaranteeing numerical conservation of the magnetic flux, the divergence free constraint is automatically satisfied by the evolved field components, to machine round off error.

motion. This requires taking a second derivative of the vector potential.

This is true regardless of the method used to compute the EMF. However, one is not completely free to choose any method to compute the EMF; numerical stability and accuracy requirements must still be met. Simply put, since

$$\epsilon_3 = v_1 B_2 - v_2 B_1, \tag{2.24}$$

some sort of space interpolation is needed to compute the components of the velocity and the magnetic field at zone corners *from the face centered values evolved in ZEUS-2D.* Simple arithmetic averaging is inadequate. Furthermore, in MHD one needs to worry about the proper evolution of shear Alfvén waves when integrating from time-step n to time-step $(n+1)$. The method used in ZEUS-2D is described below.

2.4 Method of Characteristics (MOC)

In what follows, we examine how ZEUS-2D uses the CT formalism to evolve the poloidal magnetic components. Because these components are advanced during the transport step (via the induction equation), while the poloidal velocity components are advanced during the source step, one faces the dilemma of what we define here as "numerical decoupling" between the velocity and the magnetic field. ZEUS-2D fixes this problem by delaying the transverse Lorentz acceleration (in the source step), as explained in the following sections.

2.4.1 Evolving the Poloidal Magnetic Field

We have seen in §2 that multi-dimensional MHD flows support Alfvén waves modes which propagate along *field lines* at the Alfvén speed. Such modes can include discontinuities in the velocity and magnetic field components orthogonal to the direction of propagation, but since these waves are non-compressive, no discontinuities in any other dynamical variables are present. *Finite difference approximations to the evolution equations will, of course, break down in these discontinuities.* In HD, when this situation occurs (such as shocks or contact discontinuities), the discontinuities are usually partially smeared out over several zones so that the finite difference equations may still be applied (by using, for example, artificial viscosity (see §2.2.1). In order to evolve discontinuous Alfvén waves stably, an MHD algorithm has been implemented in ZEUS-2D. It uses the MOC (Appendix B) to identify the upwind values for both fluid and Alfvén wave motion, resulting in stable evolution properties. The strength of the ZEUS-2D code is in developing a stable method for evolving Alfvén waves with the CT method. *The key point is in incorporating information from the Alfvén wave characteristics into the calculation of the EMF*[6].

For example, by substituting expressions for the magnetic fluxes in terms of the grid coordinates and magnetic field components, one can rewrite equation (2.18) as evolution equations for the field components. That is,

$$(B_1 \Delta S_1)_{i,j}^{n+1} = (B_1 \Delta S_1)_{i,j}^{n} + \Delta t^n [+(\epsilon 3_{i,j+1}^{n+1/2} - \epsilon 3_{i,j}^{n+1/2}) \Delta x_3], \tag{2.25}$$

[6]The discontinuities are found through the method of crossing characteristics.

where ZEUS-2D uses the MOC to evaluate ϵ_3 using the *characteristics of incompressible MHD flows*, at $(n+1/2)$. That is,

$$\epsilon 3_{i,j}^{n+1/2} = v1_{i,j}^{n+1/2} B2_{i,j}^{n+1/2} - v2_{i,j}^{n+1/2} B1_{i,j}^{n+1/2} \tag{2.26}$$

where quantities at time $(n+1/2)$ are evaluated from values interpolated (MOC) to the bases of the characteristics (Figure 3).

The procedure is briefly described as follows (using the 1-direction only). Firstly, ZEUS-2D finds the characteristics (see Appendix B) and then finds the bases of $C^{\pm}$ (refer to Figure 3) by using 2-point averages to estimate preliminary values of the characteristic velocities, namely:

$$C_1^{\pm} = < v_1 >_2 \mp \frac{1}{\sqrt{\rho}} < B_1 >_2 . \tag{2.27}$$

From time-step $(n+1/2)$, one follows the characteristics back to the curve on which the initial data are prescribed (at time-step n) to determine the Riemann invariants (defined as Γ in Appendix C). Using these values, one can write quantities along the characteristics $C^{\pm}$ in terms of the given data at the bases ($v_{1,2}^{\pm}$ and $B_{1,2}^{\pm}$). This is done by ensuring that, at the intersection of the characteristics, the Riemann invariants must be equal ($\Gamma^+ = \Gamma^-$) to get

$$v_2^{*,n+1/2} = \frac{1}{2}[v_2^{+,n} + v_2^{-,n} + \frac{1}{\sqrt{\rho}}(B_2^{+,n} - B_2^{-,n})] \tag{2.28}$$

$$B_2^{*,n+1/2} = \frac{1}{2}[B_2^{+,n} + B_2^{-,n} + \sqrt{\rho}(v_2^{+,n} - v_2^{-,n})]. \tag{2.29}$$

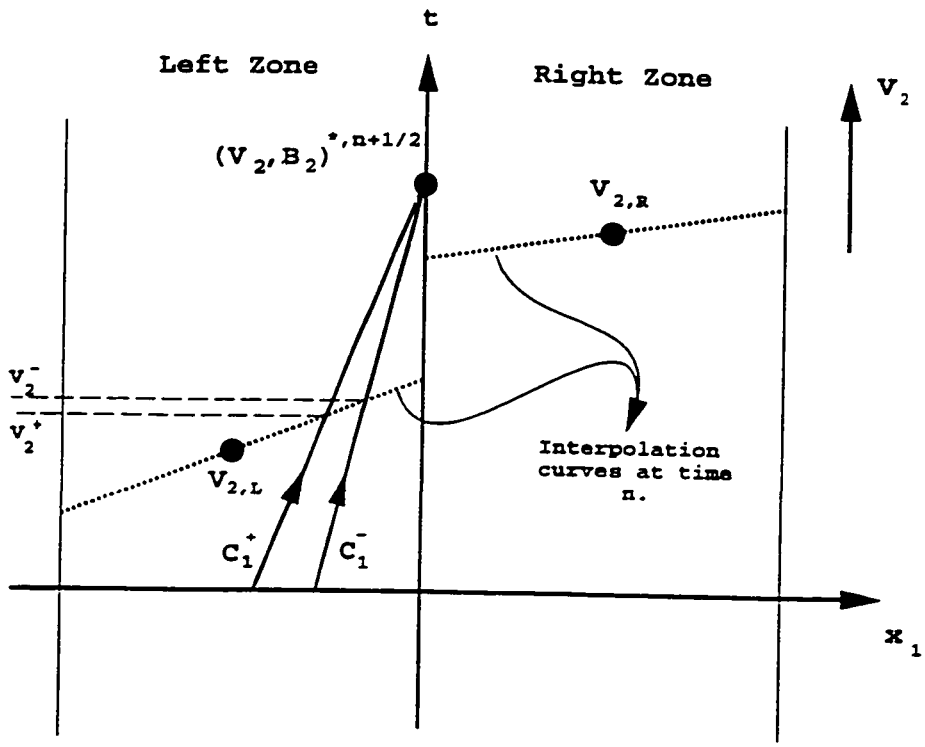

Figure 3. - A one dimensional space-time diagram showing the locations of the forward and backward facing characteristics C^+ and C^-, which are used to compute the partially advanced quantities v^* and B^* with the method of characteristics. In space, v^* and B^* are centered at zone interfaces, in time they are at the half-time step $n + 1/2$. The values for the variables at the foot-points of the characteristics are computed using upwind interpolation between quantities at time level n, located at zone centers.

Values for the variables $v_2^{+,n}$ and $B_2^{+,n}$ (on the C^+ characteristic) and $v_2^{-,n}$ and $B_2^{-,n}$ (on the C^- characteristic) are computed using upwind interpolation (donor cell, van Leer or PPA). An entirely analogous procedure is used to find $v_1^{*,n+1/2}$ and $B_1^{*,n+1/2}$, and the four starred values are used to determine $\epsilon 3$. Basically, the code uses characteristic equations (2.28) and (2.29) to compute partially advanced values for the velocities and magnetic field components, and then these values are used to generate

the EMF in the CT scheme to update the poloidal magnetic field components [7]. We refer the reader to SN for more details.

ZEUS-2D uses the Lagrange frame (the transport step) to solve the induction equation (or to evolve the poloidal magnetic field components), while the momentum equation is treated in the Eulerian frame (source step). This procedure generates asymmetric behavior of forward and backward moving Alfvén waves. To correct this problem, ZEUS-2D incorporates the information gained from the MOC into the equation of motion by splitting the Lorentz acceleration into the longitudinal term (compressional term) and the transverse term (Alfvén term). That is, while the longitudinal acceleration is performed in the source term using quantities at time n, the transverse acceleration is performed using the time advanced variables $(n+1/2)$[8].

Once the update above is completed, one can then perform the advection of the physical quantities, using one of the three interpolation algorithms installed in ZEUS-2D (donor cell, van Leer or PPA).

---

[7]Note that, due to the centering of the velocity and the magnetic field components at the same position on the mesh, ZEUS-2D can naturally apply the MOC to the coupled pairs. The resulting updated values from each direction will be known at cell corners in both cases. *In fact, it is for this reason that one chooses such an unusual centering of variables.* For grids in which the velocity and magnetic field are not co-spatial, SN92a and SN92b found that averaging of one to the position of the other interferes with the tracking of Alfvén waves with the characteristic method, and does not produce stable algorithm.

[8]SN92a and SN92b state that, " We have found by experience that a stable algorithm is not possible unless the transverse Lorentz acceleration is updated using the time advanced variables (at time-step $(n + 1/2)$)". Here, we refer the reader to Clarke (1996). Clarke designed an alternative modification to the MOC scheme where both the magnetic induction and the momentum transport steps are done simultaneously.

We will see in §3.2.3 that the **MOC** as used in ZEUS-2D presents a major inconvenience when setting up our initial state and can sometimes lead to numerical instabilities.

2.4.2 Evolving the Toroidal Magnetic Field

Here, one does not need a CT algorithm since the toroidal component will satisfy the constraint equation at all times by symmetry ($\partial/\partial\phi = 0$). However, one still requires the MOC to stably propagate *torsional Alfvén waves.* The same procedure as in §2.4.1 is used where one uses the MOC to estimate partially updated variables for v_3 and B_3 at the half time step, which can then be used in finite difference forms of the equation of motion to evolve the variables. *Here, again, the MOC is not actually used to evolve the variables, but merely as an intermediary step which might infer information about any plausible discontinuities (crossing characteristics).* We refer to SN92 for the technical details used in this procedure. Here again, once the update above is completed, the advection of the quantities is performed.

Figure 4, adopted from SN92b, summarizes the different steps used in the code.

2.5 Stability vs Accuracy

Since ZEUS-2D is an explicit code, the time-step must satisfy the *Courant-Friedrich-Lewy* (CFL) stability and accuracy condition (Courant-Friedrich-Lewy, 1948). Its precept is that no signal shall cross more than half of any mesh zone in any given

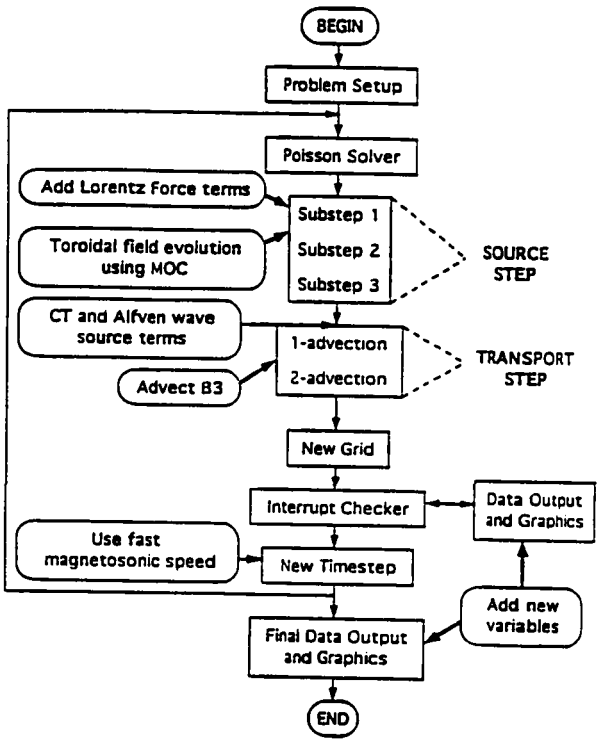

Figure 4. - A schematic flow chart of the ZEUS-2D code diagraming the major steps in the solution procedure, as described in the text (from SN92b).

time step. Physically, this is analogous to maintaining causality; each zone must *know* about each wave passing through it if the wave is to have any effect on it (Figure 5). It is expressed as,

$$\Delta t \leq min(\Delta x)/(u + C_f) \tag{2.30}$$

where u is the local fluid velocity, $C_f = \sqrt{v_A^2 + C_S^2}$ is the fast magneto-sonic speed and the minimum over all grid zones is taken. In addition, the use of artificial viscosity introduces a second time-step constraint for the time-explicit diffusion of momentum.

which is

$$\Delta t \leq (\Delta x)^2/4\mu, \tag{2.31}$$

where μ is the effective coefficient of kinematic viscosity. Both of these constraints are conveniently implemented by ZEUS-2D using

$$\Delta t = C_o/[max(\delta_1^{-2} + \delta_2^{-2} + \delta_3^{-2} + \delta_4^{-2})]^{1/2} \tag{2.32}$$

Here, the maximum is taken over all zones, C_o is the so-called *Courant number* (safety factor with $C_o \simeq 0.5$), and the various limiting times are

$$\delta_1 = [min(\Delta x_1, \Delta x_2)]/C_f \tag{2.33}$$

$$\delta_2 = \Delta x_1/(v_1 - v_{g1}) \tag{2.34}$$

$$\delta_3 = \Delta x_2)/(v_2 - v_{g2}) \tag{2.35}$$

$$\delta_4 = min(\Delta x_1/4C_2\Delta v_1, \Delta x_2)/4C_2\Delta v_2) \tag{2.36}$$

where C_2 is the dimensionless coefficient of artificial viscosity defined through $C_2 = l/\Delta x$. Physically, C_2 measures the number of zones over which the artificial viscosity will spread a shock and is typically chosen to be $C_2 \simeq 3$. Since the characteristic speeds will in general be changing as the evolution proceeds, the time step must be allowed to vary as well. In ZEUS-2D, the time step is limited to an increase of no more than 30% to maintain *accuracy*, yet may decrease by any amount to maintain

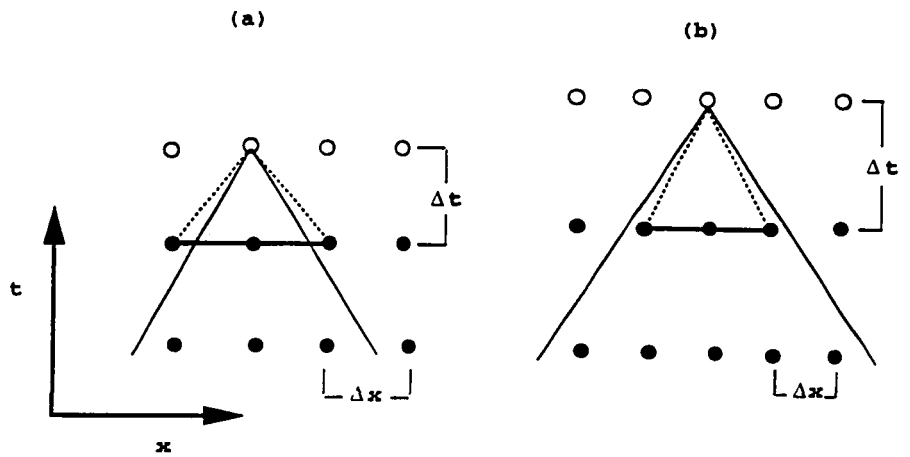

Figure 5. - CFL condition for stability of a differencing scheme. The PDEs of an initial value problem imply that the value at a point depends on information within some domain of dependency to the past. A differencing scheme is CFL stable if the differencing domain of dependency is larger than that of the PDEs. as in (a), and unstable if the relationship is the reverse. as in (b).

stability.

3. Initial Set Up

The initial equilibrium is found by solving for the momentum equation (2.12). The initial state we consider is that of a coronal gas at rest (in the active zones), before the disk is set in Kepler rotation (in the ghost zones). The corona is in pressure balance with the underlying disk. We also assume an initial magnetic structure (that threads both the corona and the disk) whose Lorentz force is zero. In this state, the

gravitational and gas pressure forces balance. Figure 6 illustrates the initial state.

Since the issue of properly setting up the initial state is addressed in detail in chapter 3, here we only highlight the related difficulties and the procedure we used to overcome them. We first explain our procedure for setting up the initial magnetic configuration and why one needs to extend the grid to do so.

3.1 Initial Magnetic Configuration

One must take care that the initial field is in fact divergence free! In practise, we find that using the vector potential to initialize a field configuration is a convenient way of achieving this. A_ϕ must be defined at zone corners as required by the mesh staggering in ZEUS-2D (since $\mathbf{B} = \nabla \times \mathbf{A}$). However, one must define the vector potential beyond the grid defined by ZEUS-2D, as explained below.

The components of the magnetic field for axisymmetric MHD (cylindrical coordinates (r, ϕ, z)) are given by

$$B_r = -\frac{\partial A_\phi}{\partial z} \quad \text{and} \quad B_z = \frac{1}{r}\frac{\partial r A_\phi}{\partial r}, \tag{2.37}$$

which in finite difference form becomes

$$B2(i,j) = -\frac{A_\phi(i+1,j) - A_\phi(i,j)}{x1a(i+1) - x1a(i)}, \tag{2.38}$$

$$B1(i,j) = \frac{1}{x2b(j)}\frac{x2a(j+1)A_\phi(i,j+1) - x2a(j)A_\phi(i,j)}{x2a(i+1) - x2a(i)}. \tag{2.39}$$

That is, since the active zones for the face centered $B1(i,j)$ run from $i = is+1, ie+2$ and $j = js, je+2$, and the active zones for the face centered $B2(i,j)$ run from $i = is, ie+2$ and $j = js+1, je+2$, one needs to add an extra row and an extra column to the mesh to define $x1a(ie+3)$ [and $A_\phi(ie+3,j)$] and $x2a(je+3)$ [and $A_\phi(i,je+3)$]. We have done that in Appendix E.

Extending the mesh to properly set the initial magnetic configuration is not the full story. One still has to ensure that the magnetic structure extends continuously and smoothly into the ghost zones. We have set the initial magnetic configuration in such a way that no kinks (or spurious currents) are introduced in the initial set up, as explained in chapter 3.

3.2 Initial Hydrostatic Equilibrium

As stated in the beginning of this section, because of the complex equations we are dealing with, we decided to only consider initial magnetic configurations for which the Lorentz force is zero ($\mathbf{J} \times \mathbf{B} = 0$). This reduces the momentum equation in such a way that only gravity and gas pressure are in play. The analytical equation of equilibrium is then

$$\frac{\nabla p}{\rho} - \nabla\Phi = 0. \tag{2.40}$$

Now, because density and forces (∇p and $\nabla\Phi$) are stored at different locations on the mesh, ZEUS-2D uses a two-point average method to estimate the density in the finite

difference form of equation (2.40). While such an approach is efficient for density distributions that are more or less uniform it is a problem in our situation where the initial density distribution is completely controlled by the gravitational potential well Φ (chapter 3) and varies as

$$\rho \propto \frac{1}{(x^2 + z^2)^{3/4}}. \tag{2.41}$$

This density distribution is obtained for a polytropic equation of state with a polytropic index $\gamma = 5/3$. As one gets closer to the surface of the central object, the two-point average method fails and the numerical solution evolves away from the exact analytical one, destroying our equilibrium.

We describe here two of the usual methods that deal with such difficulty and why they too fail in our situation, and then describe our own solution procedure. Figure 6 (see next page) illustrates the initial set up.

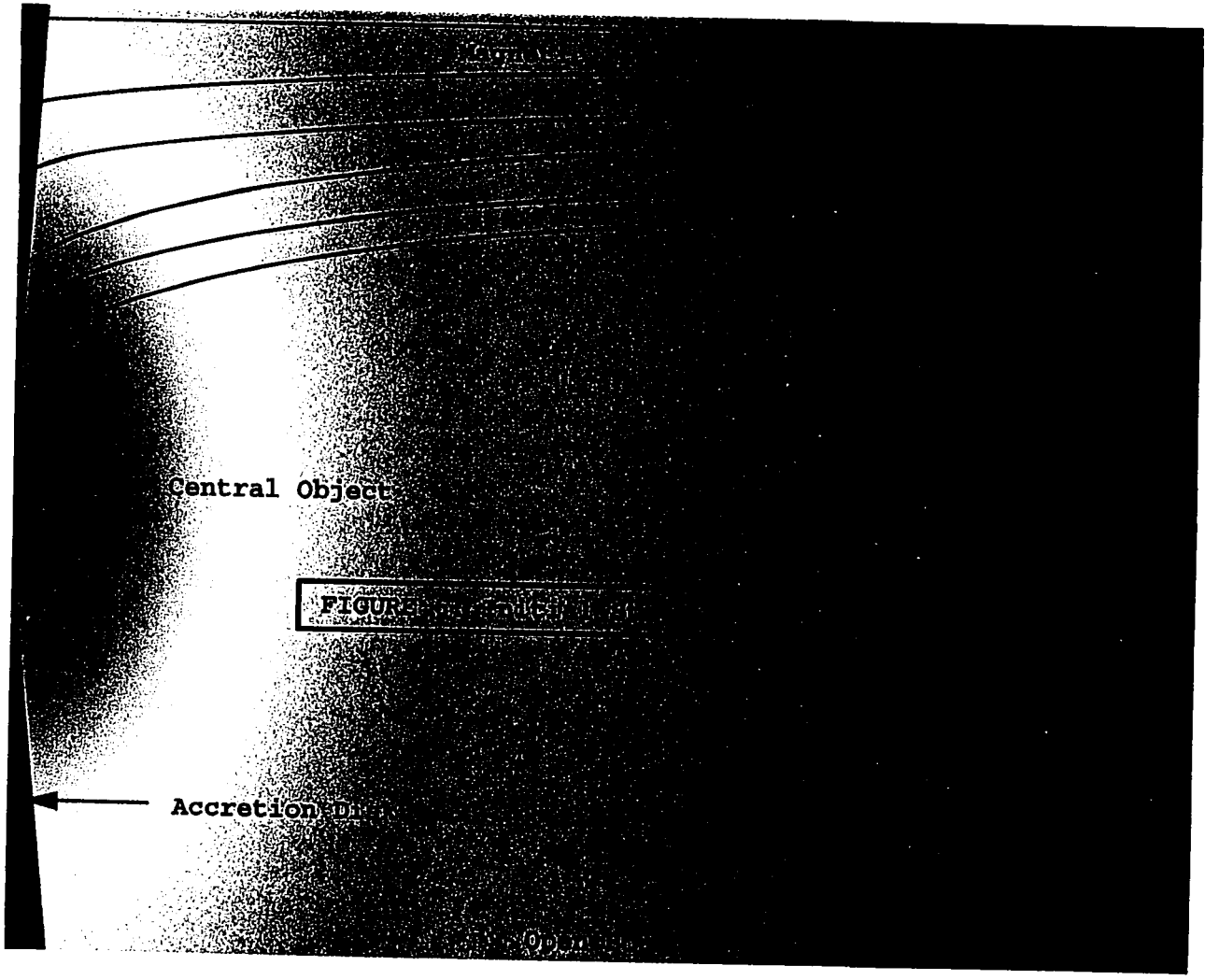
Central Object
Accretion

3.2.1 Softening Parameter

One trivial procedure is to soften the gravitational potential (hence softening the density distribution). That is,

$$\Phi = -\frac{GM}{\sqrt{x^2 + z^2 + a^2}} \tag{2.42}$$

where the softening parameter "a" is some constant. This procedure removes the divergence of $1/\sqrt{x^2 + z^2}$ as one approaches the origin. However, we ruled out such a procedure for two reasons: (1) Our results varied significantly when slightly varying the softening of the potential well. This makes our simulations unreliable (chapter 3); (2) softening the gravitational potential goes against the philosophy of this thesis: our main goal is to get as close as possible to the surface of the central object deep into the gravitational well where we believe the jets originate.

3.2.2 Numerical Equilibrium

One can also set up an exact numerical equilibrium by numerically integrating the hydrostatic equilibrium equation to calculate the pressure from a *given* density. For example equation

$$p(i+1) = p(i) - \frac{1}{\bar{\rho}} \frac{GM}{\sqrt{x1a(i)^2 + x2b(j)^2}}. \tag{2.43}$$

follows from writing the difference equations in (2.40). One then fixes a value of $p(i)$ on the boundary and computes $p(i+1)$ recursively using the above. That way one

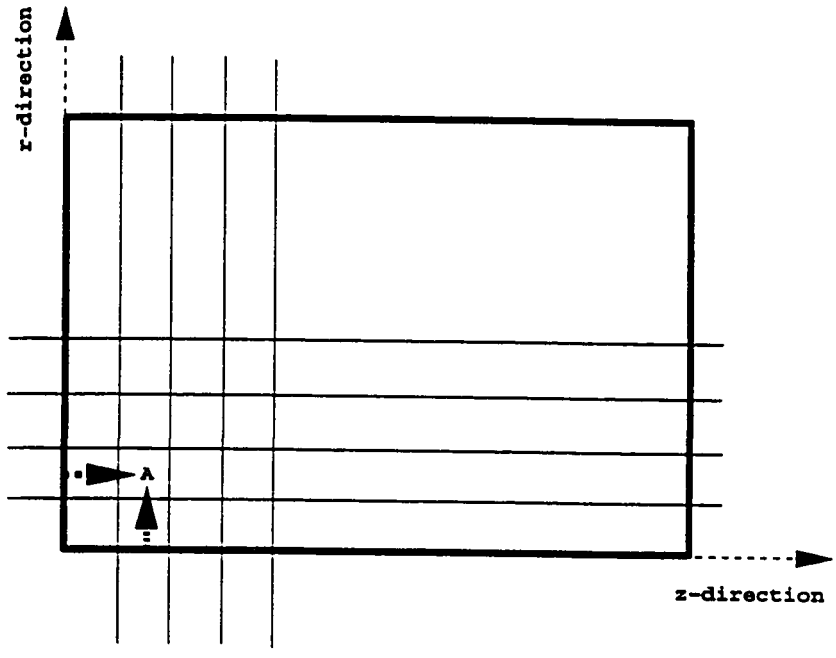

Figure 7. - Here we illustrate the difficulty in numerically setting the initial equilibrium. Horizontally integration (using the z-component of the momentum equation) gives different results than the vertical integration (using the r-component of the momentum equation).

obtains a numerical hydrostatic equilibrium. Here again we rule out such a procedure for the following reasons:

(1) While such a method works for a one-dimensional problems, it is a problem for 2-D problems. In this case, one has two equations to solve for simultaneously, the z-component and the r-component of the momentum equation. Integrating using the r-component yields a completely different solution from the z-direction integration, as illustrated in Figure 6. These two equations must be integrated simultaneously. Simply put, because we have a two-dimensional grid we have to make sure that our

numerical solution converges at the same time at every grid point. Such a procedure is not only time-consuming, but even when such a solution is found, it is not a precise one.

(2) A purely numerical technique does not always guarantee a physically acceptable pressure distribution. That is, a pressure distribution more or less close to what one would expect from analytical solution to equation (2.40). This is not trivial in our case because of the complexity of the equations involved.

We ran a few simulations using such an approach. This lead to undesired numerical instabilities with a very high growth rate. The instability seems to start from one pixel and propagates very quickly into the whole mesh, destroying our solution (see Figure 9).

While the instability appears to involve the presence of velocity shears (mainly because of the interaction of the ejected gas and the in-falling coronal gas, when the initial state is not in perfect equilibrium), it is still too early to decide whether they are physical or numerical. One needs a detailed analysis of the few pixels where such phenomena occur. This is beyond the scope of this thesis. However, for completeness, we give the reader an idea of what might be happening in our simulations in case these instabilities turn out to be of numerical nature. We refer to Clarke (1996) for details of what is summarized below.

3.2.3 Numerical Instabilities

In situations where neighboring zones have oppositely directed flows (*shear layers*). equation (2.27) becomes

$$C_1^{\pm} = \mp \frac{1}{\sqrt{\rho}} < B_1 >_2, \tag{2.44}$$

since one has

$$< v_1 >_2 \rightarrow 0. \tag{2.45}$$

This simply means that the characteristics lie on the two different sides of a zone interface (Figure 8). That is, since v_2^+ and v_2^- are now estimated at two different zones, the $(v_2^+ - v_2^-) \equiv \Delta v_2$ term in equation (2.29) will include a higher numerical error so that

$$B_2^{*,n+1/2} \propto \Delta v_2. \tag{2.46}$$

Thus, in equation (2.26), the $v_1 B_2$ term in ϵ_3 could be proportional to $v_1 v_2$ rather than $v_1 a_2$ as required if the magnetic field is to remain weak. *In a system with an otherwise dynamically insignificant magnetic field (in which case the right hand term has a higher probability of becoming larger than B), such a spurious* ϵ_3 *could generate an anomalous and possibly dynamically important magnetic flux loop in a single time step (thus the designation "explosive" instability) thereby destroying the integrity of the solution* (Clarke 1996).

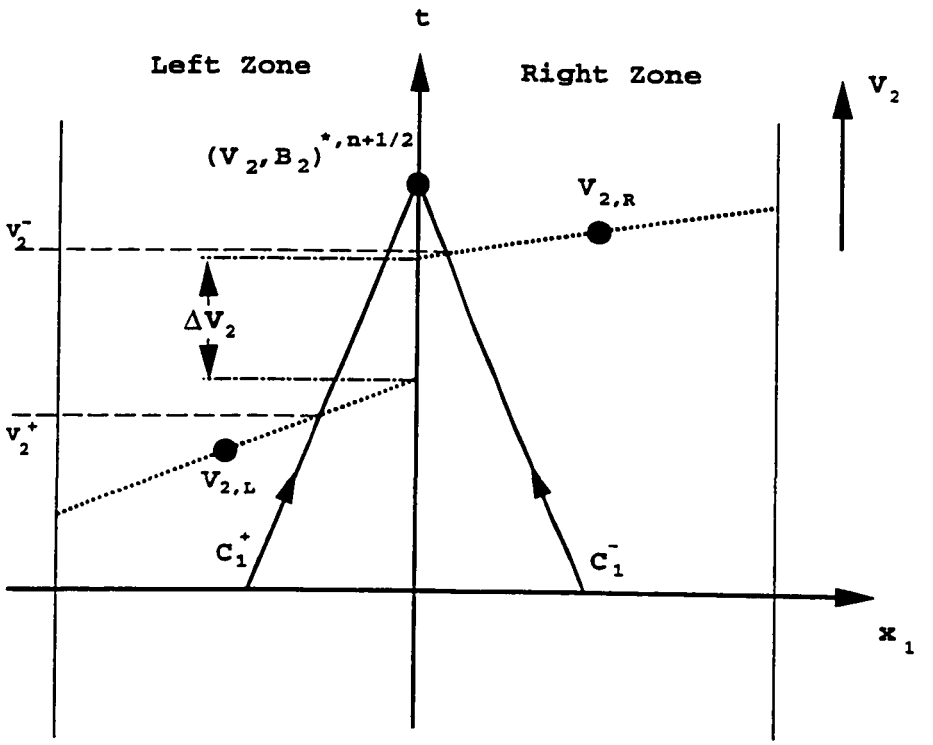

Figure 8. - A depiction of Lagrangian-like characteristics which straddle the interface. In this case, the difference $v_2^+ - v_2^-$ contains the term Δv_2 (introduced through interpolation) which, in general, is proportional to the flow velocity, not the Alfvén velocity. Thus, the estimate of B_2^* will be corrupted for sub-Alfvénic flow (dynamically insignificant magnetic field).

3.2.4 Our Solution Procedure

These instabilities disappeared as soon as we were able to set a stable initial equilibrium (chapter 3).

By restricting our simulations to polytropic gases (Appendix C) defined by an equation of state $p = K\rho^\gamma$), we write equation (2.40) as

$$\nabla(c(\gamma)\rho + \Phi) = 0. \tag{2.47}$$

where $c(\gamma)$ is a constant of the polytropic index γ. In this way we avoid the use of any averaging method to relocate the density (see Appendix F). Of course, this requires changing the finite-differenced momentum equation in ZEUS-2D and adding the necessary corrections (chapter 3). This version of the code allows us to set a realistic initial state in stable equilibrium, and this turned out to be important for the results reported in this thesis.

To summarize this section, we had to expand the code and modify it in some places in order to deal with the many difficulties related to a proper set up of the initial hydrostatic state. Furthermore, since the observations seem to suggest that thermal gas pressure alone is incapable of providing all the support needed against gravity an extra stabilizing "magnetic Alfvénic turbulent pressure" had to be included in the momentum equation (chapter 3). This completes our description of the ZEUS-2D code and how it was extended.

4. The Analysis Package

Detailed graphical diagnostics are necessary to understand the physical processes occurring in our numerical simulations. We developed an extensive graphical package to help us understand these flows. This package is now attached to the code and uses Super-Mongo (SM) graphics for the display.

The ZEUS-2D code outputs data in two file types. The subroutine "hdfall.src" writes out all dependent variables over the whole mesh in HDF scientific data set

format, while the "movie.src" writes out images as raster files. A crude vector graphics plotting package based on NCAR graphics reads the HDF files, but we find it very limited when it comes to analyzing the simulations. Here are some of the points we have added to the code for a better analysis of the simulations.

i) It is customary in analytical studies of astrophysical jets to solve for physical quantities along a given magnetic field line (e.g. Figure 15 in introductory chapter). Thus, since part of this work is to make contact with previously known analytical results, we added a subroutine to extract quantities along any given contour line (Appendix G). One can then go into SM to display the quantities as desired. We give an example in Appendix H, where the SM routine searchs for the Alfvén and FM surfaces, estimating the launch angle, etc..

ii) One of the important aspects of MHD flows is to follow the evolution of the vector current density $\mathbf{j} = \nabla \times \mathbf{B}$. For example, when the current vanishes or when it flows parallel to the magnetic surface, no magnetic acceleration is present. The way this current is distributed is of great importance for both jet collimation and acceleration. Appendix I, consists of the subroutine written to display the vector poloidal current density. To display the poloidal current vector and the poloidal magnetic field together (see Figure 7 in Chapter 3, for example) one has to go through procedure i), cited above.

iii) Creating and displaying Images:

Appendix J contains a listing of the program which displays images of the density/toroidal field and density/velocity. A series of these files are generated as user's files (raster images). To visualize these files, we use a set of image display packages, like XImage, Spyglass, Collage, etc.. that are available from NCSA. The main problem with such a display is the choice of a good color palette. Usually, the efficiency of the color palette in displaying a given physical quantity depends on how accurately the maximum and the minimum values are known. The question is *how is one supposed to set the max/min values in movie.src to get the movie files to be scaled in a sensible way?* The usual method of dealing with this is to take random measured values and adding a safety factor, but such a method works only if one has a good grasp on the physics of the simulations. Since our work is still more of an investigative type, this would be too time consuming and too risky.

To have an estimate of the maximum and minimum value representative of the entire simulation (for the variables of interest; here, density, toroidal field and velocity), we run the simulation once in order to estimate the max and min values for every HDF file generated. One then needs to take the max and min values of all the HDF files generated to get the final result[9]. The maximum and the minimum values are then stored in files that can be read directly by movie.src for the second and final run.

[9]Note that saving the data in 4-byte form as hdf files can be costly, and one must delete every hdf file once the max and min values are computed. This is simply done by the statement "Close(filenumber, status=delete)"

The subroutines *expandimage.src* allows us to expand the image by a desired factor while the subroutine *splitfile.src* splits the images generated by *movie.src* into three separate images (density/toroidal, density/velocity and density/density) for easy transport and display of the data on the screen[10].

[10]One has to take into account that the screen size is 640X480 pixels. That is, the resolution used in the simulations has to be such that one is able to display the simulations on the screen (taken image expansion into account).

Figure 9. - The next three pages display an example of a numerical instability which generates a strong bubble (low density region) around the cells (or pixels) on which the "instability occurred". The bubble starts as a small instability that spreads very quickly (in few time steps) throughout the grid. To corresponding movie can be found at the website given at the beginning of this chapter.

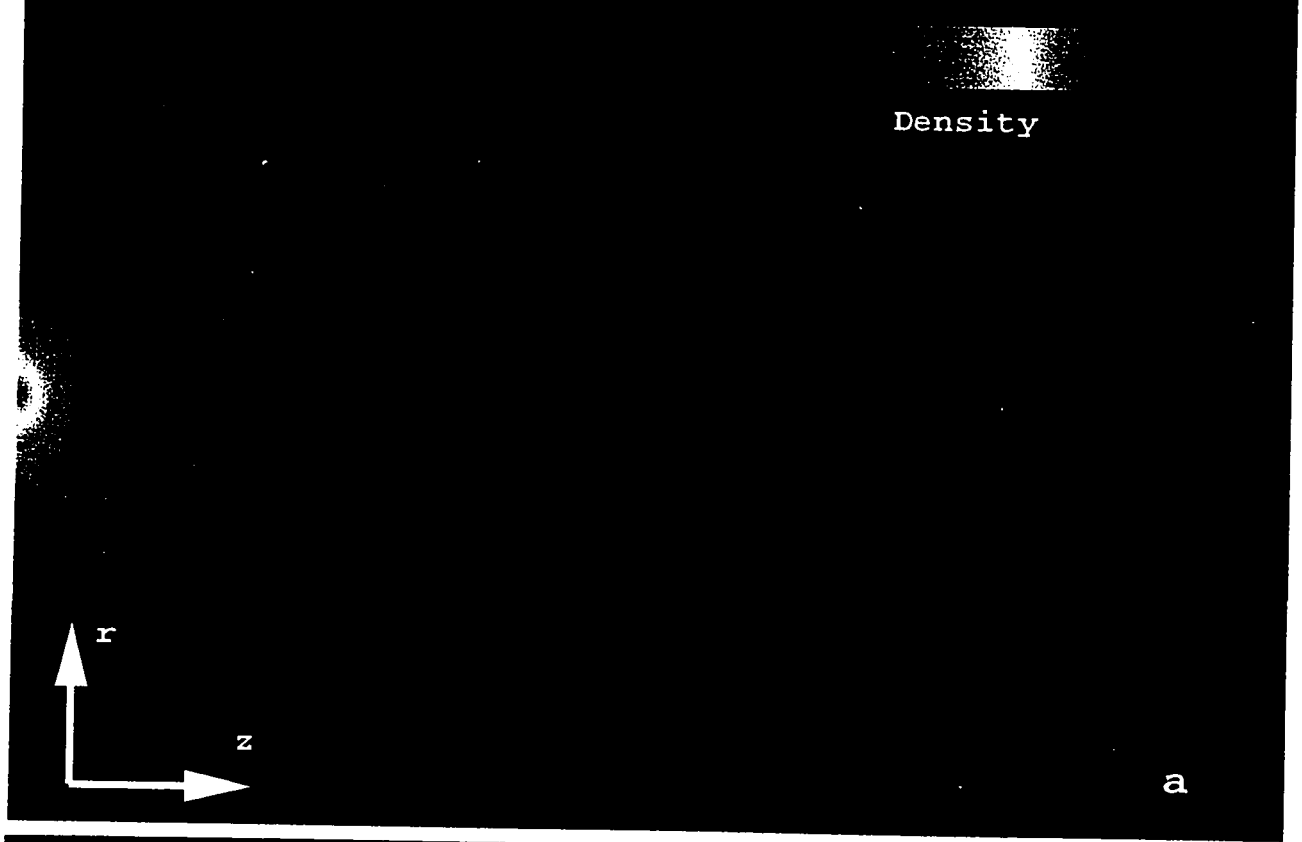
Density
r
z
a

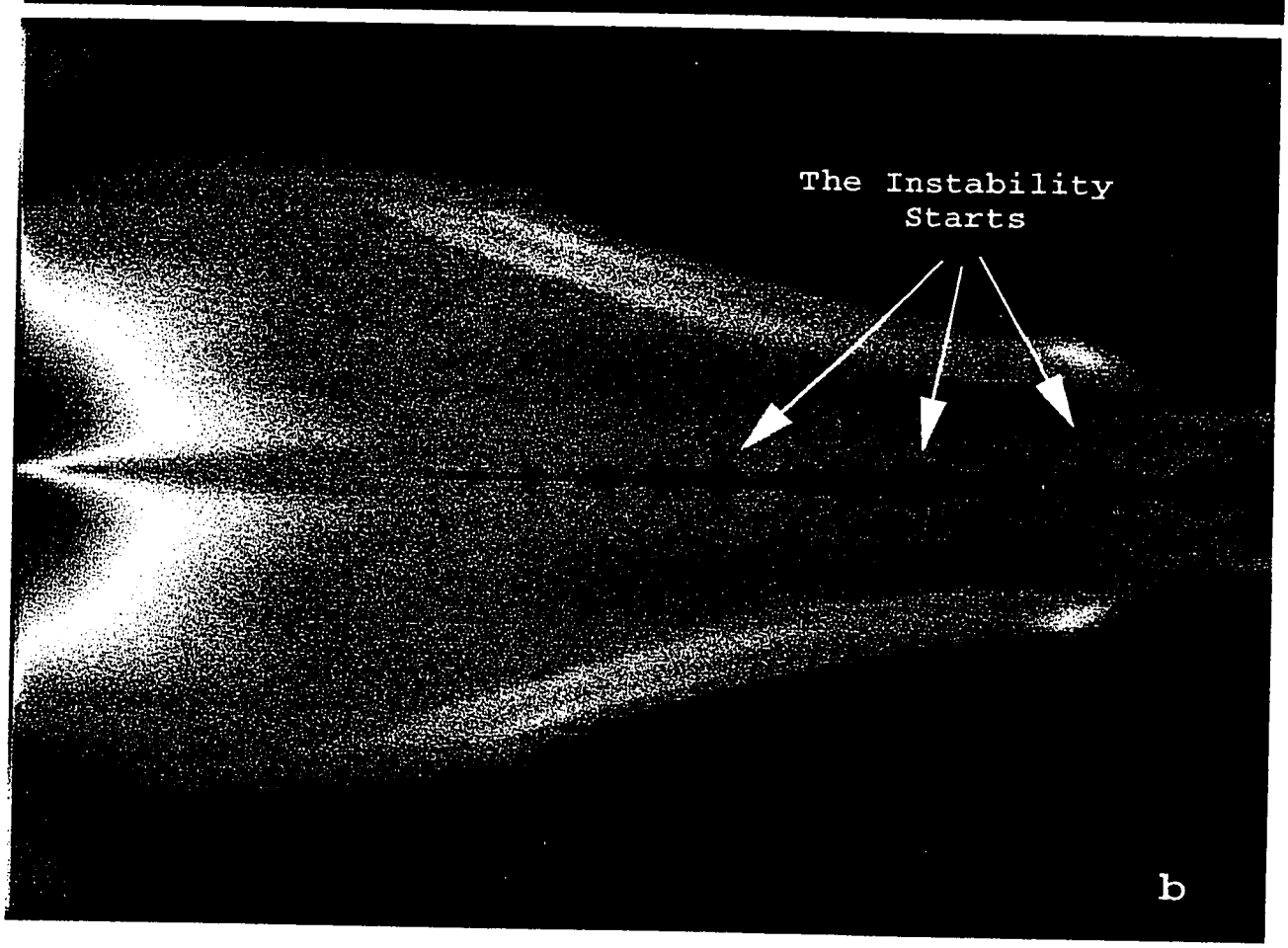
The Instability
Starts
b

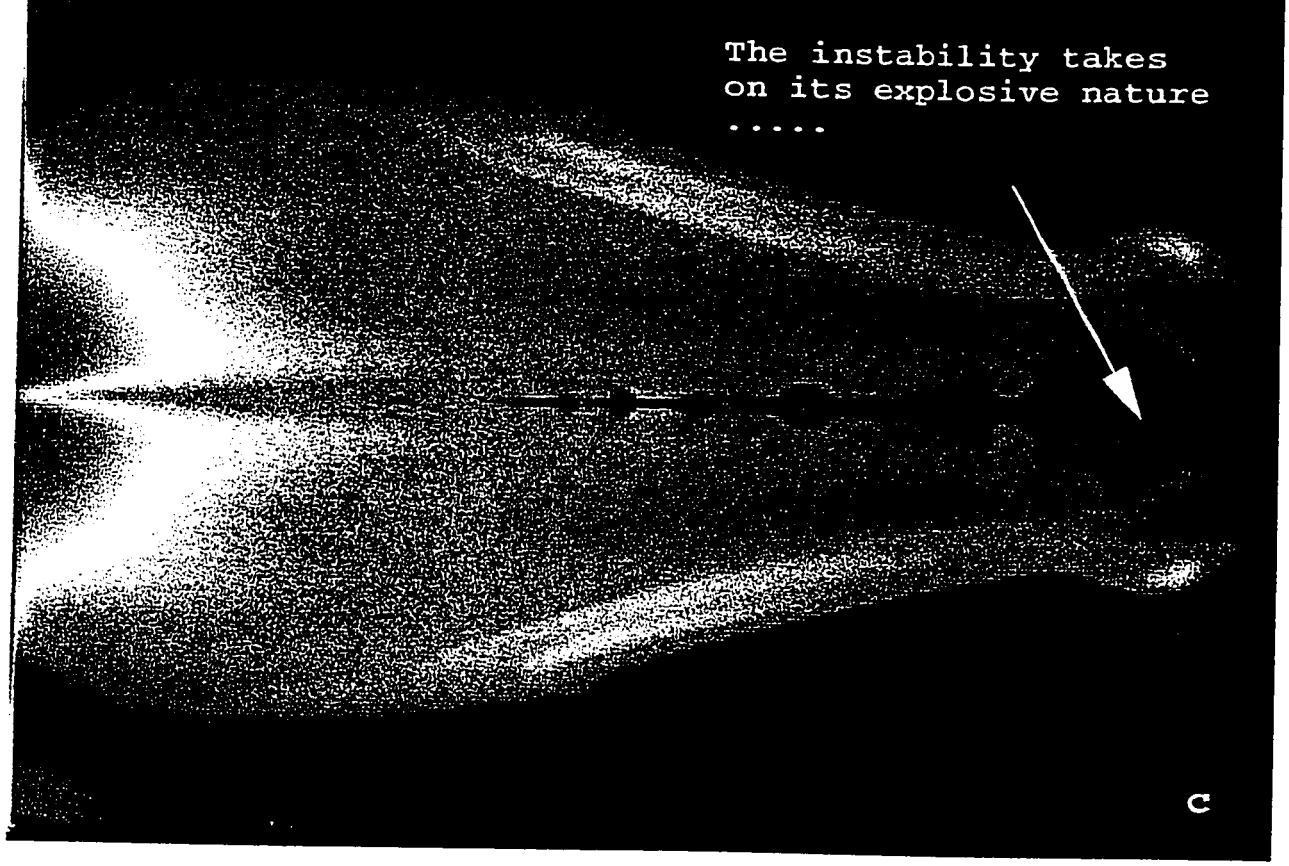
The instability takes
on its explosive nature
.....
c

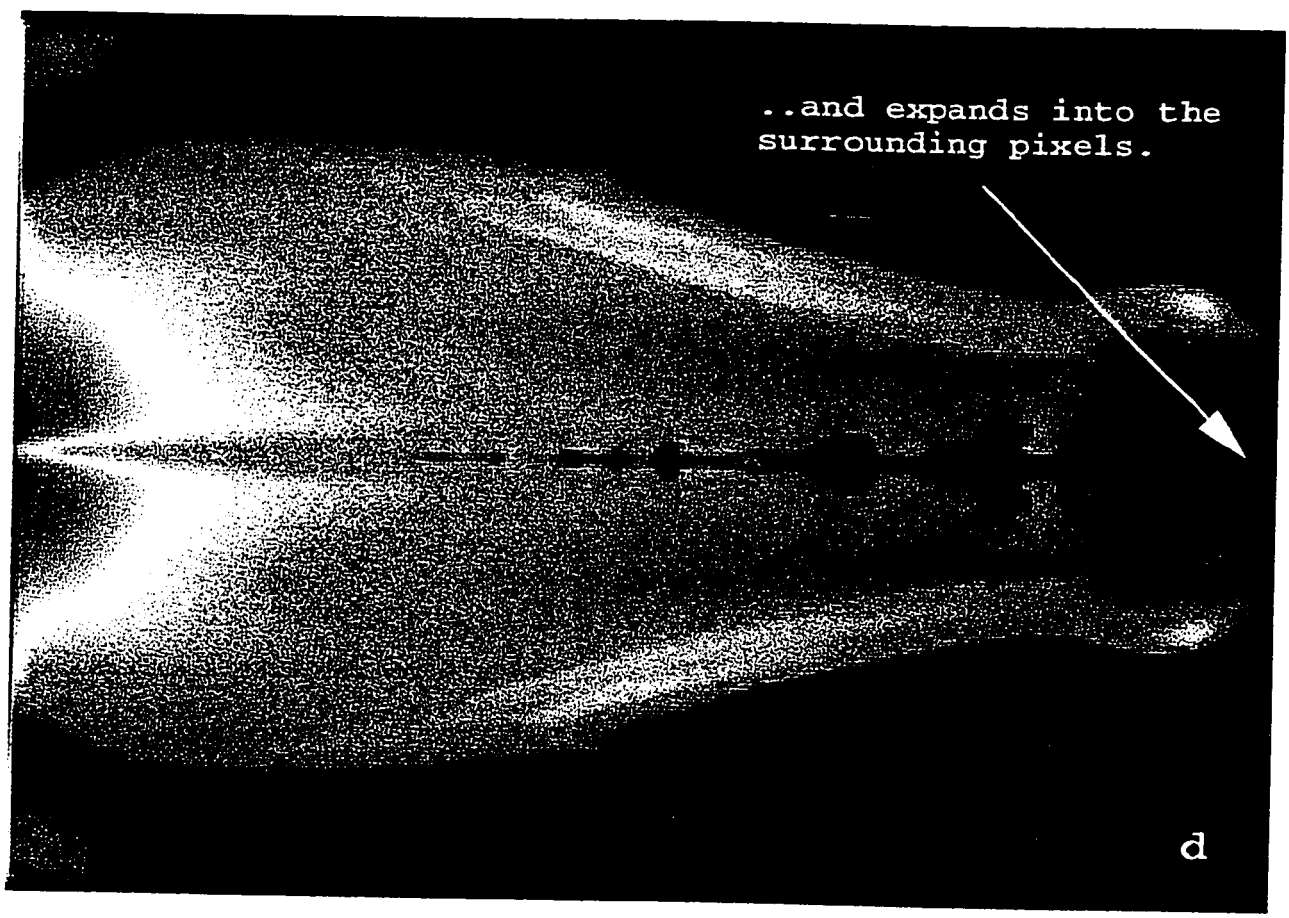
..and expands into the
surrounding pixels.
d

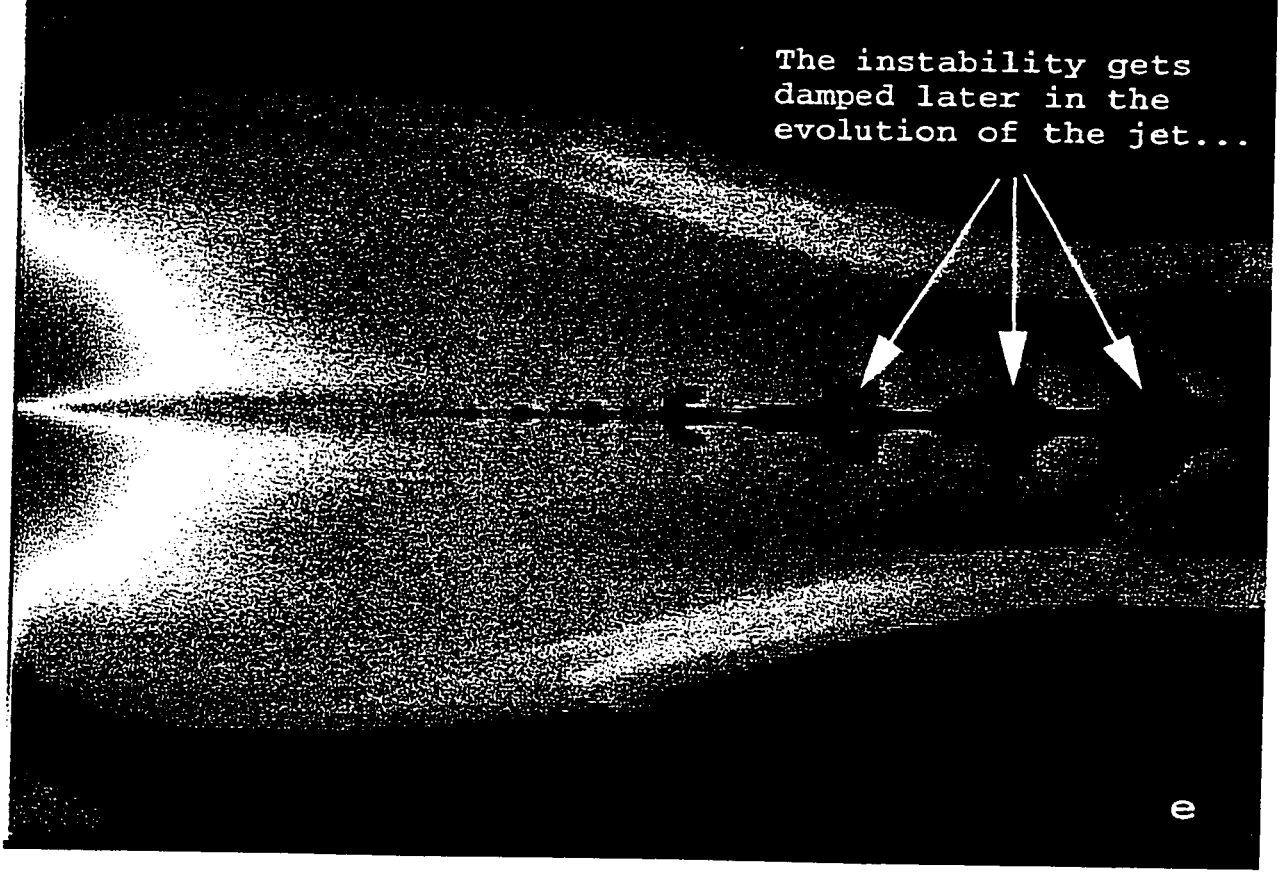
The instability gets damped later in the evolution of the jet...
e

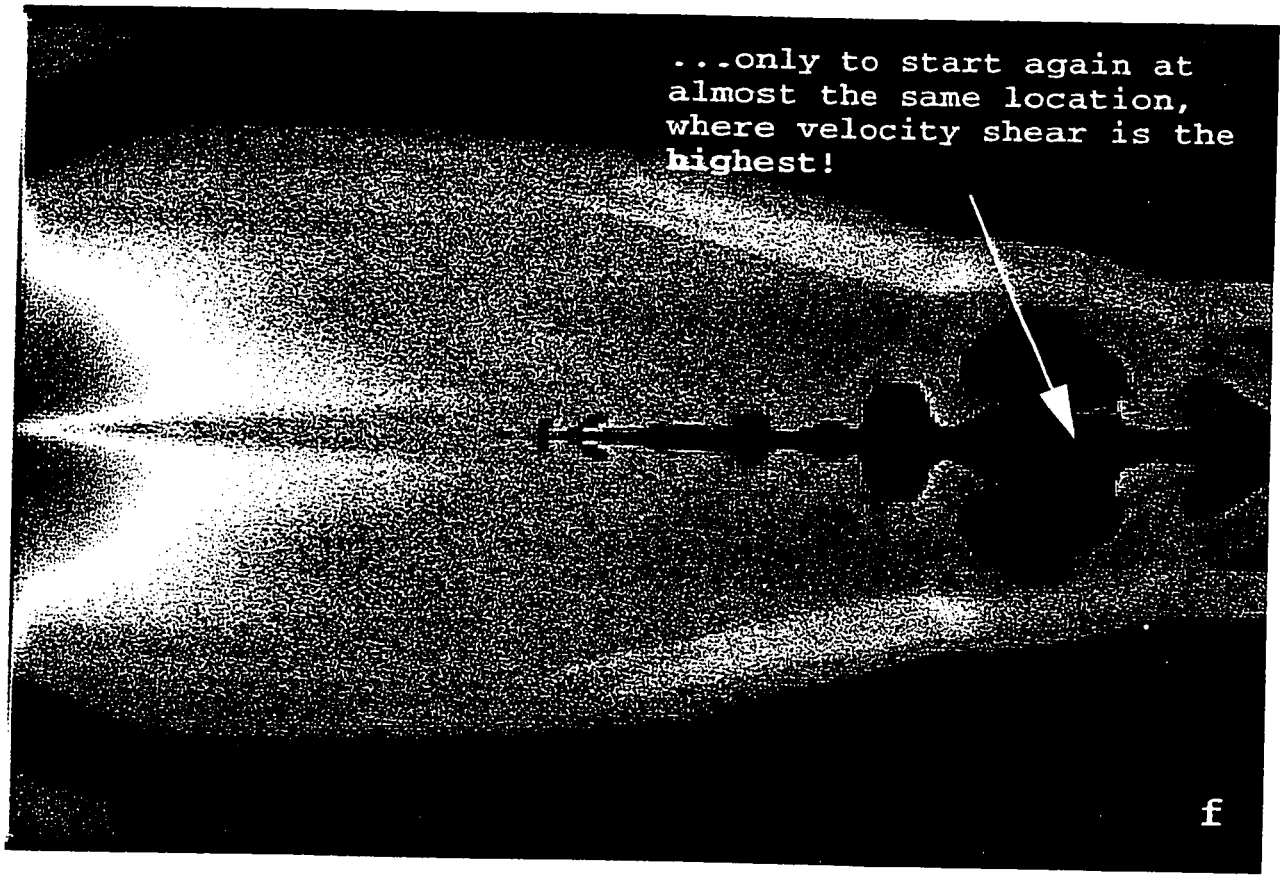
...only to start again at almost the same location, where velocity shear is the highest!
f

Chapter 3

Stationary Models

This chapter is based on the paper "NUMERICAL SIMULATIONS OF ASTROPHYSICAL JETS FROM KEPLERIAN DISKS I: Stationary Models" by Ouyed, R. and Pudritz, E. R. 1997, accepted for publication in the "Astrophysical Journal".

Here, we test some of the basic results of the steady state theory of centrifugally driven winds by means of the time-dependent, 2.5 dimensional simulations. Our initial set up is described in detail as well as the many changes introduced into the hydro-magnetic code. The analysis package we have attached to the code is put to the test with encouraging results.

Abstract

We present 2.5-dimensional time-dependent simulations of the evolution of non-relativistic outflows from Keplerian accretion disks orbiting low mass protostars or black holes accreting at sub-Eddington rates. The gas is injected at a very small speed ($v_{inj} = 10^{-3} v_K$) from the surface of the disk (a fixed boundary in our simulations) into a cold corona. The corona is in stable equilibrium and is supported by Alfvénic turbulent pressure. The initial magnetic field configuration in the corona is poloidal and given by a potential field ($\mathbf{J} = 0$). This configuration is extended smoothly into the disk where the toroidal magnetic field is taken to scale inversely with the disk radius. We present the analytical and the numerical approaches to our problem, as well as many results for a steady state simulation. We find that the gas is centrifugally accelerated through the Alfvén and the fast magnetosonic (FM) surfaces and collimated into cylinders parallel to the disk's axis. The collimation of the outflow is due to the pinch force exerted by the dominant toroidal magnetic field generated by the outflow itself. Beyond the FM surface, we found that a "Hubble" flow is present; $v_z \propto z$. The velocities achieved in our simulations are of the order of 180 km/s for our standard young stellar object (a 0.5 $M_\odot$ proto-star) and of the order or 10^5 km/s for our standard active galactic nuclei (a $10^8 M_\odot$ black hole). Our jet solutions, dominated mainly by the poloidal kinetic energy ρv_p^2, are very efficient in magnetically extracting angular momentum and energy from the disk. We find the ratio of the disk accretion rate to the wind mass flux rate to be of the order of

$\dot{m}_a/\dot{m}_w \simeq 6.0$. We find that our stationary outflows have many similarities to steady state models of MHD disk winds.

1. Introduction

One of the fundamental questions raised by observations of astrophysical jets concerns the mechanism for initiating and driving the outflows. Among the scenarios currently being actively investigated are magnetohydrodynamic (MHD) models in which magnetized accretion disks, rotating around central objects (proto-stars, black holes or white dwarfs), are involved. In general there exist two classes of models:

(i) Winds emanating directly from the surface of the disk (Blandford & Payne 1982, hereafter BP82, Uchida & Shibata 1985, hereafter US85, Camenzid 1987, Pudritz & Norman 1986, Lovelace et al. 1987, Heyvaerts & Norman 1989, hereafter HN89, Pelletier & Pudritz 1992, hereafter PP92, Appl & Camenzid 1993, Königl & Ruden 1993 to cite only few). These can be divided into two general types of models: (a) the Uchida-Shibata wind (US85) with its "uncoiling spring" picture and (b) centrifugally driven wind (BP82, PP92, for e.g.) and its "bead on a rigid wire" picture. In the US85 model, the large-scale magnetic field is twisted by the rotation of a radially collapsing, non-Keplerian, accretion disk. The magnetic twist accumulates in the disk, but eventually relaxes through the emission of large amplitude, non-linear, torsional Alfvén waves which propagate in bipolar directions along the large scale magnetic field lines. These waves eject the matter in surface layer of the disk, leading to the formation of transient bipolar mass ejections. In the centrifugally driven disk-wind model on the other hand, the gas is centrifugally flung out from the surface of

a Keplerian disk if field lines thread the disk at an angle of 60^o or less with respect to the disk surface (BP82). If r_o is the field line's footpoint at the disk surface and $r_A(r_o)$ the corresponding Alfvén point, then one can show that the dynamics of such a wind is mainly controlled by the length of the magnetic lever arm $r_A(r_o)$. Beyond the Alfvén surface, the $\mathbf{J}_p \times \mathbf{B}_\phi$ force eventually dominates providing the collimation of the outflow.

(ii) The X-wind model, wherein the wind emanates from the point where the disk corotates with its central magnetized star (Shu et al., 1994). These authors assumed that the closed magnetosphere connecting the central star and the disk becomes partly open. The excess angular momentum brought in through the disk is extracted by magneto-centrifugally driven winds which *emanate from the inner edge of the disk* and flows along the open magnetic field lines. Although Shu et al. did not show how the closed dipole field becomes open, recent 2-D numerical investigations by Hayashi (1996) have shown that the closed field lines become *partially* open through magnetic reconnection leading to the ejection of a cold wind. While such a scenario may be plausible for the case of proto-stars, it may be less relevant for jets from accreting black holes. That is, the X-wind model might not provide a universal model for explaining astrophysical jets. Furthermore, on galactic scales, the recent observed correlation between *signatures* of accretion disks (veiling, UV excess, etc..) and outflow (Cabrit et al. 1991, Edwards et al. 1993) seems to point towards the disk wind scenario. That is, since the latter mechanism might explain the physics of such winds independently

of the detailed nature of the central object (from Active Galactic Nuclei, hereafter AGNs, to Young Stellar Objects, hereafter, YSOs), we decided to only consider the case of disk winds.

The theoretical work, mentioned above, focused on formation, evolution and stability of hydromagnetic disk-winds in both self-similar and non-self-similar models. All of the analytical models to date are based on solutions to the *time-independent* equations. Therefore, important features observed in nature such as episodic outflows (Hartigan 1989, Hartigan et al. 1990, Reipurth et al. 1992, Ray & Mundt 1993, Eislöffel & Mundt 1994, Davis et al. 1995 to cite only few) or the dynamics during the initiation of these winds cannot be investigated. A *time-dependent* approach to this problem is necessary, but because of the complexity of the MHD equations, direct numerical simulation is currently the only effective tool.

A few numerical simulations of axisymmetric magnetized flows from accretion disks have been computed for two classes of models. In the first class, one attempts to follow the internal dynamics of the disk (Shibata & Uchida 1986 & 1987, hereafter SU86 & SU87, Stone & Norman 1994, hereafter SN94). For models in which the accretion disks have sub-Keplerian rotation rates (SU86, BL95), or in which the Balbus-Hawley instability is present (SN94), the disk undergoes rapid radial collapse which generates a strong toroidal twist of the threading magnetic field. This is the "coiled spring" which propagates away from the disk as a transient, non-linear torsional Alfvén wave and an associated burst of matter. These models have not been

run long enough to establish whether or not a steady state ensues, or whether such outbursts would continue over the time-scales demanded by the observations. In the second class of models, one treats the disk as a boundary condition at the base of the wind without following its internal dynamics, assuming it is in Keplerian equilibrium (Bell & Lucek 1995, hereafter BL95, Ustyugova et al. 1995, hereafter U95, and Meier et al. 1996, to cite only few). This allows one to isolate the physics of the formation of the jet for a well defined set of conditions imposed at the base of the wind.

Here, we adopt this second approach and present 2.5-dimensional, high resolution, numerical MHD simulations of the onset and collimation of outflows from the surface of a Keplerian accretion disk around a central object. In our first paper (Ouyed et al. 1997), we showed some of the basic results of our simulations which consist of both stationary and episodic outflows. In this paper, we present the technical details as well as many new results of a magnetized disk model that leads to the eventual formation of a stationary disk wind. As in Ouyed et al. (1997), the disk is treated as a boundary condition at the base of the outflow and is kept in Keplerian rotation throughout the simulation. We present a detailed analysis of such winds. We employed the ZEUS-2D numerical code, which is a two dimensional Eulerian *finite difference code.* We refer the reader to Stone & Norman (1992 a & b, hereafter, SN92a & SN92b) for the details. We extended the code in order to allow us to numerically set a stable initial equilibrium without the use of a softening parameter, and tested it. Furthermore, an isotropic Alfvénic turbulence was added to the dynamics allowing a wider range of

application of the code to the study of outflows. A complete analysis package, using SM graphics, was also written (and linked to the code). This tool turned out to be very useful in analyzing the physics involved in our simulations.

Here we describe in detail the problems inherent to the initial set up as well as many results for a simulation that ultimately achieved steady state. The organization of this paper is as follows; in §2, we introduce the reader to the dimensionless hydromagnetic wind equations used, and in §3 describe the initial set up, that is, the state of the initial equilibrium both analytically and numerically. We explain our extended version of the ZEUS-2D code §4 , and how it deals with the numerical difficulties introduced by our initial equilibrium. In §5, we present our results and the analysis package we use, followed by a discussion and conclusions in §6.

2. Basic Equations

We present a brief discussion of the equations describing the physics of magnetized astrophysical flows and of accretion disks. We adopt cylindrical coordinates (r, ϕ, z) with the central object at the origin, and take the z-axis to be perpendicular to the disk, such that the *surface* of the disk lies in the the $z = 0$ plane of our coordinate system. In general, the equations to be solved are (infinite conductor)

$$\frac{\partial \rho}{\partial t} + \nabla.(\rho \mathbf{v}) = 0, \tag{3.1}$$

$$\frac{\partial \mathbf{B}}{\partial t} - \nabla \times (\mathbf{v} \times \mathbf{B}) = 0, \tag{3.2}$$

$$\rho\left(\frac{\partial \mathbf{v}}{\partial t} + (\mathbf{v}.\nabla)\mathbf{v}\right) + \nabla(p + p_A) + \rho\nabla\Phi - \mathbf{j} \times \mathbf{B} = 0, \tag{3.3}$$

$$\rho\left(\frac{\partial e}{\partial t} + (\mathbf{v}.\nabla)e\right) + p(\nabla.\mathbf{v}) = 0, \tag{3.4}$$

$$\nabla.\mathbf{B} = 0, \tag{3.5}$$

where ρ is the density, p the gas pressure, $\mathbf{B}$ the magnetic field, v the velocity, e the internal energy, $\mathbf{j} = \nabla \times \mathbf{B}/4\pi$ is the current density and p_A the Alfvénic turbulent pressure[1] which is expected to be present in any rotating, magnetized gas (Balbus & Hawley, 1991).

The point mass gravitational potential is given by $\Phi = -GM/\sqrt{r^2 + z^2}$. We made several restrictions. First, we assume ideal MHD in our simulations. We also assume that the gas is ideal and described by a polytropic equation of state[2] $p = K\rho^\gamma$, where K is the polytropic constant and γ the polytropic exponent (which we have to distinguish from the adiabatic exponent γ_{ad})[3]. Here we adopt $\gamma = 5/3$. We also

[1]The Alfvénic turbulent pressure $p_A = |\delta\mathbf{B}|^2/8\pi$ is estimated from the time-averaged fluctuating Lorentz force $(\nabla \times \delta\mathbf{B}) \times \delta\mathbf{B}/4\pi$ (Dewar, 1970). Dewar showed for Alfvénic waves of wavelength λ small compared to the variation of the background fluid, that such disturbances propagate adiabatically conserving wave action. They induce a radiation stress on the background fluid which is readily shown to behave as an isotropic wave pressure p_A. The source of such fluctuations and the role the corresponding isotropic pressure plays in our work is described in details in §3.3.2.

[2]Since we are assuming a polytropic relation for an ideal gas, this is equivalent to adopting a certain relation $e = e(p)$. This means that one fixes the internal energy instead of determining it by the energy equation. That is, we will not solve for the energy equation (2.4), in this work (see §4.2 for more details).

[3]A polytropic change is defined to be a quasi-static change carried out in such a way that the derivative $c = dQ/dT$ (the "specific heat") varies in a specified way throughout the change. For example, in an adiabatic change $c = 0$; hence an adiabat is a polytrope of zero specific heat (Chandrasekhar 1939). Since the entropy is simply defined as $dS = dQ/T$, then shocks (requiring $dS > 0$) are not allowed for adiabatic changes ($dS = dQ/T = 0$). In our case, by taking $c \neq 0$, we allow shocks to occur. The polytropic index is $\gamma = \frac{c_p - c}{c_v - c}$, where c_p and c_v are the specific heat at

ignore radiative transfer effects.

Our goal is to solve the system of equations above using the ZEUS-2D code (SN92a & SN92b). We extended the code in order to accommodate the demands of our simulations (§4).

2.1 Dimensionless Equations

We choose a dimensionless form for our equations such that the physical quantities are given in units of their values at the innermost radius of the accretion disk r_i (r_i could be defined as being the surface of the star, the magnetopause radius of a magnetized star and surrounding disk; or the last stable Keplerian-like orbit around a a black hole for AGNs). The radial distance to the footpoint of a given field line on the disk is denoted r_o. In general then, we define our dimensionless variables as,

$$r' = \frac{r}{r_i},\ z' = \frac{z}{r_i},\ v' = \frac{v}{v_{K,i}},\ \rho' = \frac{\rho}{\rho_i},\ B' = \frac{B}{B_i},\ \Phi' = -\frac{1}{\sqrt{r'^2 + z'^2}},\ \nabla' = r_i\nabla \quad (3.6)$$

where $v_{K,i} = \sqrt{GM/r_i}$ is the Kepler speed at r_i and B_i the poloidal field at r_i. Time is given in units of $t_i = r_i/v_{K,i}$ so that the dimensionless time is

$$\tau = \frac{t}{t_i} \quad (3.7)$$

(see Table 1). The results can therefore be scaled to a central object of any desired mass (see example in Table 2).

---

constant pressure and constant volume, respectively. It is only when $c = 0$ that $\gamma = \gamma_{ad} = c_p/c_v$ (see §4.2 for more details).

Table 1. Units

Object	r_i	$v_{K,i}\ (km/s)$	$t_i \equiv \frac{1}{\Omega_{K,i}}\ (days)$
$YSOs$	$3R_*$	$104.0\ \frac{\sqrt{M/0.5M_\odot}}{\sqrt{r_i/0.05AU}}$	$0.86\frac{(r_i/0.05AU)^{3/2}}{\sqrt{M/0.5M_\odot}}$
$AGNs\ (pc)$	$10r_g a = 10^{-4}M_8$	$6.7\times10^4\sqrt{\frac{10r_g}{r_i}}$	$0.53M_8(\frac{10r_g}{r_i})^{3/2}$

[a] $r_g = 2GM/c^2$ is the Schwarzschild radius. $10r_g$ is a fiducial radius interior within which relativistic effects cannot be neglected. M_8 is the central mass in units of $10^8\ M_\odot$.

Table 2. Units for YSOs and AGNs

Central Object	$Mass\ (M_\odot)$	$r_i\ (AU)$	$v_{K,i}\ (km/s)$	$t_i\ (days)$
$Proto-Star$	0.5	0.04	120.0	0.6
$Black\ Hole$	10^8	20.6	6.7×10^4	0.53

Using these dimensionless quantities, the equation of motion becomes

$$[\frac{\partial \mathbf{v}'}{\partial \tau} + (\mathbf{v}'.\nabla')\mathbf{v}'] = -\frac{1}{\delta_i}\frac{\nabla'(p' + p_A')}{\rho'} - \nabla'\Phi' + \frac{2}{\delta_i\beta_i}\frac{\mathbf{J}'\times\mathbf{B}'}{\rho'}, \tag{3.8}$$

where we have introduced the parameters

$$\delta_i = \gamma\frac{v_{K,i}^2}{c_{si}^2}, \tag{3.9}$$

as the ratio of Kepler to thermal energy density, and

$$\beta_i = \frac{8\pi p_i}{B_i^2}. \tag{3.10}$$

as the ratio of the gas to the magnetic pressure *in the corona*, at the innermost radius of the disk.

In what follows, we present both the analytical and the numerical approaches for simulating a corona around the central object that is initially in stable equilibrium and in pressure balance with the disk surface. In general then, we solve analytically for an initial equilibrium, and test our extended version of the ZEUS-2D code to ensure that it conserves the equilibrium.

From now on, and *for simplicity, we drop the primes keeping in mind that our quantities henceforth represent dimensionless variables.*

3. Initial Conditions

3.1 Hydro-magnetic Corona

We are interested in solving the MHD equations for the region above the disk surface ($z > 0.0$) where we assume that $v_z = v_r = v_\phi = 0$. We assume, for simplicity and for clarity, that $B_\phi = 0$ in the corona and that the initial poloidal magnetic field in the disk corona threads the surface of the underlying disk. The state we consider is one which would be in hydrostatic balance in the gravitational field of the central object in the absence of rotation of the disk (the latter introduces a flux of torsional Alfvén waves and toroidal field into the corona which we study in our simulation).

Equation (2.8) above becomes

$$0 = -\frac{1}{\delta_i}\frac{\nabla(p + p_A)}{\rho} - \nabla\Phi + \frac{2}{\delta_i \beta i}\frac{\mathbf{J} \times \mathbf{B}}{\rho}. \tag{3.11}$$

It is still a difficult task to solve the equation because of the Lorentz term. *A self-similar configuration (BP82, for e.g) has the disadvantage of being mathematically difficult to deal with when solving for the initial equilibrium because its associated Lorentz force does not vanish.* We therefore consider simpler initial magnetic configurations.

3.2 Initial Magnetic Configuration in Corona

In order to allow a simple, self-consistent, initial coronal state to be established, we consider initial configurations whose Lorentz force $\mathbf{J} \times \mathbf{B} = 0$. The two magnetic configurations we have chosen both have $\mathbf{J} = 0$ which is the simplest way of satisfying this condition. The next step consists in choosing an appropriate magnetic potential $\mathbf{A} = A_\phi \mathbf{e}_\phi$, because then the divergence free condition for axisymmetric flows is automatically satisfied. In this scheme, the components of the magnetic field for axisymmetric MHD are:

$$B_r = -\frac{\partial A_\phi}{\partial z} \quad \text{and} \quad B_z = \frac{1}{r}\frac{\partial r A_\phi}{\partial r} \tag{3.12}$$

where A_ϕ is given in units of $r_i B_i$. Two particularly straight-forward initial magnetic configurations are:

(i) the uniform vertical field configuration defined by

$$A_\phi = r \tag{3.13}$$

whose associated field is $B_z = 2$ and $B_r = 0.0$.

(ii) The potential configuration.

$$A_\phi = \frac{\sqrt{r^2 + (z_d + z)^2} - (z_d + z)}{r}. \tag{3.14}$$

where from equation (3.12), and introducing z_d as the dimensionless disk thickness, $B_z = 1/\sqrt{r^2 + (z_d + z)^2}$ and $B_r = \left(1 - (z_d + z)/\sqrt{r^2 + (z_d + z)^2}\right)/r$.

Such configurations reduce the momentum equation to

$$0 = -\frac{1}{\delta_i}\frac{\nabla(p + p_A)}{\rho} - \nabla\Phi. \tag{3.15}$$

One is left with the pressure and the Alfvénic turbulence as the main mechanisms to counterbalance gravity.

3.3 Hydrostatic Equilibrium

3.3.1 Hot Corona: $p_A = 0$

This case corresponds to the simplest possible equilibrium, wherein gravity is exactly balanced by the gas pressure, the hot corona. In this case, the solution of eqn. (3.15) is

$$\frac{h}{\delta_i} + \Phi = const.. \tag{3.16}$$

where h is the dimensionless enthalpy of the gas with its usual definition $\gamma p/(\gamma - 1)\rho$.

Taking $\rho = \rho_\infty$ (with $\Phi_\infty = 0$) at infinity, we get

$$\rho = \left(\frac{(\gamma - 1)\delta_i}{\gamma} \frac{1}{\sqrt{r^2 + z^2}} + \rho_\infty^{(\gamma-1)} \right)^{\frac{1}{\gamma-1}}. \tag{3.17}$$

Imposing the inner boundary condition $\rho(r = 1, z = 0) = 1$ (or in dimensionful form, $\rho = \rho_i$ at $r = r_i$), we obtain the constraint

$$\delta_i = \frac{\gamma}{(\gamma - 1)}(1 - \rho_\infty^{(\gamma-1)}). \tag{3.18}$$

For a hot corona supported solely by thermal pressure then, we require

$$\delta_i \leq \frac{\gamma}{(\gamma - 1)} = \frac{5}{2} \tag{3.19}$$

Estimating a fiducial value for δ_i, using $m_H c_S^2/2 = kT_i$ (T_i is the temperature of the corona at r_i) and the expression for $v_{K,i}$ given in Table 1, we obtain

$$\delta_i \simeq 100 \times (\frac{M}{0.5M_\odot})(\frac{10^5 K}{T_i})(\frac{0.05AU}{r_i}), \tag{3.20}$$

for a YSO, and similarly

$$\delta_i \simeq 100 \times M_8(\frac{5 \times 10^9 K}{T_i})(\frac{10r_g}{r_i}), \tag{3.21}$$

for a black hole, where M_8 is the mass of the black hole in units of $10^8 M_\odot$. That is, δ_i is of the order of 100 on the basis of *coronal* temperatures of the order of 10^5 K for YSOs, and $5 \times 10^9 K$ for the case of AGN's (both estimated in §3.4.1).

The values estimated above reflect the need for another agent, besides thermal pressure, to provide the equilibrium. For high mass protostars and for AGNs accret-

ing at super-Eddington rates, one expects radiation pressure to provide the support needed for the equilibrium, however, since no radiation is present in our simulations we cannot simulate such objects and we are restricted to study low mass protostars and AGNs accreting below the Eddington limit.

3.3.2 Cold Corona

Here, Alfvénic turbulence is the extra agent that provides the bulk of the support against gravity. The source of such turbulent motion is likely to be magnetic in origin. The operation of the Balbus-Hawley instability (Balbus & Hawley, 1991 and 1992) is generally believed to be a mechanism of creating disk turbulence. These Alfvén waves will propagate into the corona providing the perturbations. One of the attractions of this turbulence is that the associated density fluctuations $\delta\rho$ are zero, in the linear regime, so that even though the motions might be strongly supersonic there will not be rapid dissipation through shock formation (Mestel, 1989). The associated energy input need not to be as heat, but may be as macroscopic kinetic energy (Dewar, 1970; Shu et al., 1987; McKee & Zweibel, 1992; Zweibel & McKee, 1995). This makes it straightforward to incorporate into the code (§4.2).

Magnetic turbulence is usually defined by $(\delta B)/B$ with a corresponding Alfvén velocity $v_T = \delta B/\sqrt{4\pi\rho}$. The corresponding parameter that measures the ratio of the

squares of the thermal to MHD turbulent velocities in the corona is,

$$\beta_T = \frac{c_s^2}{v_T^2}. \tag{3.22}$$

For ease of implementation, we assumed that β_T is a constant so that p_A scales with the gas pressure. In this case, one can introduce an effective enthalpy

$$h_{eff} = (c_s^2 + v_T^2) = (1 + \frac{1}{\beta_T})c_s^2 \tag{3.23}$$

so that the equilibrium equation is

$$\nabla \left(\frac{h_{eff}}{\delta_i} + \Phi \right) = 0 \tag{3.24}$$

whose solution is now,

$$\rho = \left(\rho_\infty^{(\gamma-1)} + \frac{(\gamma-1)}{\gamma} \frac{\delta_i}{(1+\frac{1}{\beta_T})} \frac{1}{\sqrt{r^2+z^2}} \right)^{\frac{1}{\gamma-1}} \tag{3.25}$$

with the inner boundary constraint (and with $\rho_\infty = 0$) implying that ,

$$\frac{\gamma}{(\gamma-1)} \frac{(1+\frac{1}{\beta_T})}{\delta_i} = 1. \tag{3.26}$$

The above equation allows us to estimate the turbulent pressure needed to support the corona for a given gas pressure. For a typical $0.5 M_\odot$ YSO, with $\delta_i \simeq 100$, we estimate a sound speed of the order of 15 km/s. That is, using equation (3.26) we find $\beta_T = 0.03$ which corresponds to a turbulence velocity of the order of $v_T = 50$ km/s. Such values for turbulence are smaller then the line-widths of the observed forbidden-lines around YSOs (Ouyed & Pudritz, 1994b). For the case of AGNs, and

for a typical $10^8\ M_\odot$ black hole we estimate a sound speed of the order of 8.6×10^3 km/s and a corresponding turbulence velocity of 3.1×10^4 km/s.

Alfvén turbulence as described by Dewar (1970) is applicable only for wavelength much smaller than the scale we are simulating. Any super-Alfvénic fluctuations ($\delta v = v_T > v_A$) will rapidly decay through compressive shocks and will heat up the corona. One usually imposes the condition

$$\delta v = v_T \leq v_A \quad \text{or} \quad \beta_c \leq \beta_T \tag{3.27}$$

Now the β corresponding to the mean magnetic field in the corona is not a constant in our model. However, a tractable analytical solution for the initial coronal structure requires that β_T is constant. Thus, the condition (3.27) is rewritten as

$$\bar{\beta}_c \leq \beta_T \tag{3.28}$$

where $\bar{\beta}_c$ is the average coronal β. For our fiducial parameters this implies that

$$\bar{\beta}_c \leq \beta_T \simeq 0.03. \tag{3.29}$$

It turned out that for our chosen magnetic configurations, sub-Alfvénic and super-Alfvénic turbulent regions co-exist. While models of of Alfvénic turbulence suggests that $\gamma = 1/2$ for a pure non-damping gas (McKee & Zweibel, 1992; Zweibel & McKee, 1995), we choose $\gamma = 5/3$ because of the coronal heating arising from the expected dissipation in super-Alfvénic turbulent regions (which we do not explicitly simulate).

The coronal density distribution that we adopt in all our numerical simulations is ($\gamma = 5/3$ and $\rho_\infty \simeq 0$),

$$\rho = \left(\frac{1}{\sqrt{r^2+z^2}}\right)^{\frac{3}{2}} \tag{3.30}$$

with

$$\rho_i = \frac{\beta_i \delta_i}{2} \frac{B_i^2/4\pi}{v_{K,i}^2} \tag{3.31}$$

at r_i. The above expression can explicitly be written as

$$\rho_i = 3.74 \times 10^{-14} \beta_i \delta_i (\frac{B_i}{10G})^2 (\frac{r_i}{0.05AU})(\frac{0.5M_\odot}{M}) \quad g/cm^3, \tag{3.32}$$

for YSOs, and

$$\rho_i = 9.01 \times 10^{-18} \beta_i \delta_i (\frac{B_i}{100G})^2 (\frac{r_i}{10r_G}) \quad g/cm^3, \tag{3.33}$$

for AGNs. The choice of 100 G for typical AGN coronal field is compatible with sub-Eddington luminosity (see §5.4).

3.4 Conditions in the Underlying Disk Surface

The Keplerian accretion disk surface (the base of the corona) provides fixed boundary conditions and is defined in the $z < 0$ region. Here we have no feedback from the jet to the disk[4].

[4]The disk is undeniably important in providing the initial conditions at the base of the jet. That is, one cannot have a complete understanding of the dynamics of the jet without including the physics of the underlying disk. One has to match disk solutions to wind solutions, at the disk surface, to

3.4.1 Pressure Balance

The surface of the disk is placed in pressure balance with the atmosphere above. This implies that

$$p_d = p_{eff_o} = (1 + \frac{1}{\beta_T})p_o \tag{3.34}$$

where the subscript "d" stands for disk and "o" for coronal quantities at $z = 0$. Using an adiabatic equation of state for the gas in the disk's surface $\left(p_d = p_{d_i}(\frac{\rho_d}{\rho_{d_i}})^\gamma\right)$, it is trivial to show that there must therefore exist a density jump across the disk surface of the order;

$$\frac{\rho_d}{\rho_o} = \frac{\rho_{d_i}}{\rho_i} = const = \eta_i, \tag{3.35}$$

where η_i is our third free parameter. Furthermore, for an ideal gas, one can write (3.28) as

$$c_{s,d}^2 = \frac{\gamma - 1}{\gamma}\frac{\delta_i}{\eta_i} \times c_{s,o}^2, \tag{3.36}$$

or

$$T_d = \frac{\gamma - 1}{\gamma}\frac{\delta_i}{\eta_i} \times T_o, \tag{3.37}$$

---

completely study the origin, evolution and stability of jets. Such studies have been carried out by many authors (Königl 1989, Ferreira & Pelletier 1995, Wardle & Königl 1993, Li 1995) who derived some physical conditions required to magnetically launch the jet and produce a super-Alfvénic wind. However, these studies had to assume stationarity and self-similarity in order to solve the full set of non-linear differential equations. These assumptions prevent one from studying time-dependent jets

where $T_o = T(r, z = 0)$ and

$$T(r, z) = \frac{1}{\sqrt{r^2 + z^2}}. \tag{3.38}$$

Thus, our pressure balance condition implies that the temperature at the surface of the disk scales with disk radius as

$$T_d = \frac{\gamma - 1}{\gamma} \frac{\delta_i}{\eta_i} \times \frac{1}{r}. \tag{3.39}$$

This is different from the $r^{-\frac{1}{2}}$ variation which fits the observed flat spectrum in CTTSs (Adams et al., 1987, Beckwith et al. 1990, for YSOs) or the $r^{-\frac{3}{4}}$ variation as derived from the theory of optically thick Keplerian accretion disks for both YSOs and AGNs (Frank et al., 1992).

The above equation relates the disk's temperature to the coronal temperature so that if we assume a typical disk thickness of $z_d \simeq 0.1$ ($\equiv \eta_i \simeq 100$)[5], eq. (3.31) implies

$$T_{d,i} \simeq \frac{2}{5} T_i \tag{3.40}$$

3.4.2 Thin vs Thick Accretion disk models

For thin disks, the condition

$$c_{s,d} << v_K, \tag{3.41}$$

[5]It is straightforward to show that $z_d = 1/\sqrt{\eta_i}$.

is always satisfied, as long as

$$\eta_i \geq \frac{\gamma - 1}{\gamma}\delta_i \tag{3.42}$$

(from eq. (3.3)), since $c_{s,o} << v_K$. That is, the density jump is of the order of δ_i or more, applicable only for disks whose thickness is

$$z_d \leq \sqrt{\frac{\gamma}{(\gamma - 1)\delta_i}}. \tag{3.43}$$

Hence, if $\delta_i \simeq 100.0$ then $z_d \leq 0.1$ as expected for a thin Keplerian disk.

The theory of thin Keplerian disks, assuming they are optically thick, shows that the temperatures in the inner parts of the disk can be written as (Frank et al., 1992)

$$T_{d,i} = 4.1 \times 10^3 (\frac{\dot{m}_a}{10^{-6} M_\odot/yr})^{1/4} (\frac{M_*}{0.5 M_\odot})^{1/4} (\frac{0.05AU}{r_i})^{3/4} \ K \tag{3.44}$$

for YSOs, and

$$T_{d,i} = 10^5 (\frac{\dot{m}_a}{0.2 M_\odot/yr})^{1/4} M_8^{1/4} (\frac{10 r_G}{r_i})^{3/4} \ K \tag{3.45}$$

for AGNs. That is, the typical inner disk temperatures in YSOs is of the order of 4000 K and of about 10^5 K in AGNs. While such disk models are appropriate for YSOs, they have difficulties for the case of AGNs, as explained below.

For the case of a black hole, the standard thin disk model above has a problem with the spectrum. Indeed, extensive observations of black hole systems by *Ginga*, *Grant* and the *Compton Gamma Ray Observatory* (Johnson et al. 1994; Kinzer et al. 1994 and Gilfanov et al. 1995, to cite only few) suggest radiation from an optically

thin plasma with temperatures $T > 10^9$ K. This is much higher than the one given in eq. (3.45). Inner disk temperatures of $10^9 - 10^{10}$ K arise naturally in the theory of geometrically thick, optically thin advective disks however (Esin et al. 1996). We will assume therefore that for AGNs, thick disks provide us with the fixed boundary at the base of the corona. Such disks may have considerable radial inflow speeds, but we ignore these in our simulations. Our chosen model is in agreement with the convective disk model which is only applicable for black holes accreting at sub-Eddington rates (Esin et al. 1996).

From the above discussion and using eq. (3.40), we estimate coronal temperatures of about 10^5 K for YSOs and about 5×10^9 K for AGNs. These values have been used in our estimate of δ_i in §3.3.

3.4.3 The Disk's Current

Thus, the radial balance equation describing the surface of our Keplerian disk, for the configurations chosen, becomes

$$0 = \rho_d \frac{v_\phi^2}{r} - \rho_d \frac{\partial}{\partial r}(\Phi) - \frac{2}{\delta_i \beta i} \frac{B_\phi}{4\pi} \frac{\partial}{\partial r}(r B_\phi) \tag{3.46}$$

in the r-direction. Thus, to be consistent, the last term in eq. (3.40) must be unimportant. This can occur either because of weak toroidal fields ($B_\phi^2/8\pi << \rho v_\phi^2/2$); or when $B_\phi \propto 1/r$ for strong toroidal fields. In the first case, we ran simulations with $B_\phi = 0$ in the disk and found that B_ϕ is nevertheless generated in the corona by

inertial effects (this production of B_o at the base of the corona in turn generates a strong magnetic torque on the surface of the disk which then launchs an outflow, as described in equations (5.69) and (5.70)). The coronal B_ϕ would propagate into the disk leaving it with non zero toroidal field. Our boundary conditions do not allow such a wave to propagate into the disk however. Thus we anticipate that disks must have non-zero toroidal fields.

We model such a field as

$$B_\phi = \frac{\mu_i}{r}, \tag{3.47}$$

which is a current free configuration (PP92), where

$$\mu_i = \frac{B_{\phi_i}}{B_i} \tag{3.48}$$

is introduced as our fourth free parameter. For completeness, the mean field β of the gas in the disk is simply given as

$$\beta_d = \frac{(\gamma - 1)}{\gamma}\delta_i\beta_o. \tag{3.49}$$

For the potential configuration that we study in this paper.

$$\beta_o \simeq \beta_i r_o^{-1/2}. \tag{3.50}$$

That is, β_d falls from the innermost value of $\frac{(\gamma-1)}{\gamma}\delta_i\beta_i$ to an outermost value of

$\frac{(\gamma-1)}{\gamma}\delta_i\beta_i r_e^{-1/2}$. The disk radius at which β_d is unity is simply given as

$$1 = \frac{(\gamma-1)}{\gamma}\delta_i\beta_i r_1^{-1/2} \tag{3.51}$$

or

$$r_1 = (\frac{2}{5}\delta_i\beta_i)^2. \tag{3.52}$$

Interior to r_1 we expect both global and local modes of the BH instability to be present while the linear stage of this instability will dominate in the regions exterior to r_1 (Balbus & Hawley 1991 & 1992). But, again, because we treat the disk simply as a boundary condition at the base of the corona, we cannot study how the instability will affect the physics of the outflow.

3.4.4 The Magnetic Field of the Disk

The initial radial and vertical magnetic field components in the disk, defined by A_ϕ, are matched continuously and smoothly onto the field in the corona. That is, we avoid the presence of any kind of kink in the initial magnetic configurations that might introduce some undesired spurious effects. In the potential field configuration this is true as long as

$$(z_d + z) > 0 \quad \text{for} \quad z < 0 \tag{3.53}$$

To summarize this analytical part of the paper, we have solved for a cold corona in hydrostatic equilibrium. Such a corona is defined by the two free parameters δ_i

and β_i. Underlying it is the surface of a Keplerian disk with which it is in pressure balance. The disk is in centrifugal balance and is defined by three free parameters, the density jump η_i, the azimuthal to the poloidal magnetic field ratio μ_i, and the injection velocity $v_{inj} \equiv v_p/v_K$ defined as the ratio of the poloidal to the Kepler speed in the disk. To be more concise, the parameters δ_i and μ_i prescribe the strength of the coronal poloidal and toroidal fields; δ_i the thermal energy of the corona; and η_i and v_{inj} together determine the mass and momentum injection rate into the corona. Note that β_T is directly linked to δ_i via eq. (3.26), and is not an independent parameter. That is, our initial set up is completely defined by a set of five free parameters, namely (δ_i,β_i,η_i, μ_i, v_{inj}).

4. Numerical Approach

4.1 The Finite Difference Grid in ZEUS-2D

Here, we briefly introduce the reader to the the ZEUS-2D grid as it is important in understanding the following sections. We refer the reader to SN92 for more details.

In Figure 1 (adapted from SN92), we show the two-dimensional staggered grid used by ZEUS-2D. The, "a-grid", is defined by the co-ordinates ($x1_a(i)$,$x2_a(j)$) while the "b" grid, co-ordinates ($x1_b(i)$,$x2_b(j)$), define the zone centers. g_2, g_{31} and g_{32} are the scale factor variables of the diagonal metric tensor which describes the particular orthogonal system of work (here, in cylindrical coordinates, $g_2 = 1$ and $g_{31} = g_{32} =$

r). In such a mesh, the scalar variables (ρ, e) are "zone centered" while the vector variables ($\mathbf{v}, \mathbf{B}$) are "face-centered". Thus, gradient components of zone centered scalars are face-centered quantities, divergences of face-centered vectors are zone-centered, and curl components of face-centered vectors (e.g. the current density $\mathbf{J} = \nabla \times \mathbf{B}$) are "edge-centered".

Note too that grid variables have specific locations attributed to them. Thus, $x1_a(i)$ is a face-centered quantity while $dx1_a(i) = x1_a(i+1) - x1_a(i)$ is a zone-centered quantity..etc.. In this scheme, the MHD equations can be differenced directly. All difference equations use the following nomenclature. The indices (i,j) denote the variable value at the (i,j)th zone located at one of the zone center, zone face, or zone edge as discussed above. The indices is and js stand for the starting indices with ($x1a(is) = x2a(js) = 0.0$), at the origin of the a-mesh.

Two rows of "ghost" zones, defined beyond the computational domain (at (is -1), (is -2), (js-1) and (js-2)) are added along each boundary, as required by the Piecewise Parabolic Advection (PPA) scheme implemented in ZEUS-2D. Values for the variables in the ghost zones are specified using boundary conditions appropriate to the geometry and physics of the problem being solved. Thus evolution equations are not solved for the ghost zones. However, *it is important to know that the ZEUS MHD algorithms will evolve the magnetic field components in a divergence free manner, even in the ghost zones.* This is an important point when considering the evolution of our initial magnetic configuration. In the "active" zones, the evolution equations

are used to update the variables.

4.2 Setting up the Initial Hydrostatic State

Our initial setup, while analytically simple, turned out to be a problem for the ZEUS-2D grid as described above. Our initial state solution requires that for the equilibrium to be achieved, the pressure gradient ∇p has to scale exactly with the potential gradient $\nabla\Phi$ due to the point mass gravitational potential field. But, since forces and density are defined at different locations on a staggered mesh, one has to use averaged densities in the momentum equations as depicted in equations (2.8). While such a procedure makes the code as general as possible, it presents a problem in our case. The difficulty is that because our density profile goes as $1/(r^2+z^2)^{3/4}$, a simple two-point extrapolation scheme fails to properly calculate the density at the zone interface (where forces are located) destroying the initial equilibrium.

Usually, one deals with such a problem by adding a softening parameter. However, *our results changed significantly for slight variations of the softening parameter*, such an approach unreliable[6]. Here, since the momentum equation we have finite differenced is

$$\left[\frac{\partial \mathbf{v}}{\partial \tau} + (\mathbf{v}.\nabla)\mathbf{v}\right] = -\nabla\left(\rho^{n-1/2} - \Phi\right) \tag{3.54}$$

[6]Bell & Lucek (1995) also came to the conclusion that the softening of the gravitational potential may be having a significant effect on the results. The effect of reducing their gravitational softening appears to favour the production of stronger jets.

(for polytropes), the interpolation problem is automatically taken care of, allowing easy implementation of the initial equilibrium. In addition, and for accuracy purposes, we have located the point mass gravitational potential Φ at zone centers[7] in the b-mesh.

The equation above (applicable for simulating polytropic gases only) is different from the form used in ZEUS-2D. In particular, pressure does not appear explicitly in the momentum equation making it independent of the energy equation, which we don't solve for here. It is straightforward to show that the thermodynamic entropy increases across shocks. However, one still needs to account for energy conservation by justifying some convenient energy source to take away the right amount of entropy. We showed that radiation from the forbidden-line emission detected in jets is a plausible candidate (Ouyed & Pudritz 1994a & 1994b). With our PDEs we only solve for flows that possess no contact discontinuities (discontinuities moving with the flow) since we cannot have a jump in density without a jump in pressure.

Our approach preserves the initial equilibrium to machine round-off accuracy. The avoidance of any gravitational *softening* parameter allows us to simulate outflows from the near vicinity of the central object. This last point is important for the understanding of the physics of astrophysical jets. Indeed, in Ouyed & Pudritz II (1997), we show that because of the $1/r^{1/2}$ rotational (Keplerian) velocity law, the

[7] In the original ZEUS-2D code, the point mass gravitational potential is defined by the central object located at the origin of the a-mesh $(x1a(is), x2a(js))$.

twisting of the magnetic field lines strongly increases as one approaches the surface of the central object. This creates a strong gradient in the generated toroidal magnetic field, opening up even an initially vertical magnetic structure. Conditions favorable for ejection set themselves up automatically. The gas is centrifugally ejected from the portion of the disk surface where the magnetic field lines have opened to less than the critical angle ($\simeq 60^o$), as expected from the centrifugally driven wind theory.

Finally, having introduced an effective pressure one also must ensure the accuracy and stability of the code. That is, one ensures that no signal shall cross more than half of any mesh zone in any given time step (physically, this is analogous to maintaining causality: each zone must know about each wave passing through it if the wave is to have any effect on it). This is done by taking into account the effective sound wave propagation in the Courant-Friederich-Levy analysis[8] (Courant & Friederich, 1984). The feasibility and the conservation of the initial equilibrium with the extra term was successfully tested and satisfied to within machine round-off error.

4.3 Initial Magnetic Configuration

We define A_ϕ at zone corners as required by the mesh staggering in ZEUS-2D. However, one must define the vector potential beyond the grid defined by ZEUS-2D. One therefore needs to add an extra row and an extra column for A_ϕ.

A_ϕ is defined analytically in (§3.2) for the two configurations we are dealing with

[8]This is set in the subroutines *nudt.src* and *setup.src* in ZEUS-2D code

here. The potential configuration, as written in (3.14), presents a numerical difficulty; since A_ϕ is defined at the zone corners one faces the problem of a singularity on the axis ($A_\phi \propto 1/x2a(j)$ with $x2a(js) = 0$). Fortunately, we can deal with such a problem by using the stream function[9]

$$\Phi_m = rA_\phi = \sqrt{r^2 + (z_d + z)^2} - (z_d + z), \tag{3.55}$$

with the field components given as

$$B_z = \frac{1}{r}\frac{\partial \Phi_m}{\partial r} \quad \text{and} \quad B_r = -\frac{1}{r}\frac{\partial \Phi_m}{\partial z}. \tag{3.56}$$

Because B_z is located at the face center in a zone, that is at $(x1a(i), x2b(j))$, it has no singularity on the axis (since $x2b(js) \neq 0$). As already explained in §3.2, our configuration, extends continuously and smoothly into the disk ($z < 0$) eliminating any kinks that might introduce spurious current sheets, in the initial set up. Numerically, since the disk's midplane is defined in the ghost zones, at $z = x1a(is - 2)$, one has to artificially set $z_d \geq x1a(is - 2)$ for condition (3.53) to be true. One has to remember that this is just a numerical artifact and that it doesn't change the way our physics is defined and set.

4.4 Parameters and Boundary Conditions

The set of 5 free parameters in our model consists of $(\delta_i, \beta_i, \eta_i, \mu_i, v_{inj})$, and any

[9]This configuration is similar to one given in Cao & Spruit (1995). It can be derived by taking $z_d = 1$. However, while their $z = 0$ surface corresponds to the disk's midplane, here it represents the surface of the disk.

given simulation will be assigned a set of these parameters. Since one of our main goals is to show the self-collimation of jets via self-generation of B_ϕ, we use open boundaries to avoid any artificial collimation due to reflective boundaries. We use inflow boundary conditions (the values of all the variables in the ghost zones are held equal to a set of predetermined values, and outflow is not permitted) at the disk surface (except for the magnetic field for which we use open boundaries, so that it evolves through the $\nabla.\mathbf{B} = 0$ constraint) and open outflow conditions (i.e., *zero normal gradient*) on the remaining boundaries. Along the axis of symmetry, coinciding with the disk axis, reflecting boundaries (i.e., *the normal components of velocity and magnetic field are reflected, while the tangential components are continuous*) are used. Because of the axisymmetry, we compute in only one quadrant. Figure 2., illustrates the initial setup and the open boundary mesh.

The conditions describing the central object and the accretion disk surface are set in the ghost zones and are fixed once and for all (they are fixed boundaries). In all our simulations, the gas is injected (inflow boundary) from the ghost zones into the active zones (the corona) at a velocity $v_p = 10^{-3} v_K$ (or $v_{inj} = 10^{-3}$)[10] with $\mathbf{v}_p \parallel \mathbf{B}_p$. Introducing the launching angle $\theta_o = tan(B_r/B_z)$, the velocity field in the ghost zone is

$$\mathbf{v} = (v_r, v_\phi, v_z) \;=\; (v_p sin(\theta_o), v_K, v_p cos(\theta_o)) \qquad \text{if } r \geq 1 \tag{3.57}$$

[10]The injection velocity is taken to be the hundredth of the disk's sound speed.

$$= (0,0,0) \qquad \text{if } r < 1 \tag{3.58}$$

The second constraint incorporates a region interior to r_i (which might be an empty magnetosphere or simply a slowly rotating object) in which the disk is absent.

In the ghost zones, we also have

$$B_\phi = \frac{\mu_i}{r}, \tag{3.59}$$

while the poloidal field is given by (4.28) for $z < 0$. The disk's density is given as

$$\rho_d = \eta_i \rho_o = \eta_i r^{-3/2}. \tag{3.60}$$

4.5 Time Scales

There are three important initial timescales defined at the disk's surface, where $t_x = r/v_x$, and v_x is the velocity of the wave considered. These are the Kepler time

$$\tau_K = min(\frac{t_{orb}}{t_i}) = min(\frac{r}{v_K}), \tag{3.61}$$

the Alfvén time

$$\tau_A = min(\frac{t_A}{t_i}) = min(\frac{r}{v_A}), \tag{3.62}$$

and the magnetic braking time

$$\tau_B = min(\frac{t_B}{t_i}) = min(\eta_i \frac{r}{v_{A_o}}) = \eta_i \times \tau_A, \tag{3.63}$$

which is the time it would take a torsional wave propagating onto the external medium

to traverse an amount of material whose moment of inertia is the same as the moment of inertia of the disk (Mouschovias & Paleologou, 1980, hereafter MP80). *Note that because of the large density jump ($\eta_i \geq \delta_i = 100$), this time is unimportant in the dynamics* (§5.2.1). The timescales above depend on the magnetic configuration chosen. However, it is straightforward to show that

$$(\tau_K, \tau_A, \tau_B) = (1, \sqrt{\delta_i \beta_i / 2}, \eta_i \sqrt{\delta_i \beta_i / 2}), \tag{3.64}$$

where we naturally take $min(\tau_K) = 1$ at $r = 1$.

5. Numerical Results: Testing Steady State Models

Here we present some preliminary results for a steady state simulation based on the potential field discussed in §4.3. The parameters are

$$(\delta_i, \beta_i, \eta_i, \mu_i, v_{inj}) = (10^2, 1.0, 10^2, 1.0, 10^{-3}) \Rightarrow (\tau_K, \tau_A, \tau_B) = (1.0, 7.07, 707.1). \tag{3.65}$$

The simulation was run in the domain $(z, r) = (80, 20)$ with a resolution of $(500, 200)$ cells, for up to 500 time units ($< \tau_B$).

5.1 Steady State Theory

Before analyzing the above simulation we present a brief introduction to the main results of the theory of steady state MHD winds. This will guide us in the choice of the appropriate diagnostics for steady state solutions. We remind the reader that all quantities are in their dimensionless form.

It is well known that, in the steady state limit, all equations (2.1–2.4) can be integrated once to yield the conservation of total specific energy $e(a)$ and angular momentum $l(a)$ along each field line ($2\pi a$ is the magnetic flux along a magnetic tube),

$$e(a) = \frac{v_p^2}{2} + \frac{v_\phi^2}{2} + h + \Phi - r\frac{B_\phi \Omega}{4\pi k} \tag{3.66}$$

$$l(a) = r v_\phi - \frac{r B_\phi}{4\pi k} \tag{3.67}$$

where $k(a)$ is the mass flux per unit magnetic flux in the flow (also constant along a magnetic tube)

$$k(a) = \frac{\rho v_z}{B_z}. \tag{3.68}$$

To locate the position of the Alfvén point along a given field line one needs to combine equation for l and k above and the Alfvén critical condition $l(a) = \Omega r_A^2$ (see BP82, for e.g), to find that

$$\left((\frac{r_A}{r_o})^2 - 1\right) = \frac{v_{A\phi}}{v_\phi}\frac{v_{Az}}{v_z}|_{z=0}, \tag{3.69}$$

where

$$v_{Az} = \frac{B_z}{\sqrt{4\pi\rho}} \quad \text{and} \quad v_{A\phi} = \frac{B_\phi}{\sqrt{4\pi\rho}}. \tag{3.70}$$

The ratio r_A/r_o is the so-called Alfvén lever arm which defines the efficiency of the magnetic torque in extracting angular momentum through the surface of the disk.

The quantities on the RHS are estimated at the disk surface, $(r, z = 0)$.

5.1.1 Centrifugally Driven Winds

The mechanism for centrifugally driven winds, in the MHD limit, was first worked out by BP82 who constructed cold, time-independent, axisymmetric self-similar wind solutions above infinitely-thin Keplerian disks. The gas is centrifugally flung out from the surface of a Keplerian accretion disk. Such winds can be launched if the field lines are inclined by no more than 60^o from the surface of the disk (we call this the launching condition). These wind solutions are controlled mainly by two dimensionless parameters which characterize the mass loss rate (the κ of BP82) and the total specific angular momentum (their λ)[11]. In the BP82 scheme, it is easy to show that

$$\lambda = (\frac{r_A}{r_o})^2 \quad \text{and} \quad \frac{B_\phi}{B_z} \mid_{z=0} = -\kappa(\lambda - 1) \tag{3.71}$$

For a given field line, these two equations allow us to make contact with BP82 results (see §5.3.1).

In their Figure 4, BP82 show the behavior of the physical quantities along a field line. Beyond the Alfvén surface (one of the wind's critical points), the $\mathbf{J_p} \times \mathbf{B}_\phi$ force (where B_ϕ is self-generated in the flow) eventually dominates providing *the self-collimation* of the outflow. The *final velocities* achieved by such winds are of the order

[11]The requirement that their solution passes smoothly through the Alfvén critical point fixes the third parameter, namely the launching angle $\theta_{o,BP}$.

of few times the Kepler velocity, along a given field line.

5.2 Evolution of the Outflow

The evolution of the flow can be described in three stages:

5.2.1 The Emission of Torsional Alfvén Waves

The early stage of the outflow is dominated by the propagation of a torsional Alfvén wave front from the disk surface. The *linear regime* of propagation of torsional waves is well presented in MP80. Briefly, the equation for propagation of linear torsional waves in the external medium can be shown to be

$$\frac{\partial^2 B_\phi}{\partial t^2} = v_{A,ext}^2 \frac{\partial^2 B_\phi}{\partial z^2} \tag{3.72}$$

Waves are launched because of the existence of an initial gradient of B_ϕ in the z-direction. This arises from the fact that in our initial state, $B_\phi = 0$ in the corona while $B_\phi \propto 1/r$ in the disk. Now, because $v_{A,ext} \propto (r^2 + z^2)^{-1/4}$, torsional waves starting at different footpoints will travel into the corona at different velocities. This fact gives a conical shape to the Alfvén front, as is seen in the simulation.[12]. In our simulations we can see these torsional Alfvén waves leaving the mesh while the outflow hasn't completely started yet. The magnetic configuration and the density distribution is still more or less in its initial state. As the gas becomes super-Alfvénic

[12]In the vertical field configuration, because $v_{A,ext} \propto (r^2 + z^2)^{3/8}$ we obtain a completely different wave front (Ouyed & Pudritz II, 1997).

it catches up with the Alfvén front and goes beyond it.

Note that in the classical scenario of the magnetic braking of an aligned rotator (which can be pictured as a rotating flat structure or fly-wheel that is threaded by straight magnetic field lines), the torsional waves propagate into the external medium thereby slowing down the rotor. Physically, one expects such a fly-wheel to slow down significantly when the hydromagnetic waves propagating away from the cloud set into rotational motion an amount of external matter with moment of inertia equal to that of the cloud. This evolution of a disk is not expected in our simulation since the central object forces the gas to remain in near Kepler rotation at all times. For this reason, the conditions in the ghost zones (the disk surface) are set once for all and are time independent (remember that the disk is just a boundary condition, it never evolves in time). However, as already mentioned in §4.5, for the large density jump η_i expected for our accretion disk model, the timescale τ_B is very long which reduces the braking effect in our simulations ($\tau_S < \tau_B$).

5.2.2 Interaction of the Outflow with the Corona

We find that an outflow is indeed launched from the disk surface. To illustrate the structure and dynamics of the outflow, we plot in Fig. 3 the evolution of the density (left panels) and of the toroidal magnetic field (right panels). In Fig. 4, we illustrate more of the dynamics of the jet-like outflow by plotting the density (left panels) and the toroidal magnetic field (right panels) along a cut parallel to the disk's

axis. The cut is taken directly in Fig. 3 at $r_o = 5r_i$ The frames (for both figures) are for different time steps which are $\tau = 0.0$, $\tau = 100.0$, $\tau = 200.0$ and $\tau = 400.0$ from top to bottom, respectively. The bow shock (at $\tau = 200$ in Fig. 3) traces the working surface of the outflow with respect to the undisturbed corona. There is also a highly collimated jet-like stream of gas that starts at the disk surface and terminates in a shock behind the working surface (at $\tau = 200$ in Fig. 4). The pivotal role that is played by the toroidal field is clearly shown. The outflow density along the outflow axis is clearly delimited by the region of strong toroidal field. Such features have been seen in pure MHD jet simulations (Clarke et al. 1986, Lind et al. 1989). The physical reason for this is the strong radial pinch force that is exerted towards the jet axis by the magnetic force arising through the combination of a dominant toroidal field, and its associated current which flows primarily along the outflow axis.

In Fig. 3, it is clearly seen that the jet is hollow (on radial scales $< r_i$) and no motion (outflow or inflow) is present within this hollow region. This is possible only under a strict initial equilibrium and is a consequence of our boundary condition that assumes the absence of a disk inside r_i. The density contrast between the interior of this region and the jet is of the order of 4. Such a region could provide a *channel* for the relativistic beams usually associated with the innermost regions of AGNs jets (Sol et al. 1989 and Pelletier & Sol 1991, for e.g).

The thickness of the working surface of the jet (Fig. 4 at $\tau = 200$) is $3-4\ r_i$. It is better seen in Fig. 4 (at $\tau = 200$) where a density jump of about 4 is seen within

the layer. The density features seen in Fig. 3 (at $\tau = 300$) are transient and the jet evolves quickly into the steady state.

Fig. 5 shows the evolution of the initial potential magnetic field (left panels) as well as of the launching angle (right panels). The frames are for different time steps which are $\tau = 0.0$, $\tau = 100.0$, $\tau = 200.0$ and $\tau = 400.0$ from top to bottom, respectively. As it evolves in time, the jet adjusts the launching angle along the disk surface (through the radial gradient of the generated B_ϕ) so as to make each field line go smoothly through the Alfvén and the FM critical points.

The poloidal velocity field (Fig. 6) shows in that the highest speed gas is nearest the outflow axis, and farthest from the source!

5.2.3 Cylindrical Collimation

In the late stages of the outflow and beyond the Alfvén surface, the wound up field collimates the gas towards the axis, as seen in the lower left panel at $\tau = 400.0$. We found that our winds always collimate into cylinders along the symmetry axis at large distances from the source as predicted by HN89. Fig. 7 shows the poloidal current density current ($\tau = 400$ for a $(z \times r) = (100 \times 50)$ mesh). Our final poloidal current is a nonvanishing one as required by HN89 solutions. When compared to the poloidal magnetic field lines, it is clearly seen that the jet is far from a force-free solution ($\mathbf{J}_p \parallel \mathbf{B}_p$). The current completes a circuit by flowing downwards along the jet axis, radially outwards through the accretion disk, and then upwards along the

flank of the bow-shock closing the circuit by returning to the outflow axis.

5.3 Steady State Solutions

A robust diagnostic for the existence of a steady state solution is to compute the angular momentum l, and the mass flux to magnetic flux ratio k along any given field line. A steady state is achieved when these three quantities are constant along the field line. An example is given in Fig. 8 for an inner field line ($r_o \simeq r_i$). The dot represents the location of the Alfvén point while the square is the FM point, along the chosen field line. Note that beyond the FM surface our solution seems to deviate away from the steady state but nonetheless it still oscillates around it.

Once the steady state is achieved, we estimate, from our numerical data, B_z, B_ϕ and ρ at the footpoint of the given field line and compute the theoretical lever arm as given by (5.69). This is done for the simulation as a whole as shown in the lower panel of Fig. 8 where we compare the Alfvén lever arms (filled hexagons) to the predictions from the steady state theory (squares). We find good agreement for streamlines which originate from the inner disk. Streamlines from the outer regions of the disk leave the mesh through the outer radial boundary before reaching the FM point, and this may affect the solution in the acceleration zone.

5.3.1 Driving Mechanism

A fundamental question arising from these results is to identify the force respon-

sible for driving the mass outflow. We show in Ouyed et al. (1997) that the outflow is a result of the centrifugal wind mechanism. We showed the existence of an acceleration region, very close to the disk surface. The value of v_ϕ increases until the Alfvén critical point is reached as the matter is accelerated along the field lines by the magnetic stresses. Beyond the Alfvén point, the inertia of the matter dominates the azimuthal flow and v_ϕ decreases as the matter attempts to conserve its angular momentum independently of the magnetic field. Beyond the Alfvén surface, the $\mathbf{J_P} \times \mathbf{B_\phi}$ force eventually dominates providing *the collimation* (where B_ϕ is self-generated in the flow). The *final velocities* achieved by such winds are of the order of 2 times the Kepler velocity, along a given field line (see Fig. 3 in Ouyed et al. (1997)).

Estimating r_A/r_o, B_ϕ/B_z and the injection angle θ_o (from our numerical data), for our chosen field line, we then use equations (5.71) to calculate the corresponding BP82 parameters κ and λ. In Fig. 9, we plot the standard κ-λ graph (upper panel) and the κ-θ_o graph (lower panel) with the location of the launching angle θ_o. In this simulation, the flow from the outer parts of the disk is particle-dominated ($\kappa \geq 1.0$ for the outer few field lines). This explains why the outer parts of the jet show less collimation compared to the inner part. It turns out that this is a boundary effect that can be taken care of by extending the size of the mesh (radially) and by increasing the computation time. We find that κ and λ can always be related by a simple relation.

That is,

$$\lambda \simeq \frac{2.4}{\kappa^{2/3}}. \tag{3.73}$$

Simply put, since our launching angle becomes constant along the disk's surface (in the late stages of the simulation), the outflow manages to go smoothly through the Alfvén critical point and the FM point by finding the right combination of κ, and λ at each disk's radius. The difference between the self-similar study (BP82 found $\lambda \simeq \frac{1}{\kappa}$) and our result may be due to the different magnetic field distribution used; our outflow is not self-similar.

Finally, we find that the acceleration of material occurs in two separate spatial stages. In stage 1 (the region along a field line between the disk and the FM point) the centrifugal effect dominates. In stage 2, (region beyond the FM point), a "Hubble flow" character of the flow with $v_z \propto z$ develops. While such behavior has been predicted for purely hydrodynamic flows (Raga & Kofman, 1992) our solution predicts it for MHD flows as well. With a simple MHD approach one can show that such a feature develops because the flow is highly super-Alfvénic and is cylindrically collimated (our case). Under these conditions, the force on the gas vanishes, $dv_z/dt \simeq 0$. The self-similar solution of this condition is just the Hubble flow. This is better illustrated in Figure 10 where we show the axial velocity along a cut taken parallel to the disk's axis, at $j = 40$ (here we've extended the domain of simulation up to $z = 100.0$ and found that the so-called Hubble flow still persists).

5.4 Fluxes and Accretion Rates

In this scheme, mass flux is defined as

$$\dot{m}_w = \int_{r=0}^{r=r_{max}} 2\pi\rho v_z dr. \tag{3.74}$$

For the protostellar case, defining $M_{0.5} = M_*/0.5M_\odot$, mass flux is given in units of

$$\dot{m}_i = 2\pi r_i^2 \rho_i V_{K,i} = 2.13\beta_i\delta_i \times 10^{-8} M_{0.5}^{-1/2} \left(\frac{r_i}{0.05AU}\right)^{5/2} \left(\frac{B_i}{10G}\right)^2 \; M_\odot/yr \tag{3.75}$$

The momentum flux is in units of

$$(\dot{m}v)_i = 2\pi r_i^2 \rho_i V_{K,i}^2 = 2.22\beta_i\delta_i \times 10^{-6} \left(\frac{r_i}{0.05AU}\right)^2 \left(\frac{B_i}{10G}\right)^2 \; M_\odot km/s/yr \tag{3.76}$$

while, the kinetic flux is in units of

$$(\dot{m}v^2)_i = 2\pi r_i^2 \rho_i V_{K,i}^3 = 1.46\beta_i\delta_i \times 10^{31} M_{0.5}^{1/2} \left(\frac{r_i}{0.05AU}\right)^{3/2} \left(\frac{B_i}{10G}\right)^2 \; erg/s \tag{3.77}$$

Similarly for AGNs, one gets the mass flux in units of

$$\dot{m}_i = 2\pi r_i^2 \rho_i V_{K,i} = 5.62\beta_i\delta_i \times 10^{-4} M_8^2 \left(\frac{r_i}{10r_g}\right)^{5/2} \left(\frac{B_i}{10^2G}\right)^2 \; M_\odot/yr \tag{3.78}$$

The momentum flux is in units of

$$(\dot{m}v)_i = 2\pi r_i^2 \rho_i V_{K,i}^2 = 3.77\beta_i\delta_i \times 10^1 \left(\frac{r_i}{10r_g}\right)^2 \left(\frac{B_i}{10^2G}\right)^2 \; M_\odot km/s/yr \tag{3.79}$$

while, the kinetic flux is in units of

$$(\dot{m}v^2)_i = 2\pi r_i^2 \rho_i V_{K,i}^3 = 1.6\beta_i\delta_i \times 10^{42} \left(\frac{r_i}{10r_g}\right)^{3/2} \left(\frac{B_i}{10^2G}\right)^2 \; erg/s \tag{3.80}$$

We have used expression (3.33) and (3.33) for ρ_i and replaced $v_{K,i}$ using Table 1.

For the case of AGNs , assuming an accretion *efficiency* ϵ, the accretion luminosity can be written as (see Frank et al. 1992, for example)

$$L_{acc} = \epsilon \dot{m}_a c^2 \tag{3.81}$$

Using the Eddington luminosity defined as $L_E = \dot{m}_E c^2$ where $\dot{m}_E = 4\pi G m_p / c\sigma_T$ is the Eddington accretion rate (σ_T is the Thomson cross section for electron scattering), we find that

$$\frac{L_{acc}}{L_E} = \epsilon \frac{\dot{m}_a}{\dot{m}_E} = \epsilon (\frac{\dot{m}_a}{\dot{m}_w})(\frac{\dot{m}_w}{\dot{m}_i})(\frac{\dot{m}_i}{\dot{m}_E}) \tag{3.82}$$

For AGNs with sub-Eddington luminosities (§3.3.1), we require

$$\frac{L_{acc}}{L_E} = 2.81 \times 10^{-4} (\frac{\epsilon}{0.1})(\frac{\dot{m}_a}{\dot{m}_w})(\frac{\dot{m}_w}{\dot{m}_i}) \beta_i \delta_i M_8^{-3} \left(\frac{r_i}{10 r_g}\right)^{5/2} \left(\frac{B_i}{10^2 G}\right)^2 < 1, \tag{3.83}$$

where we have used eq.(5.78) for m_i and $\dot{m}_E = 0.2 M_8 \ M_\odot / yr$. Since steady state theory predicts $\dot{m}_a / \dot{m}_w \simeq 10$ (BP82; PP92) and assuming $\dot{m}_w / \dot{m}_i < 1$, the above constraint becomes

$$\frac{L_{acc}}{L_E} = 0.281 (\frac{\epsilon}{0.1}) M_8^{-3} \left(\frac{r_i}{10 r_g}\right)^{5/2} \left(\frac{B_i}{10^2 G}\right)^2 < 1, \tag{3.84}$$

for our fiducial parameters. This simple estimate shows why we take $B = 100$ G for sub-Eddington AGNs. in our model. We show from the following analysis that our simulations give values for $\dot{m}_a / \dot{m}_w$ and $\dot{m}_w / \dot{m}_i$ that are consistent with the above condition.

In Figure 11, we quantify the strength of the observed outflow. The solid line denotes the energy, momentum, and mass fluxes across the inner ($z = 0.0$) boundary. The short dashed line denotes these fluxes across the outer radial boundary ($r = 20.0$). Finally, the dotted line denotes these fluxes across the outer axial boundary ($z = 80.0$). At later times, the fluxes in the outflow are comparable to the the fluxes at the inner boundary. When given in cgs units (and assuming values for the free parameters appropriate to a protostellar disk and/or black holes), then the typical mass, momentum and energy flux rates given in Table 3.

We further quantify the strength of our flow by plotting, in Figure 12, the bulk energies involved (integrated over the entire computing volume). While the upper panel shows that most of the magnetic energy is in the form of the toroidal ($B_\phi^2/8\pi$) form, the lower panel indicates that most of the kinetic energy is in the form of the bulk kinetic energy of the poloidal flow ($\rho v_p^2/2$). In general, our solution corresponds to flow in which most of the energy is shared between the bulk poloidal kinetic energy (2/3 of the total energy) and the toroidal magnetic energy (1/3 of the total energy). If we assume that the total kinetic and magnetic power put into the jet is equal to half the total gravitational binding energy that can be released in the accretion disk ($L_w = \frac{1}{2}\frac{GM\dot{M}_a}{r_i}$ from Pringle 1981; the other half of $\frac{GM\dot{M}_a}{r_i}$ being dissipated in the boundary layer; protostar or black hole), then we can write, in dimensionless form.

that

$$3L_w = \frac{1}{2}\dot{m}_a \tag{3.85}$$

where L_w is the total kinetic power of the flow from each surface of the disk, given in the upper panel of Figure 9. The factor 3 in front comes from the fact that one has to consider the two surfaces and the fact that $L_{mag} \simeq L_w/2$. Since $L_w \simeq \dot{m}_w = 0.3$ (see Figure 11), we then find that,

$$\dot{m}_a \simeq 6.0\dot{m}_w. \tag{3.86}$$

Hence, only a fraction of the accreted gas needs to participate in the outflow, which clearly shows the high efficiency of centrifugally driven wind mechanism in magnetically extracting mass and energy from the disk. For AGNs and for our typical black hole, with an accretion *efficiency* ϵ of 0.1, condition (5.84) is then satisfied since

$$\frac{L_{acc}}{L_E} = 0.05 < 1. \tag{3.87}$$

Finally; in Figure 13, we show a snapshot (at $\tau = 400$) of the dependence of the mass outflow rate upon the poloidal velocity of the jet. The top panel shows that the velocity peaks at $r \simeq 6r_i$). The middle panel confirms the fact that most of the material is carried out between $3r_i < r_{wind} < 15r_i$. The lower panel indicates that the bulk of the material moves at speeds ($\simeq 0.6v_{K,i}$). *Note that Fig. 13 is taken at a snapshot time during which the highest velocities registered were only* ($\simeq 0.8v_{K,i}$).

However, velocities as high as $2.1v_{K,i}$ *are reached in our flow.*

6. Summary and Conclusions

We have presented 2.5D simulations of outflows accelerated from the surface of Keplerian accretion disks orbiting protostars or black holes. Our model is applicable for low mass protostars and for the non-relativistic regions of disks in AGNs accreting at sub-Eddington rates. In this paper, we have introduced the reader to our initial set up and our extended version of the ZEUS-2D code. We have avoided the use of any softening parameter and reduced the number of free parameters to five. The steady state outflow achieved in this simulation has properties that confirm many of the results of steady state, MHD wind theory. The acceleration of the flow from the disk occurs by a centrifugal effect whereby, at some point along sufficiently inclined field lines, centrifugal force dominates gravity and gas is flung away like "beads on a wire". Thus, toroidal field component is created because the field lines co-rotate with the underlying disk. The inertia of the matter in the flow region ultimately forces the field to fall behind the rotation of the disk, which produces the toroidal field component. This process is responsible for collimating the flow, and enforcing its collimation far from the acceleration region near the disk and over the length of the jet.

Our main conclusions can be summarized as follow:

(i) We found that collimation due to B_ϕ is always present in our simulations.

Table 3. Fluxes and Energetics

Central Object	$Mass\ (M_\odot)$	$\dot{m}_w\ (M_\odot/yr)$	$\dot{m}_w v\ (M_\odot km/s/yr)$	$\frac{1}{2}\dot{m}_w v^2\ (erg/s)$
$Proto-Star$	0.5	9.1×10^{-7}	2.8×10^{-5}	8.0×10^{32}
$Black\ Hole$	10^8	2.2×10^{-2}	7.5×10^2	1.2×10^{43}

A cylindrical configuration is always reached as predicted by HN89. Our outflows rapidly achieve a highly collimated, even jet-like character.

(ii) The wind becomes super-Alfvénic and reaches *terminal velocities* of the order of $1-2v_{K,i}$. That is, an average velocit of $V_{wind} \sim 180$ km/s, for our typical protostar, and of about 10^5 km/s for a $10^8 M_\odot$ black hole.

(iii) Beyond the FM surface, the outflow is completely dominated by the so-called Hubble flow profile, $v_w \propto z$. Large scale simulations will be important in determining whether or not such behaviour persists on larger physical scales.

(iv) We find that κ and λ are simply related; $\lambda \simeq 2.4/\kappa^{2/3}$. The difference between the self-similar study (BP82 found $\lambda \simeq \frac{1}{\kappa}$) and our result may be due to the different magnetic field distribution used.

(v) Most of the energy in our outflow is shared between the bulk poloidal kinetic energy (2/3 of the total energy) and the toroidal magnetic energy (1/3 of the total energy).

(vi) In 1000 years, for example, and for our standard YSO; we estimate that our jet-like outflow carries a a total energy of 3×10^{43} *ergs* sufficient to produce the

observed molecular outflows (Lada, 1985; Chernin & Masson, 1991).

(vii) We found our flow to be very efficient in extracting energy from the disk since only a tiny part of the accreted gas needs to be converted into a wind. We estimate that the effective accretion rate through the underlying disk is, $\dot{m}_a \simeq 6.0\dot{m}_w$. For the model parameters characterizing our simulation, the YSO accretes at a rate of about $5.5 \times 10^{-6}\ M_\odot/yr$ while a $10^8 M_\odot$ black hole at a rate of about $0.1\ M_\odot/yr$. Our solution correspond to an AGN with a sub-Eddington luminosity; $L/L_E = 0.05$.

Our conclusions must be tempered by emphasizing the assumptions we have made. For example, we have assumed axisymmetry and that the equation of state is polytropic. We have also assumed ideal MHD. The primary effect of reducing the dimensionality of the dynamics is to eliminate some modes of MHD instability. These modes can play an important role in the dynamics of outflows. It is clear that investigating the effects of the missing physics cited above is an important avenue for future research. While our present simulations show that the precepts of steady state MHD wind theory are essentially correct, nature, it seems, rarely chooses such solution. We present in an upcoming paper (paper II) a magnetic configuration that gives rise to an episodic outflow.

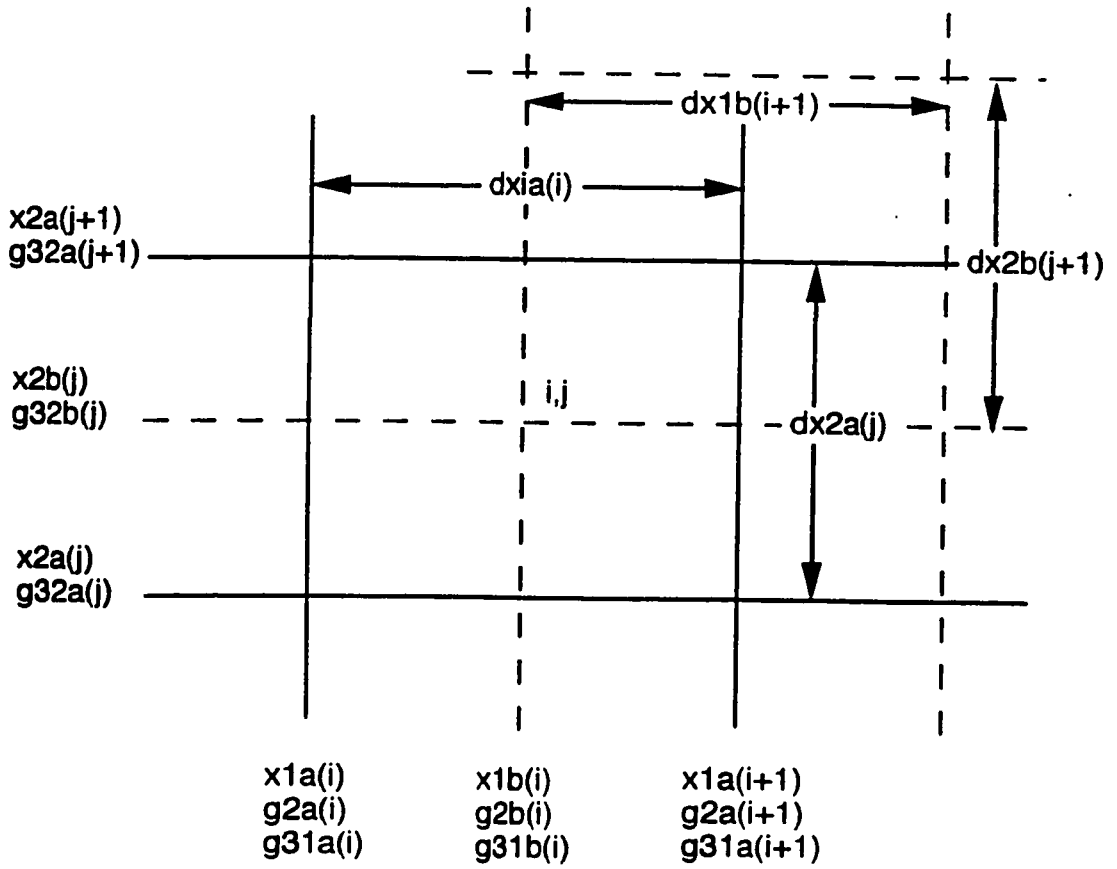

Figure 1. - Coordinate grid definitions on the staggered grid used in ZEUS-2D: solid lines="a-mesh"; dashed lines="b-mesh". g_2, g_{31} and g_{32} are the scale factor variables of the diagonal metric tensor which describes the particular orthogonal system of work (here, in cylindrical coordinates, $g_2 = 1$ and $g_{31} = g_{32} = r$).

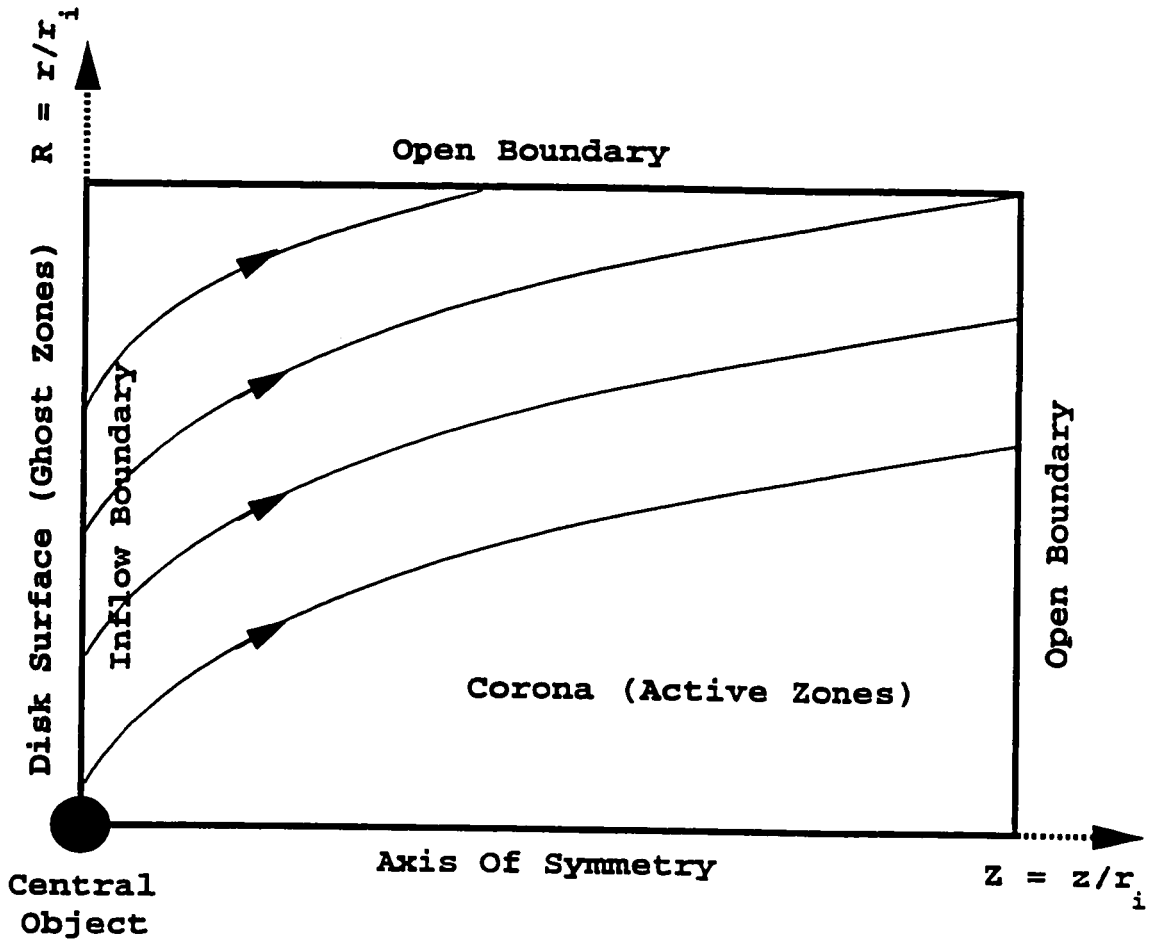

Figure 2. - Setup of the numerical simulation. In this figure (and in all the figures), the axis of symmetry is plotted horizontally and the equatorial plane vertically. Note because of axisymmetry we only compute in one quadrant. The ghost zones ($z < 0.0$) define the surface of the Keplerian disk while the actives zones (which are evolved in time) define the corona. The magnetic field continues smoothly into the disk surface.

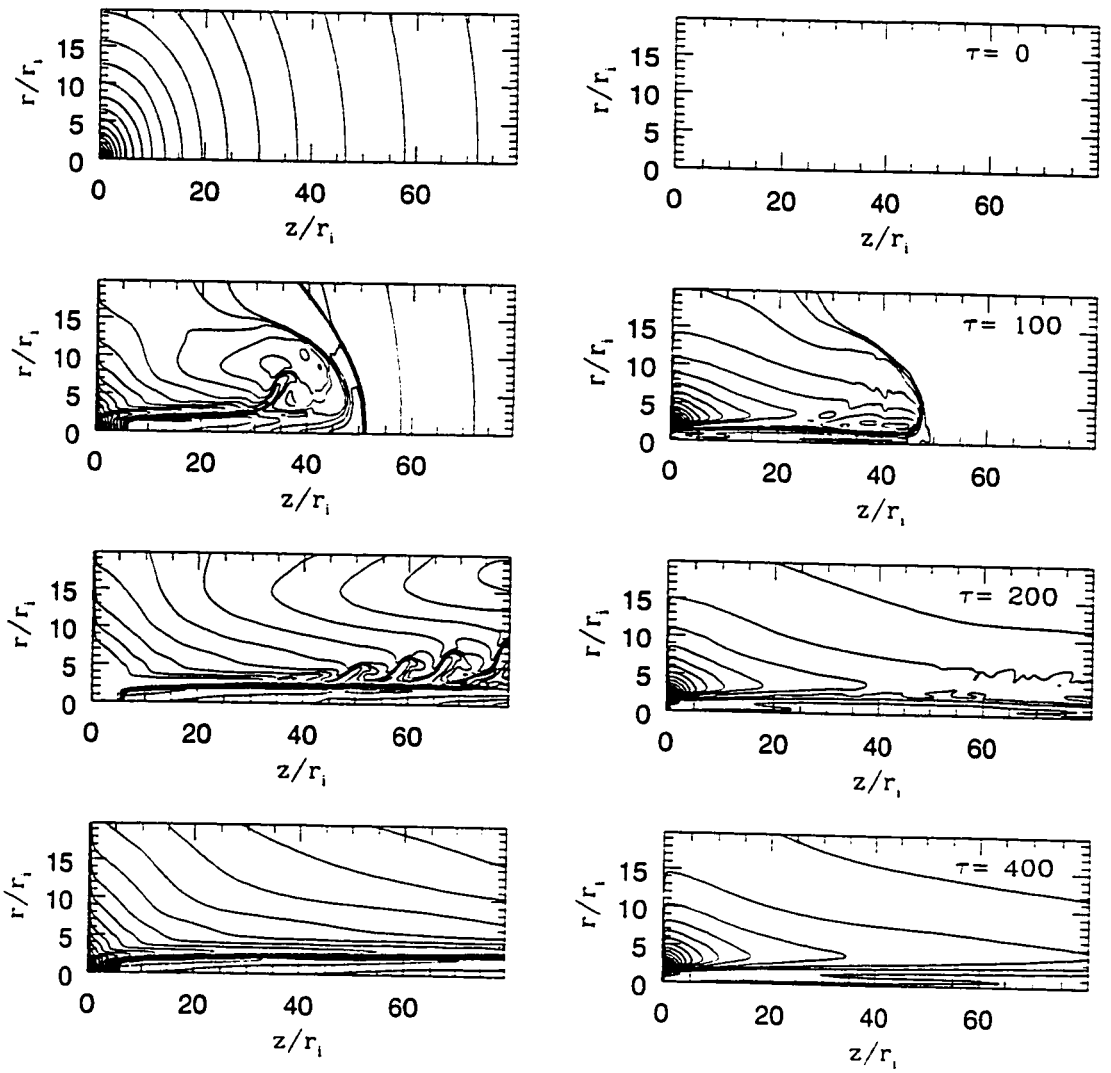

Figure 3. - Evolution of the density (isocontours shown in the left panels) and the toroidal magnetic field (isocontours shown in the right panels). The initial density distribution, as given by (3.30), is shown in the upper left panel. Initially $B_\phi = 0.0$ in the corona (upper right panel). The mesh is $(z \times r) = (80 \times 20) r_i$ with a resolution of (500×200) zones. 20 logarithmically spaced contour lines are shown for the density, and 20 linearly spaced contours for B_ϕ. The evolution is shown at four different times: $\tau = 0$, $\tau = 100$, $\tau = 200$ and $\tau = 400$ from top to bottom.

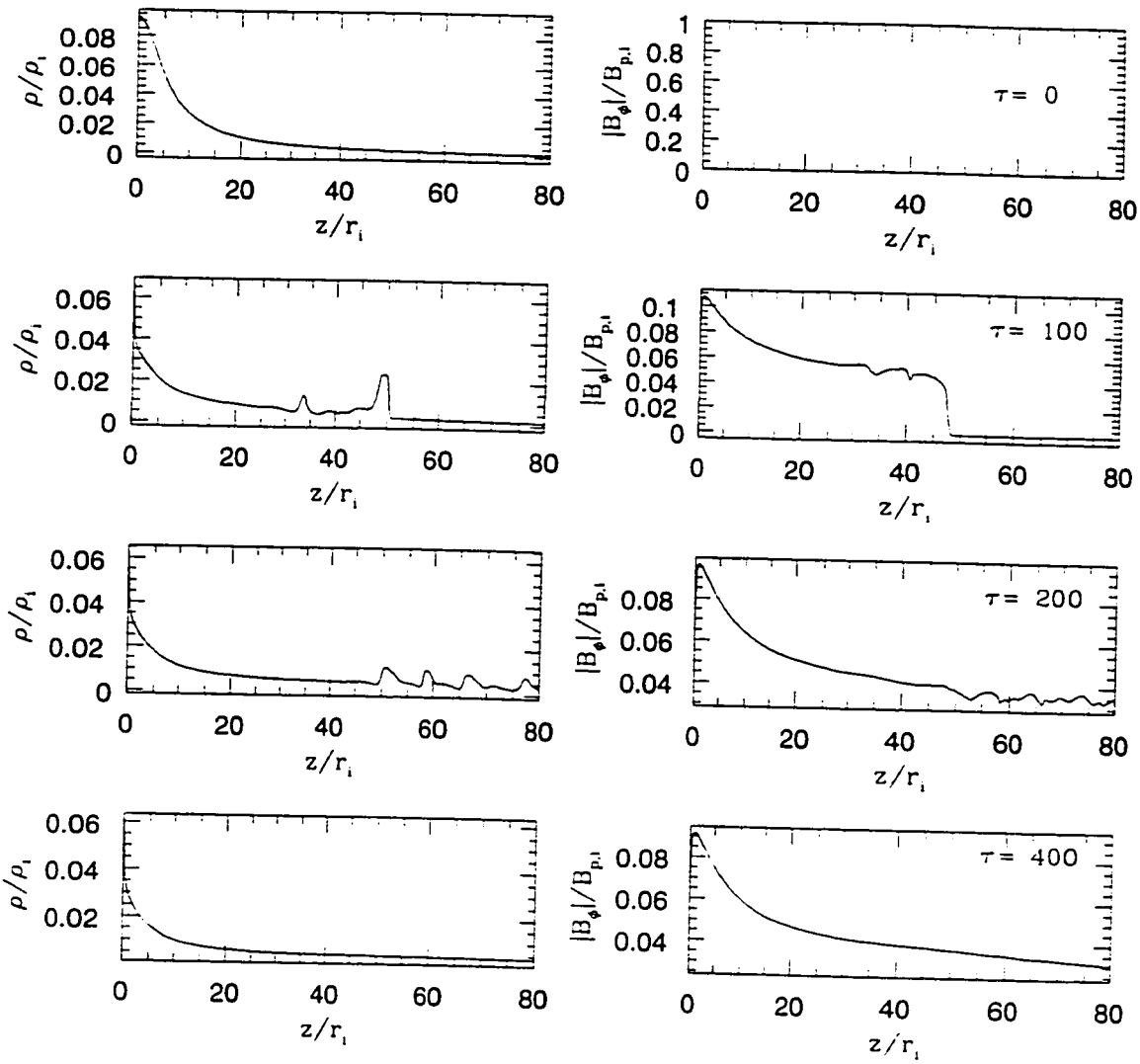

Figure 4. - To complete Figure 3. we plot here the density (left panels) and $|B_\phi|$ (right panels) along a cut parallel to the disk's axis. The cut is taken directly in Figure 3 at $r_o = 5r_i$ (as in Figure 3. the panels are for four different time: $\tau = 0$, $\tau = 100$, $\tau = 200$ and $\tau = 400$ from top to bottom). This figure illustrates the values of the contour levels as well as the jet to the ambient density ratio during the evolution of the outflow.

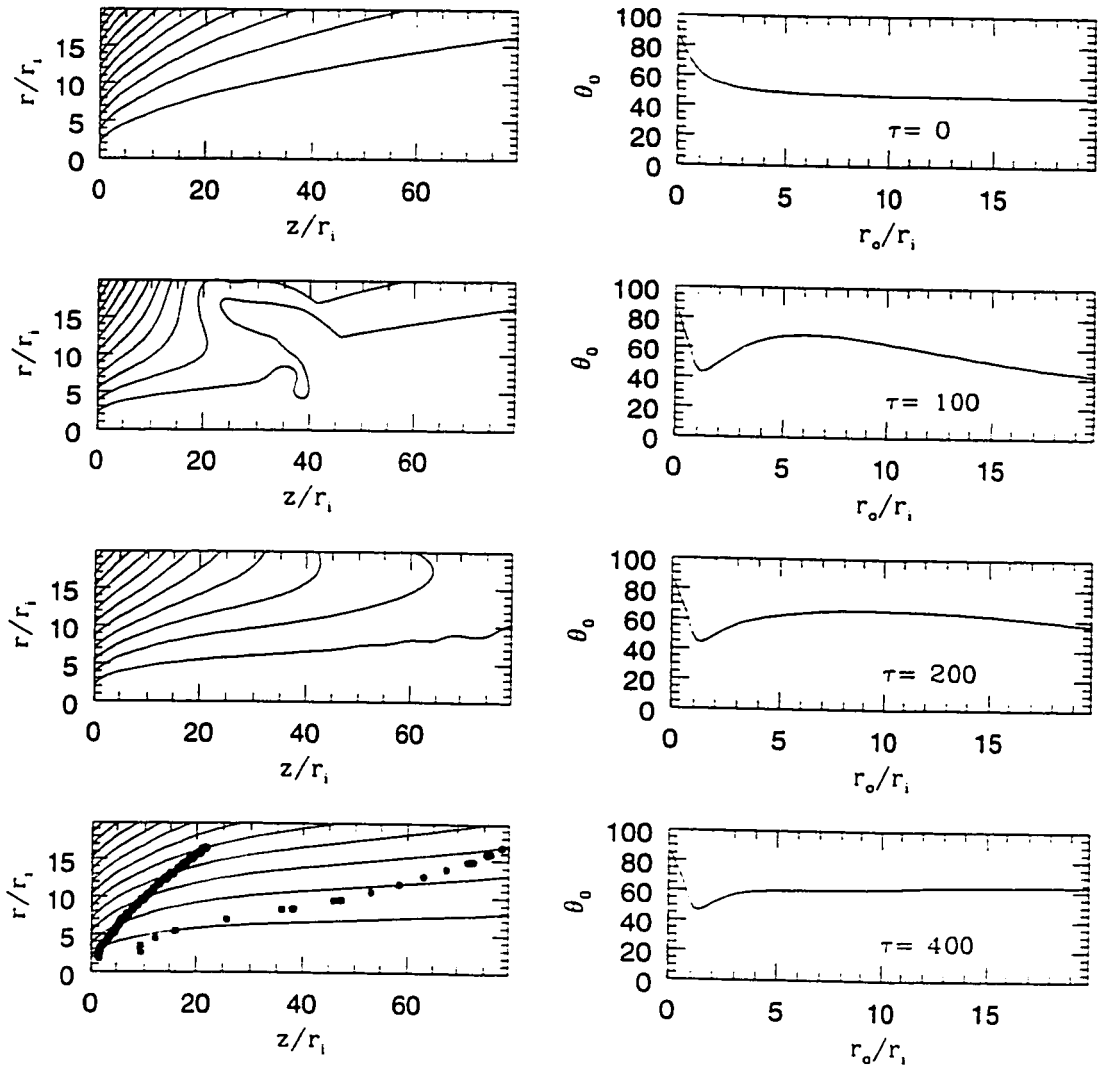

Figure 5. - Evolution of the poloidal magnetic field (left panels) and the launching angle at the disk's surface (right panels). The initial magnetic potential configuration (J = 0), as given by (4.55), is shown in the upper left panel. The mesh is $(z \times r) = (80 \times 20) r_i$ with a resolution of (500 × 200) zones. The evolution is shown at four different times: $\tau = 0$, $\tau = 100$, $\tau = 200$ and $\tau = 400$ from top to bottom. In the lower left frame, is displayed the location of the Alfvén critical surface (filled hexagons) and of the fast magnetosonic surface (stars).

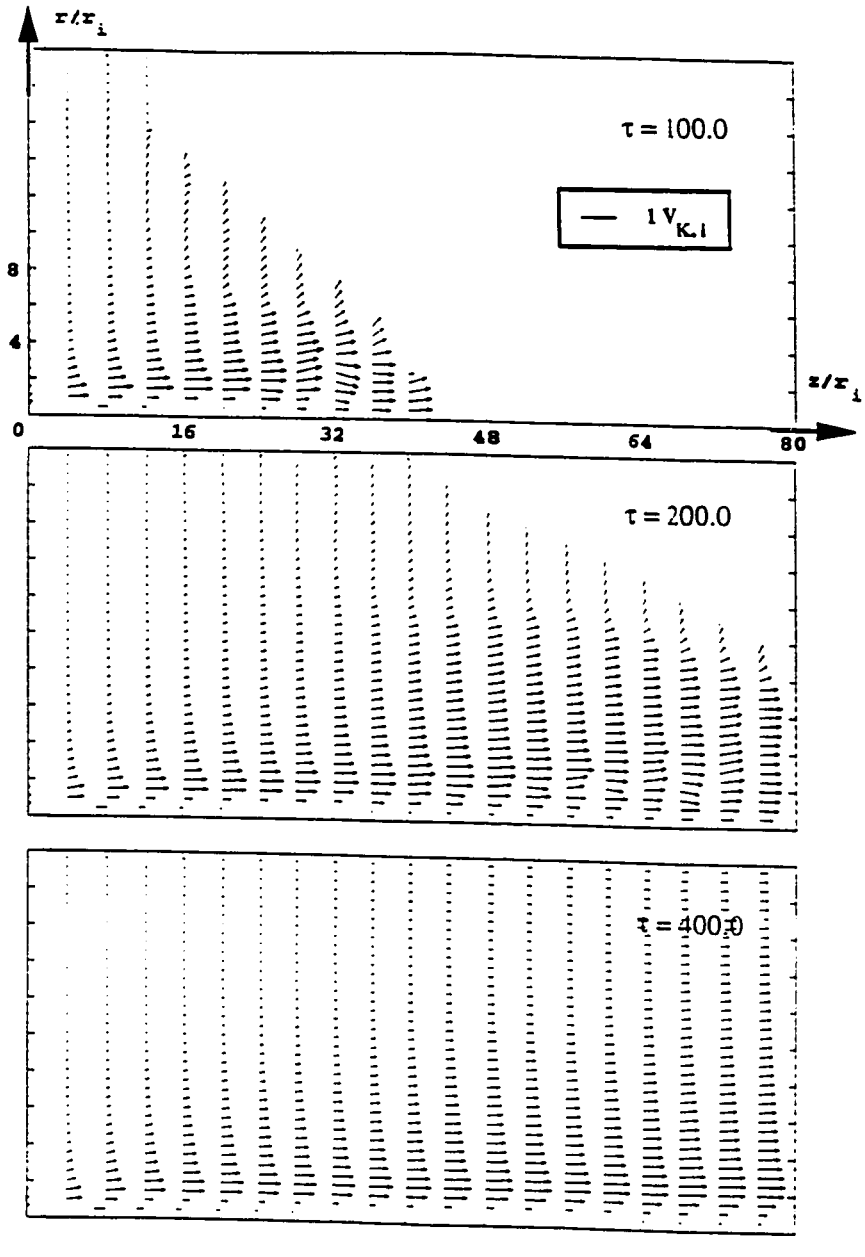

Figure 6. - Poloidal vector velocity $\mathbf{v}_p$ at $\tau = 100$, $\tau = 200$ and $\tau = 400$, respectively from top to bottom.

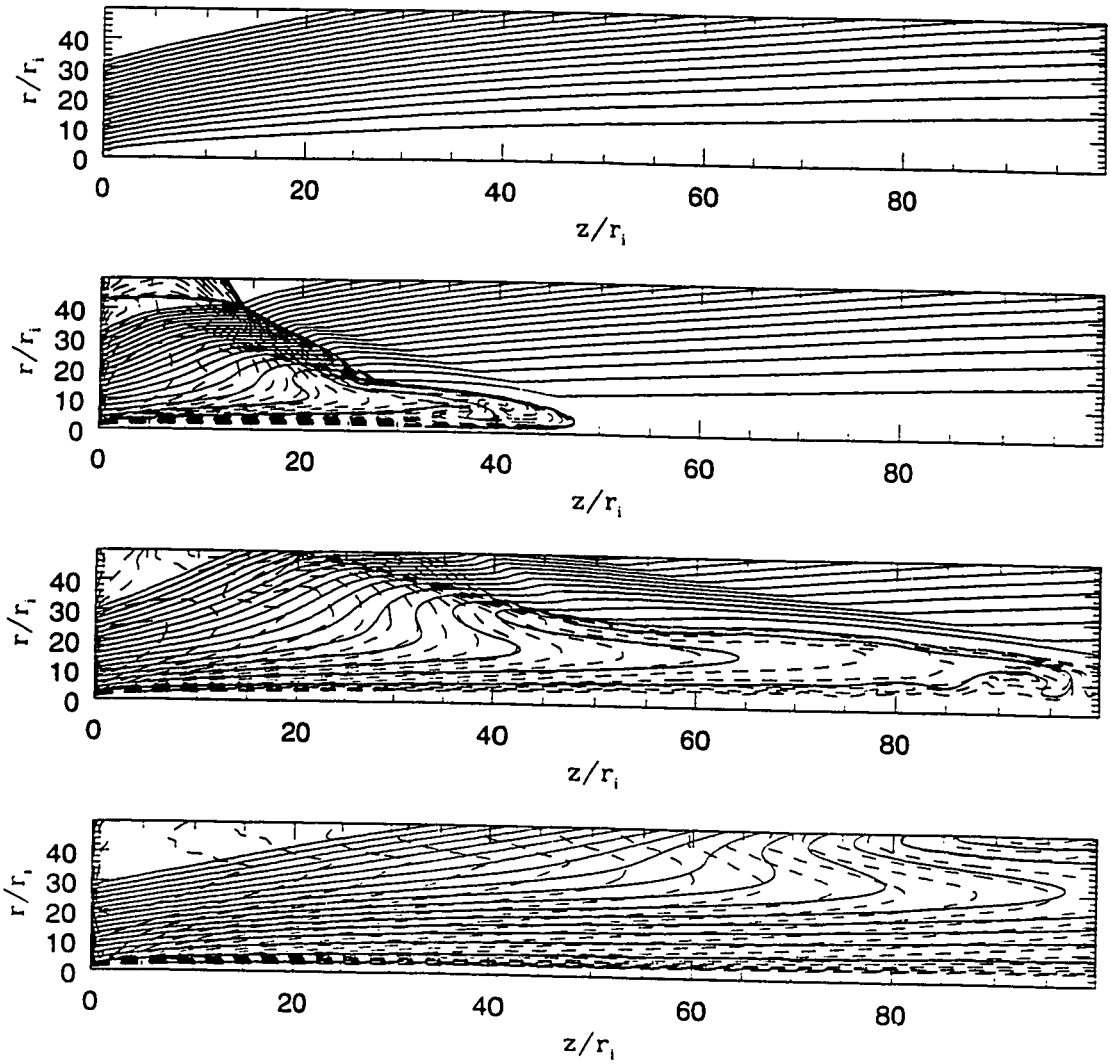

Figure 7. - Isocontours of the poloidal current density ($\mathbf{J}_p$, dotted lines) and poloidal magnetic field lines ($\mathbf{B}_p$, solid lines) at time $\tau = 0$, $\tau = 100$, $\tau = 200$ and $\tau = 400$ from top to bottom, respectively. The jet is far from a force-free solution ($\mathbf{J}_p \parallel \mathbf{B}_p$). The current completes a circuit by flowing downwards along the jet axis, radially outwards through the accretion disk, and then upwards along the flank of the bow-shock, closing the circuit at the outflow axis.

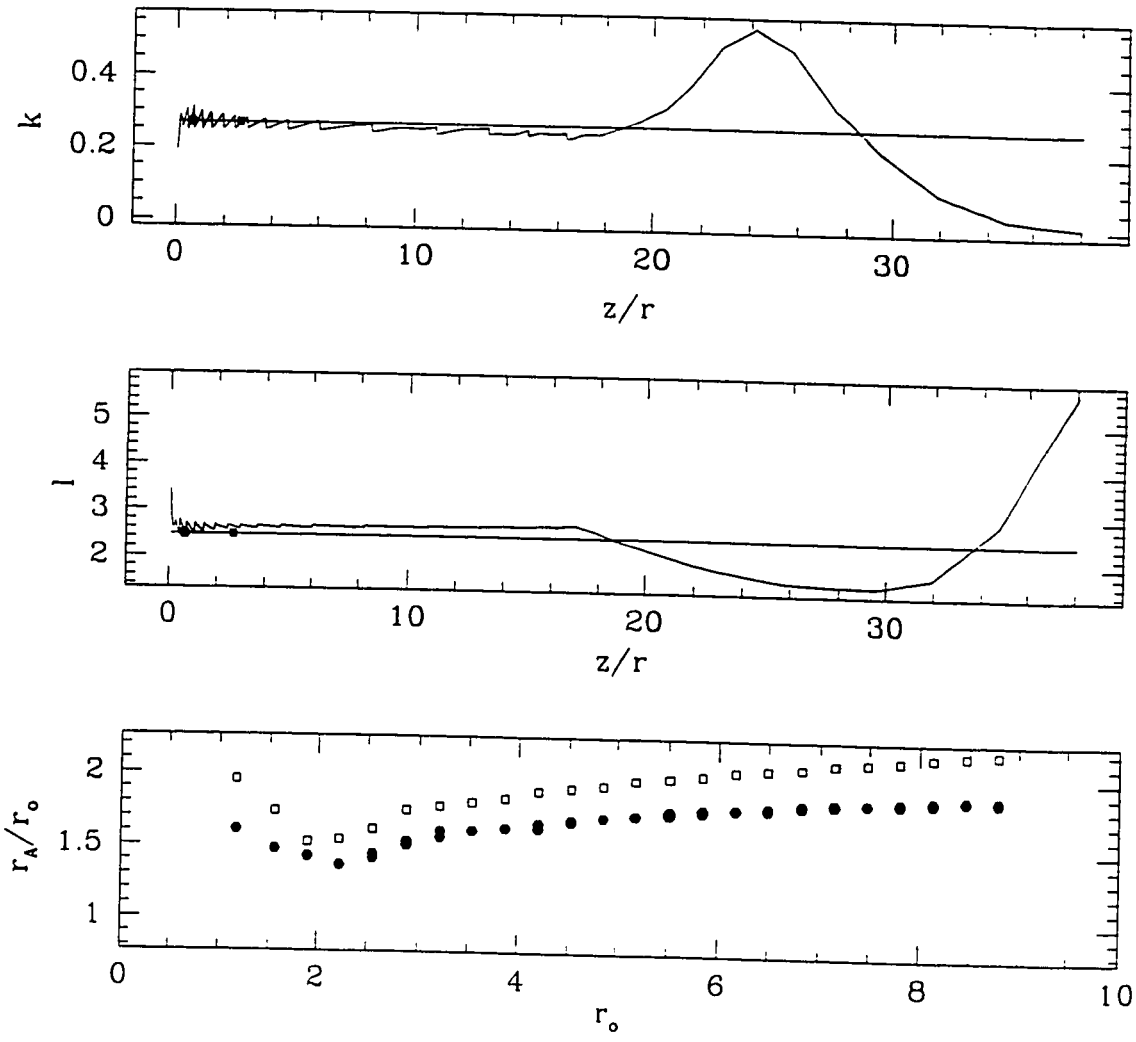

Figure 8. - Steady state analysis of the innermost field line. This figure shows the mass to magnetic flux ratio k (upper panel) and the specific angular momentum l (middle panel) plotted against $z/r = tan^{-1}(\psi)$ where ψ is the polar angle as measured from the origin of the coordinate system. The steady state theory (the solid line) predicts that these two quantities are constant along a given field line. The filled dot and the squared dot are the location of the Alfvén point and of the FM point, respectively, as found in our simulation, along the chosen field line. There is good agreement within the FM region. Beyond the FM point, the solution oscillates around the steady state behavior. In the lower frame, the Alfvén lever arms (r_A/r_o, for a field line anchored at r_o on the disk's surface), found in our simulation (filled hexagons) are compared to the prediction from the steady state theory (squares).

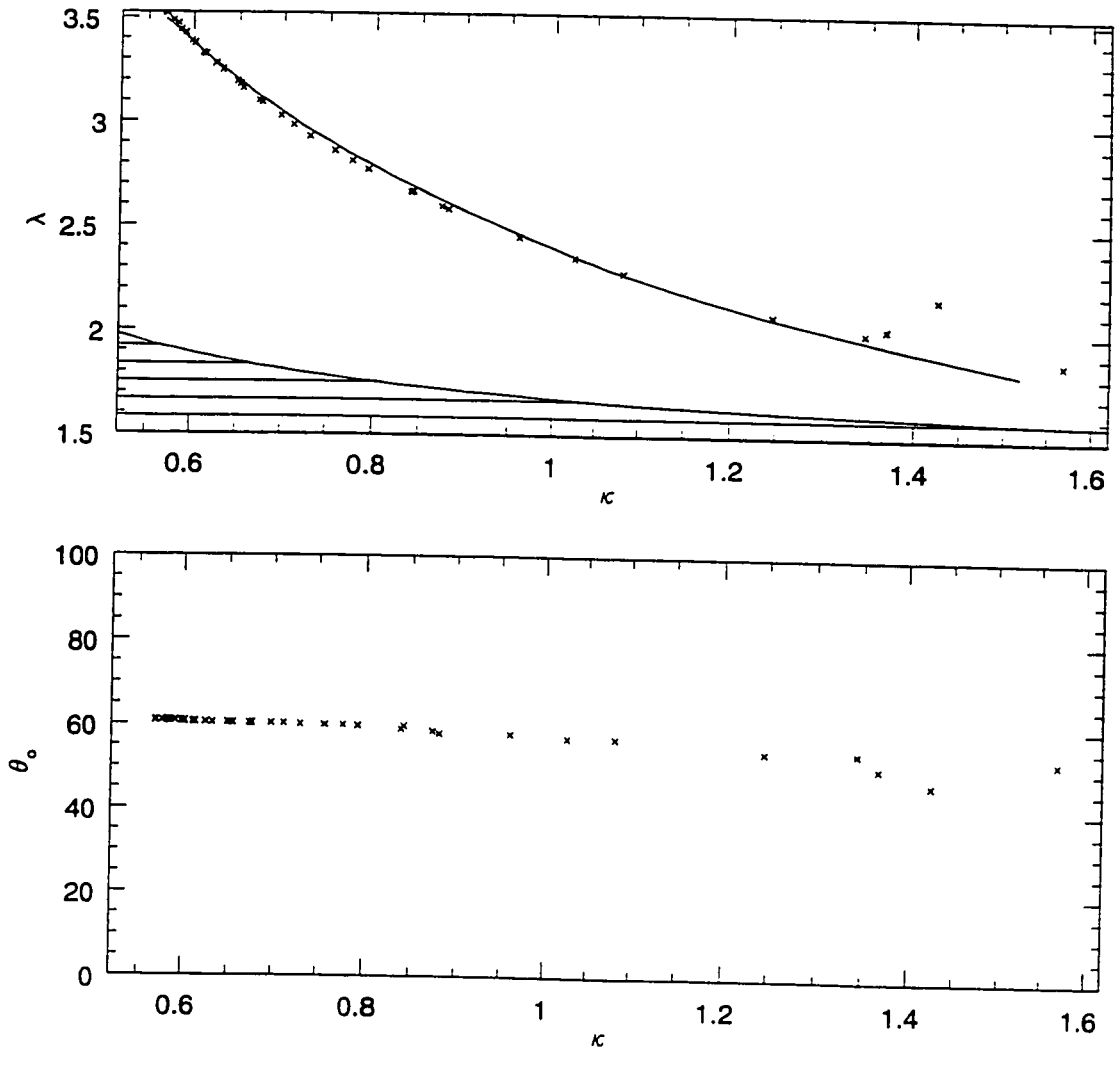

Figure 9. - The κ-λ space (upper panel) and the κ-θ_o space (lower panel) and the location of our solution, at $\tau = 400$. The two-regimes of the jet, the magnetically-dominated jet with $\kappa < 1$ (inner parts of the jet) and the particle-dominated jet with $\kappa \geq 1$ are shown. In the upper panel, the dashed area represents the sub-Alfvénic flows $\left(4\pi\rho v_p^2 < B_p^2 \quad \text{or} \quad \kappa\lambda(2\lambda-3)^{1/2} < 1\right)$. The fitting curve is given by $\lambda = 2.4/\kappa^{2/3}$.

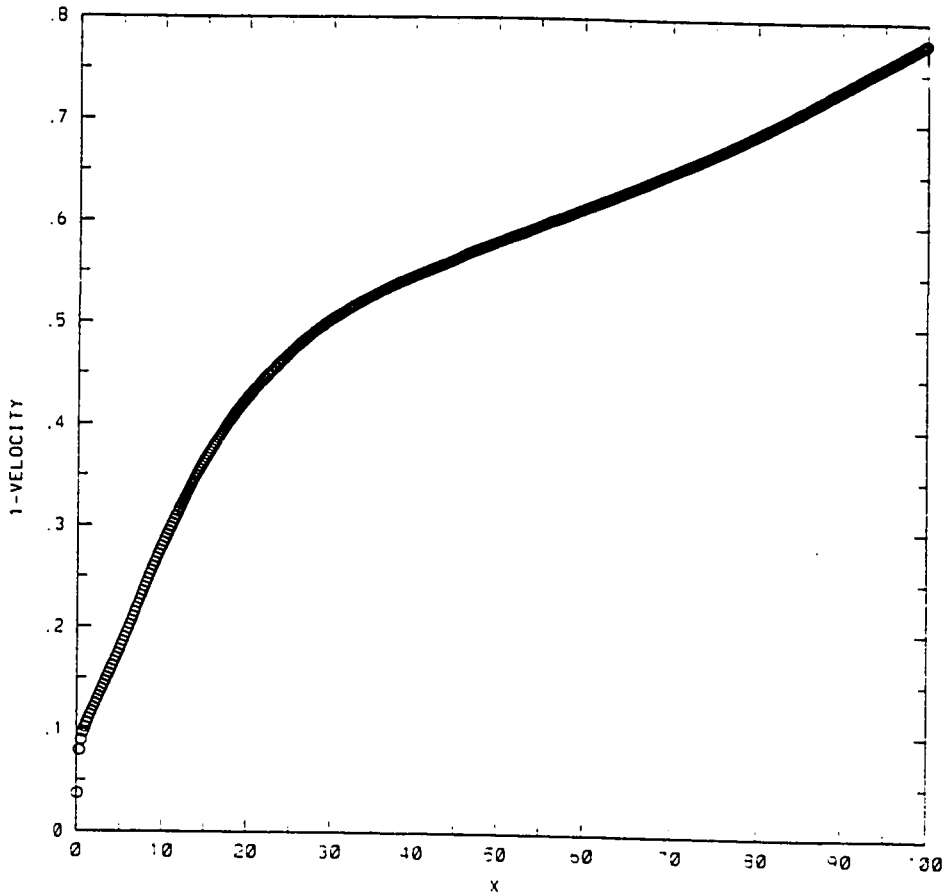

Figure 10. - A cut parallel to the disk axis ($j = 40$) showing the velocity (v_z, in units of $v_{K,i}$) and its Hubble profile.

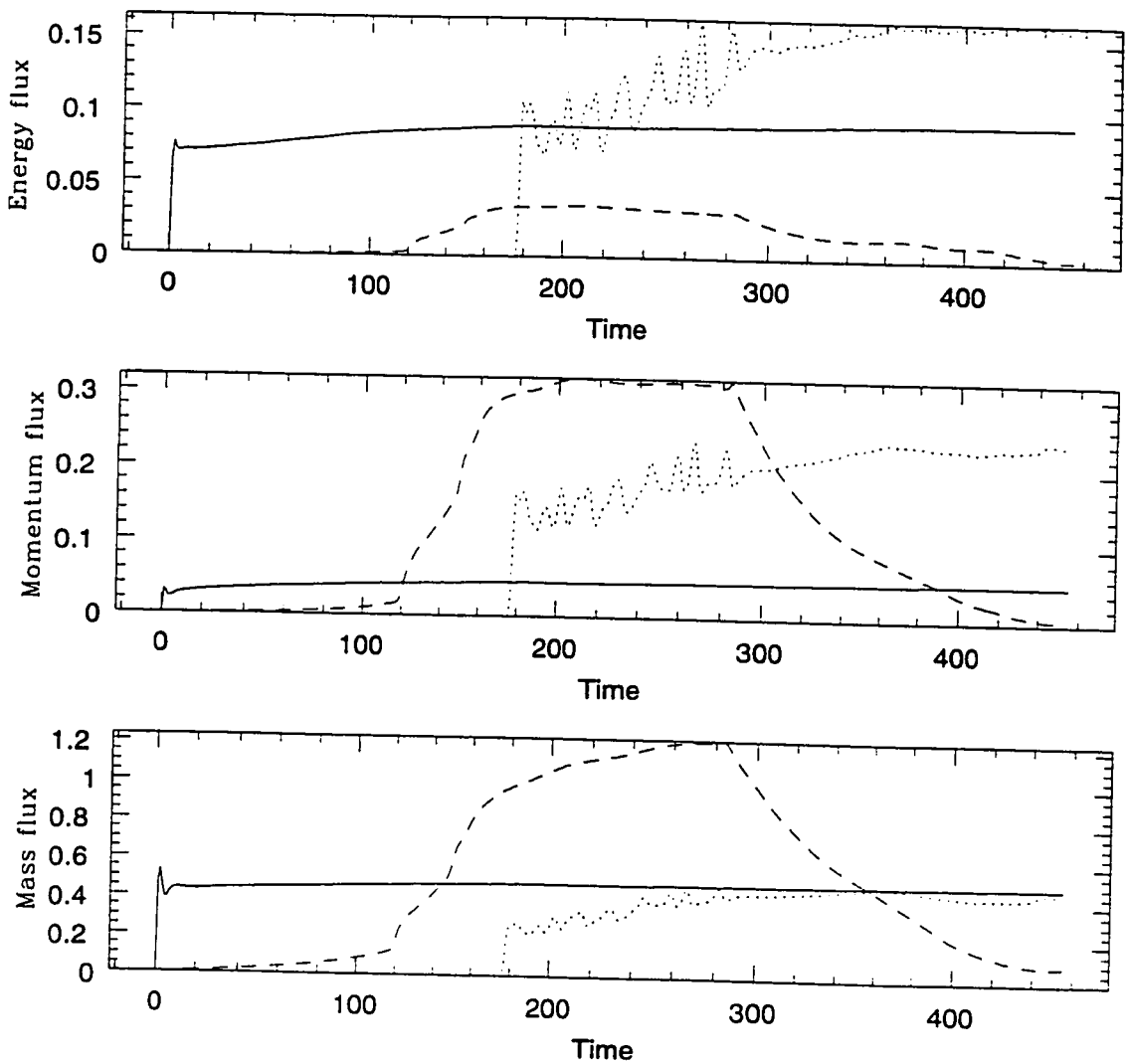

Figure 11. - Here, we quantify the different fluxes carried by the jet. The bottom panel represents the mass flux, the middle panel the momentum flux while the top panel represents the kinetic flux. The solid lines denotes the fluxes across the inner (z=0) boundary. The short dashed lines denotes the fluxes across the outer radial boundary ($r = r_e$). Finally, the dotted lines denotes the fluxes across the outer axial boundary ($z = z_e$) while the dashed line denotes the flux crossing the outer radial boundary. As the flow evolves in time it gets more collimated until most of the flux crosses the outer axial boundary (dotted line).

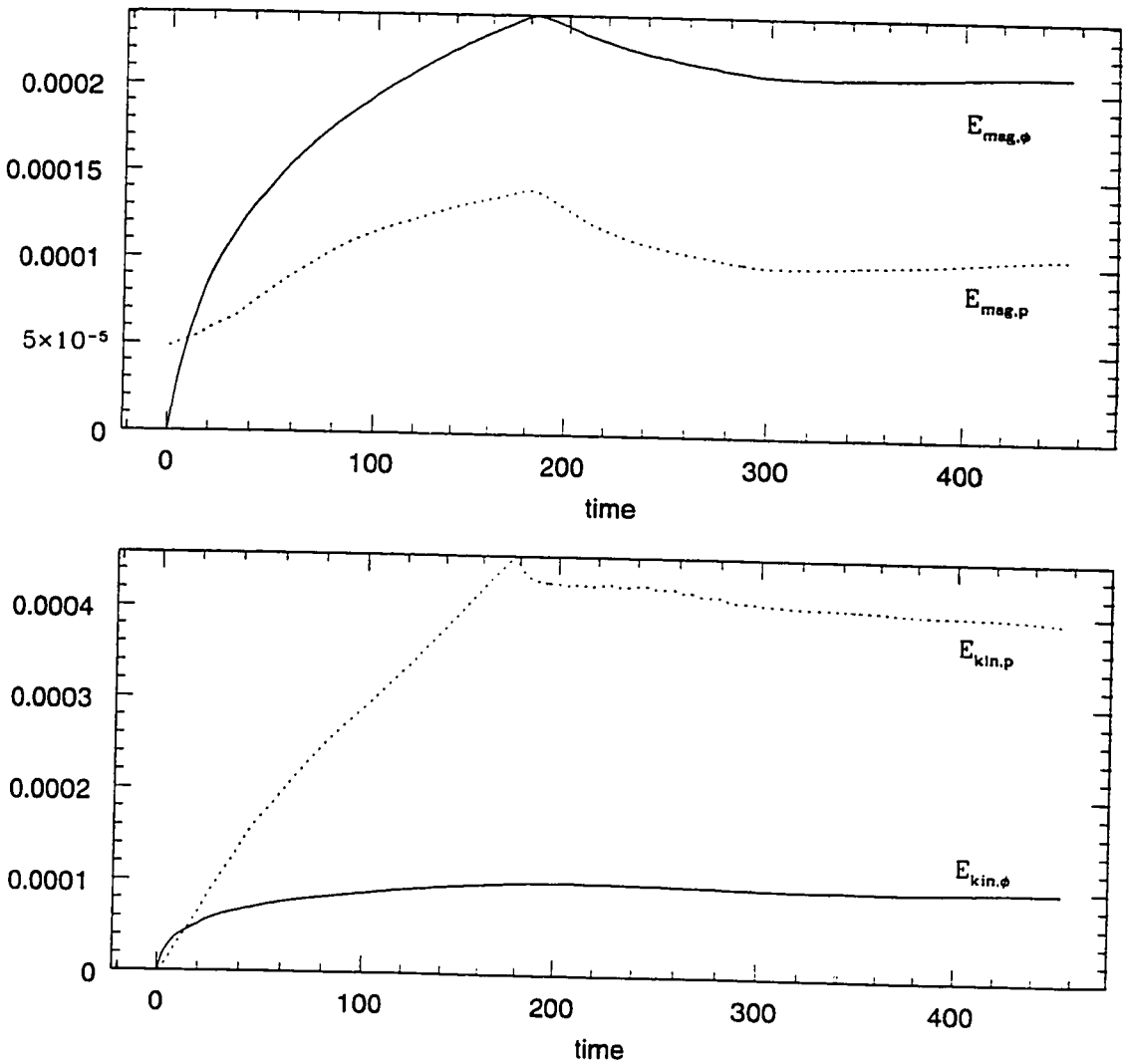

Figure 12. - Quantification of the energies involved in the flow. In the upper/lower panel the poloidal magnetic/kinetic energy is compared to the toroidal part.

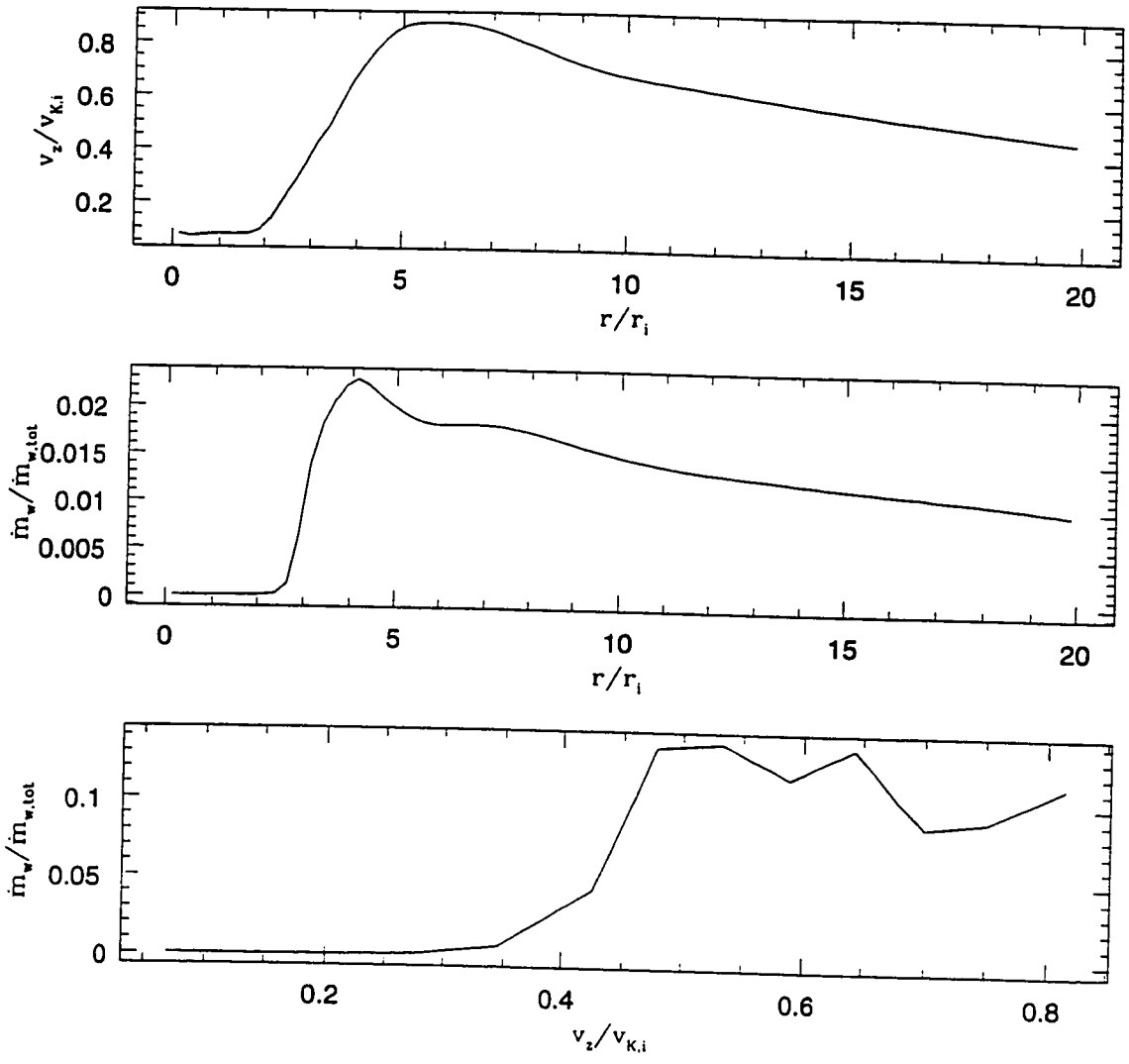

Figure 13. - A snapshot (at $\tau = 400$) of the dependence of the mass outflow rate upon the poloidal velocity of the jet (lower panel). The top panel shows that the velocity peaks at $r \simeq 6r_i$). The middle panel shows size of the wind region ($3r_i < r_{wind} < 15r_i$).

Chapter 4

Episodic Outflows

This chapter is based on the paper "NUMERICAL SIMULATIONS OF ASTROPHYSICAL JETS FROM KEPLERIAN DISKS II: Episodic Outflows" by Ouyed, R. and Pudritz, E. R. 1997, accepted for publication in the "Astrophysical Journal".

Here, the initial magnetic configuration is taken to be uniform and parallel to the disk axis. We show that outflows are initiated by centrifugal force, and demonstrate that the outflow is made possible by the strong gradient in the generated toroidal component of the magnetic field. We find that knots are a generic property of the dynamics of the jet. They are independent of the underlying accretion disk.

Abstract

We present 2.5-dimensional time-dependent simulations of the nonlinear evolution of outflows from Keplerian accretion disks. The gas is injected from the surface of the disk (which is a fixed platform in these simulations) into a cold corona in stable equilibrium. The initial magnetic field lines are taken to be uniform and parallel to the disk axis (z-axis). Because of the gradient force in the non-linear torsional Alfvén waves generated by the rotor at the foot-points of the field lines, the initial magnetic configuration opens up in a narrow region located at $1r_i < r < 8r_i$ with r_i being the innermost radius of the disk. Within this narrow region, a wind is ejected from the field lines that have opened to less than the critical angle ($\simeq 60^o$), as expected from the centrifugally driven wind theory. Our simulations show that the strong toroidal magnetic field generated recollimates the flow towards the disk's axis and, through magneto-hydrodynamic (MHD) shocks, produces knots. The knot generation mechanism occurs at a distance of about $z \simeq 8r_i$ from the surface of the disk. Knots propagate down the length of the jet at speeds less than the diffuse component of the outflow. The knot generator is episodic, and is inherent to the jet.

1. Introduction

One of the most challenging aspect of theories and models of astrophysical jets is to provide a natural explanation for common features such as the episodic outbursts and the knots observed in astrophysical jets. Among the models so far proposed are the magnetohydrodynamic (MHD) winds from a Keplerian disk (Blandford & Payne 1982, hereafter BP82, Uchida & Shibata 1985, hereafter US85, Camenzid 1986, Pudritz & Norman 1986, Lovelace et al. 1987, Heyvaerts & Norman 1989, Pelletier & Pudritz 1992, Appl & Camenzid 1993, Königl & Ruden 1993, Sauty & Tsinganos, 1994 to cite only few). However, while the existing stationary wind models help us understand the basic physics of such winds (acceleration and collimation), they are limited by their assumptions of self-similarity and stationarity. Such assumptions are made because of the complexity of MHD equations one needs to solve. Numerical simulations are therefore a complementary step and a necessary tool in the study of astrophysical jets (Shibata & Uchida 1986&1987, Kössl et al. 1990, Stone & Norman 1994, Bell & Lucek 1995, and Ustygova et al 1995, to cite only a few). In paper I (Ouyed & Pudritz 1997, hereafter OPI), we introduced the reader to the general set up and the initial conditions corresponding to a central object surrounded by a Keplerian disk and an overlying cold corona in stable equilibrium. We presented an extended version of ZEUS-2D designed to overcome the numerical difficulties related to the realization of this initial set up, as well as results for a steady state simulation

using a simple initial potential (J = 0) field configuration.

In this paper, we present a complete study of a uniform vertical configuration, where the magnetic field lines are parallel to the disk's axis. This magnetic configuration was chosen because it is the simplest one to study and is not expected to produce an outflow in steady state theory.

As before, our disk is treated as a boundary condition at the base of the outflow. The disk is kept in Keplerian rotation throughout the simulation. Our results are remarkable in that outflow is both self-initiated by toroidal magnetic field pressure generated in the jet which opens up the field lines, and episodic in that it generates a large number of knots that continue to be produced for many disk dynamical time scales and grid crossing times. The knots originate near to the compact object with temporal frequencies that roughly match the observations. Here, we present a sample of simulations from a dozen that we carried out over the last year which show that whereas some of the predictions of steady- state models are borne out (OPI), there exist magnetic configurations which produce episodic jets, as the observations demand (Ouyed et al., 1996).

The paper is organized as follows. In §2, we briefly remind the reader of our initial set up, that is, the state of corona and of the overlying Keplerian accretion disk as well as the initial magnetic configuration. In §3, the development of the outflow and its interaction with the surrounding corona is presented in detail. §4, deals with the details of the knot generator while §5 investigates at the physics behind the ejection

and the acceleration mechanism. The strength and the energetics of our outflow is presented in §6. Finally, a summary of our results and a conclusion are given in §7.

2. Initial Set Up

2.1 Disk Surface and Boundary Conditions

As in Chapter 3, the Keplerian accretion disk surface (the base of the corona) provides fixed boundary conditions for the velocity at every disk radius; the rotational speed is Keplerian v_K. The rest of the boundaries are similar to what is described in Chapter 3 (refer to figure). Here, however,

$$\beta_d = (\gamma - 1)\delta_i \beta_o \tag{4.1}$$

with

$$\beta_o = \beta_i r_o^{-5/2}. \tag{4.2}$$

implying that β_d falls from the innermost value of $(\gamma - 1)\delta_i\beta_i$ to an outermost value of $(\gamma - 1)\delta_i\beta_i r_e^{-5/2}$. The disk radius at which β_d is unity is simply given as

$$1 = (\gamma - 1)\delta_i \beta_i r_1^{-5/2} \tag{4.3}$$

or

$$r_1 = (\frac{2}{3}\delta_i\beta_i)^{2/5}. \tag{4.4}$$

Interior to r_1 we expect both global and local modes of the BH instability to be present while the linear stage of this instability will dominate in the regions interior to r_1. But, again, because we treat the disk simply as a boundary condition at the base of the corona, we cannot study how the instability will affect the acceleration of the outflow (see Chapter 3).

2.2 Initial Magnetic Configuration

In this paper, a vertical configuration is used with the initial surfaces of constant magnetic flux prescribed by the level surfaces of a scalar function (given in units of $r_i B_i$)

$$A_\phi = r \tag{4.5}$$

That is,

$$B_z = 2.0 \quad \text{and} \quad B_r = 0.0. \tag{4.6}$$

While our vertical magnetic configuration was chosen to overcome some mathematical difficulties, we feel that it is still a good starting model for the kind of problems we are investigating in this paper. Indeed, it is possible for such a configuration to be created in a situation where accretion flow into a turbulent disk (of high magnetic Prandtl number) drags an external magnetic field into the central object from the surrounding medium (Lubow et al. 1994, Reys-Ruis & Stepinski 1996).

The initial radial and vertical magnetic field components in the disk are continuous with the field in the corona (see Chapter 3, for more details). That is, the magnetic structure penetrates the disk and the overlying corona without any kink in the initial magnetic configurations that might introduce some undesired spurious effects (due to current sheets).

3. Evolution of the Outflow

Our first simulation (**Simulation A**) was run in the domain $(z, r) = (80, 20)$ with a resolution of $(500, 200)$ cells, for up to 500 time units ($< \tau_B$). This allows us to have a more global look at the jet and its interaction with the corona, reasonably far from the central object. The set of parameters is

$$(\delta_i, \beta_i, \eta_i, \mu_i, v_{inj}) = (10^2, 1.0, 10^2, 1.0, 10^{-3}) \Rightarrow (\tau_K, \tau_A, \tau) = (1.0, 7.07, 707.1). \quad (4.7)$$

3.1 Magnetic Torque and the generation of Torsional Alfvén Waves

Here, we briefly review the notion of torsional Alfvén waves as they first appear in our simulation (figure 1). Below, we describe the two distincts regions which separate the linear regime from the non-linear one. The latter one occurs in the innermost parts of the disk where $(B_\phi/B_p)_i = 1$ to start with, and where the winding of the field line (through v_ϕ) is also the strongest. As one goes radially outwards, B_ϕ decreases sharply with radius ($B_\phi \propto r^{-1}$) and so is $v_\phi \propto r^{-1/2}$ making $B_\phi/B_p << 1$.

3.1.1 Linear regime ($\delta\rho = 0$ with $B_\phi/B_p << 1$)

The linear regime of propagation of torsional waves is presented in Mouschovias& Paleologou (1980, hereafter MP80). Such a regime is seen in the early times ($\tau \leq 50$)[1] of the simulation, far from the source where gravity can be neglected.

To illustrate that, let us start with the flux-freezing equation. Since we initially have $\mathbf{B}_p = (0, 0, B_z)$, then

$$\frac{\partial B_\phi}{\partial \tau} = r(\mathbf{B}_p.\nabla)\Omega = rB_z\frac{\partial \Omega}{\partial z}. \tag{4.8}$$

The ϕ-component of the magnetohydrodynamic force equation is

$$\frac{\partial \Omega}{\partial \tau} = \frac{1}{\beta_i\delta_i}\frac{B_z}{4\pi r\rho_{ext}}\frac{\partial B_\phi}{\partial z} \tag{4.9}$$

Combined with the equation above we obtain

$$\frac{\partial^2 \Omega}{\partial \tau^2} = \frac{1}{\beta_i\delta_i}v_{A,ext}^2\frac{\partial^2 \Omega}{\partial z^2} \tag{4.10}$$

Similarly one can show that

$$\frac{\partial^2 B_\phi}{\partial \tau^2} = \frac{1}{\beta_i\delta_i}v_{A,ext}^2\frac{\partial^2 B_\phi}{\partial z^2} \tag{4.11}$$

which is the equation for propagation of linear torsional waves in the external medium. Notice that such a situation occurs because of the existence of the gradient of Ω

[1]This is the time during which v_z is negligibly small (compared with the Alfvén velocity). One can show that velocities in the radial direction also vanish, as found in the outermost regions of the disk. It then follows from flux freezing that B_r and B_z are constants of the motion ($B_r(\tau) = 0$ and $B_z(\tau) = const.$).

along the flow axis (z) which correspond to our initial equilibrium. Here, because $v_{A,ext} \propto (r^2+z^2)^{3/8}$, torsional waves starting at different foot-points in the disk, will travel into the external medium at different velocities. This gives rise to the conical shape of the Alfvén front, as is clearly seen in Figure 1 (the fastest wave starts from the outermost radius of the disk). A direct application of equation (3.24) implies that

$$\tau \simeq \frac{1}{2}\sqrt{\frac{\beta_i \delta_i}{2}}\frac{z}{(r^2+z^2)^{3/8}}. \tag{4.12}$$

That is, a wave leaving the disk surface at $r_o = 20r_i$ should leave the mesh ($z_e = 80r_i$) at about $\tau = 34.5$. This is in good agreement with our solution (figure 1).

3.1.2 Non-Linear regime ($\delta\rho \neq 0$ with $B_\phi/B_p \geq 1$)

Very close to the central object, non-liner torsional Alfvén waves (see §5 and related figures, for details) generate a strong gradients of magnetic pressure $\nabla(B_\phi^2)$. In fact, the boundary between the linear and the non-linear region ($B_\phi/B_p \simeq 1$) can be followed as the flow evolves in time. In general, in the region of the corona where only linear waves are launched, the density remains undisturbed and conserves its initial distribution. In the region where non-linear torsional Alfvén waves are generated, the density is somewhat affected by the toroidal field. Later in the evolution of the outflow a jet-like outflow is produced that eventually catches up with the Alfvén front.

3.2 Onset and Evolution of the Outflow

Figure 2a shows the evolution of the flow at $\tau = 100$, $\tau = 200$, $\tau = 300$, and $\tau = 400$. According to steady-state models (BP82, Königl 1989, Ferreira & Pelleteir 1995, Wardle & Königl 1993, Li 1995), our initial magnetic configuration is unfavorable for launching an outflow. The flow is nonetheless launched from the accretion disk (see §5). In this figure, the density is shown in the left panels while the toroidal magnetic field is in the right panels.

The jet-like flow has a density structure that is dominated by discrete knots which are part of a highly collimated flow. At times 100 and 200 the head of the outflow is clearly seen. It advances into the flow with a swept-back material shock emanating from its flanks. This surface leaves our grid long before 400 time units.

The density structure *never* achieves steady state. We have run simulations for up to 1000 time units and find that the episodic nature of the flow persists unabated. The density contours show that our jet is more highly collimated and narrow. This again shows that the outflow region is strongly confined near the axis (but off the axis since our jet is a hollow one; as better illustrated in Figure 2b.)[2], but that there is a larger, lower density region surrounding the jet on larger radial scales.

The map of the associated toroidal field in the flow reveals that the toroidal field is strongly *anti-correlated* with the knots (see Figure 2b.). Generally speaking,

[2]The presence of the hollow region is interesting in its own respects. For AGNs this could provide the funnel needed to explain the relativistic pc-scale jets associated with the kpc-scale (non-relativistic) jets, as we have discussed in the introductory chapter. As for YSOs, such a hollow region would be a good candidate for the stellar wind. Note that this region is only $1r_i$ in radius (0.04 AU for our fiducial $0.5M_\odot$ YSO, and about 10^{-4} pc for a typical $10^8 M_\odot$ black hole) and would be difficult to resolve however.

high density knots are associated with regions of low toroidal field strength. Such structures have been seen in pure MHD jet simulations (Clarke et al. 1986, Lind et al. 1989) where magnetized jets are launched into a uniform medium through a narrow orifice.

In figure 3, we show the evolution of the poloidal magnetic field (left panels) and of the launching angle θ_o (right panels). The initially vertical configuration opens up very close to the central object allowing for a gas to be ejected into the corona above. A closer look deep into the central gravitational well (see §4) reveals that only a tiny fraction of the field lines get opened up and participate in the outflow. As the small knots move away from the disk surface they interact with bigger knots formed further down the stream. Numerical reconnections (refer to Fig.3) occur within the large knots (at $z \simeq 60 - 70r_i$, we see reconnections occurring) but they quickly dissipate as they leave the mesh allowing a smoother magnetic configuration. Note however that the field lines are well behaved away from the complex and complicated large knots.

Figure 4a-d shows the complexity of the vector velocity around the knots. In particular, there is evidence for gas back-flowing along the flank of the working surface. The high velocity feature seen in the center or the large knots are probably produced by the numerical reconnections that disappear later in the evolution of the jet. Around the small knots there is a clear evidence of collimation and decollimation of the jet due to the confining effects of the toroidal magnetic field.

3.3 Knots

Recent observational studies of knots in few jets were carried using narrow band CCD imaging (Eislöffel & Mundt, 1994). These studies showed that practically all knots in jets move with tangential velocities comparable to measured radial velocities and therefore any models explaining the knots by stationary shocks can be excluded. Furthermore, the ratio of the knot pattern speed relative to the fluid speed was measured to be between 0.2 and 1, with tangential velocities of the knots between 100 km/s to more than 300 km/s.

From our simulation, the velocity of the knots is lower than that of the diffuse material between the knots, a property which corresponds well with the above observations. The typical ratio of the velocity in the knots to that of the diffuse jet material is 0.3-0.5, with the highest outflow velocities about equal to $v_{K,i}$. Although this velocity is not as large as is sometimes observed in real outflows such as HH30 (Reipurth, 1989), our simulations explore only a limited region of parameter space. Movies of this simulation show that the knot generator stays fixed in space and that the knots, once formed, persist as coherent structures that propagate down the length of the jet.

Figure 5 is a density cut, taken at $r_o = 3r_i$, along the body of the knots. At $\tau = 100$, we clearly discern the bow shock. The typical density jumps in the knots are ≤ 4. Some of the small knots continue to evolve as a shock discontinuity while

Table 1. Knots Parameters

	Small Knots	Large Knots
$z_{Generator}$	$\simeq 8r_i$	$\simeq 60r_i$
$Size\ (Radius)$	$\simeq 5r_i$	$\simeq 10r_i$
Δz_{knot}	$5r_i$	$15r_i$
v_{knot}/v_{jet}	$0.3 - 0.5$	$0.1 - 0.3$
Δt_{knot}	$11 - 13t_i$	$150 - 200t_i$

others combine to form larger knots. At $\tau = 200$, the first large knot has formed (at $\simeq 60r_i$) and then propagates down the length of the jet as a separate entity. At $\tau = 400$, another large knot is formed at the same location as the previous one and evolves in a similar way. It is interesting to note that the region between the two large knots becomes very sparse in gas and is characterized by a smooth monotonically increasing velocity profile (a consequence of mass conservation). This region is clearly seen at $\tau = 300$ at $40r_i < z < 80r_i$ (refer to figures 2,3 and 4 too).

In general then we find two type of knots that can be summarized as follow:

i) Small Knots

The smaller knots are typically *separated* by a distance of $\simeq 5r_i$ and their size is of the order of $\simeq 5r_i$ in radius. These knots are produced every $11t_i$. These knots start as shocks and some of them evolve as shocks until they dissipate when they encounter the larger knots described below.

ii) Large Knots

The larger knots appear to be more slowly moving structures that build up by

Table 2. Knots Parameters for a $0.5M_{\odot}$ Proto-Star

	Small Knots	Large Knots
$z_{Generator}\ (AU)$	0.3	2.4
$Size\ (Radius, AU)$	0.2	0.4
$\Delta z_{knot}\ (AU)$	0.2	0.6
$v_{knot}\ (km/s)$	60.0	40.0
$\Delta t_{knot}\ (days)$	38.0	525.0

Table 3. Knots Parameters for a $10^8 M_{\odot}$ Black Hole

Small Knots	Large Knots	
$z_{Generator}\ (AU)$	164.8	1237.0
$Size\ (Radius, AU)$	103.1	206.2
$\Delta z_{knot}\ (AU)$	103.1	309.0
$v_{knot}\ (km/s)$	3.0×10^4	2.0×10^4
$\Delta t_{knot}\ (days)$	36.0	495.0

absorbing some of the more quickly moving knots produced at the generator. Some of the small knots go through the first large knot and form another larger knot farther down the flow. These larger knots are typically *separated* by a distance of $\simeq 15r_i$ and their size is of the order of $\simeq 10r_i$ in radius. These knots are produced every $200t_i$.

4. The Knot Generator

For the same set of parameters as in **Simulation A**, we performed a second simulation (**Simulation B**). It was run, in the domain $(z, r) = (20, 10)$ with a resolution of $(500, 200)$ cells, for up to 50 time units ($< \tau_B$). The purpose of simulation B is to give a close-up view of the physics of flow acceleration and knot generation.

In Figure 6, we show the magnetic field configuration of the outflow at times 37.2, 40.8, 44.4 and 48.0 during which a knot (B) is formed (knot A moves away from the generating region as knot B is formed). This whole process takes a time $\tau_{knot} \simeq 11$ time units. The knots are *spatially* separated by a distance of $z \simeq 5r_i$ (confirming the results found in the large scale simulation) and move at a speed of $\simeq 0.5v_{K,i}$ out of this generating region. This figure is complementary to figure 5 in Ouyed et al. (1996, to which we refer the reader) where it is clearly seen that both knots are produced at a distance of

$$6r_i \leq z_{Generator} \leq 8r_i \tag{4.13}$$

from the central object. Once formed, the shocked gas (see below) comprising knot A appears to detach from the inner velocity stream (see lower panels in figure 5 of Ouyed et al. 1997), and moves down the jet. *The high toroidal magnetic field strength between the knots provides the confining pressure that allows the knots to remain as distinct entities* (see Figure 2b.).

4.1 How are the Knots generated?

There are various attempts in the theory literature to identify the knot spacings with the resonant wavelength pinch mode. While some of the conditions in our knot generating region seem to point towards such a scenario (in particular the high B_ϕ/B_z ratio), we are nonetheless able to rule it out by comparing simulations at

different β (Ouyed& Pudritz, in preparation, hereafter OPIII). Indeed, we found that simulations with even lower value of β_i don't produce knots, which is not what one would expect if they were pinch mode instabilities (in fact, we find that only when β_i is around unity are knots produced). We haven't encountered any of the pinching instabilities for our choice of parameters, confirming several results in the literature. For example, we confirm the result of Appl & Camenzid, (1992) that the axisymmetric ($m = 0$) mode is entirely stabilized for low β, current-carrying, cylindrical jets (our case). Kelvin-Helmholtz instabilities are also ruled out as an explanation for knot generation for two reasons. Firstly, the flow is super-Alfvénic: a regime that should be quite stable (Birkinshaw, 1990) and secondly, as already mentioned above, simulations we performed at even higher values of β (OPIII) do not produce knots.

We find that the knots are initially produced in shocks in a region of the flow beyond the Alfvén surface (marked on the field lines in Fig. 6) in the outflow, around $z_{Generator} \simeq 6 - 8r_i$. Cuts of density (figure 7a), v_z (figure 7b) and $|B_\phi|$ (figure 7c), taken parallel to the z-axis at $r_o = 3r_i$ (along the body of the jet) reveals more information on the physics of the knots. These figures clearly show the location of the knot generator at about $z \simeq 8r_i$. The density jump associated with a decrease in velocity and an increase in the poloidal magnetic field (see corresponding number in Table 3) is a strong indication of fast MHD shocks (Ouyed& Pudritz, 1994, hereafter OP94). In such shocks, the kinetic energy of the flow is converted into both magnetic

energy (amplifying the field) and thermal energy. When superimposed, fig. 7a and fig.7c confirm the anti-correlation between the density and the toroidal magnetic field, and the fact that the knots are confined between regions of strong B_ϕ.

One important property we found is the spin-up of the jet material crossing the shocks (Table 3). This is simply due to the conservation of angular momentum

$$l = rv_\phi + \frac{r|B_\phi|}{k}. \tag{4.14}$$

with $k = \rho v_z/B_z$. Thus any decrease in B_ϕ (as it happens across the shock)[3] must be followed by an increase in v_ϕ. This result is similar to what was found by Kössl et al. (1990)[4] but there is an important difference: the absolute value of v_ϕ they obtain is much smaller than the sonic velocity throughout their simulation. Therefore the influence of the rotation on the propagation of the jet is almost negligible. In our case, the outflow is mainly in rotation to start with. The shock spins it up by no more than a factor of 1.4 in the strongest jumps.

Our result is interesting in view of recent investigations of line profiles emerging from the vicinity ($3r_i < r < 12r_i$) of YSOs. In the case of FU orionis, Calvet et al. (1990) showed that absorption features of observed lines are likely to form in a differentially expanding wind which is rapidly rotating. Rotational velocities of about

[3]It is straightforward to show that k is a constant across the shock (equations (3.21) and (3.22) in OP94).

[4]These authors studied the evolution of jets in helical magnetic field configurations and found that the maximum values of the toroidal velocity can be observed downstream the terminal Mach disk (see their figures 17-19). The acceleration of the jet material in ϕ-direction is due to the angular momentum generated by a gradient in $B_p B_\phi$.

60−70 km/s are needed in their models to fit the observed profiles. Here, we found the highest rotational velocity no more than 0.8 $v_{K,i}$ (76 km/s for a 0.5 $M_\odot$ proto-star, like FU orionis).

The question one can ask now is: why and how does the first shock come about? By looking at the distribution of the magnetic pressure associated with the self-generated toroidal field in the narrow band of outflowing, we see that the pressure force (∇B_ϕ) acts both radially outwards, and *inwards towards the axis.* Hence, the accelerating outflow, on encountering the inwardly directed pressure gradient, is reflected back towards the axis. Now, because the outflow is rotating, the gas spins up as it moves inwards and reflects off an inner "centrifugal barrier" when it reaches a radius comparable to its foot-point radius, as fig. 8 clearly shows (the poloidal vector velocity in fig8 shows that the flow recollimates towards the axis, and then reflects back into the slower moving body of the jet). The resulting nearly harmonic oscillation has been predicted by Sauty& Tsinganos (1994). *In our case, however, the corresponding variations in flow speed rapidly steepen into fast MHD shocks.* Estimating that the toroidal Alfvén speed in our simulation is

$$v_{A,\phi} \simeq 0.5 - 0.6 v_{K,i}, \tag{4.15}$$

and the width of the jet to be

$$\delta r_j \simeq 3 - 4 r_i, \tag{4.16}$$

the oscillation period of the jet is

$$t_{osc} = 2\delta r_j / v_{A,\phi} \simeq 11 - 13 t_i, \tag{4.17}$$

which is indeed the knot measured production time scale in our simulation. *By contrast, the initial magnetic pressure in the steady flow case (see OPI) drops significantly as one moves outwards from the axis. Thus, the accelerating outflow does not encounter a strongly magnetically overpressured outer barrier, and continues to expand radially finally achieving a quiet, cylindrically collimated state.*

To summarize, this section, we found that knots are produced very close to the source, at a distance from the central source of about $7r_i$. **Simulation B** shows that the knot generation is inherent to the dynamics of the jet itself[5]. It also shows that the knot generator stays fixed in space and that the knots, once initially formed as fast MHD shocks, persist as coherent structures that propagate down the length of the jet. We summarize in Table 1 the general results cited above. Table 2 gives the numbers for our fiducial parameters as applied to a typical $0.5 M_\odot$ YSO and a typical $10^8 M_\odot$ AGN.

5. The Outflow and Acceleration Mechanism

We have shown in figure 6 that a narrow region of field lines in the innermost parts of the disk is opened up, making an angle of 50^o with respect to the disk surface. This

[5]Our result show that an episodic behavior of the jet is possible independently of the underlying disk or central object.

narrow region, located at $r_i < r < 8r_i$, drives the outflow. In fact, we found that the size of the disk that participate in the wind is simply determined by

$$\beta_d \leq 1.0. \tag{4.18}$$

On using equation (2.16), this becomes

$$r_{wind} \leq r_1 = (\frac{2}{3}\beta_i\delta_i)^{2/5} \simeq 6r_i \tag{4.19}$$

for our parameters. which is indeed close to the size of the wind region. To be more concise, the outflow is triggered when a toroidal magnetic field is generated at the shear between the disk and corona at $\tau = 0$, and then propagates to larger z via a torsional Alfvén wave. Because of the higher Kepler shear, the strongest toroidal field is generated in the inner regions of the disk (where β is also high). Thus, a radial, outwardly directed magnetic pressure gradient is produced by the newly created toroidal field. This pushes open the field lines setting up a condition favorable for outflow. This is shown in figure 9 which plots the ratio $|B_\phi|/B_p$ versus the poloidal magnetic structure. Because, $|B_\phi|/B_p \simeq 20$ in the inner parts of the disk and only $|B_\phi|/B_p \simeq 0.4$ in the outer parts, a strong magnetic pressure gradient opens up the field lines into a configuration favorable for a wind to be ejected. This ejection is seen in figure 10 where we see that the magnetic pressure gradient, $\nabla(B_\phi^2)$, not only opens up the initial configuration but it also clears up the immediate surrounding corona.

For $r \geq r_1$ (or $\beta_d \leq 1.0$), the field is more rigid as one moves radially so that this determines the radial extent of the ejection region. That is, the wind production region on the surface of the disk depends on the ease with which field lines can be pushed aside by the toroidal field pressure (OPIII, in preparation).

5.1 Centrifugal Outflow

In general, the physics of how a flow starts and is accelerated is dictated by the interplay between three forces. The gas is then centrifugally accelerated along the open structure and quickly becomes collimated by the self-generated Lorentz force $\mathbf{J}_p \times \mathbf{B}_\phi$.

Figure 11 displays the evolution of the Alfvén surface as the knots are being generated. One sees that the Alfvén surface remains fix in space and there achieves a steady state. That is, we have found two regions to our episodic outflow; the acceleration region (interior to the Alfvén surface) where the physics is very steady and stable; and the knot region (beyond the Alfvén surface) where the flow becomes episodic. The FM surface turned out to be very complicated and unsteady as it gets sometimes destroyed by the knots.

In order to investigate the stationary region, interior to the Alfvén surface, we applied the steady state analysis package introduced in OPI. That is, for the field lines involved in the outflow, we estimated the two corresponding BP82 parameters κ (characterizing the ratio of the mass flux to the magnetic flux) and λ (the total

Table 4. Fluxes and Energetics

Central Object	$Mass\ (M_\odot)$	$\dot{m}_w\ (M_\odot/yr)$	$\dot{m}_w v\ (M_\odot km/s/yr)$	$\dot{m}_w v^2\ (erg/s)$
Proto − Star	0.5	6.3×10^{-7}	2.2×10^{-5}	1.5×10^{33}
Black Hole	10^8	0.5	0.3	3.0×10^{45}

specific angular momentum). We then plot (figure 12) the standard κ-λ graph (upper panel) and the κ-θ_o graph (lower panel) with the location of the launching angle θ_o. As can be seen in the κ-λ figure, the outflow is clearly particle dominated ($\kappa \geq 1$) and one expects such flows to be dominated by rotation, unlike the magnetically dominated outflow obtained in OPI where $\kappa < 1$.

6. Jet Fluxes and Energetics

Finally, we quantify, in Figure 13, the strength of our simulated large scale outflow (Simulation A; see OPI for the units). The quantities of observational interest are the mass flux, the momentum flux and the kinetic flux. The solid line denotes the fluxes across the inner ($z = 0.0$) boundary. The short dashed line denotes the fluxes across the outer radial boundary ($r = 20.0$). Finally, the dotted line denotes the fluxes across the outer axial boundary ($z = 80.0$). At later times the fluxes in the outflow are comparable to the fluxes at the inner boundary. When given in cgs units (and assuming values for the free parameters appropriate to a proto-stellar disk and/or black holes), then the typical mass, momentum and energy flux rates are given

in Table 4. While these fluxes are small when compared to the results of the steady state simulation (a factor of 5) (OPI), they are still capable of driving the observed weak outflows. (Lada, 1985; Chernin & Masson, 1991, Frank et al., 1992). Figure 14 quantifies the bulk energies involved in our flow (integrated over the entire large scale computing volume). It shows that our solution, unlike the stationary one (OPI), corresponds to a flow in which most of the energy is in the form of the bulk toroidal kinetic energy (lower panel). A result which is expected since our flow is particle dominated (rotating flow since $\kappa \geq 1$, as explained in §5.1).

Finally; in Figure 15a, we show a snapshot (at $\tau = 400$) of the dependence of the mass outflow rate upon the poloidal velocity of the jet, for the large scale simulation. The top panel shows that the velocity peaks in two dominant streams ($r \simeq 1.5r_i$ and $r \simeq 7r_i$). The middle panel confirms the fact that most of the material is carried out between $r_i < r_{wind} < 8r_i$. The lower panel indicates that the bulk of the material moves at small speeds ($\simeq 0.15v_{K,i}$) while much smaller amounts of diffuse gas moves at high speed ($\simeq 0.2v_{K,i}$). *Note that fig. 15a is taken at a snapshot time during which the highest velocities registered were low ($\simeq 0.2v_{K,i}$). However, velocities as high as $0.7v_{K,i}$ are reached in our flow..* Figure 15b is similar to Fig. 15a except that it is for the small scale simulation and the snapshot is taken at $\tau = 40$. Here, we reach velocities as high as $0.5v_{K,i}$ but still confirm that the bulk of the material moves at small speeds ($\simeq 0.2v_{K,i}$). While this last result is in reasonable agreement with large

scale observations[6], one needs data at scales comparable to the ones we are simulating in order to make any definite conclusions.

7. Summary and Conclusions

In this paper II, we have presented results from a numerical study of the origin and the evolution of winds from accretion disks threaded by vertical field lines. The main points discovered in our present work can be summarized as follow:

(i) Self-Starting Jets: We have discovered that *no special initial magnetic field structure* is required in order to launch the outflows in our simulations. Rather, conditions favorable for ejection seem to set themselves up automatically through the flow of non-linear torsional Alfvén waves that builds a radially directed, toroidal magnetic pressure gradient that adjusts the structure of the coronal field. *We found that vertical magnetic configuration with a coronal β of order of unity in the inner parts of the disk is most favorable for the formation of episodic jets.* The flow is centrifugally ejected from the portion of the disk surface where the magnetic field lines have opened to less than the critical angle ($\simeq 60^o$), as expected from the centrifugally driven wind theory.

(ii)Knots and the Knot Generator: While there are models for the formation of episodic jets that involve eruptions in time variable accretion disks (Stone & Nor-

[6]It is observed in CO-outflows that almost all the material is traveling at relatively small speeds (10-30 km/s), and only a small fraction has a velocity near the observed maximum value (300 km/s). See Figure 2 in Masson & Chernin, 1992.

man 1994, Raga & Koffman 1990). our simulations show that this is not necessarily required. We found that the knot generator is inherent to the jets themselves and produces eruptions with roughly the correct time scale to understand episodic events (on small scales). The knot generator is fixed in space and is simply the strong toroidal magnetic field generated which by recollimating the flow towards the disk's axis produces knots through magneto-hydrodynamic (MHD) shocks. The knots produced are not related to any of the known classic instabilities.

(iii) Disk Surface: We hypothesize that real physical systems are episodic because the physics of their central accretion disks leads typically to situations where the threading mean magnetic fields are such that the β in the surface of the disk decreases with the disk radius. It is still too early to tell whether or not this condition naturally arises in models of accretion disks that have MHD turbulence. The rigidity of such a magnetic structure determines the portion of the disk that participates in the flow.

(iv) Terminal Velocities: The outflow velocities achieved are still too small (by a factor of 2) to match the fastest structures seen in observed YSO jets. However, one has to remember that our two simulations, while typical of several dozen that we have carried out, still only probe a small part of parameter space. Large scales simulations will certainly help in studying the evolution of the flow farther away from the source.

Our conclusions must be tempered by several assumptions we have made. For example, we have assumed axi-symmetry and the thermodynamics is polytropic. Most importantly we have assumed ideal MHD. Finally, let us mention that the primary

effect of reducing the dimensionality of the dynamics is to eliminate some modes of MHD instabilities. These modes can play an important role in the dynamics of such winds. It is clear that investigating the effects of the missing physics cited above on astrophysical jets is an important avenue for future research.

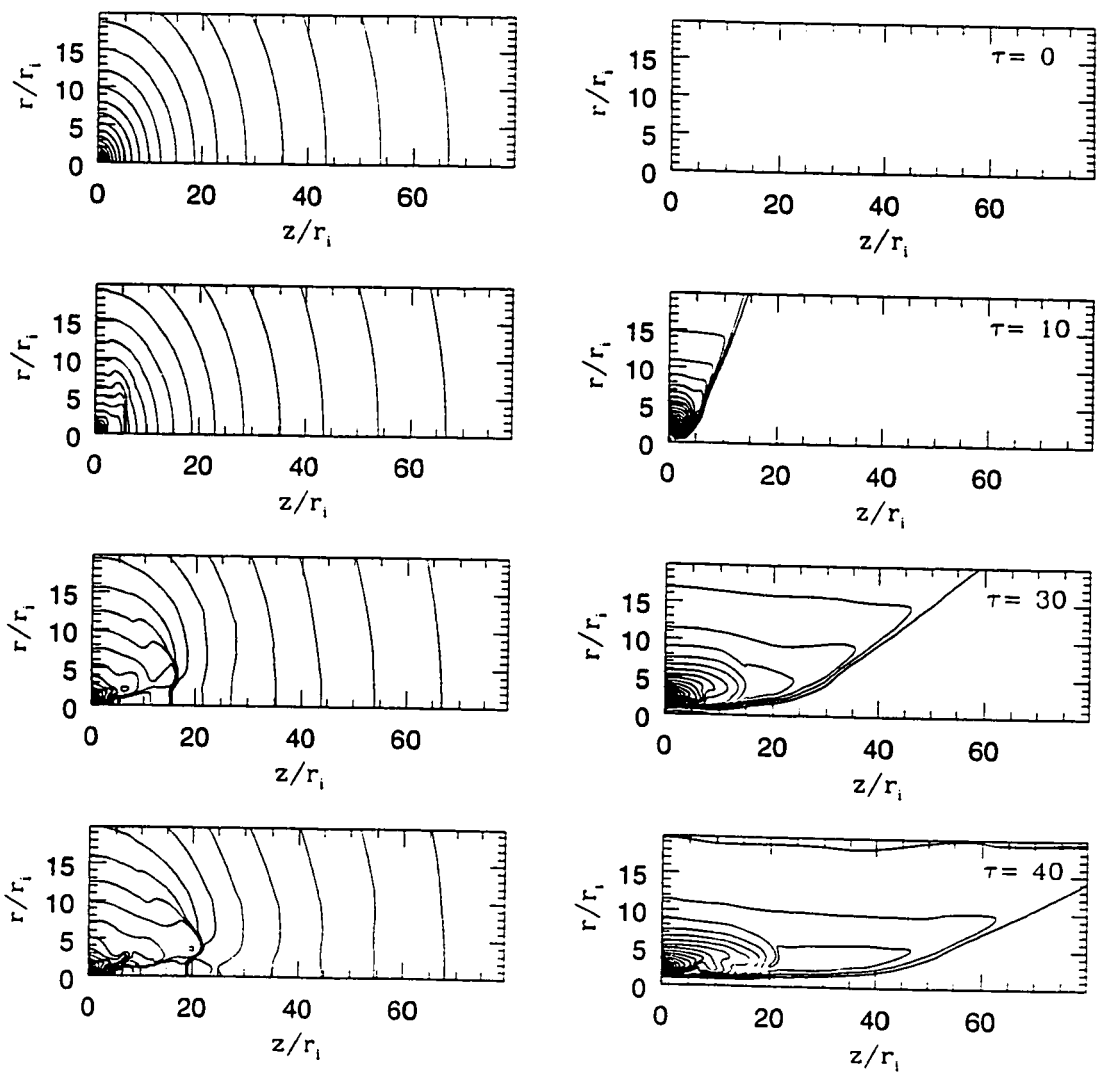

Figure 1. - Evolution of the density (isocontours shown in the left panels) and the toroidal magnetic field (isocontours shown in the right panels) showing the propagation of the initial torsional Alfvén waves. The initial density distribution, as given by (2.3), is shown in the upper left panel. Initially $B_\phi = 0.0$ in the corona (upper right panel). The mesh is $(z \times r) = (80 \times 20) r_i$ with a resolution of (500×200) zones. The evolution is shown at four different times: $\tau = 0$, $\tau = 10$, $\tau = 20$ and $\tau = 40$ from top to bottom. 20 logarithmically spaced contour lines are shown for the density, and 20 linearly spaced contours for B_ϕ. In this figure (and in all the figures), the axis of symmetry is plotted horizontally and the equatorial plane vertically. Note because of axi-symmetry we only compute in one quadrant.

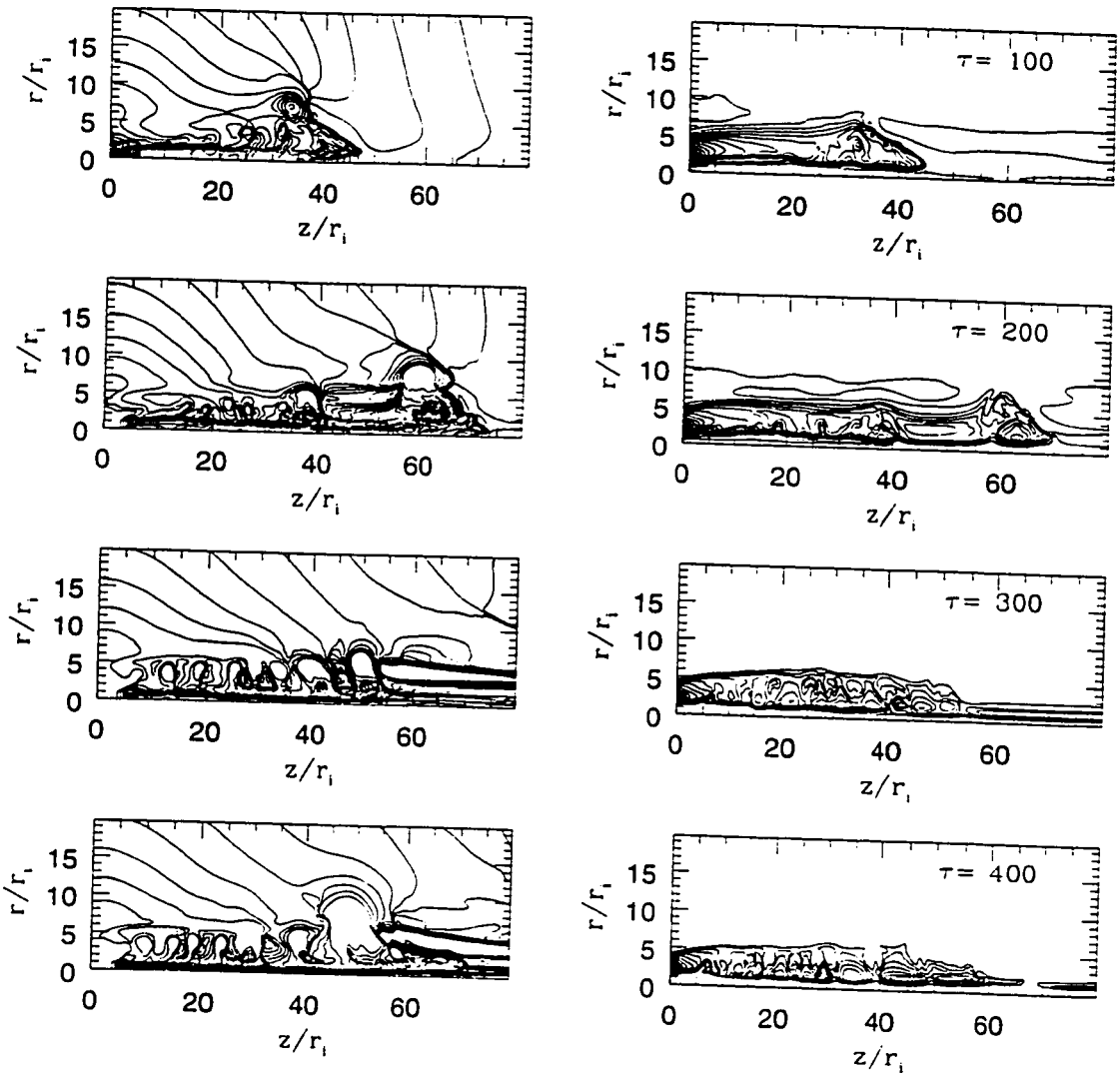

Figure 2a. - Evolution of the density (isocontours shown in the left panels) and the toroidal magnetic field (isocontours shown in the right panels) showing the evolution of the episodic outflow. The mesh is $(z \times r) = (80 \times 20)r_i$ with a resolution of (500×200) zones. The evolution is shown at four different times; $\tau = 100$, $\tau = 200$, $\tau = 300$ and $\tau = 400$ from top to bottom. 20 logarithmically spaced contour lines are shown for the density, and 20 linearly spaced contours for B_ϕ.

Figure 2b. (next page)- The density (lower panel) against the toroidal magnetic field (upper panel) illustrating the sandwiching of the knots between regions of high toroidal magnetic field. The mesh is $(z \times r) = (80 \times 20)r_i$ with a resolution of (500×200) zones. The evolution is shown at times; $\tau = 200$.

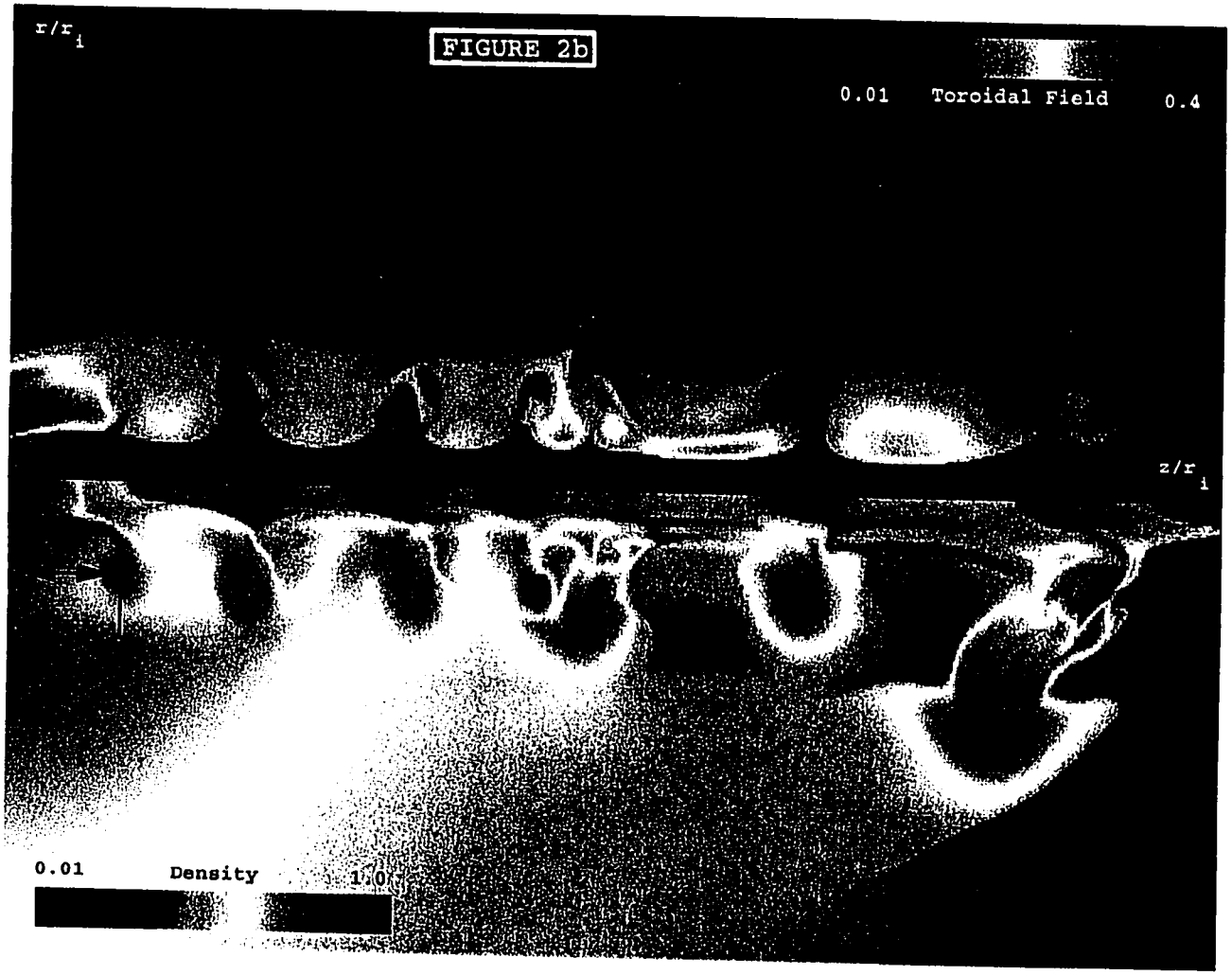
r/r i
FIGURE 2b
0.01
Toroidal Field
0.4
z/r i
0.01
Density
1.0

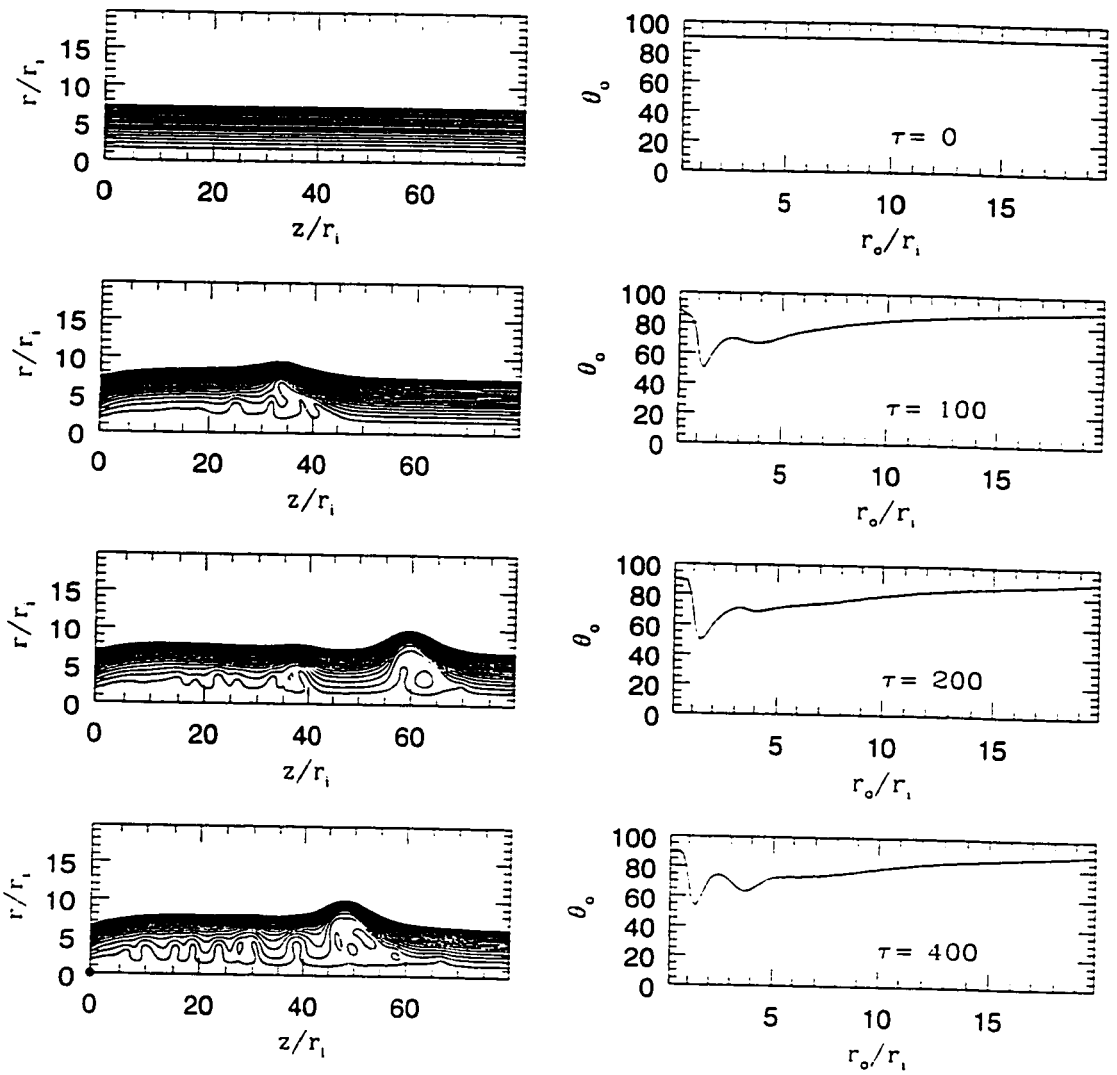

Figure 3. - Evolution of the poloidal magnetic field (left panels) and the launching angle at the disk's surface (right panels). The initial magnetic potential configuration, as given by (2.7), is shown in the upper left panel. The mesh is $(z \times r) = (80 \times 20)r_i$ with a resolution of (500×200) zones. The evolution is shown at four different times: $\tau = 0$, $\tau = 100$, $\tau = 200$ and $\tau = 400$, respectively from top to bottom.

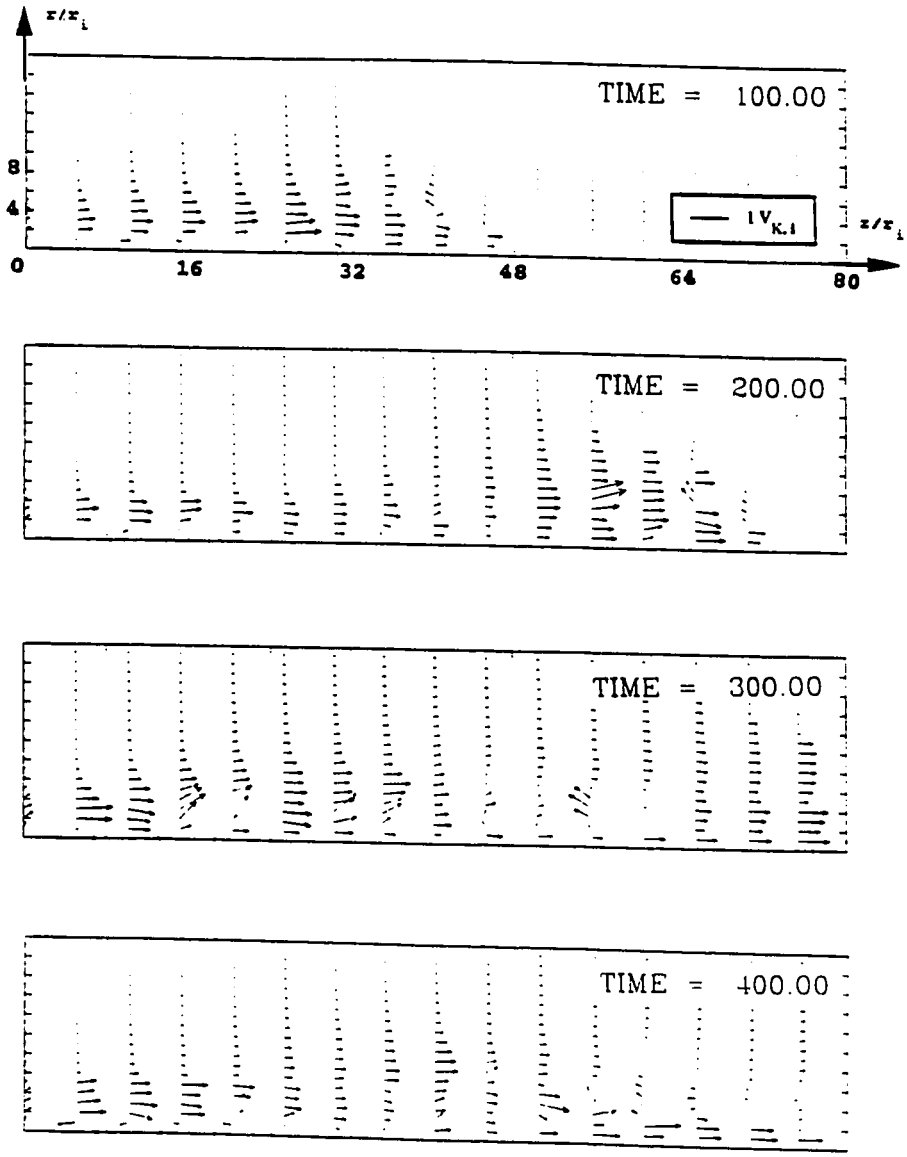

Figure 4. - Poloidal vector velocity $\mathbf{v}_p$ at $\tau = 100$, $\tau = 200$, $\tau = 300$ and $\tau = 400$, respectively from top to bottom.

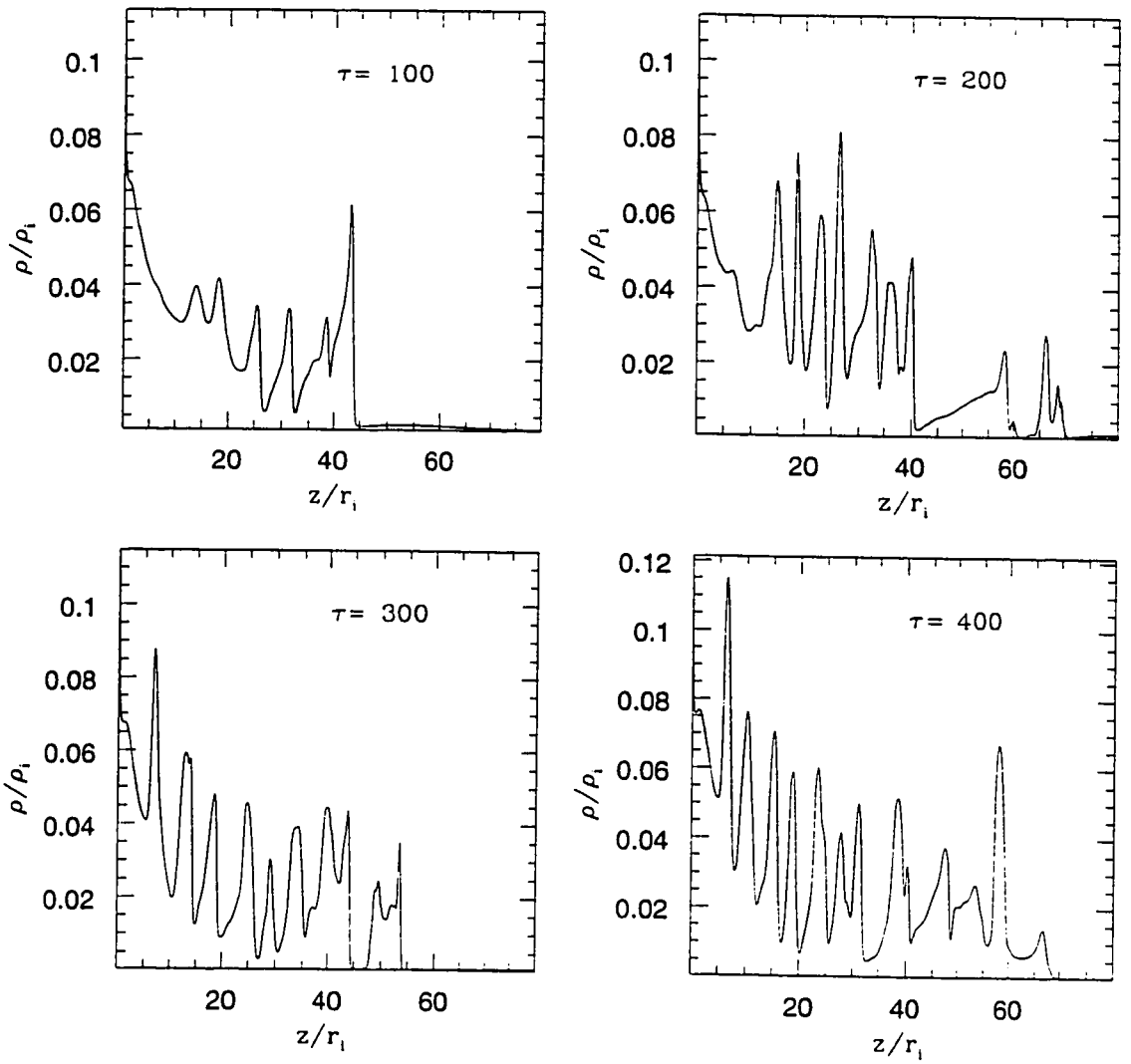

Figure 5. - Density (ρ) cut parallel to the z-axis. The cut is taken directly in Figure 1, at $r_o = 3r_i$. This figure illustrates the values of the contour levels as well as the jet to the ambient density ratio during the evolution of the outflow. The evolution of the knots can be seen with some of the small knots turning into shocks further down the jet. The complex structure of the large knots, located using figure 2, is also seen.

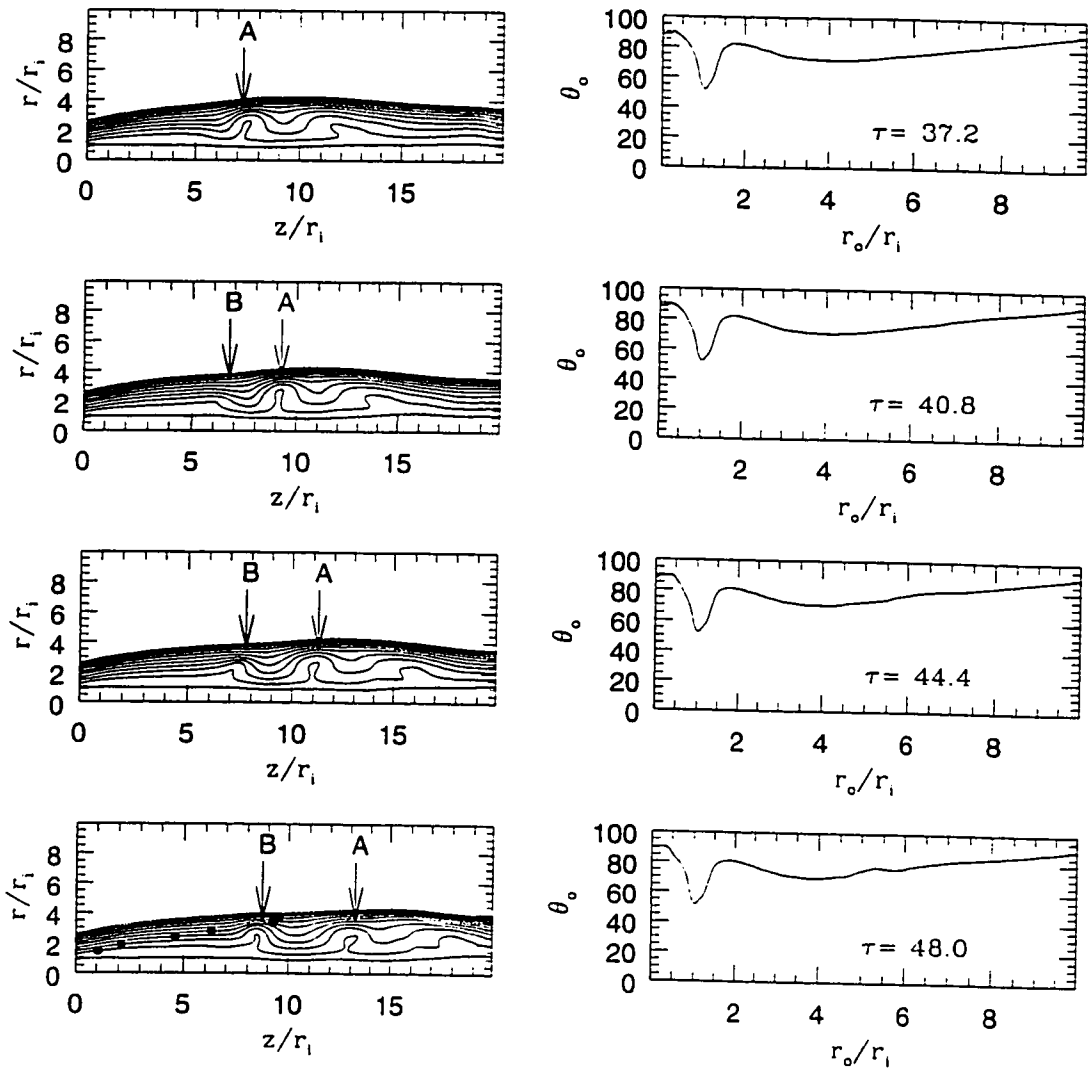

Figure 6. Simulation B: The left panels show the magnetic field structure of the knot generating region, at the four times; 37.2, 42.6, 44.0 and 48.0 inner time units. The right panels show the angle θ_o of field lines at the disk surface, at these times. Note the narrow band of field lines which is sufficiently opened ($\theta_o \leq 60^o$) so as to drive the outflow. Only field lines involved in the knot generation process are shown; field lines at larger disk radius stay reasonably vertical as seen in the right panels.

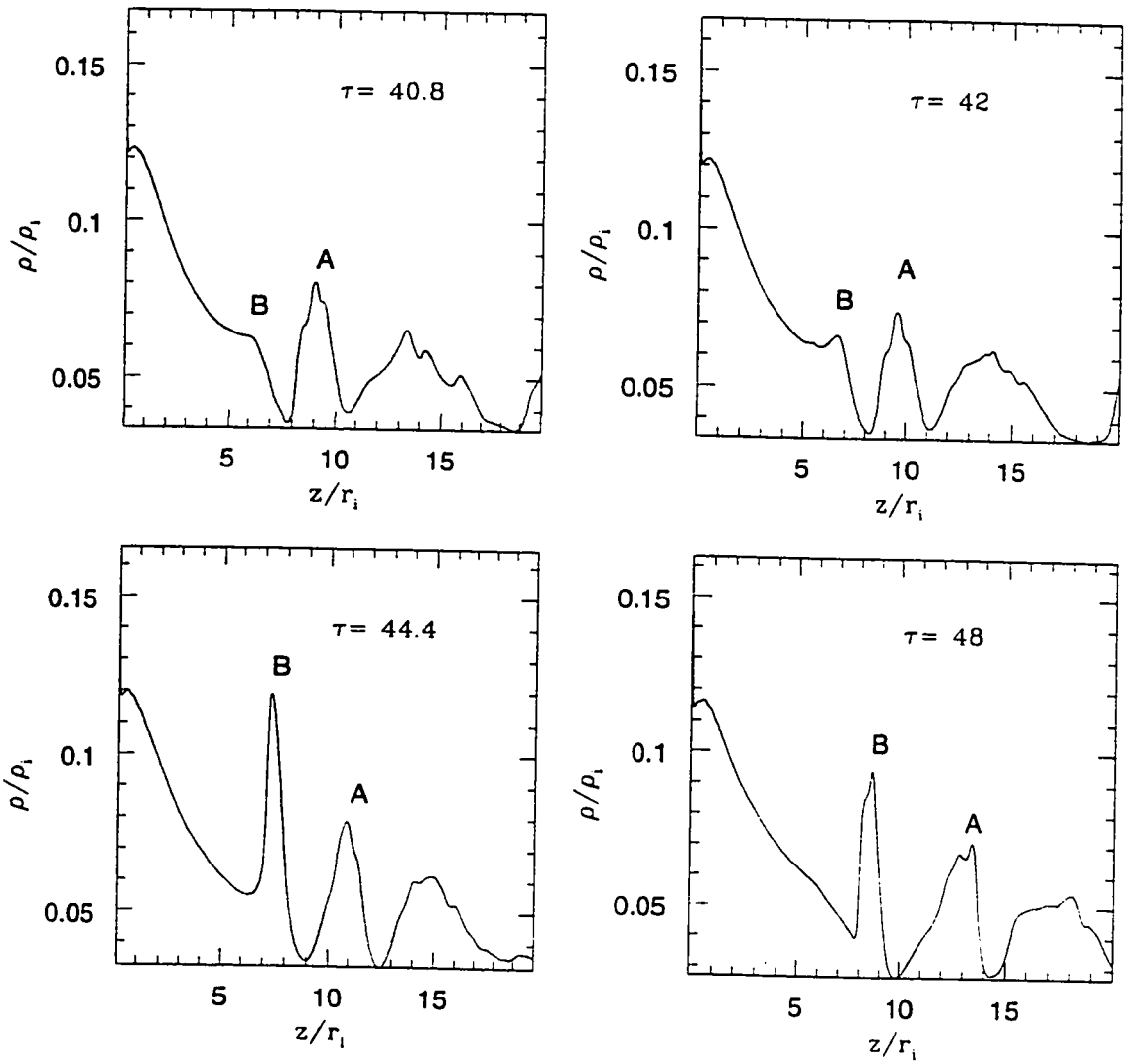

Figure 7a. - Density (ρ) cut parallel to the disk's axis. The cut is taken directly in Figure 6, at $r_o = 3r_i$. This figure illustrates the values of the contour levels as well as the jet to the ambient density ratio during the evolution of the outflow. The production/evolution of knot A and knot B are is also shown.

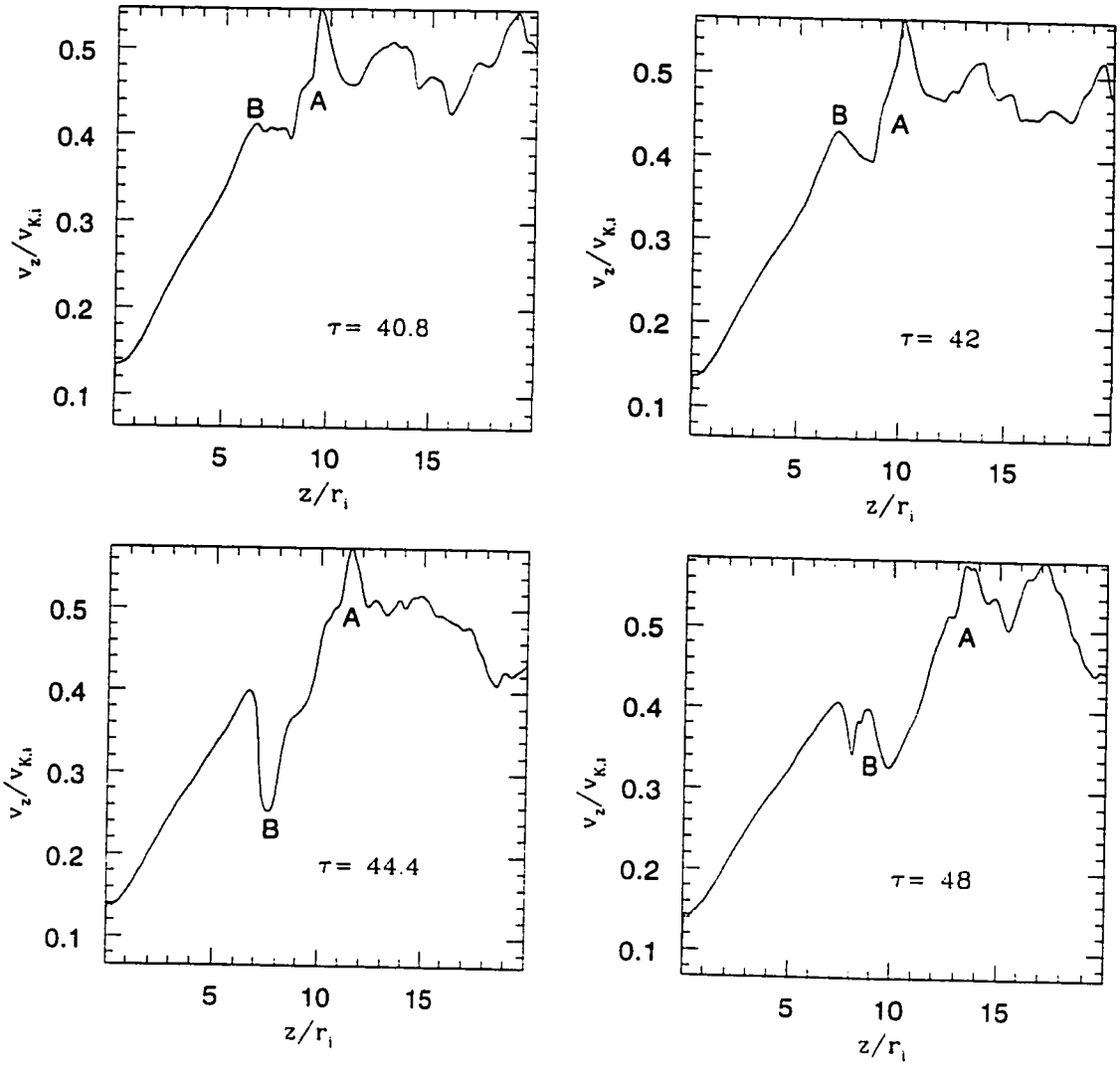

Figure 7b. - v_z cut parallel to the disk's axis. The cut is taken directly in Figure 6. at $r_o = 3r_i$. The production/evolution of knot A and knot B are is also shown.

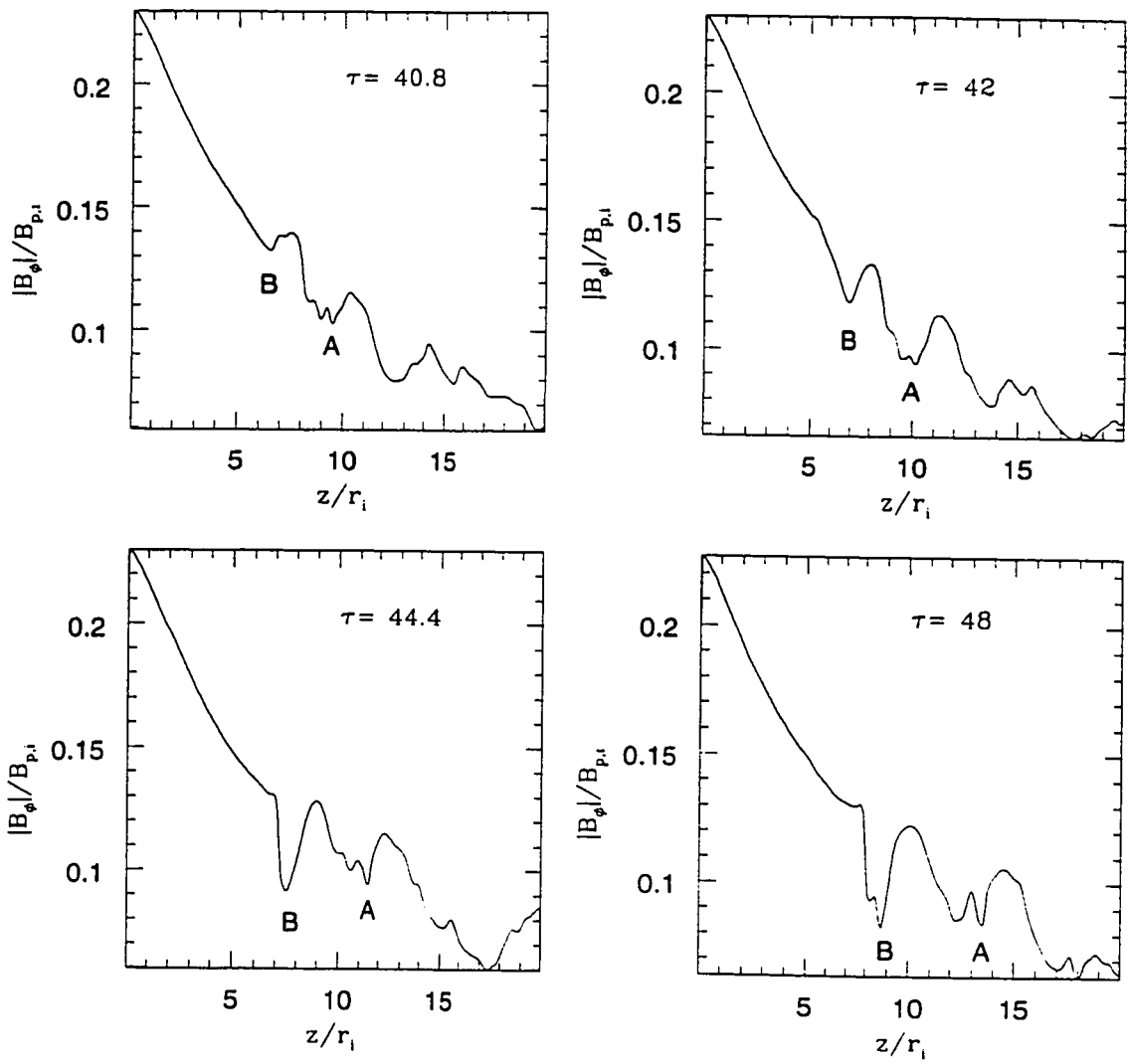

Figure 7c. - $|B_\phi|$ cut parallel to the disk's axis. The cut is taken directly in Figure 6, at $r_o = 3r_i$. The production/evolution of knot A and knot B are is also shown.

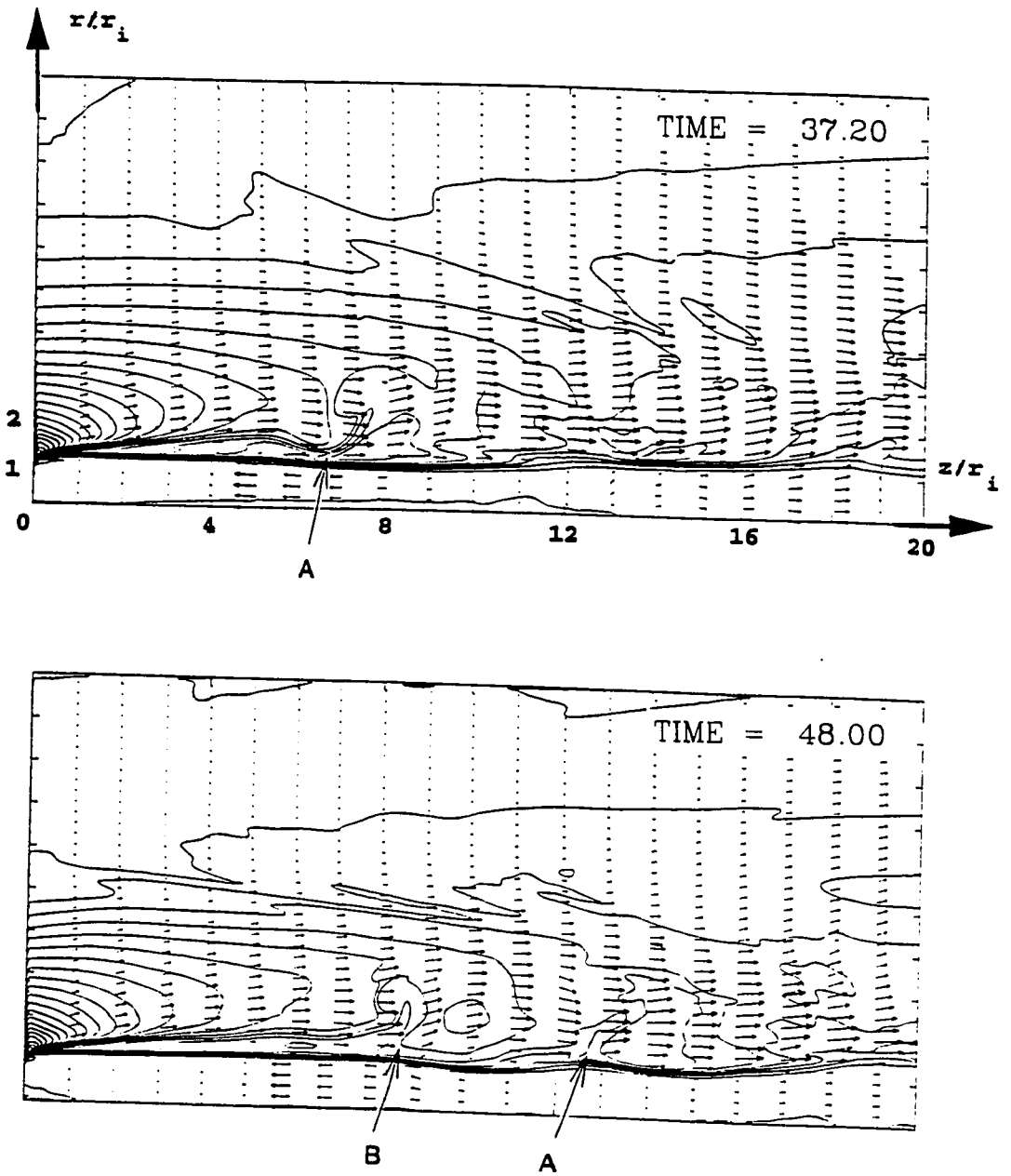

Figure 8. - The poloidal vector velocity ($\mathbf{v}_p$) and isocontours of the toroidal magnetic field (B_ϕ) at $\tau = 37.2$ and $\tau = 48.0$. 20 linearly spaced contours are shown for B_ϕ. As the flow recollimates towards the axis, it then reflects back into the slower moving body of the jet. Generally speaking, high velocity regions (associated with the knots) are associated with regions of low toroidal field strength.

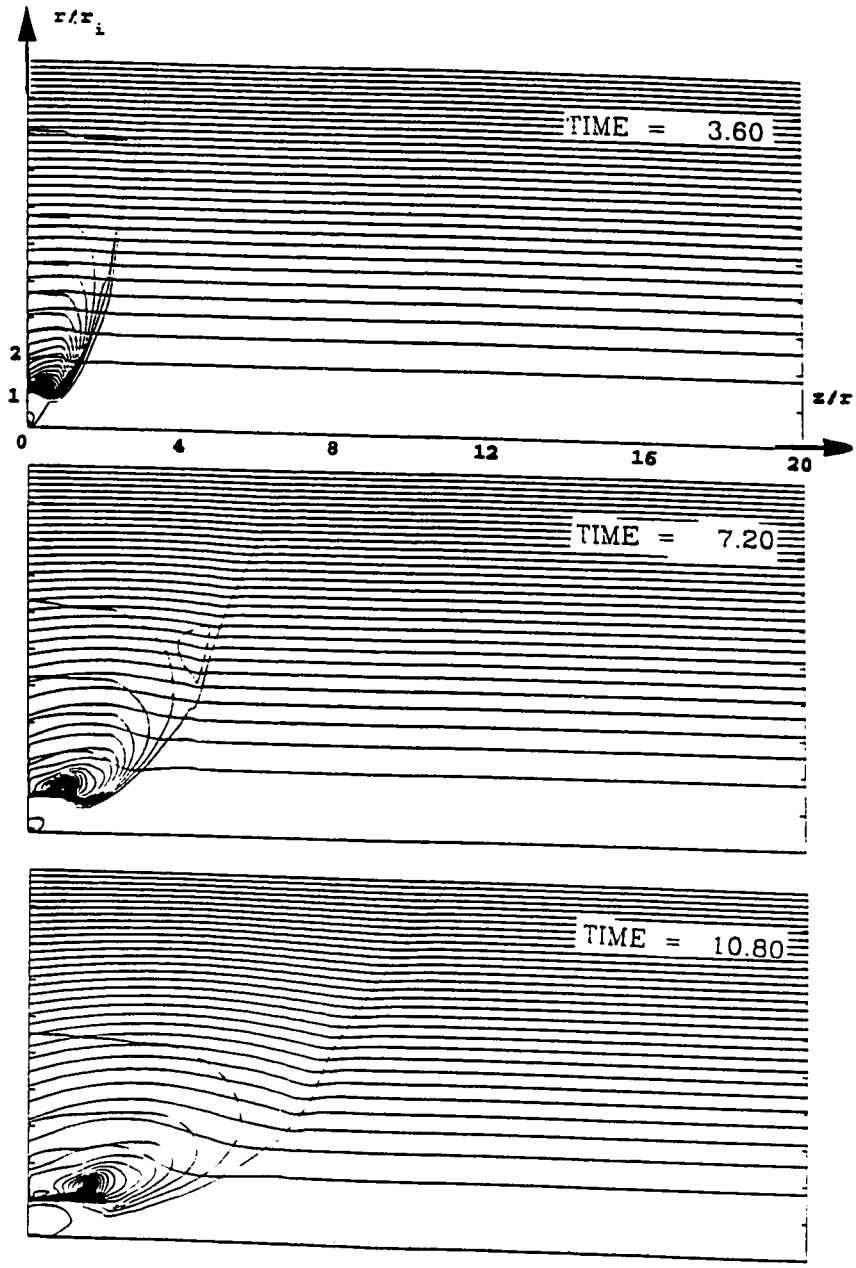

Figure 9. - This Figure displays the $\nabla(B_\phi^2)$ force (20 linearly spaced contours are shown for B_ϕ/B_p) opening up the initially vertical magnetic configuration. In the inner parts of the disk, where $|B_\phi|/B_p \simeq 20.0$, the non-linear torsional Alfvén waves control most of the dynamics. Here $\tau = 3.6$, $\tau = 7.2$ and $\tau = 10.8$, from top to bottom.

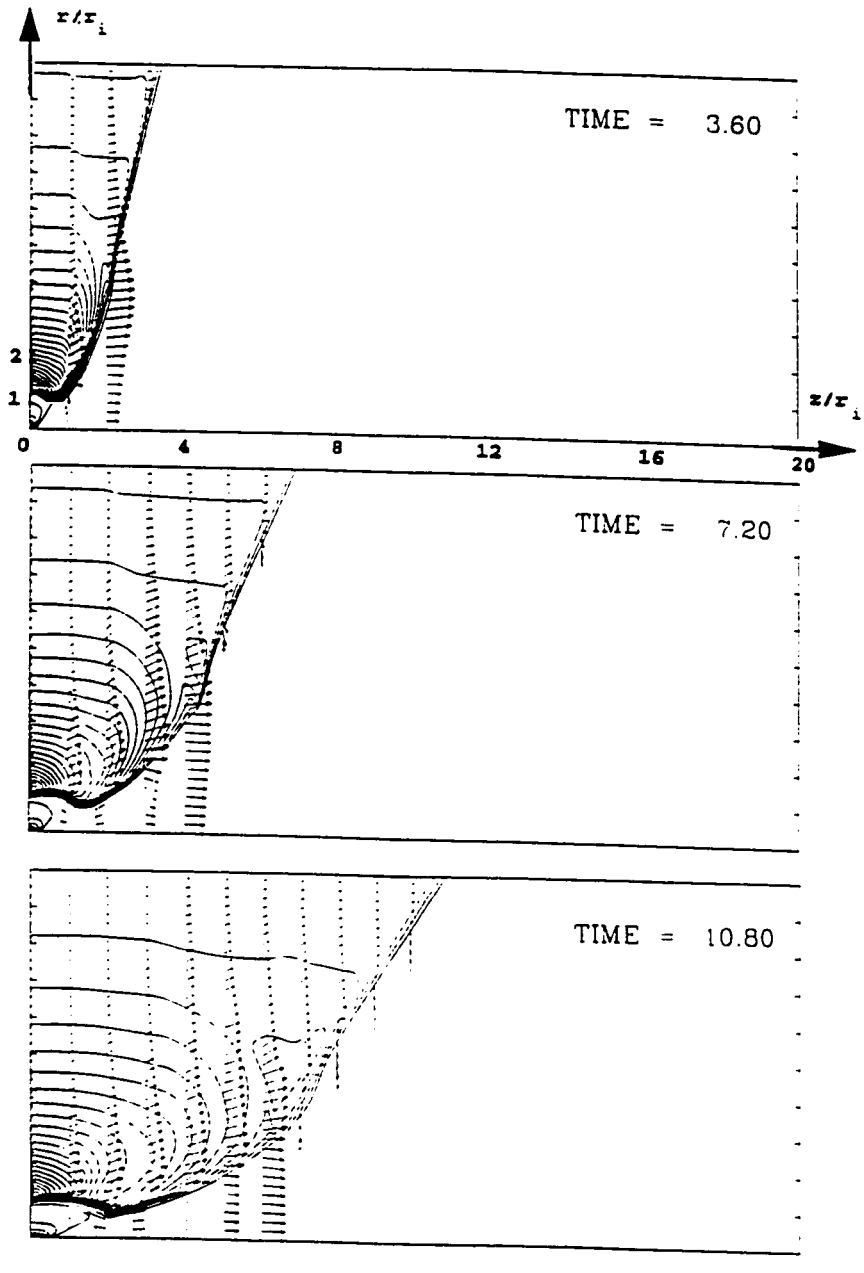

Figure 10. - This Figure displays the major role played by the $\nabla(B_\phi^2)$ force (20 linearly spaced contours are shown for B_ϕ) as it clears up the immediate surroundings of the disk. A wind is centrifugally ejected from the inner most field lines. Here $\tau = 3.6$, $\tau = 7.2$ and $\tau = 10.8$, from top to bottom.

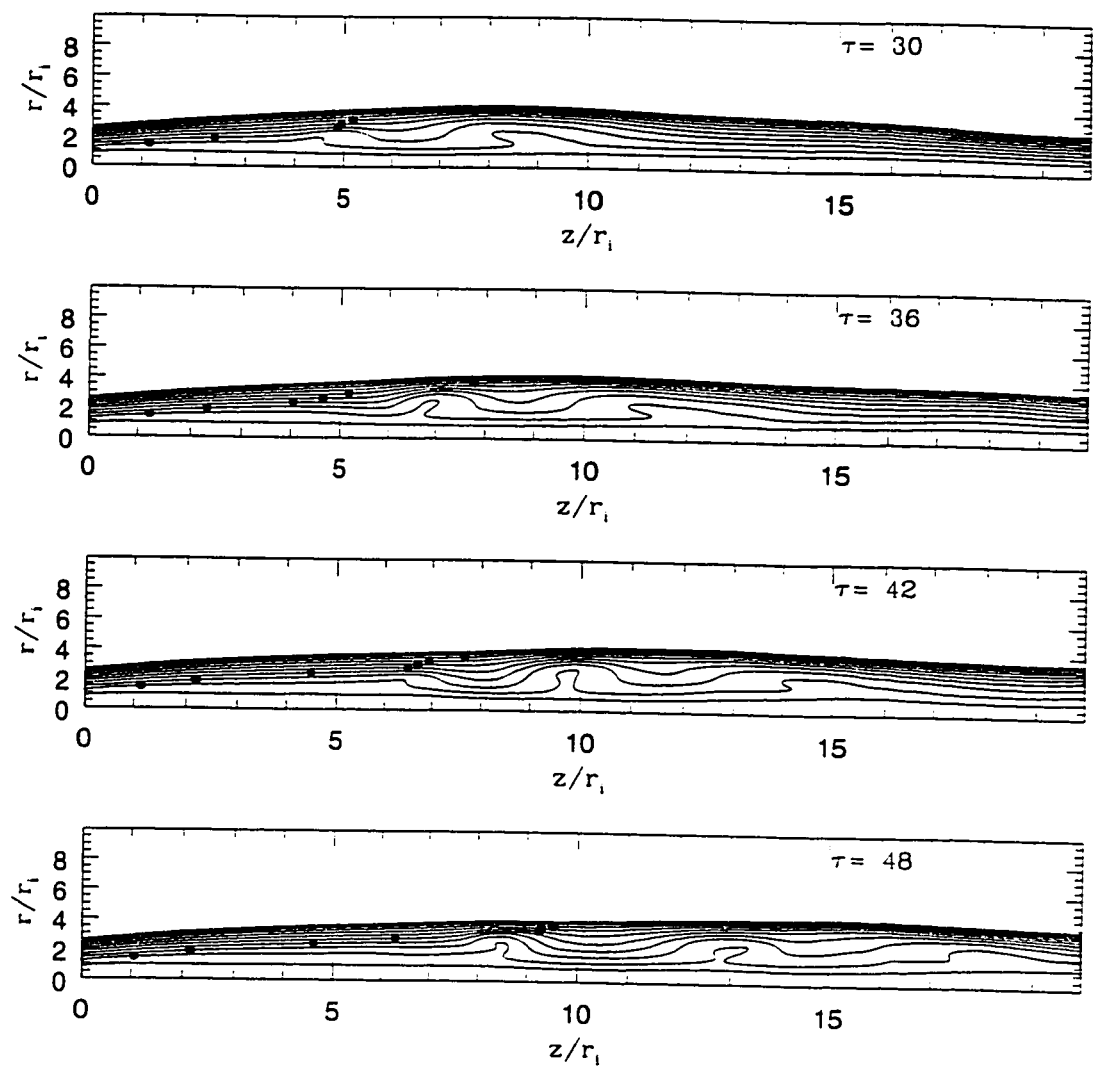

Figure 11. - Evolution of the Alfvén surface. This shows that throughout the strongly episodic outflow, the Alfvén surface stays fix in space.

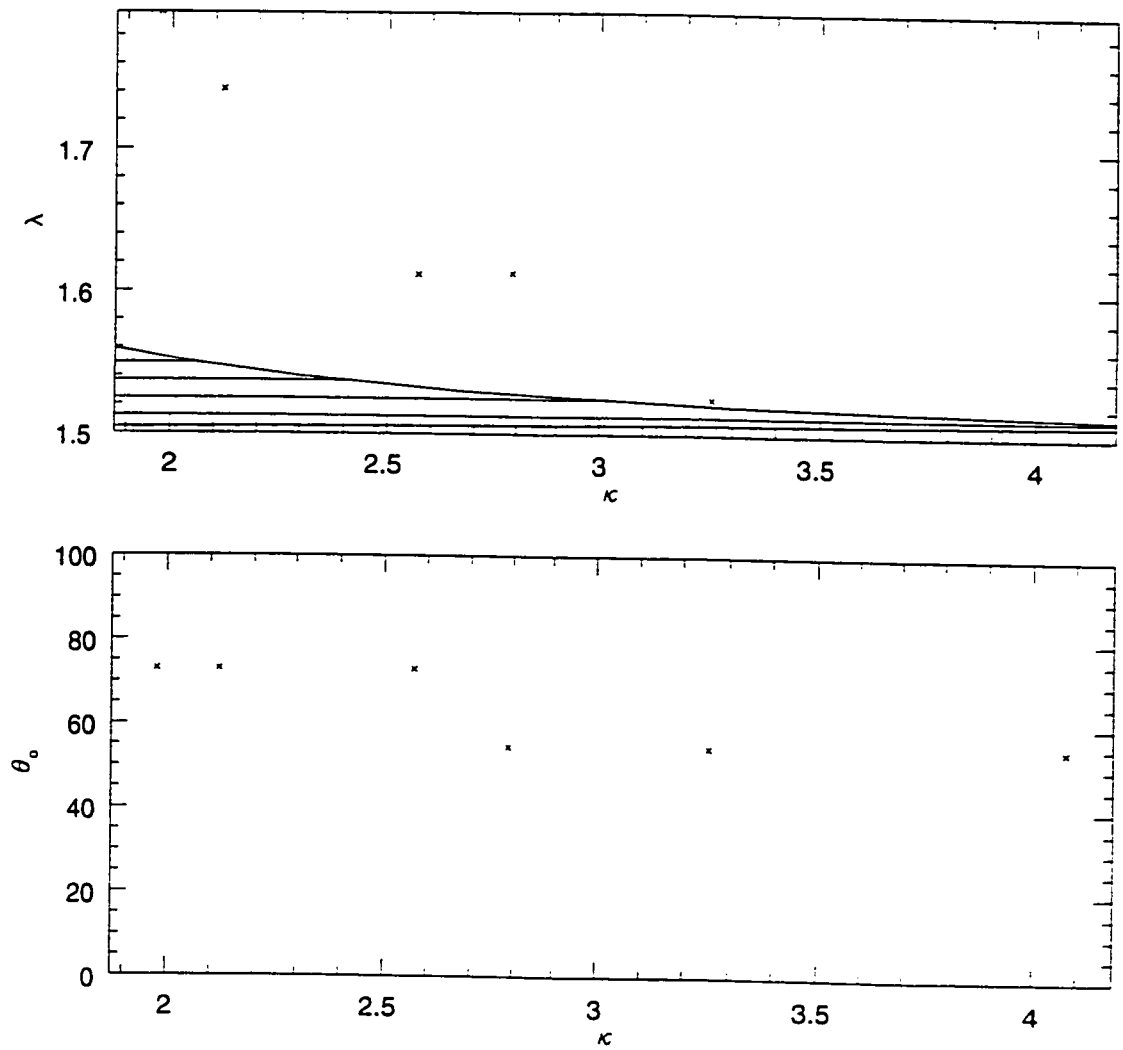

Figure 12. - The κ-λ space (upper panel) and the κ-θ_o space (lower panel) and the location of our solution. at $\tau = 400$. Our solution is a particle-dominated jet with $\kappa \geq 1$. In the upper panel. the dashed area represents the sub-Alfvénic flows $\left(4\pi\rho v_p^2 < B_p^2 \quad \text{or} \quad \kappa\lambda(2\lambda-3)^{1/2} < 1\right)$.

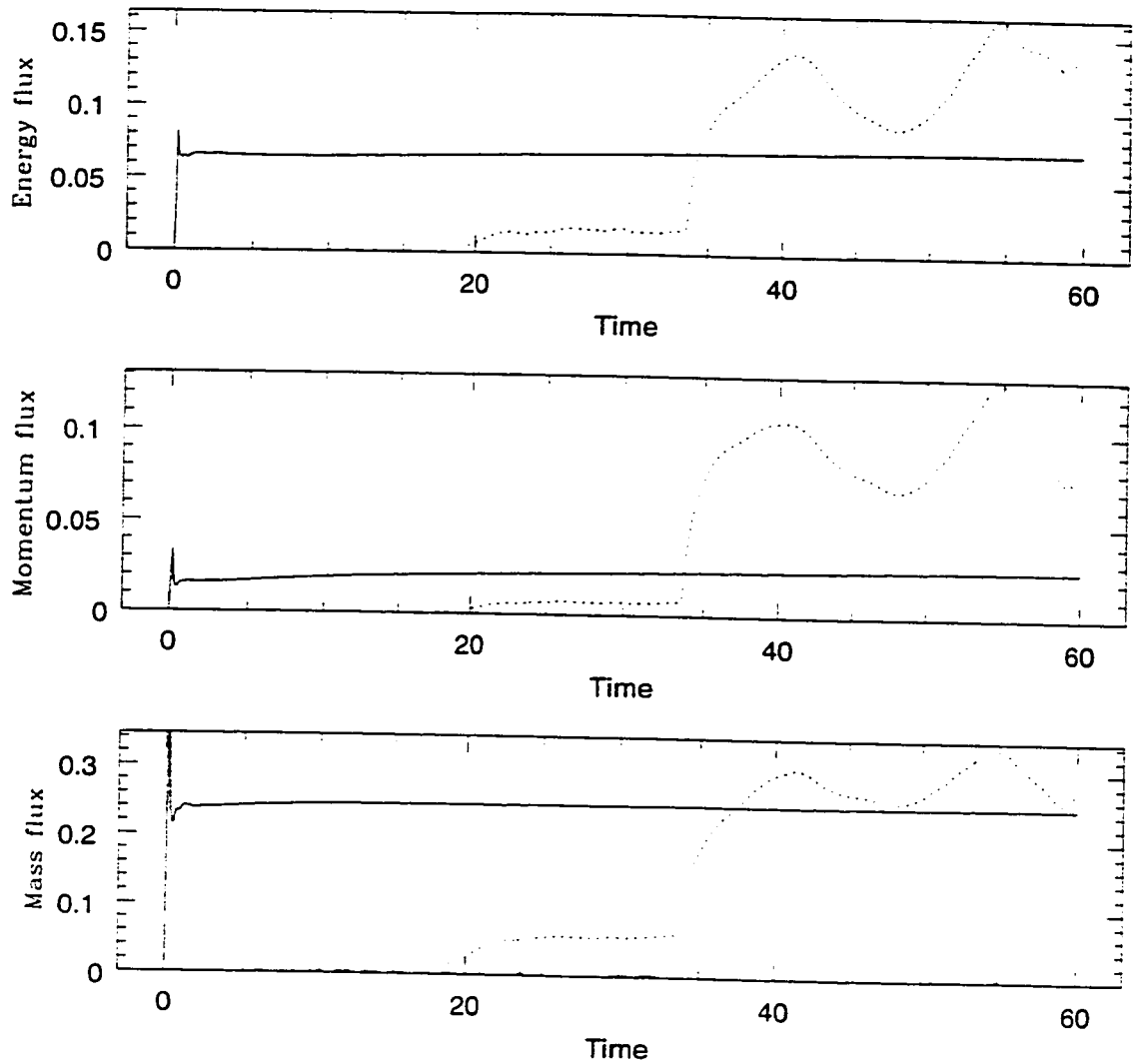

Figure 13. - Here, we quantify the different fluxes carried by the jet. The bottom panel represents the mass flux, the middle panel the momentum flux while the top panel represents the kinetic flux. The solid lines denote the fluxes across the inner (z=0) boundary. The short dashed lines denote the fluxes across the outer radial boundary ($r = r_e$). Finally, the dotted lines denote the fluxes across the outer axial boundary ($z = z_e$). Note the effect of the knotty structure on the flow crossing the outer axial boundary (dotted line).

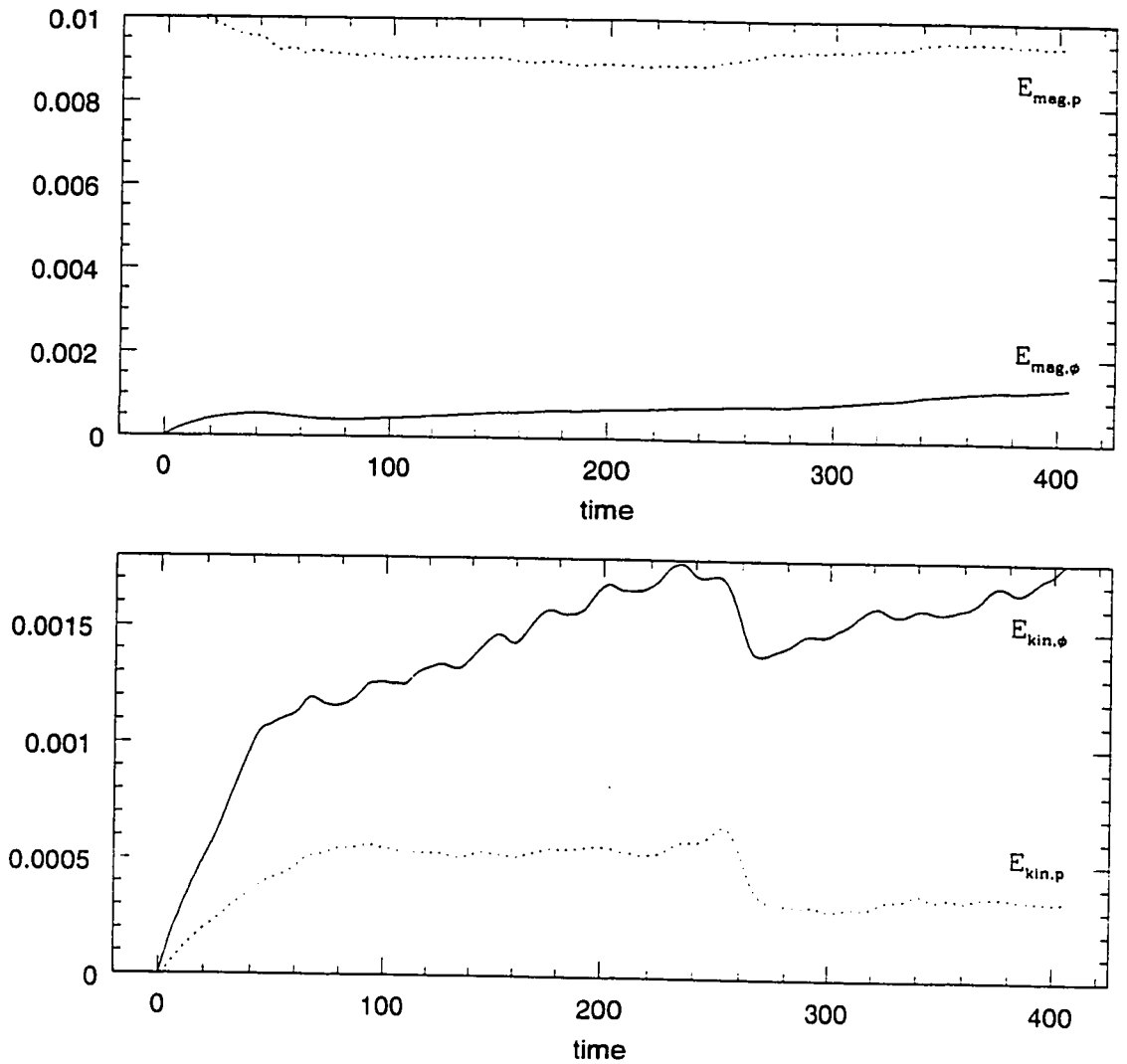

Figure 14. - Quantification of the energies involved in the flow. In the upper/lower panel the poloidal magnetic/kinetic energy is compared to the toroidal part.

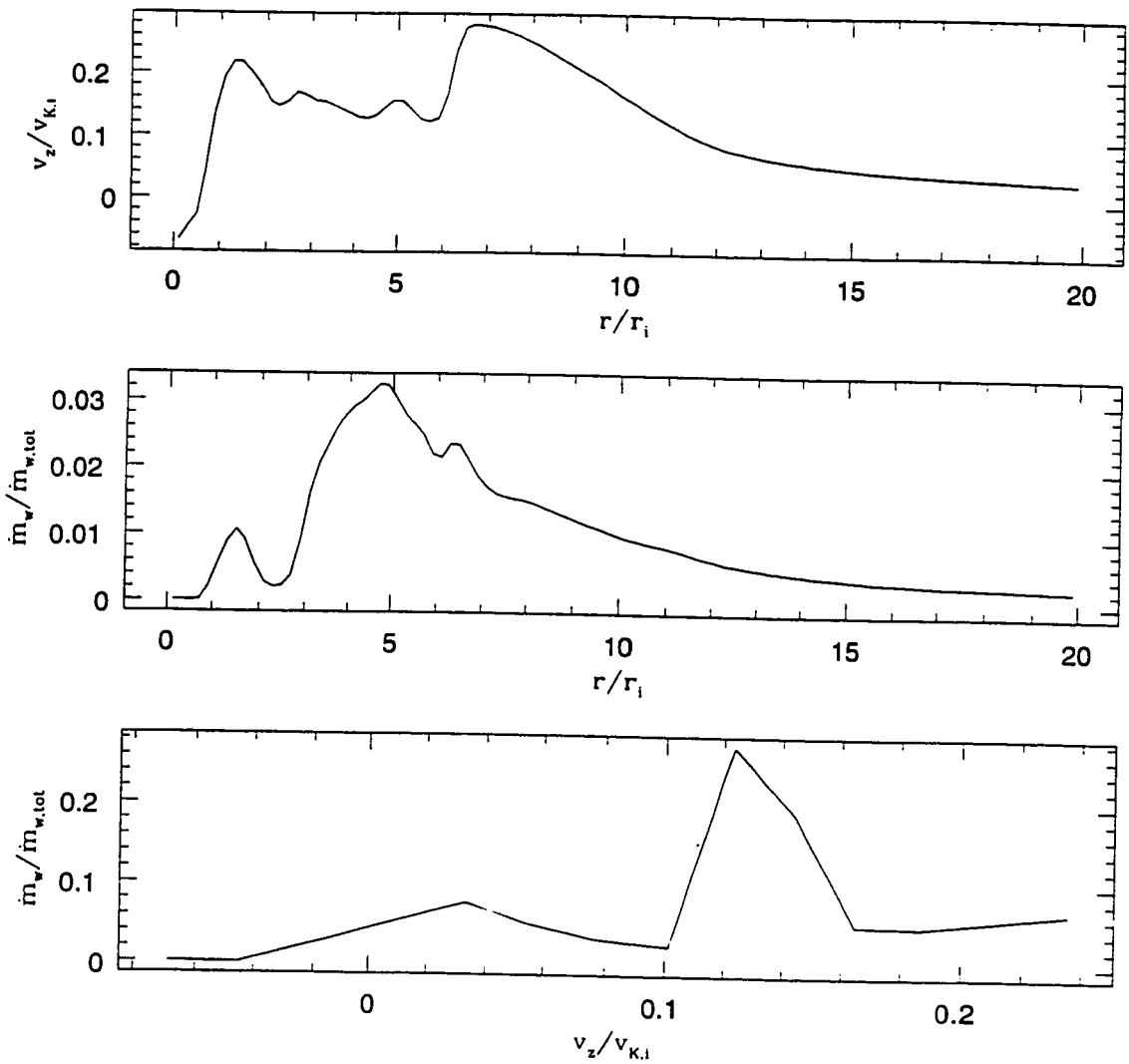

Figure 15a. - Simulation A; A snapshot (at $\tau = 400$) of the dependence of the mass outflow rate upon the poloidal velocity of the jet (lower panel). The top panel shows that the velocity peaks in two dominant streams ($r \simeq 1.5r_i$ and $r \simeq 7r_i$). The middle panel shows size of the wind region ($1r_i < r_{wind} < 8r_i$).

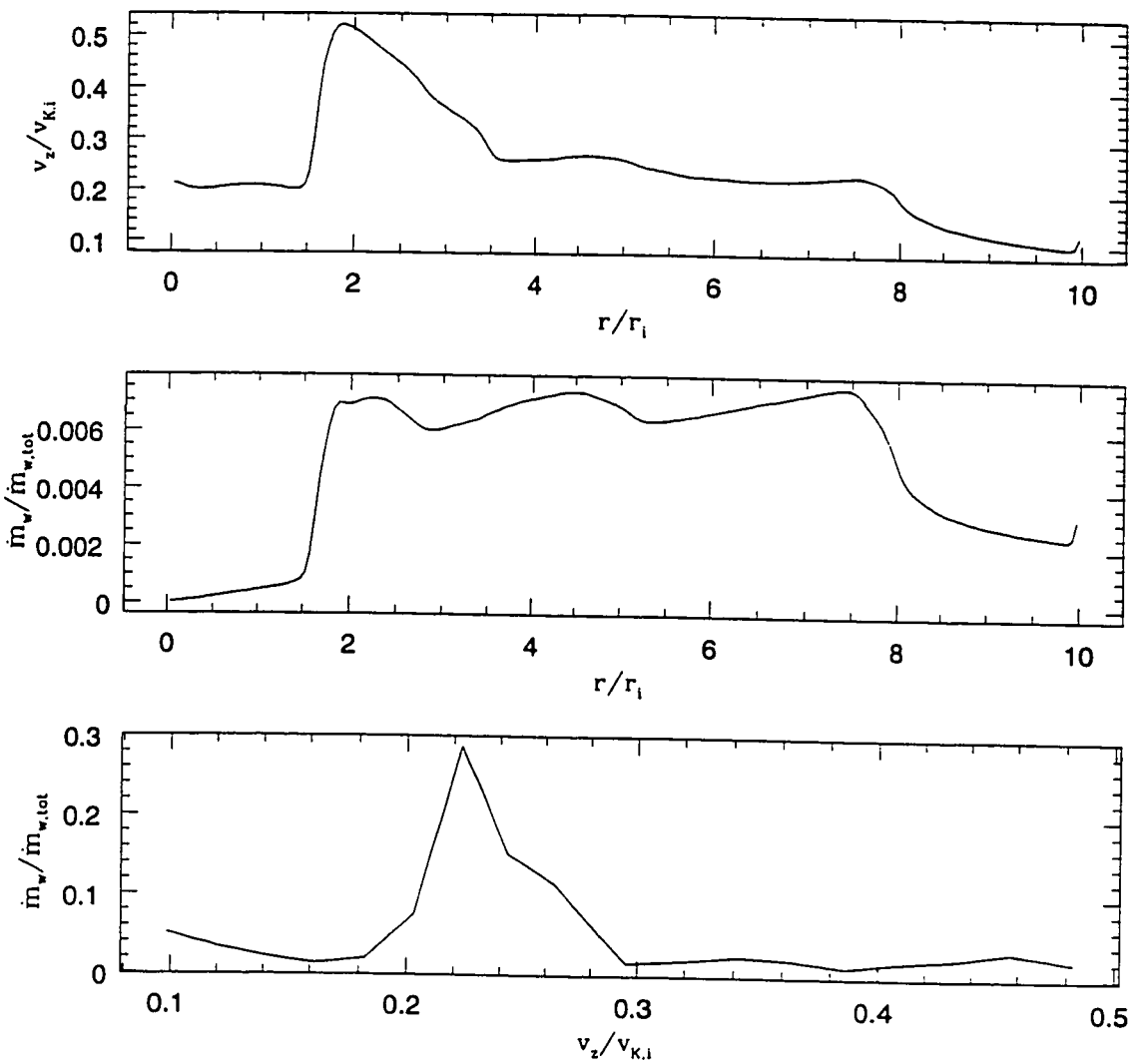

Figure 15b. - Simulation B: A snapshot (at $\tau = 40$) of the dependence of the mass outflow rate upon the poloidal velocity of the jet (lower panel). The top panel shows that the velocity peaks in two dominant streams ($r \simeq 1.5r_i$ and $r \simeq 4.5r_i$). The middle panel shows size of the wind region ($1r_i < r_{wind} < 8r_i$).

Chapter 5

Episodic Jets From Black Holes and Protostars

This chapter is a preprint of the paper: "Episodic Jets From Black Holes and Protostars" by Ouyed, R. Pudritz, E. R. & Stone, M. J. 1997, accepted for publication in "Nature".

This paper is complementary to the two previous chapters. here, we show how our image analysis package can be used to further our understanding of the physics behind our jets.

Episodic Jets From Black Holes and Protostars

Rachid Ouyed*, Ralph E. Pudritz*, & James M. Stone† *Department of Physics and Astronomy, McMaster University, Hamilton, Ontario, L8S 4M1, Canada †Department of Astronomy, University of Maryland, College Park, MD 20742, USA

Energetic, highly collimated, bipolar jets are observed in active galactic nuclei, in regions of star formation, and in binary stellar systems that harbour black holes or white dwarfs. Time-dependent magnetohydrodynamical simulations are used to demonstrate that magnetic fields anchored in a gaseous accretion disk orbiting a star or black hole can accelerate an outflow and collimate it into a bipolar jet. For certain magnetic field geometries, time variability in the acceleration zone close to the central object leads to the production of episodic knots within the jet.

There is now substantial evidence that jets in diverse systems are associated with gaseous disks[1]–[5]. Such jets are powerful, with kinetic luminosities comparable to the radiative luminosity of the central source in some cases[6]. Outflows are also long lived; for protostars they persist for several hundred thousand years[7] which is comparable to the star formation time-scale. It is crucial to understand how accreting black holes[8], stellar remnants, or pre-main-sequence stars produce jets.

One unifying idea is that the detailed nature of the central body is itself unimportant, rather its primary role in the jet phenomenon is in providing a deep gravitational

potential well which is the ultimate energy source for the outflows. Gas in any astrophysical environment has some angular momentum so that independently of how it is supplied to the vicinity of the central object, it will form a disk in Keplerian motion around the centre. The removal of the angular momentum of the gas allows it to spiral slowly inwards through the disk and onto the central object, releasing gravitational potential energy as it goes. If the only torques on the disk are *internal* (e.g. through magnetohydrodynamic (MHD) turbulence driven by the magnetorotational instability described by Balbus and Hawley[9]–[13]), then angular momentum will be redistributed within the disk. The fraction of disk gas that loses angular momentum is accreted, releasing gravitational binding energy as heat which is subsequently radiated away[14]–[16]. On the other hand, a number of steady state MHD models[17]–[23] of accretion disks have been constructed which rely on an *external* magnetic torque exerted on the disk by a jet or wind that can efficiently extract angular momentum. A significant fraction of the gravitational binding energy, instead of being liberated as heat, is converted into the mechanical energy of the jet. Thus, jets are powerful because they efficiently tap the gravitational potential energy reservoir of the central object.

This work investigates how jets are produced, not on how jets interact with the environment on much larger scales. We use numerical algorithms to construct solutions to the time-dependent, nonlinear equations of axisymmetric ideal MHD to study outflows driven from the surfaces of an accretion disk. This allows us to re-

lax the highly restrictive mathematical assumptions imposed by existing steady state theories[17],[20],[24]–[26]. Only time-dependent studies can follow the apparently universal, episodic, behaviour of jets[7],[27]. Numerical simulations of axisymmetric magnetized accretion disks in which the internal dynamics of the disk is followed find a rapid radial collapse of the disk. While the highly twisted magnetic field generated in this process does push out a burst of matter as it "uncoils"[28]–[30], these models have not yet demonstrated that truly episodic ejection develops.

We adopt a different approach that allows us to isolate the physics of the formation of the jet for a well defined set of conditions imposed at the base of the wind[31]. Accordingly, we present high resolution, MHD simulations of the onset and collimation of outflows from the surface of a Keplerian accretion disk around a central object for two different initial magnetic configurations which provide the external disk torque. We present the results of twelve simulations which show that outflows either self-collimate into stationary, jet-like flows or remain episodic for the duration of the calculation. We have also found that for each of our initial magnetic structures, the rate at which matter enters the corona from the disk is an important factor in determining whether outflows are ultimately stationary or episodic. This implies that the internal dynamics of the disk ultimately may be crucial to understanding the operation of the outflow mechanism.

Model description

The numerical model for both types of simulations are solutions to the time-dependent MHD equations in cylindrical coordinates (r,ϕ,z) calculated with the ZEUS-2D code described by Stone and Norman[32],[33]. The model consists of a point mass representing a star or black hole, the *surface* of a surrounding accretion disk which is taken to have an inner radius r_i (this can be either the surface of the star, the magnetopause radius of a star with the disk, or the last stable Kepler-like orbit around a black hole), an initial disk corona which is in hydrostatic equilibrium within the gravitational field of the central object as well as in pressure balance with the disk below, and an initial magnetic field that threads the disk and corona. We set the initial toroidal field component B_ϕ and gas velocity everywhere in the corona equal to zero, and choose two initial magnetic configurations which are force-free. We avoid the use of a softening parameter for the (Newtonian) potential[29],[31] and thus take particular care to establish the disk corona in *numerical* hydrostatic equilibrium so that there are no initial motions.

The Keplerian accretion disk surface (the base of the corona at $z = 0$) provides fixed boundary conditions for the velocity at every disk radius; the rotational speed is Keplerian v_K and since any radial inflow speed is expected to be tiny compared to this, we ignore it. Matter is introduced into the corona (active zones of the grid) from the disk at very small injection speeds v_{inj}; for Figs. 1 - 6, $v_{inj} \simeq 10^{-3} v_K$ (one hundredth of the disk's sound speed). The disk's toroidal magnetic field is assumed to scale with radius as[20] $B_\phi \propto 1/r$. The initial radial and vertical magnetic field

components in the disk are continuous with the field in the corona. There is no disk, rotation, or toroidal field inside the radius r_i.

All length scales and speeds in the simulations are measured in units of innermost disk radius r_i and the Kepler speed at that radius, $v_{K,i}$, so that results can be scaled to a central object of any desired mass. All time scales are measured in units of $t_i = r_i/v_{K,i}$. Typical conditions in protostellar or AGN disks are summarized in the Table where for the former we take r_i to be 3 stellar radii, $= 0.04$ astronomical units (AU)[34], and for the latter, at 10 black hole radii[35].

Our numerical simulations are governed by five parameters defined at r_i, the most important being the ratio of the thermal gas pressure to the magnetic field pressure at the base of the corona, $\equiv \beta_i$; and the mass injection rate per unit area of the disk into the corona, $= (\rho v)_{inj,i}$. The results in Figs. 1 - 4 pertain to a domain of $(z \times r) = (80.0 \times 20.0) r_i$ in size, while those in Figs. 5 and 6 pertain to a domain $(20.0 \times 10.0) r_i$ in size. As expected, the first stage of evolution in our simulations is a brief transient as a torsional Alfvén wave front propagates through the corona from the disk surface. The flow that develops in the next stage either relaxes to a steady state pattern, or to an episodic outflow, as discussed below.

Steady state outflow

We show a series of snapshots of the flow in Fig. 1 that illustrate the eventual realization of a stationary hydromagnetic outflow. In Fig. 1a, we plot surfaces of

constant magnetic flux for an assumed potential field configuration and density isocontours at the initial instant. The evolution of the two- dimensional magnetic field structure is shown in Figs. 1b and 1c, at 100 inner time units, and at 400 time units by which time the working surface of the jet has long left the end of our mesh. At time 100, the region behind the working surface of the flow has already achieved a cylindrically collimated state while the region ahead of the working surface still retains the original field structure. At time 400, the entire flow in our mesh has been collimated. Cylindrical collimation is predicted for steady MHD winds[26]. There are three wave families and corresponding critical surfaces in MHD (in contrast to only one in ordinary hydrodynamics) and we plot two of them in Fig. 1c; the points at which the flow speed along streamlines is equal to the Alfvén speed (filled hexagons), or the fast magnetosonic (FM) speed (stars). There is good agreement between our numerical results and steady state theory for the position of the Alfvén surface as is shown in Fig. 1d. At the base of the outflow, the flux surfaces in Fig. 1c (or equivalently, the stream-lines) make an angle of $\simeq 55^o$ with respect respect to the disk across most of its surface. This geometry satisfies the condition, from steady state centrifugally driven wind theory[17], that the opening angle be less than 60^o.

We plot in Fig. 2 the two-dimensional distribution of the toroidal magnetic field and vertical outflow speed as compared with the density, at time 180. An obvious bow shock traces the working surface of the outflow with respect to the undisturbed corona. There is also a highly collimated jet-like stream of gas that starts at the disk

surface. The comparison of the jet density (upper panel) and toroidal magnetic field (lower panel) in Fig. 2a shows that the outflow density is delimited by the region of strong toroidal field. The physical reason for this is the strong radial pinch force that is exerted towards the jet axis by the magnetic force arising through the combination of a dominant toroidal field, and its associated current which flows primarily along the outflow axis. The velocity field (Fig. 2b) is interesting in that the highest speed gas is nearest the outflow axis with lower speeds at larger radii.

In order to show the details of the acceleration mechanism, we plot in Fig. 3 the values of various physical quantities at increasing distance along a fiducial field line, anchored near $r_o = r_i$. Fig. 3a shows that MHD analogues of the Mach number in hydrodynamics, the Alfvén and FM Mach numbers, achieve values of 5 and 1.5 respectively. The ratio of the toroidal to poloidal field strength builds from an initial value of unity to 3 (Fig. 3b). Thus, beyond the FM surface, the toroidal magnetic field dominates the dynamics of the jet. Fig. 3c shows that the poloidal speed of the gas along a field line starts at its input value of a thousandth of the Kepler speed at the base of that field line ($v_{K,o}$), reaches 1.5 times this value at the FM point, and continues to accelerate to 2.1 $v_{K,o}$ at the end of the grid. Thus, flow speed from our fiducial, low mass young stellar object reaches upwards of 220 km s^{-1}, comparable to observed values. The density of the flow decreases as one moves outwards along the field line because of the divergence of the flow streamlines (Fig. 1c).

The outflow achieved in this simulation has properties predicted by steady MHD

Table		
	Proto-Star	Black Hole
$Mass\ (M_\odot)$	0.5	10^8
$r_i\ (AU)$	0.04	20.65
$v_{K,i}\ (km/s)$	120.0	6.7×10^4
$t_i\ (days)$	0.62	0.53
$\dot{m}_w\ (M_\odot/yr)$	9.1×10^{-7}	2.2×10^{-2}
$\dot{m}_w v\ (M_\odot km/s/yr)$	2.8×10^{-5}	7.5×10^2
$\frac{1}{2}\dot{m}_w v^2\ (erg/s)$	8.0×10^{32}	1.2×10^{43}

disk-wind theory. The acceleration of the flow from the disk occurs by a centrifugal effect whereby, at some point along sufficiently inclined field lines, centrifugal force dominates gravity and gas is flung away like "beads on a wire"[36]. This toroidal field component is created because the field lines are forced to co-rotate with the underlying disk. At larger z, the inertia of matter in the flow region ultimately forces the field to fall behind the rotation of the disk, producing the toroidal field component. The acceleration of material occurs in two separate stages. In stage 1 (the region along a field line between the disk and the FM point) the centrifugal effect dominates. In stage 2, (region beyond the FM point), the flow speed scales as $v_z \propto z$, which is theoretically expected when outflow becomes super-Alfvénic (supersonic for hydrodynamic jet models[37]).

The Table lists the mass, momentum and energy flux rates across the outer axial boundary ($z = 80.0$) of our simulation, evaluated at 400 time units. These numbers are comparable to those for AGN and protostellar outflows observed on much larger

physical scales[38],[39]. The disk accretion rate deduced from our mass outflow rate is $\dot{M}_a \simeq 6\dot{M}_w$.

Episodic outflow

We show a series of snapshots of the evolution of an episodic flow in Figs. 4 - 6. The field lines comprise an initially uniform and vertical magnetic field structure that penetrates the disk and overlying corona, perhaps produced by dragging an external magnetic field into the disk by the accretion flow[40],[41]. According to steady-state models, this configuration is unfavourable for launching an outflow. In two snapshots taken at 100 and 400 time units. Fig. 4 shows that outflow is nevertheless launched from the accretion disk for reasons we describe below. The highly collimated, jet-like flow has a density structure (upper panels) that is dominated by discrete knots. At time 100 the working surface of the outflow is clearly evident. The working surface in this simulation has the shape of a cone that advances into the flow with a swept-back bow shock along its flanks[43],[44]. This surface leaves our grid long before 400 time units have elapsed.

The density structure in this simulation *never* achieves steady state. We have run simulations for up to 1000 time units and find that the episodic nature of the flow persists unabated. The density contours show that the jet is strongly confined near the axis. We find that the associated toroidal field in the flow is tightly anti-correlated with the knots[42]; high (low) density regions are associated with the lowest (highest)

toroidal field strength. The average speed of material in this outflow is $0.5v_{K,i}$, with the highest outflow velocities $\simeq v_{K,i}$. Although this velocity is not as large as is sometimes observed on larger scales in real outflows[14] , our simulations explore only a limited region of physical and parameter space. Movies of this simulation (see our website) show that the knot generator stays fixed in space and that the knots, once formed, persist as coherent structures that propagate down the length of the jet. The larger knots in our simulation appear to be more slowly moving structures that build up by absorbing the more quickly moving knots produced at the generator.

To explore the knot generating region further, we performed a simulation at 4 times the axial and twice the radial resolution, but otherwise identical to that shown in Fig. 4; $(10 \times 20)r_i$. In Fig. 5 we show two snap shots of this innermost region of the outflow, at times 37.2 and 48.0. The upper panel in each of these snapshots shows the flow density, and the lower panel, the associated flow velocity v_z. In frame 5a we see a knot (labeled A), and 11 time units later, in frame 5b we see a newly formed knot (B) in the same position as A had, while knot A has moved down the flow. Both knots are produced at a distance of $z_{knot} \leq 6 - 7r_i$ from the central source. Since the variation in axial velocity associated with the knots is supersonic, they are associated with MHD shocks [15],[46].

In Figure 6 we show the magnetic field configuration of the outflow at times 37.2, 42.6, and 48.0 during which the new knot (B) is formed (knot A moves away from the generating region as knot B is formed). This process takes a time $\tau_{knot} \simeq 11$ time

units. Comparison of frames a and c shows that knots are *spatially* separated by a distance of $\delta z_{knot} \simeq 5r_i$ and thus move at a speed of $\simeq 0.5v_{K,i}$ out of this generating region.

How is the outflow and its knots generated? The plots in the right hand panels of Fig. 6 reveal that a narrow radial region of field lines in the innermost parts of the disk has been opened up, making an angle of 50° with respect to the disk surface. This narrow region drives the outflow and is produced by the toroidal field which is strongest in the inner regions of the outflow where the underlying Kepler rotation is the largest. A radial, outwardly directed, toroidal magnetic pressure gradient is produced by the newly created toroidal field and this pushes open the field lines setting up a condition favourable for outflow. The knots are produced in a region of the flow beyond the Alfvén (marked on the field lines in Fig. 6c) and FM surface in the outflow.

The size of the wind production region on the surface of the disk depends upon the ease with which field lines can be pushed aside by the toroidal field pressure. The rigidity of the field is measured by the β parameter and is very different for our two cases. For the more magnetically dominated episodic case, the magnetic pressure associated with the self-generated toroidal field in the narrow band of outflowing gas has a local maximum so that the pressure force, acts both radially outwards, and *inwards towards the axis.* The accelerating outflow, on encountering the inwardly directed pressure gradient, is reflected back towards the axis. Because the outflow is

rotating however, the gas spins up as it moves inwards and reflects off an inner "centrifugal barrier" when it reaches a radius comparable to its footpoint radius[20],[45],[46], as Fig. 6 clearly shows (the field lines in Fig 6a and c show that the flow recollimates towards the axis, and then reflects back into the slower moving body of the jet). The resulting nearly harmonic oscillation in the width of the flow[24] between these two "barriers" must, by mass conservation, lead to variations in flow velocity (much like a constricted garden hose). These variations in flow speed rapidly steepen into fast MHD shocks[46]. Estimating that the toroidal Alfvén speed in our simulation is $v_{A,\phi} \simeq 0.5 - 0.6 v_{K,i}$, and the width of the jet to be $\delta r_j \simeq 3 - 4 r_i$, the oscillation period of the jet is $t_{osc} = 2\delta r_j / v_{A,\phi} \simeq 11 - 13 t_i$, which is the knot production time scale. By contrast, the initial magnetic pressure in the steady flow case drops significantly as one moves outwards from the axis. The accelerating outflow does not encounter a strongly magnetically overpressured outer barrier, and continues to expand radially finally achieving a quiet, cylindrically collimated state.

Outflow formation may be a robust process wherein the Keplerian disk generates the toroidal magnetic field whose radial pressure gradient sculpts a favourable coronal magnetic field structure. Jets are capable of producing episodic events[47]; our simulations show that fast knot production time-scales occur which are a factor of a few shorter than is observed for knot emergence in jets on much larger scales. Finally, gas in our episodic model has significant rotation $\simeq 0.6 v_{K,i}$ on the innermost scales which agrees with observations of rotating, outflowing gas within $12 r_i$ of certain

young stellar objects[48].

Transition from Episodic to Stationary Flow

Given the importance of toroidal field in producing episodic jet behaviour, what happens if the ram pressure of gas injected into the corona is comparable to the confining pressure of the toroidal field? The preceding discussion suggests that when the number $N = (B_\phi^2/8\pi\rho v^2)_{inj} > 1$ (which is a constant for the uniform field configuration), then the outer, toroidal barrier is strong and flow should be episodic (in Figs. 4 - 6, $N = 36$). However, if $N < 1$, then the toroidal magnetic pressure should be overwhelmed and a stationary flow should result. We performed a series of eight simulations identical to those shown in Figs. 5 - 6 except that the injection speed in the initially uniform vertical field configuration was varied from a value of 0, to a maximum of $10^{-2}v_{K,i}$. For injection speeds 5 and 10 times larger than those shown in Figs. 1-6 (for which $N = 1.45$ and 0.36, respectively), *stationary* outflows did indeed develop whose terminal speeds were $\simeq v_{K,i}$. For injection speeds 5 and 10 times smaller (for which $N > 1$), the outflows were episodic and had terminal speeds and knot properties similar to those reported above. In the simulation where we had *no* mass injection, a transient outflow composed of coronal gas developed which gradually died out as the initial coronal material in the jet zone was depleted. Experiments with our potential flow configuration showed that at mass injection speeds of $v_{inj,i} = 10^{-4}v_{K,i}$, rather diffuse knots appeared but these appeared to dissipate as

they moved away from the generating region.

Our simulations only sparsely sample a rather large parameter space, and have much smaller scales than can be directly imaged by HST. The major constraint in our study is that the accretion disk is not allowed to respond to the changing torques exerted by the jet. In spite of the limitations, we suggest that these simulations provide some important insights into the nature of astrophysical jets.

REFERENCES

[1] Blandford, R. D. In SAAS Fée Lectures on Advanced Astrophysics, *Active Galactic Nuclei*, eds. R. D. Blandford, H. Netzer and L. Woltjer, Berlin:Springer, 161-269 (1990)

[2] Rees, M. J., A. Rev. Astr. Astrophys., 22, 471-506 (1984)

[3] Cabrit, S., & André, P., Astrophys. J., 379, L25-L28 (1991)

[4] Edwards, S., Ray, T. P. & Mundt R. In *Protostars and Planets III*, eds. E. Levy and J. Lunine, University of Arizona Press, 567-602 (1993)

[5] Osterloh, M. & Beckwith, S. V. W., Astrophys. J., 439, 288-302 (1995)

[6] André, P., Ward-Thompson, D., & Barsony, M., Astrophys. J., 406, 122-141 (1993)

[7] Parker, N. D., Padman, R. & Scott, P. F., Mon. Not. R. Astr. Soc., 252, 442-461 (1991)

[8] Hjellming, R.M, & Rupen, M.P., Nature, 375, 464-468 (1995)

[9] Balbus, S. A. & Hawley, J. F., Astrophys. J., 376, 214-222 (1991)

[10] Hawley, J. F. & Balbus, S. A., Astrophys. J., 376, 223-233 (1991)

[11] Hawley, J. F., Gammie, C.F., & Balbus, S. A., Astrophys. J., 464, 690-703 (1996)

[12] Stone, J. M., Hawley, J. F., Gammie, C. F. & Balbus, S. A., Astrophys. J., 463, 656-673 (1996)

[13] Curry, C., & Pudritz, R.E., Mon. Not. R. Astr. Soc., 281, 119-136 (1996)

[14] Adams, F. C., Lada, C. J. & Shu, F. H., Astrophys. J., 312, 788-806 (1987)

[15] Beckwith, S.V.W., Sargent, A.I., Chini, R.S., & Güsten, R., Astron. J., 99, 924-945 (1990)

[16] Collin-Souffrin, S. In AIP Conf. No. 254, *Testing the AGN Paradigm*, eds. S. S. Holt, S. G. Neff and C. M. Urry, 119-128 (1991)

[17] Blandford, R. D & Payne, D. R, Mon. Not. R. Astr. Soc., 199 , 883-903 (1982)

[18] Königl, A., Astrophys. J., 342, 208-223 (1989)

[19] Lovelace, R. V. E., Wang, J. C. L., & Sulkanen, M. E., Astrophys. J., 315, 504-535 (1987)

[20] Pelletier, G. & Pudritz, R. E., Astrophys. J., 394, 117-138 (1992)

[21] Cao, X. & Spruit, H. C., Astr. Astrophys., 287, 80-86 (1994)

[22] Hartigan, P., Edwards, S. & Ghandouri, L., Astrophys. J., 452, 736-768 (1995)

[23] Hartmann, L., Kenyon, S. & Hartigan, P., In *Protostars and Planets III*, eds. E. Levy and J. Lunine, University of Arizona Press, 497-518 (1993)

[24] Sauty, C., & Tsinganos, K., Astr. Astrophys., 287, 893-926 (1994)

[25] Li, Z-H., Astrophy. J., 444, 848-860 (1995)

[26] Heyvaerts, J. & Norman, C., Astrophys. J., 347, 1055-1081 (1989)

[27] Reipurth, B. in *Low Mass Star Formation and Pre-Main-Sequence Objects*, ed. Bo Reipurth, Garching: ESO, 247-279 (1989)

[28] Uchida, Y., & Shibata, K., Publ. Astron. Soc. Japan, 37, 515-535 (1985)

[29] Bell, A. R. & Lucek, S. G., Mon. Not. R. Astr. Soc., 277, 1327-1340 (1995)

[30] Stone, J. M., & Norman, M. L., Astrophys. J., 420, 237-246 (1994)

[31] Ustyugova, G. V., Koldoba, A. V., Romanova, M. M., Chechetkin, V. M. & Lovelace, R. V. E., Astrophys. J. L., 439, L39-L42 (1995)

[32] Stone, J. M., & Norman, M. L., Astrophys. J. S., 80, 753-790 (1992)

[33] Stone, J. M., & Norman, M. L., Astrophys. J. S., 80, 791-818 (1992)

[34] Stahler, S. W., Astrophys. J., 332, 804-825 (1988)

[35] Shapiro, S. L. & Teukolsky, S. A., *Black Holes, White Dwarfs and Neutron Stars-The physics of Compact Objects*, Wiley (1983)

[36] Henriksen, R. N. & Rayburn, D. R., Mon. Not. R. Astr. Soc., 152, 323-332 (1971)

[37] Raga, A. C. & Kofman, L., Astrophys. J., 386, 222-228 (1992)

[38] Chernin, M. L. & Masson, R. C., Astrophys. J., 382, L93-L96 (1991)

[39] Frank, J., King, R. A. & Raine, J. D., *Accretion Power in Astrophysics*, Cambridge University Press (1992)

[40] Lubow, S. H., Papaloizou, J. C. B., & Pringle, J. E., Mon. Not. R. Astr. Soc., 268, 1010-1014 (1994)

[41] Reys-Ruis, M. & Stepinski, T., Astrophys. J., 459, 653-665 (1996)

[42] Clarke, A. D., Norman, L. M. & Burns O. J., Astrophys. J., 311, L63-L67 (1986)

[43] Lind, R. K., Payne, G. D., Meier, L. D. & Blandford, D. R., Astrophys. J., 344, 89-103 (1989)

[44] Eislöffel, J. & Mundt, R., Astr. Astrophys., 284, 530-544 (1994)

[45] Ouyed, R., & Pudritz, R.E., Astrophys. J., 419, 255-267 (1993)

[46] Ouyed, R., & Pudritz, R.E., Astrophys. J., 423, 753-776 (1994)

[47] Rees, M.J., Mon. Not. R. Astr. Soc., 184, 61P-65P (1978)

[48] Calvet, N., Hartmann, L., & Kenyon, J.S., Astrophys. J., 402, 623-634 (1993)

Figure Captions

Figure 1: In all figures, the axis of symmetry is plotted horizontally and the disk surface, vertically. The gas has a polytropic ($\gamma = 5/3$) equation of state. The corona has a turbulent pressure proportional to the thermal pressure. The equilibrium density structure is $\rho \propto (r^2 + z^2)^{-3/4}$. Surfaces of constant magnetic flux are specified by the level surfaces of the scalar function A_ϕ where $\mathbf{B} = \nabla \times (A_\phi \mathbf{e}_\phi)$.

The value of β at the base of the disk's corona falls from the innermost value of unity, to an outermost value (at $20r_i$) of 0.2 for our steady outflow simulation, and 10^{-3} for our episodic model. The remaining parameters are the square of the ratio of the Kepler speed to the sound speed, $\equiv \delta_i$; the ratio of the disk density to the coronal density, $\equiv \eta_i$; and the disk's toroidal to poloidal field ratio, $\equiv \mu_i$. For all Figures, the injection speed is $v_{inj,i}/v_{K,i} = 10^{-3}$; and $(\beta_i, \delta_i, \eta_i, \mu_i)$= (1.0,100.0,100.0,1.0). All the models are run at high spatial resolution of (500 x 200) zones. We use inflow boundary conditions at the disk surface and open outflow conditions (i.e., *zero normal gradient*) on the remaining boundaries (except along the axis of symmetry, coinciding with the disk axis, taken to be reflecting (i.e., *zero normal velocity*)).

Frame 1a. (top). The initial magnetic configuration (left panel) is the current-free "potential field" solution: $A_\phi \propto \left(\sqrt{r^2 + (z_d + z)^2} - (z_d + z)\right)/r$, where z_d is the disk half-thickness. The right panel shows the initial isodensity contours of the corona. Frames b and c show the evolution of the initial magnetic and density structure (the left and right panels respectively) at 100 and 400 inner time units. Frame c shows the

location of the Alfvén critical surface (filled hexagons) and of the FM surface (stars). Frame d compares the Alfvén lever arm r_A/r_o (the footpoint of each field line on the disk is r_o) for each field line in the simulation (filled hexagons), with predictions of steady state theory (squares).

Figure 2: illustration of the structure and dynamics of the outflow for the potential field configuration. Frames 2a & 2b show a snapshot of the flow at 180 inner time units. In frame 2a. the density (upper panel) is compared to the toroidal magnetic field (lower panel). The linear scale, colour palette for all figures, has red as high and blue as low value for all physical quantities. The density is given in units of ρ_i and the velocity in units of $v_{K,i}$ in all colour plots. A tick mark on the r-axis of the upper panel marks a distance of 1 r_i. Frame 2b shows the evolution of the density as compared to the velocity v_z. Note that in all Figs.. there is no outflow on radial scales $< r_i$. This is a consequence of our boundary condition that assumes the absence of a disk inside r_i.

Figure 3: Physical quantities, along the field line whose footpoint is anchored at r_i plotted against $z/r = cotan^{-1}(\upsilon)$ where υ is the polar angle as measured from the origin of the coordinate system. Frame 3a shows the Alfvén Mach numbers m_A and the FM numbers m_F while the ratio of the toroidal to poloidal magnetic field along the field line is shown in Frame 3b: Frame 3c shows the poloidal velocity v_p and the toroidal velocity v_o, in units of the Kepler speed at the footpoint of the field line:

and Frame 3d shows the density ρ in units of the density at the footpoint of the field line. The position of the Alfvén critical point (marked A) and the FM point (marked FM) on the field line are also given. This figure can be compared with the results of Blandford& Payne[17](their Fig. 4).

Figure 4: Snapshots of the jet density at times 100 and 400. The jet is produced in an initially uniform and vertical magnetic field prescribed by the vector potential $A_\phi \propto r$.

Figure 5: Close-up, snapshots of the knot generating region of the outflow at 37.2 and 48.0 inner time units. The density is in the top panel (the tick mark on the r-axis denotes a distance of 1 r_i), and the v_z in the lower panel in each frame. Two knots, denoted A and B, are shown which develop within a background of the faster moving flow. These knots are separated by a region of high toroidal magnetic field strength.

Figure 6: The left panels show the magnetic field structure of the knot generating region, at the three times: 37.2, 42.6, and 48.0 inner time units. The right panels show the angle θ_o of field lines at the base of the flow, with the disk surface, at these times. Note the narrow band of field lines which is sufficiently opened ($\theta_o \leq 60^o$) so as to drive the outflow. Only field lines involved in the knot generation process are shown: field lines at larger disk radius stay reasonably vertical as seen in the right panels.

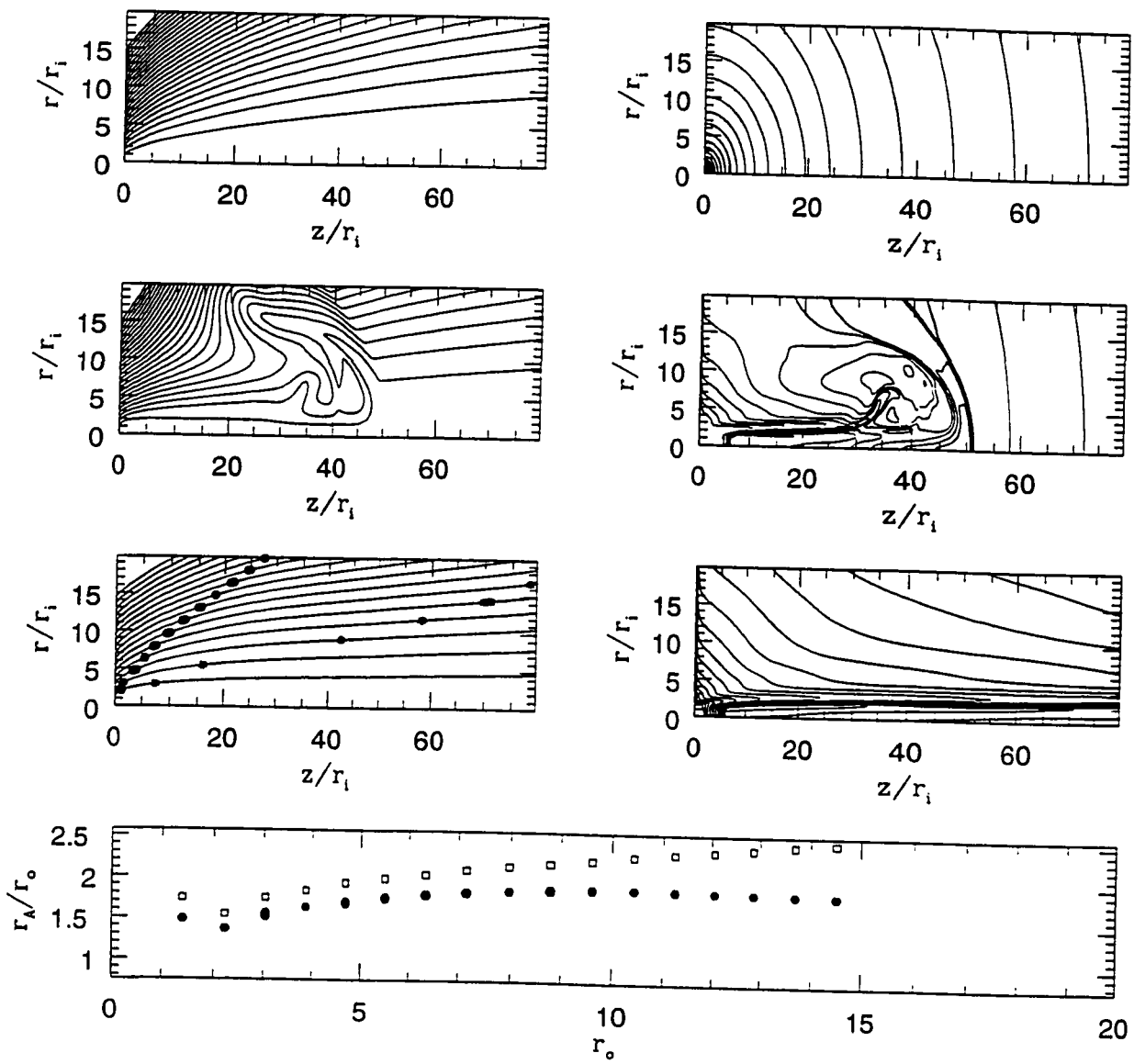

Figure 1.

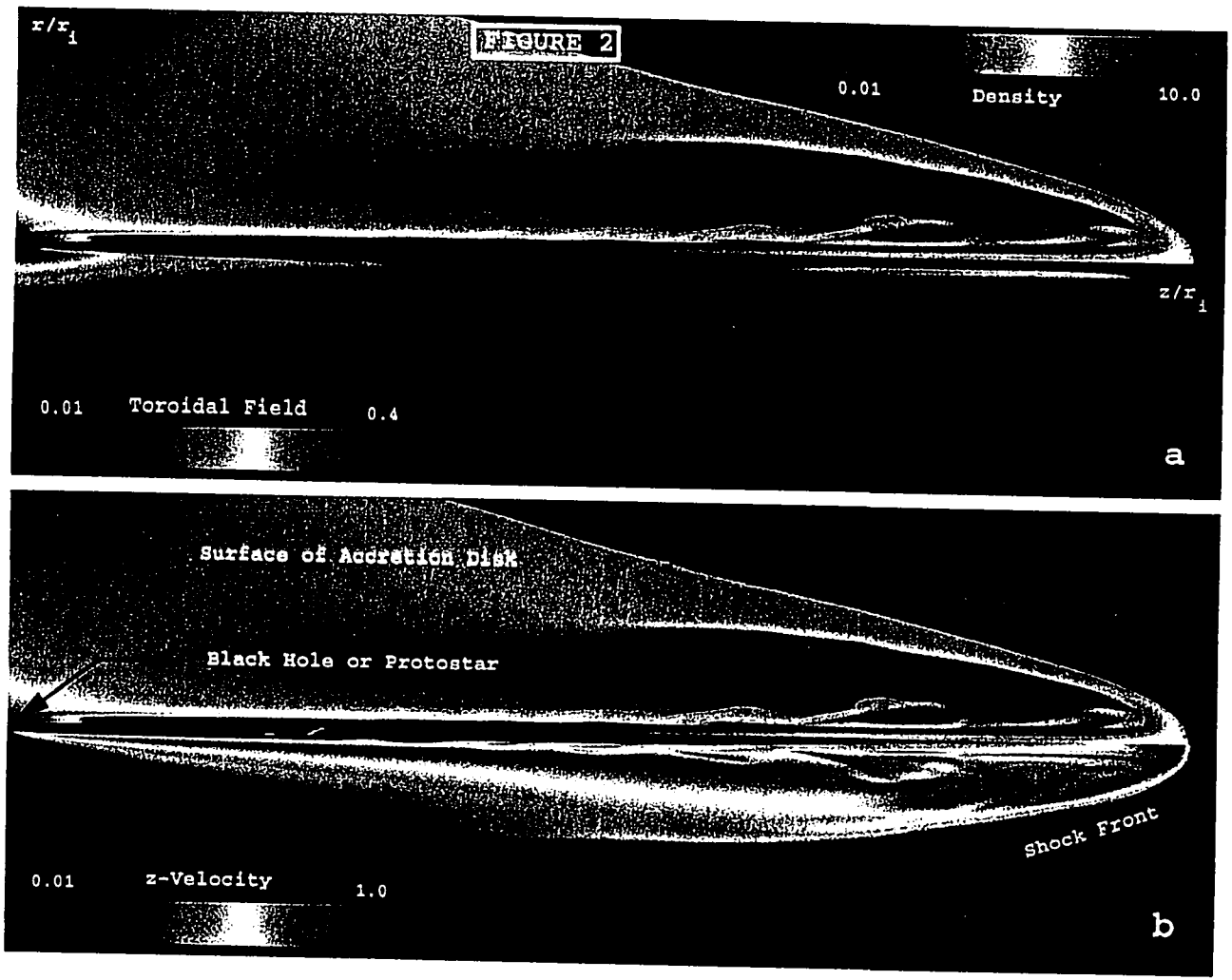
r/r_i
FIGURE 2
0.01
Density
10.0
z/r_i
0.01
Toroidal Field
0.4
a
Surface of Accretion Disk
Black Hole or Protostar
Shock Front
0.01
z-Velocity
1.0
b

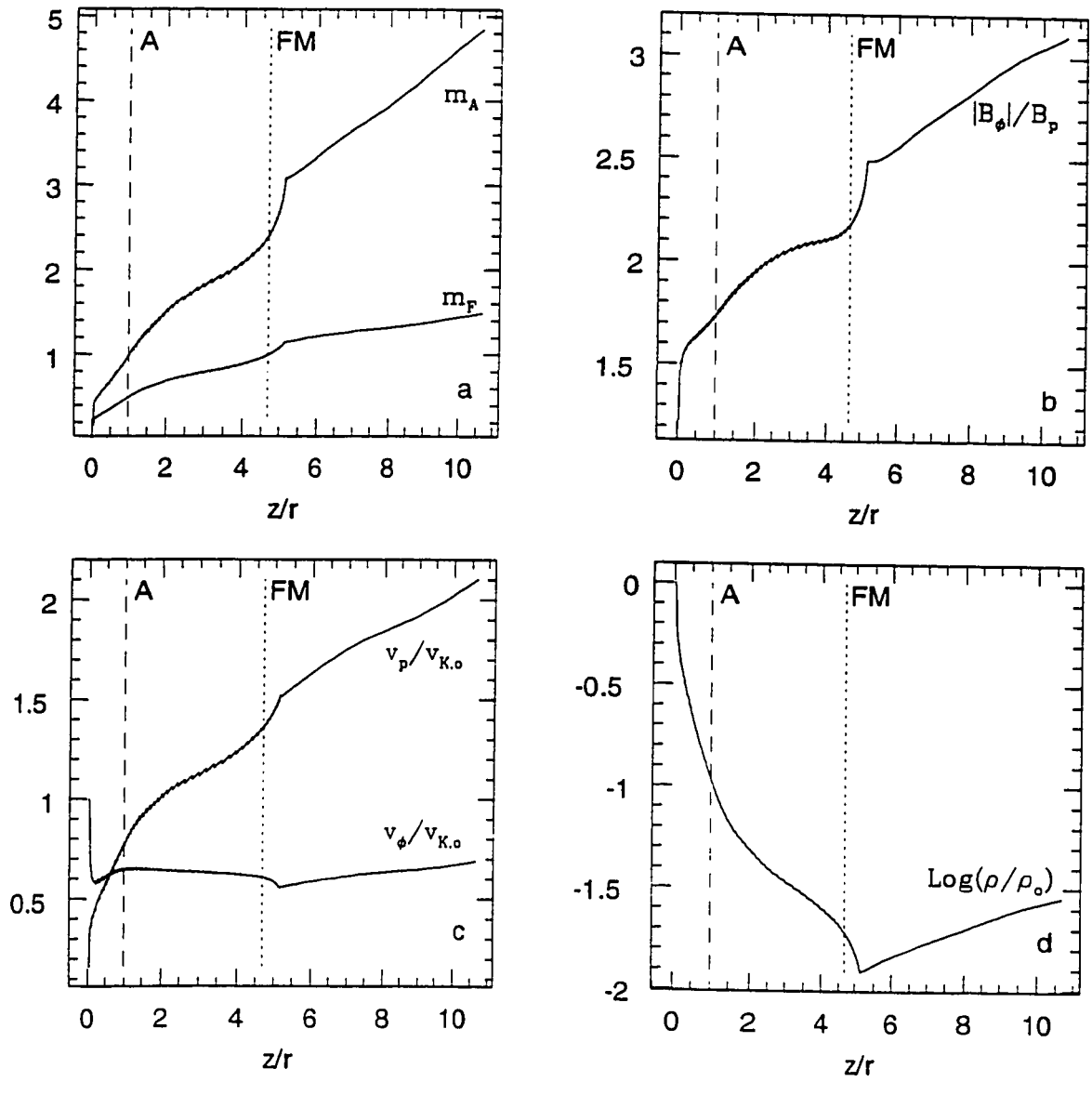

Figure 3.

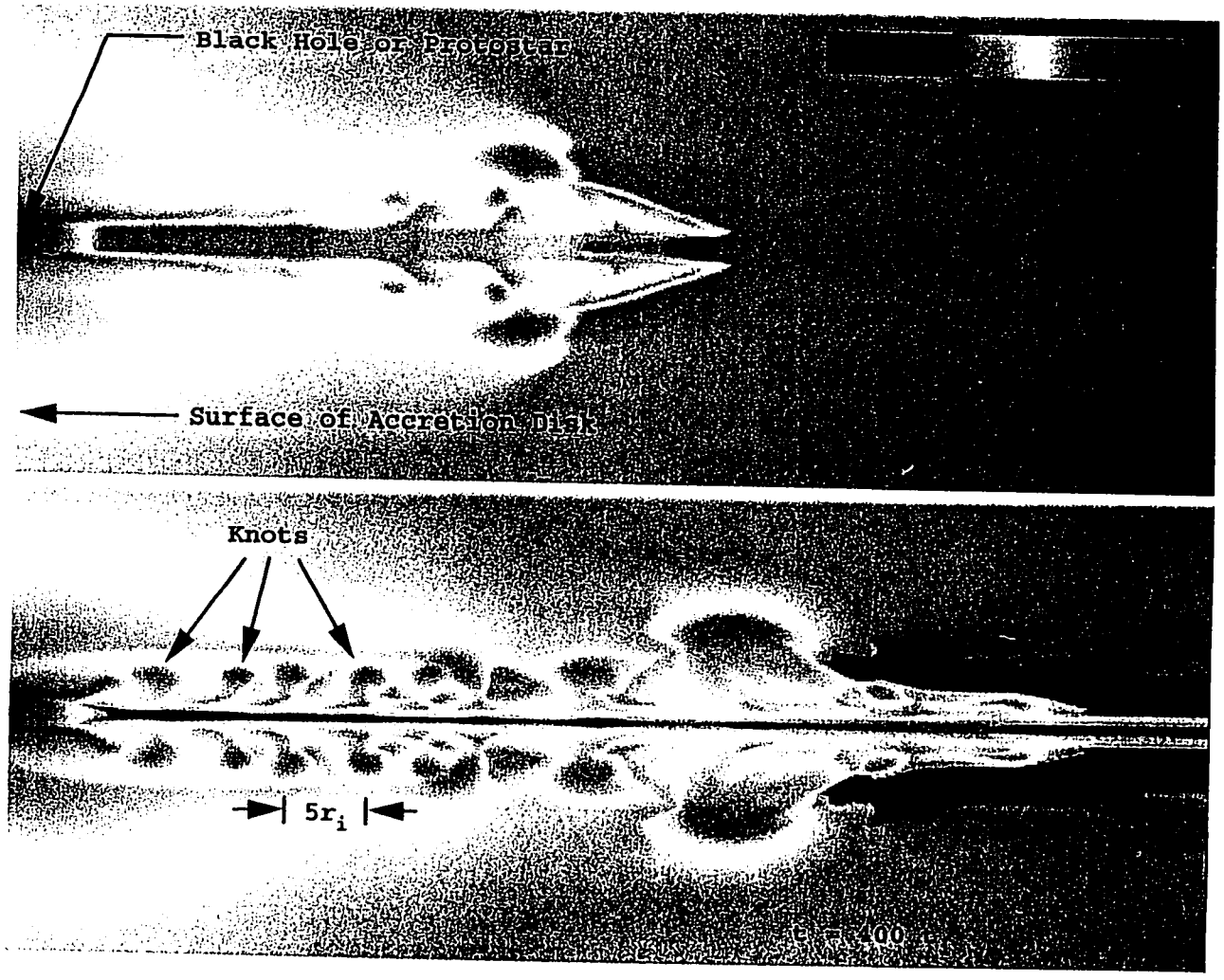
Black Hole or Protostar
Surface of Accretion Disk
Knots
$5r_i$
t = 400

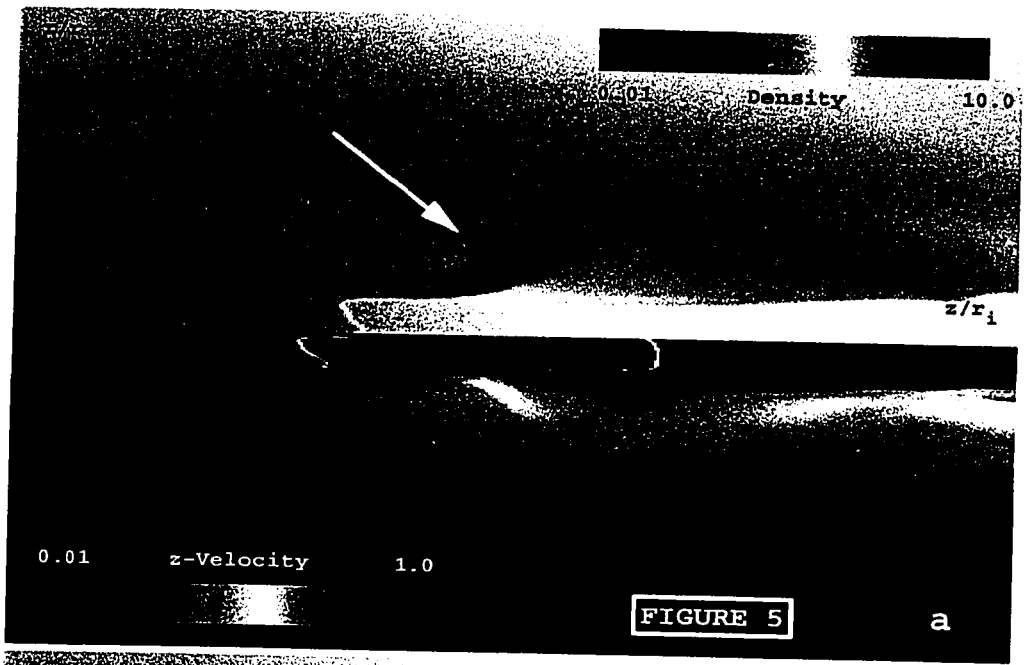
0.01
Density
10.0
z/r_i
0.01
z-Velocity
1.0
a

FIGURE 5

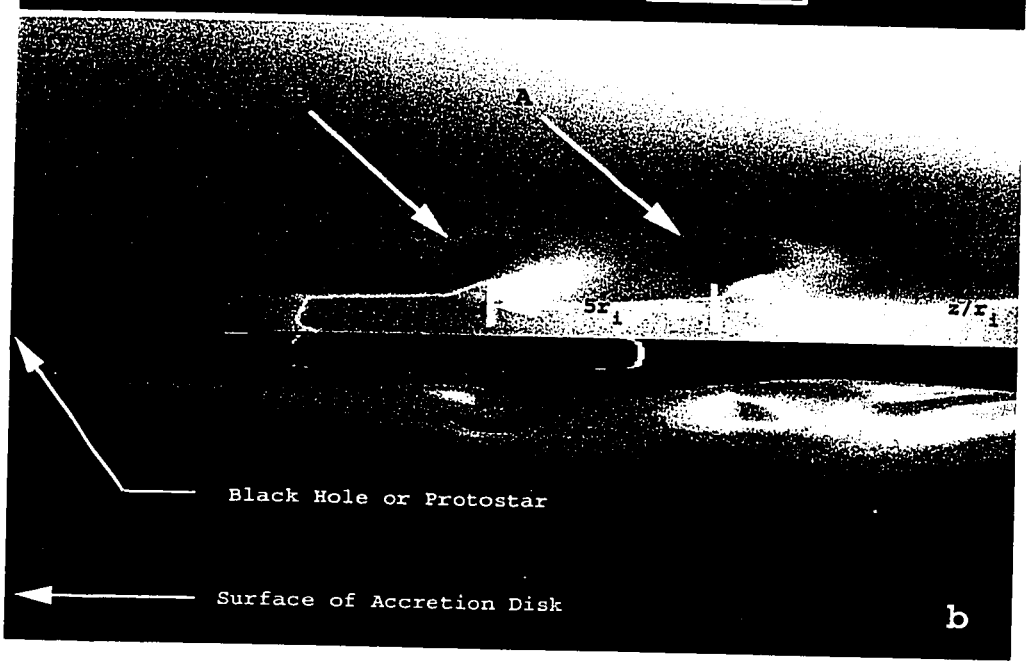
A
$5r_i$
z/r_i
Black Hole or Protostar
Surface of Accretion Disk
b

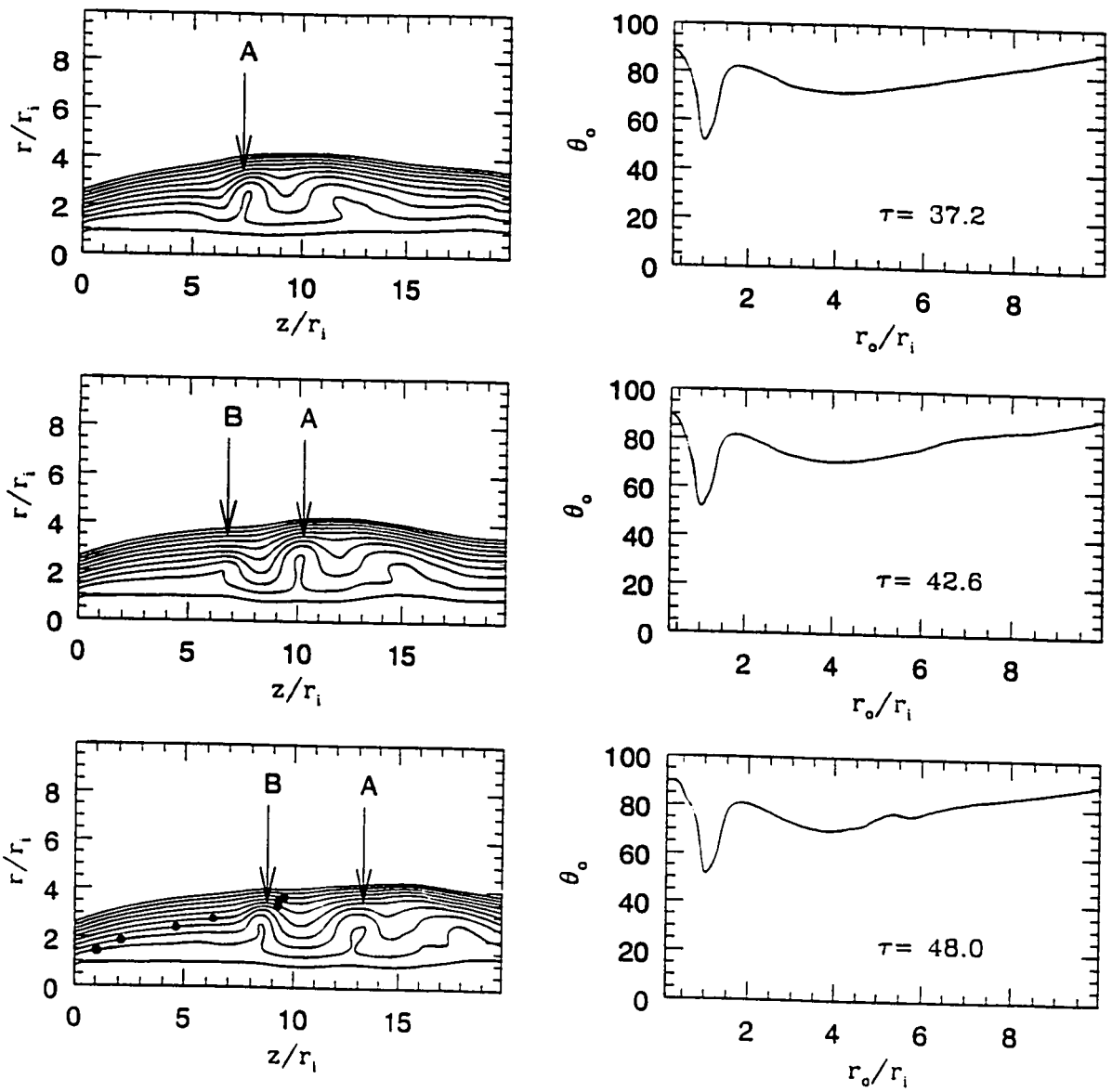

Figure 6.

Appendix A

Difficulty With A Simple Eulerian Algorithm

The problem of advective transport as it rises with the Eulerian algorithm may be looked at in a simple example (Richtmyer & Morton, 1967; Roache, 1972 and Shulz, 1884). Let us consider a model equation

$$\frac{\partial u}{\partial t} + v\frac{\partial u}{\partial x} = 0 \tag{A.1}$$

where u is an arbitrary function of t and x. Equations (2.3) and/or (2.6) have this structure. In Eq. (2.3), u is ρ; while in Eq. (2.6), u is $\mathbf{v}$. We simplified the vectors x into one dimension and taken v to be constant in the equation above. We then readily obtain an analytical solution for $u(x,t)$ as

$$u(x,t) = f(x - vt), \tag{A.2}$$

where f is an arbitrary function (simple wave function). On the other hand, a numerical approximation to Eq. (A.1) may be

$$\frac{u_j^{n+1} - u_j^n}{\Delta t} = -v.\frac{u_{j+1}^n - u_{j-1}^n}{2\Delta x}, \tag{A.3}$$

where Δt and Δx are the time-step and spatial grid step respectively. Equation (A.3) is re-arranged into the form

$$u_j^{n+1} = u_j^n - \frac{v\Delta t}{2\Delta x}(u_{j+1}^n - u_{j-1}^n). \tag{A.4}$$

Now, let u vary like $u_j^n \propto exp[i(kxj - \omega n\Delta t)]$, where x_j is the j-th grid point coordinate $j\Delta x$. From (A.4) we obtain

$$e^{-i\omega\Delta t} = 1 - \frac{v\Delta t}{2\Delta x}(e^{-ik\Delta x} - e^{ik\Delta x}), \tag{A.5}$$

which with, $g \equiv e^{-i\omega\Delta t}$, leads to the amplification factor ($g = u_j^{n+1}/u_j^n$)

$$g = 1 - i\frac{v\Delta t}{\Delta x}sin(k\Delta x). \tag{A.6}$$

The square modulus of Eq. (A.6) is

$$|g|^2 = 1 + (\frac{v\Delta t}{\Delta x})^2 sin^2(k\Delta x) > 1, \tag{A.7}$$

which suggests that such an integration scheme is *always* numerically unstable. This indicates that simple algorithms cannot be used *when advective terms are present in the PDEs*, and one needs to overcome such a difficulty by spatially and temporally averaging the variables involved.

Appendix B

The Method of Characteristics

The summary of the method of characteristics presented in this Appendix is based on the work presented in Landau & Lifshitz (1960) and Kantrowitz & Petsheck (1966) to whom we refer the reader for ample details.

Consider the equation

$$v_t + a(x,t)v_x = 0, \tag{B.1}$$

where $v_t = \partial v/\partial t$ and $v_x = \partial v/\partial x$. Let us search for parametrization curves $x(s)$, $t(s)$ along which v is constant. We have

$$\frac{d}{ds}v(x,t) = v_x\frac{dx}{ds} + v_t\frac{dt}{ds}. \tag{B.2}$$

Thus one should choose

$$\frac{dt}{ds} = 1, \quad \frac{dx}{ds} = a(x,t), \tag{B.3}$$

to get $\frac{d}{ds}v(x,t) = 0$; i.e v is a constant along the curve path s. These curves are the so-called **characteristics**. If initial data are given on a curve C that is transverse to the characteristics (i.e, nowhere tangent to them), then Eq. (B.1) is solved by setting $v(x_0, t_0)$= *the value of the initial data on the curve* C *at the point where* C *intersects the characteristic through* (x_0, t_0). See Figure 1.

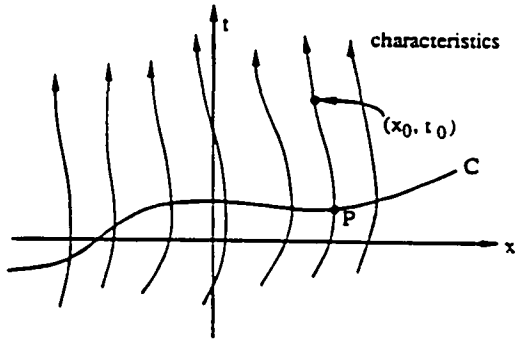

Figure 1. Characteristics in the (x,t) plane. Initial data (information) is given on a curve C and is carried along the characteristics.

Equation (B.1) is a special case of a first-order quasi-linear hyperbolic system in one dimension, i.e, a special case of the system

$$\mathbf{u}_t + A(x,t,\mathbf{u})\mathbf{u}_x = \mathbf{B}(x,t,\mathbf{u}) \tag{B.4}$$

where $\mathbf{u} = \mathbf{u}(x,t)$ is an n-component vector function of x and t, and A is an $n \times n$ matrix function of x, t, $\mathbf{u}$ that has n distinct real eigenvalues and hence n linearly independent eigenvectors (i.e, as a real matrix, A is a diagonalizable). One should think of the MHD equations as an example. In general, then, there are n characteristics through each point and the characteristics depend on $\mathbf{u}$.

While in the simple case of Eq. (B.1) it is the solution itself (here, v) that is constant along the characteristics. it is not always the case. One then needs to solve for the so-called **Riemann invariants** Γ defined as

$$\frac{d\Gamma}{ds} = 0. \tag{B.5}$$

The **method of characteristics** can be summarized as follows; if, by some device, the characteristics can be found, then from (x, t) follow the characteristics back to the curve on which initial data are prescribed to determine the Γ s. Using these values, solve (B.5) for the variables and the result will be the values of the components of $\mathbf{u}$ at (x, t).

Appendix C

Polytropic Changes for a Perfect Gas

A detailed presentation of the following topic can be found in Chandrasekhar (1939) and Clayton (1983). Here, I have only summarized the points of interest to the present work.

Polytropic changes are a generalization of adiabatic changes, in a thermodynamic system. A polytropic change is a quasi-static change carried out in such a way that the derivative

$$c \equiv \frac{dQ}{dT} \tag{C.1}$$

(the "specific heat") varies in a specified way throughout the change.

Let p, V, T be the pressure, volume and temperature of a given mass of fluid. The fluid is said to be perfect gas if (i)

$$pV = (\frac{R}{\mu})T \tag{C.2}$$

and (ii) its internal energy e is a function of its temperature only. In that case all the work done in compressing it at constant temperature is converted into internal energy. If when its volume alters by dV and its temperature by dT, its internal energy alters by de, the quantity of heat communicated dQ is defined by the relation

$$dQ = de + pdV. \tag{C.3}$$

By hypothesis, e is a function of T only, so that

$$de = \frac{de}{dT}dT = c_V dT \tag{C.4}$$

say, where c_V is defined to be the specific heat at constant volume. Combining this with (C.2), one finds

$$dQ = (c_V + \frac{R}{\mu})dT - Vdp \tag{C.5}$$

An **adibatic transformation** is defined by $dQ = 0$, which implies the differential equation

$$\frac{dp}{p} = \frac{(c_V + \frac{R}{\mu})}{c_V}\frac{dV}{V}. \tag{C.6}$$

This is readily integrated to find

$$pV^\gamma = const. \tag{C.7}$$

where

$$\gamma = \frac{(c_V + \frac{R}{\mu})}{c_V} = \frac{c_p}{c_V}. \tag{C.8}$$

On the other hand, a **polytropic transformation** is defined by the condition

$$c \equiv \frac{dQ}{dT} = const. \tag{C.9}$$

Then

$$cdT = c_V dT + pdV. \tag{C.10}$$

In terms of dV and dp this reduces to

$$(c_p - c)pdV + (c_V - c)Vdp = 0. \tag{C.11}$$

Put

$$\gamma' = \frac{c_p - c}{c_V - c}. \tag{C.12}$$

then (D.11) integrates in the form

$$pV^{\gamma'} = const. \tag{C.13}$$

Any sequence of changes of a perfect gas may be described by a curve in the (p, V)-plane. That is, a "Polytrope" is a path of constant heat capacity dQ/dT. It follows that (C.13) is the general equation of polytropes. A polytrope is an adiabatic in the particular case $c = 0$.

Appendix D

Shocks under Polytropic Changes

In this Appendix, I give the reader a brief introduction to the notion of shocks and discontinuities as presented in Landau & Lifshitz (1960) and Liberman & Velikovich (1986).

Let us first illustrate the notion of discontinuity by integrating equations (2.3)-(2.7) over a small box (Figure 1). In the limit where the volume goes to zero (discontinuity), only gradient terms (∇) remain since they are infinite (it is important to understand that no physical quantity (here, Q) becomes infinite at the discontinuity; only their gradients). That is, one ends up with

$$\int_{Volume} \nabla(Q).\mathbf{dV} = 0. \tag{D.1}$$

Using Gauss's theorem, it follows that the normal component of the quantity Q is

conserved through the discontinuity. Indeed, (D.1) can be written as

$$\int_{\mathbf{Surface}} \mathbf{Q}.\mathbf{dS} = 0 \tag{D.2}$$

or

$$\int_{S_1} \mathbf{Q_1}.\mathbf{dS_1} + \int_{S_2} \mathbf{Q_2}.\mathbf{dS_2} = 0 \tag{D.3}$$

and since $\mathbf{dS_1} = -\mathbf{dS_2}$, this becomes

$$\mathbf{Q_{n1}} - \mathbf{Q_{n2}} = 0 \tag{D.4}$$

$\mathbf{n}$ being the normal vector to the shock front. It is standard to define $[\mathbf{Q}]$ as the jump of the quantity Q across the discontinuity so that (D.3) is generally written as

$$[\mathbf{Q}] = 0 \tag{D.5}$$

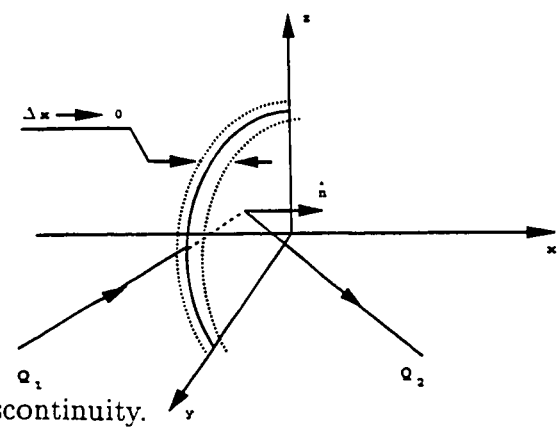

Figure 1. Illustration of a discontinuity.

The integration of the system of equations (2.3)-(2.7) is only possible by matching the independent variables (appearing only in the derivatives) on both sides of the characteristic surface. Hence, one models the shock front mathematically by a plane

discontinuity , and the two states that it separates are taken to be uniform (i.e the MHD approximation holds behind the shock front as well).

The Rankine-Hugoniot relations connect two different states of a gas separated by a discontinuity. It is convenient to pick a coordinate system whose velocity at some fixed time, say t_0, equals that of the discontinuity. In such a frame these relations are (ignoring the magnetic forces for simplification purposes),

$$\rho_0 u_0 = \rho_1 u_1, \tag{D.6}$$

$$\rho_0 u_0^2 + p_0 = \rho_1 u_1^2 + p_1, \tag{D.7}$$

$$(e_0\rho_0 + \frac{1}{2}\rho_0 u_0^2 + p_0)u_0 = (e_1\rho_1 + \frac{1}{2}\rho_1 u_1^2 + p_1)u_1, \tag{D.8}$$

where the subscripts indicate the different sides (0) or (1) of the discontinuity.

Let $M = \rho_0 u_0 = \rho_1 u_1$. If $M = 0$ we call the discontinuity **contact discontinuity** or a **slip line**. Since $u_0 = u_1 = 0$, these discontinuities move with the fluid. From (D.7), $p_0 = p_1$, but in general $\rho_0 \neq \rho_1$.

If $M \neq 0$, we call the discontinuity a **shock**. Since $u_0 \neq 0$, $u_1 \neq 0$, gas is crossing the shock, or equivalently, the shock is moving through the gas. The side that consists of gas that has not crossed the shock is called the **front** of the shock and it is identified by 0. The other side, denoted by subscript 1, is called the **back**.

It is easy to combine the equations above to get

$$(e_1 - e_0) + \frac{p_0 + p_1}{2}(\tau_1 - \tau_0) = H(\tau, p) = 0 \tag{D.9}$$

to obtain the so-called **Hugoniot equation** for the shock. Here, $\tau = 1/\rho$. In our case, since we are dealing with an ideal gas, then $e = \frac{1}{\gamma-1}p\tau$ and the Hugoniot equation becomes

$$(\tau - \mu^2\tau_0)p - (\tau_0 - \mu^2\tau)p_0 = 0, \tag{D.10}$$

where $\mu^2 = \frac{\gamma-1}{\gamma+1}$. In our case then, the Hugoniot curve $H(\tau, p) = 0$ is the hyperbola shown in Figure 2. Equation above states that (τ_1, p_1) lies on this hyperbola. The hyperbola represents all possible states that can be connected to the initial state (τ_0, p_0).

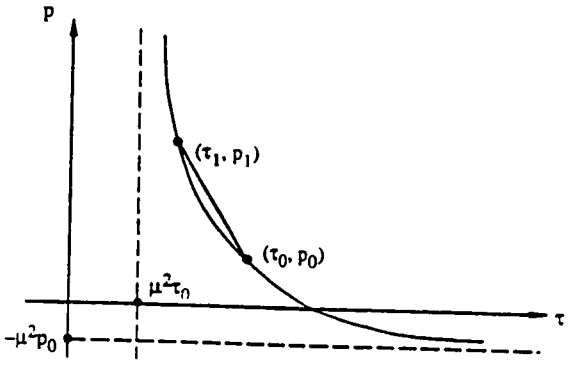

Figure 2. The Hugoniot Curve. The hyperbola represents all possible states that can be connected to the initial state (τ_0, p_0) through a shock.

Now, by assuming a polytropic change, that is, by not solving the energy equation we are using a peudo Hugoniot equation which is simply

$$p\tau^\gamma = p_0\tau_0^\gamma, \tag{D.11}$$

which is different from (D.10). That is, our shocks violate the energy conservation, except if one can find a sink for the energy. We showed that radiation from the

forbidden-line emission detected in jets is a plausible candidate (Ouyed& Pudritz 1994).

2. Entropy Principle

The entropy follows from equation (D.1) and is

$$dS = \frac{dQ}{T} = c\frac{dT}{T} \tag{D.12}$$

This proves that unlike adiabatic ($dQ = 0$) and isothermal ($dT = 0$) changes, polytropic changes allow shocks to occur without violating the entropy principle, namely that entropy must increase across a shock. This is further confirmed from Figure 2. Indeed, the curve $H(\tau, p) = 0$ through (τ_0, p_0) is drawn as well as the curves $p\rho^{-\gamma} = const$; one sees that $p\rho^{-\gamma}$ increases as one moves along $H(\tau, p) = 0$ in the direction of increasing p (or entropy), as required by the second law of thermodynamics.

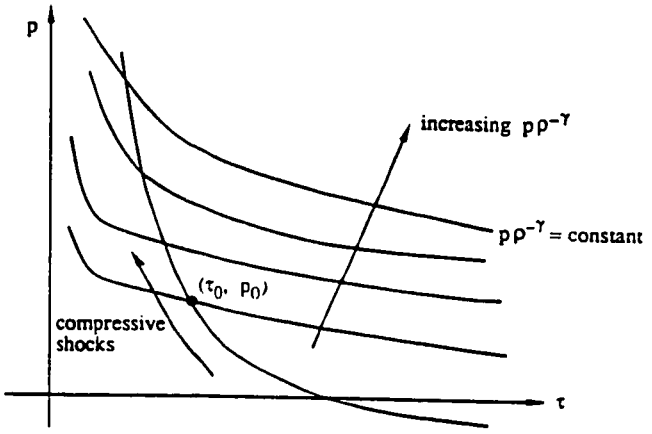

Figure 3. Geometric entropy condition.

Appendix E

Numerical Set Up Of The Initial Magnetic Configuration

```
#include "zeus2d.def"
c=======================================================================
c//////////////////////  SUBROUTINE magnetic\\\\\\\\\\\\\\\\\\\\\\\\\\
c
      subroutine magnetic(configuration)
c
c     written by: Rachid OUYED
c
c     PURPOSE:
c
c      This subroutine is called by the user's supplied PROBLEM.
c      Estimates the magnetic field components from a potential
c      field Aphi Equations (2.38) and (2.39)).
c      Aphi is located at the zone corners, and requires an extra
c      zone and an extra row to be fully defined. Other magnetic
c      configurations could easily be added here as long as one
c      defines the appropriate parameters.
c
c-----------------------------------------------------------------------
      implicit NONE
#include "param.h"
#include "grid.h"
#include "field.h"
#include "root.h"
#include "scratch.h"
#include "bndry.h"
#include "gravity.h"
```

```
      integer i,j,configuration
      real aphi(in+1,jn+1)
      real deltai,betai,caphi  ! Our Parameters (Refer to Chapter 3)
      real  x1aiep3, x2ajep3, dvl2ajep3, dvl1aiep3
      common/parameters/betai,deltai,etai,mui
c//////////////////////////////////////////////////////////////////////
c  Compute constants needed: betai,deltai,etai,mui are passed from
c  the user's supplied PROBLEM.
       caphi = sqrt(1.0/deltai/betai/2.0) ! The constant defining Aphi
c//////////////////////////////////////////////////////////////////////
c       Now we add the extra row (x2a(je+3)=x2ajep3) and
c       the extra column (x1a(ie+3)=x1aiep3), needed to
c       compute Aphi everywhere.
        x1aiep3 = x1a(ie+2) + dx1a(ie+2)
        x2ajep3 = x2a(je+2) + dx2a(je+2)
c
c       We also need the volume difference elements
c       dvl2a(je+3)=dvl2ajep3 and dvl1a(ie+3)=dvl1aiep3
c
        dvl2ajep3 = 0.5*x2ajep3**2.0 - 0.5*x2a(je+2)**2.0
        dvl1aiep3 = x1aiep3 - x1a(ie+2)
c\\\\\\\\\\\\\\\\\\\\\\\\\\\\\\\\\\\\\\\\\\\\\\\\\\\\\\\\\\\\\\\\\\\\\\\\\\\\
c       The two different vector potentials we are studying are defined
c       by the parameter ''configuration'' which is directly passed from
c       user's supplied PROBLEM.
c       (configuration is an integer read by PROBLEM from the input deck
c        z2dinput)
c//////////////////////////////////////////////////////////////////////
c.....................................................................
        if (configuration.eq.1) then  ! Vertical Configuration (Chapter 4).
        do 10 i=is-2,ie+2
        do 20 j=js-2,je+2
                aphi(i   ,j   ) =  caphi*x2a(j)
                aphi(ie+3,j   ) =  caphi*x2a(j)
20      continue
aphi(i   ,je+3) =  caphi*x2ajep3
10      continue
aphi(ie+3,je+3) =  caphi*x2ajep3
        endif
c.....................................................................
        if (configuration.eq.2) then   ! Potential field (aphi = r*aphi)
```

```
                                          ! (Chapter 3).
      do 30 i=is-2,ie+2
      do 40 j=js-2,je+2
        aphi(i   ,j   ) = caphi*(sqrt(x2a(j)**2.0+(x1a(is+3)+x1a(i))**2.0)
     &                     - (x1a(is+3)+x1a(i)))
        aphi(ie+3,j   ) = caphi*(sqrt(x2a(j)**2.0+(x1a(is+3)+x1aiep3)**2.0)
     &                     - (x1a(is+3)+x1aiep3))
40      continue
aphi(i   ,je+3) = caphi*(sqrt(x2ajep3**2.0+(x1a(is+3)+x1a(i))**2.0)
     &                     - (x1a(is+3)+x1a(i)))
50      continue
aphi(ie+3,je+3) = caphi*(sqrt(x2ajep3**2.0+(x1a(is+3)+x1aiep3)**2.0)
     &                     - (x1a(is+3)+x1aiep3))
c////////////////////////////////////////////////////////////////////////
c       The magnetic field components:
c
c b1(i,j) for the axial component (Bz)
c b2(i,j) for the radial component (Br)
c
c  are then estimated as
c\\\\\\\\\\\\\\\\\\\\\\\\\\\\\\\\\\\\\\\\\\\\\\\\\\\\\\\\\\\\\\\\\\\\\\\\\\\\
        if (configuration.eq.1) then    ! directly from Aphi
      do 60 i=is-1,ie+1
      do 70 j=js  ,je+1
          b1(i   ,j   ) = (g32a(j+1)*aphi(i,j+1)
     &                     - g32a(j  )*aphi(i,j  ))/(g2a(i)*dvl2a(j))
70    continue
          b1(i   ,je+2) = (x2ajep3*aphi(i,je+3)
     &                     - g32a(je+2)*aphi(i,je+2))/(g2a(i)*extradvl2a)
60      continue
      do 80 j=js+1,je+1
      do 90 i=is-2,ie+1
          b2(i   ,j   ) = -(g2a(i+1)*g31a(i+1)*aphi(i+1,j)
     &                     - g2a(i  )*g31a(i  )*aphi(i  ,j))/dvl1a(i)
90    continue
          b2(ie+2,j   ) = -(aphi(ie+3,j)
     &                     -aphi(ie+2,j))/extradvl1a
80    continue
c.....................................................................
        else                        ! from phi=const (Aphi = r Aphi)
      do 100 i=is-1,ie+2
```

```
      do 110 j=js  ,je+1
         b1(i   ,j   ) = (aphi(i,j+1)
     &                    - aphi(i,j  ))/(g2a(i)*dvl2a(j))
110    continue
         b1(i   ,je+2) = (aphi(i,je+3)
     &                    - aphi(i,je+2))/(g2a(i)*extradvl2a)
100     continue
      do 120 j=js+1,je+2
      do 130 i=is-2,ie+1
         b2(i   ,j   ) = -(g2a(i+1)*g31a(i+1)*aphi(i+1,j)
     &                     -g2a(i  )*g31a(i  )*aphi(i  ,j))/dvl1a(i)
     &                     /x2a(j)
130    continue
         b2(ie+2,j   ) = -(aphi(ie+3,j)
     &                     -aphi(ie+2,j))/extradvl1a
     &                     /x2a(j)
120   continue
      endif
c.....................................................................
c       Now because of the axisymmetry we set
c.....................................................................
      do i=is-1,ie+2
              b1(i,js-1)   =   b1(i,js  )
              b1(i,js-2)   =   b1(i,js+1)
      enddo
      do i=is-2,ie+2
              b2(i,js  )   =   0.0
              b2(i,js-1)   =   -b2(i,js+1)
      enddo
c//////////////////////////////////////////////////////////////////////
c       Checking the initial divB = 0 constraint
c---------------------------------------------------------------------
      do 1010 i=is-1,ie+1
      do 1000 j=js-1,je+1
       divb(i,j) = (g2a(i+1)*g31a(i+1)*b1(i+1,j)
     &              -g2a(i  )*g31a(i  )*b1(i  ,j))/dvl1a(i)
     &              + (g32a(j+1)*b2(i,j+1)
     &              -g32a(j  )*b2(i,j  ))/(g2b(i)*dvl2a(j))
1000  continue
1010  continue
c\\\\\\\\\\\\\\\\\\\\\\\\\\\\\\\\\\\\\\\\\\\\\\\\\\\\\\\\\\\\\\\\\\\\\\\\
```

```
      endif
    return
    end
```

Appendix F

The Momentum Equation For Polytropes

```
#include "zeus2d.def"
c=======================================================================
c//////////////////////////  SUBROUTINE NEWSTV1  \\\\\\\\\\\\\\\\\\\\\\\\\
c
      subroutine newstv1(j,st1)
c///////////////////////////////////////////////////////////////////////
c
c       Written By Rachid Ouyed
c       Based on stv1.src in ZEUS-2D
c
c       PURPOSE: Calculates the source terms in the equation of motion
c for v1 over the entire grid (a similar subroutine is written for v2).
c This the finite-difference approach to the analytical solution
c of the hydro-dynamic balance of polytropic gas as given by equation
c (3.21) in Chapter 3.
c
c Note that, while in the original version of the code, the ptmass
c gravitational potential is defined by the central object located
c at the origin (r=0,z=0; for izero = is), here, we have defined the
c       point mass gravitational potential at zone centers as:
c
c       grav(i,j) = 1/sqrt(r^2 + z^2)
c
c We find that accuracy is improved this way.
c
c       This shouldn't be confused with self-gravity phi(i,j) as generated
c       by the Poisson solver in the code.
c\\\\\\\\\\\\\\\\\\\\\\\\\\\\\\\\\\\\\\\\\\\\\\\\\\\\\\\\\\\\\\\\\\\\\\\\\\
c       Note that only source terms due to "real physics" are included here.
```

```
c       Source terms due to artificial viscosity are in the routine VISCUS.
c
c       INPUT ARGUMENTS:
c       j  = index of j sweep
c       OUTPUT ARGUMENTS:
c       st1 = array of source terms at interfaces along 1-direction
c       EXTERNALS: [none]
c       LOCALS:
c       rhoi = inverse density at interface in 1-direction
c-----------------------------------------------------------------------
      implicit NONE
#include "param.h"
#include "grid.h"
#include "field.h"
#include "gravity.h"
#include "root.h"

      integer  i,j
      real st1(ijn),grav(in,jn)
      real     rhoi,r2i,j2
c=======================================================================
      do 10 i=iip1(j),io(j)
        rhoi = 2.0/(d(i-1,j) + d(i,j))
grav(i,j) = - 1.0 / sqrt(x2b(j)**2.0 + x1b(i)**2.0)
        st1(i) = - (d(i,j)**(gamma-1.) - d(i-1,j)**(gamma-1.))*dx1bi(i)
     &           - (  grav(i,j)         -  grav(i-1,j)       )*dx1bi(i)
#ifdef GRAV
        st1(i) = st1(i) + (phi(i,j) - phi(i-1,j))*dx1bi(i)
#endif
        st1(i) = st1(i) +
     &        (0.25*( v2(i  ,j) + v2(i  ,j+1)
     &              + v2(i-1,j) + v2(i-1,j+1) ))**2*dg2ad1(i)/g2a(i)
#ifdef ROTATE
        st1(i)= st1(i) + (0.5*(v3(i,j)+v3(i-1,j)))**2*dg31ad1(i)/g31a(i)
#endif
#ifdef MHD
        j2 = -(g31b(i  )*b3(i  ,j)-g31b(i-1)*b3(i-1,j))*dx1bi(i)/g31a(i)
        st1(i) = st1(i) + rhoi*(0.5*(b3(i,j) + b3(i-1,j))*j2
     &   -0.5*((g2b(i)*b2(i,j+1)-g2b(i-1)*b2(i-1,j+1))/(g2a(i)*dx1b(i))
     &        +(g2b(i)*b2(i,j  )-g2b(i-1)*b2(i-1,j  ))/(g2a(i)*dx1b(i)))
     &          *0.25*(b2(i,j) + b2(i,j+1) + b2(i-1,j) + b2(i-1,j+1)))
```

```
#endif
10    continue
c=======================================================================
      return
      end
```

Appendix G

Physical Quantities Along A Contour Line

```
C//////////////////////////////////////////////////////////////////////////
C.........................................................................
        SUBROUTINE drlin3 (Z,L,MM,NN,filename)
C
C PURPOSE:
C
C THIS SUBROUTINE IS AN EXTENSION OF drlin3 WHICH CAN BE FOUND IN
C uconxy.src IN ../src DIRECTORY (THE ORIGINAL drlin3 TRACES
C A CONTOUR LINE WHEN GIVEN THE BEGINNING
C BY stlin3).
C
C       WE HAVE EXTENDED THE ROUTINE INTO FINDING AND WRITTING OUT
C THE VALUES OF ANY VARIABLE ALONG ANY GIVEN CONTOUR.
C HERE, WE SHOW HOW IT IS DONE FOR EXTRACTING QUANTITIES ALONG
C MAGNETIC FIELD LINES.
C
C NOTE THAT ''filename'' IS NOW PASSED AS A PARAMETER.
C.........................................................................
#include "common.h"
      SAVE
      DIMENSION       Z(L,NN)
      INTEGER CONNUM
      COMMON /CONRE2/ IX          ,IY          ,IDX         ,IDY         ,
     1                IS          ,ISS         ,NP          ,CV          ,
     2                INX(8)      ,INY(8)      ,IR(5000)    ,NR
      COMMON /CONRE1/ IOFFP       ,SPVAL
      COMMON /CONRE3/ IXBITS      ,IYBITS
```

```
      COMMON /OUYED/ CONNUM
      LOGICAL         IPEN        ,IPENO

      integer iouyed,jmonger,icontour,kunit
      character*11 hdfstore
      character*8 filename
      integer ord
      data icontour/1/
      DATA IPEN,IPENO/.TRUE.,.TRUE./

      IXYPAK(IXX,IYY) = ISHIFT(IXX,IYBITS)+IYY
      C(P1,P2) = (P1-CV)/(P1-P2)
C
C
      M = MM
      N = NN
      IF (IOFFP .EQ. 0) GO TO 101
      ASSIGN 110 TO JUMP1
      ASSIGN 115 TO JUMP2
      GO TO 102
  101 ASSIGN 112 TO JUMP1
      ASSIGN 117 TO JUMP2
  102 IXO = IX
      IYO = IY
      ISO = IS
      IF (IOFFP .EQ. 0) GO TO 103
      IX2 = IX+INX(IS)
      IY2 = IY+INY(IS)
      IPEN = Z(IX,IY).NE.SPVAL .AND. Z(IX2,IY2).NE.SPVAL
      IPENO = IPEN
  103 IF (IDX .EQ. 0) GO TO 104
      Y = IY
      ISUB = IX+IDX
      X = C(Z(IX,IY),Z(ISUB,IY))*FLOAT(IDX)+FLOAT(IX)
      GO TO 105
  104 X = IX
      ISUB = IY+IDY
      Y = C(Z(IX,IY),Z(IX,ISUB))*FLOAT(IDY)+FLOAT(IY)
  105 CALL FRSTD (fxxy(X,Y),fyxy(X,Y))
C
C HERE, IF THE CONTOURS TO BE PLOTTED ARE THE
```

```
C MAGNETIC FIELD LINES, THEN EXTRACT THE
C DESIRED PHYSICAL QUANTITIES.
C
      if ((z(x,y).eq.b(x,y)).and.(icontour.eq.1)) then
      read(filename,44) ord
 44   format('hdf',i3.3,'aa')
      write(hdstore,45) ord,icontour
 45   format('b',i3.3,'.',i3.3)
      kunit    = icontour*100
      open(kunit,file=hdfstore,status="unknown")
      write(kunit,2100)'#i','j','z(r0)','r(r0)','vphi','v2','v1','b3'
     &                    ,'b2','b1','ma','mf','d'
2100  FORMAT(a2,4x,a2,4x,a5,4x,a5,4x,a5,4x,a5,4x,a5,4x,a5,4x,a5,4x,a5
     &       ,4x,a5,4x,a5,4x,a5,4x,a5)
      endif

  106 IS = IS+1
      IF (IS .GT. 8) IS = IS-8
      IDX = INX(IS)
      IDY = INY(IS)
      IX2 = IX+IDX
      IY2 = IY+IDY
      IF (ISS .NE. 0) GO TO 107
      IF (IX2.GT.M .OR. IY2.GT.N .OR. IX2.LT.1 .OR. IY2.LT.1) GO TO 120
  107 IF (CV-Z(IX2,IY2)) 108,108,109
  108 IS = IS+4
      IX = IX2
      IY = IY2
      GO TO 106
  109 IF (IS/2*2 .EQ. IS) GO TO 106
      GO TO JUMP1,(110,112)
  110 ISBIG = IS+(8-IS)/6*8
      IX3 = IX+INX(ISBIG-1)
      IY3 = IY+INY(ISBIG-1)
      IX4 = IX+INX(ISBIG-2)
      IY4 = IY+INY(ISBIG-2)
      IPENO = IPEN
      IF (ISS .NE. 0) GO TO 111
      IF (IX3.GT.M .OR. IY3.GT.N .OR. IX3.LT.1 .OR. IY3.LT.1) GO TO 120
      IF (IX4.GT.M .OR. IY4.GT.N .OR. IX4.LT.1 .OR. IY4.LT.1) GO TO 120
  111 IPEN = Z(IX,IY).NE.SPVAL .AND. Z(IX2,IY2).NE.SPVAL .AND.
```

```
     1       Z(IX3,IY3).NE.SPVAL .AND. Z(IX4,IY4).NE.SPVAL
  112 IF (IDX .EQ. 0) GO TO 113
      Y = IY
      ISUB = IX+IDX
      X = C(Z(IX,IY),Z(ISUB,IY))*FLOAT(IDX)+FLOAT(IX)
      GO TO 114
  113 X = IX
      ISUB = IY+IDY
      Y = C(Z(IX,IY),Z(IX,ISUB))*FLOAT(IDY)+FLOAT(IY)
  114 GO TO JUMP2,(115,117)
  115 IF (.NOT.IPEN) GO TO 118
      IF (IPENO) GO TO 116
C
C END OF LINE SEGMENT
C
      CALL LASTD
      CALL FRSTD (fxxy(XOLD,YOLD),fyxy(XOLD,YOLD))
C
C CONTINUE LINE SEGMENT
C
  116 CONTINUE
  117 CALL VECTD (fxxy(X,Y),fyxy(X,Y))
C
C HERE THE DESIRED VARIABLES ARE BEING EXTRACTED.
C
      YOLD = Y
      if (z(x,y).eq.b(x,y)) then
      iouyed=x
      jmonger=y
      write(kunit,2000) iouyed,jmonger,fxxy(XOLD,YOLD),fyxy(XOLD,YOLD),
     &        v3(iouyed,jmonger),v2(iouyed,jmonger),v1(iouyed,jmonger),
     &        b3(iouyed,jmonger),b2(iouyed,jmonger),b1(iouyed,jmonger),
     &        ma(iouyed,jmonger),mf(iouyed,jmonger),d(iouyed,jmonger)
       endif
2000  FORMAT(I3,2x,I3,2x,11F15.11)

      IF (IS .NE. 1) GO TO 119
      NP = NP+1
      IF (NP .GT. NR) GO TO 120
      IR(NP) = IXYPAK(IX,IY)
  119 IF (ISS .EQ. 0) GO TO 106
```

```
      IF (IX.NE.IX0 .OR. IY.NE.IY0 .OR. IS.NE.IS0) GO TO 106
C END OF LINE
C
  120 CALL LASTD
C
C HERE WE GO ON INTO THE NEXT CONTOUR.
C NOTE: WE HAVE DEFINED THE NUMBER OF CONTOURS
C IN THE SUBROUTINE con.src in ../src.
C
      if ((z(x,y).eq.b(x,y)))
     &   icontour=icontour+1
        close(kunit)
      RETURN
      END
```

Appendix H

SM Routine

```
#////////////////////////////////////////////////////////////////////////
# Written by Rachid OUYED
#////////////////////////////////////////////////////////////////////////
# This supermongo macro computes the parameters $k$
# and $1$ (Blandford and Payne Parameters, see Chapter 3)
# along a given field line (contour line).
# It also looks for the Alfven and FM
# points along that same field line, and then displays
# the location on the screen (see Figure 7 in Chapter 3).
# The data is read in from the file generated by the
# subroutine presented in the previous Appendix G.
# The three unknowns are
# $1= the variable (here b),
#        $2= the file,
#                $3 = the contour number.
#-----------------------------------------------------------------------
figure5 3
        erase
        window 1 2 1 2
        data $1$2"."$3
        read z 3
        read r 4
        read v3 5
        read v2 6
        read v1 7
        read b3 8
        read b2 9
        read b1 10
        read d 13
```

```
        read ma 11
        read mf 12
        set zr = z/r
        set k  = d*v1/b1
        limits zr k
        box
        ltype 0
        connect zr k
#-----------------------------------------------------------------------
# Now, we start looking for the Alfven and FM points. This is done
# one contour line at a time. For a given contour line we increment
# by one (''inca'' for an Alfven point and ''incf'' for an FM point)
# everytime a critical point is found.
#-----------------------------------------------------------------------
        set dimen(ra) = dimen(r)
        set dimen(za) = dimen(z)
        set dimen(rf) = dimen(r)
        set dimen(zra) = dimen(zr)
        set dimen(zrf) = dimen(zr)
        define inca 0
        define incf 0
        do i = 0,(dimen(d)-1){
        if (ma[$i]>1.0 && ma[($i+1)]<1.00){
        set zra[$inca] = zr[$i]
        set ra[$inca] = r[$i]
        set za[$inca] = z[$i]
        define inca ($inca +1)
        }
        if (mf[$i]>1.0 && mf[($i+1)]<1.00){
        set zrf[$incf] = zr[$i]
        set rf[$incf] = r[$i]
        define incf ($incf +1)
        }
        set dimen(rra)= $inca
        set dimen(zza)= $inca
        set dimen(rrf)= $incf
        set dimen(zzra)= $inca
        set dimen(zzrf)= $incf
        }
        do i=0,($inca-1){
        set zzra[$i] = zra[$i]
```

```
        set rra[$i] = ra[$i]
        set zza[$i] = za[$i]
        }
        do i=0,($incf-1){
        set zzrf[$i] = zrf[$i]
        set rrf[$i] = rf[$i]
        }
#-------------------------------------------------------------------
# Here, we estimate the parameters $k$ at the footpoint
# of the chosen contour line, that is $k0$ (see
# Chapter 3 for more details).
#-------------------------------------------------------------------
        window 1 2 1 2
        define k0 (d[dimen(r)-1]*v1[dimen(r)-1]/b1[dimen(r)-1])
        define p1 (zr[0])
        define p2 (zr[dimen(zr)-1])
        rel $p1 $k0
        draw $p2 $k0
        define m1 (zzra[$inca-1]) # This locates the Alfven point.
        define m2 (zzrf[$incf-1]) # This locates the FM point.
#-------------------------------------------------------------------
# Having located the Alfven point and the FM point we display
# them on the windows as dots.
#-------------------------------------------------------------------
        if (zzra[$inca-1]!=0.0){
        ptype 4 3
        rel $m1 $k0
        expand 1.2
        dot
        ctype red
        dot
        }
        if (zzrf[$incf-1]!=0.0){
        rel $m2 $k0
        expand 1.2
        dot
        ctype yellow
        dot
        }
        ctype white
        ylabel k
```

```
        angle 0.0
        xlabel z/r
#-----------------------------------------------------------------------
# Now, we repeat the same procedure for the parameter $1$.
#-----------------------------------------------------------------------
window 1 3 1 2
        data $1$2"."$3
        read z 3
        read r 4
        read v3 5
        read v1 7
        read b3 8
        read b1 10
        read d 13
        read ma 11
        set zr = z/r
        set k  = d*v1/b1
        set l  = r*(v3-b3/k)
        limits zr l
        box 1 2 0 0
        ltype 0
        connect zr l
define l0 (r[dimen(r)-1]*v3[dimen(r)-1]
-(r[dimen(r)-1]*b3[dimen(r)-1]/$k0))
        define pp1 (zr[0])
        define pp2 (zr[dimen(zr)-1])
        rel $pp1 $l0
        draw $pp2 $l0
        define mm1 (zzra[$inca-1])
        define mm2 (zzrf[$incf-1])

        if (zzra[$inca-1]!=0.0){
        ptype 4 3
        rel $mm1 $l0
        expand 1.2
        dot
        ctype red
        dot
        }
        if (zzrf[$incf-1]!=0.0){
        rel $mm2 $l0
```

```
expand 1.2
dot
ctype yellow
dot
}
ctype white
ylabel l
angle 0.0
xlabel z/r

ltype 0
ctype white
```

Appendix I

The Poloidal Current Density

```
#include "pltz2d.def"
c=======================================================================
c//////////////////////  SUBROUTINE POLCUR  \\\\\\\\\\\\\\\\\\\\\\\\\\
c
        subroutine polcur(pa3)
c
c       written by: Rachid Ouyed
c
c Purpose:
c
c COMPUTES THE POLOIDAL CURRENT VECTOR POTENTIAL FROM Bphi
c This subroutine is called by ''plot2.src''. Contour
c lines of the variables 'pa3'' (giving the poloidal
c current vector) are then plotted.
c
c       ASSUMES CYLINDRICAL MESH WITH UNIFORM ZONES.
C
c-----------------------------------------------------------------------
      implicit NONE
#include "common.h"
      real pa1(in+1,jn+1),pa3(in,jn),dr,dz
      integer i,j
c\\\\\\\\\\\\\\\\\\\\\\\\\\\\\\\\\\\\\\\\\\\\\\\\\\\\\\\\\\\\\\\\\\\\\\\\\\
c=======================================================================
      dz = x1(2)-x1(1)
      dr = x2(2)-x2(1)
      pa1(nx1z+1,1) = 0.0
      do 10 i=nx1z,1,-1
        pa1(i,1) = pa1(i+1,1) + jr(i,1)*dz
```

```
10    continue
        do 20 j=1,nx2z
      do 30 i=1,nx1z+1
          pa1(i,j+1) = pa1(i,j) + jz(i,j)*x2(j)*dr
30    continue
20      continue

      do 50 j=1,nx2z
        do 40 i=1,nx1z
          pa3(i,j) = 0.25*(pa1(i,j)+pa1(i+1,j)+pa1(i,j+1)+pa1(i+1,j+1))

40      continue
50    continue
      return
      end
```

Appendix J

Image Analysis

1. Image Dumping

```
#include "zeus2d.def"
c=======================================================================
c//////////////////////////  SUBROUTINE MOVIE  \\\\\\\\\\\\\\\\\\\\\\\\
c
      subroutine movie(filename)
c
c     DUMPS VARIABLES FOR ANIMATION
c
c     Original Version: Jim Stone
c     Heavily Modified by: Rachid OUYED
c
c     PURPOSE:  Dumps raster images for animation by Imagetool, Spyglass
c     VIEW, etc.  Add new variables as
c     needed.  Min/max of density during simulation
c     are estimated before hand for a better use of
c     the pallette. This routine is intended as a USER dump.
c
c Refer to the color images in chapter 5, for an example of
c images generated by this subroutine.
c
c-----------------------------------------------------------------------
      implicit NONE
#include "param.h"
#include "grid.h"
#include "field.h"
#include "root.h"
```

```
#include "scratch.h"
      character*8  filename
      integer  i,j,irecl,jdim,idim
      integer jst,ist,twonx2,fournx2
      real dmin,dmax,dden,emin,emax,deen,qmin,qmax,dqen
      real b3min,b3max,db3en,mfmin,mfmax,dmfen
      real v1min,v1max,dv1en
      real a3min,a3max,a3v1en
      character*1 fech(in*6*jn),expand(in*6*nintp*nintp*jn), ico
c=======================================================================
        open(10,file="maxmind.data",status="unknown")
        open(14,file="maxminb3.data",status="unknown")
        open(15,file="maxminv1.data",status="unknown")
        read(10,*) dmin,dmax
        read(14,*) b3min,b3max
        read(15,*) v1min,v1max
c
c Note that the minimum and the maximum values for the
c variables to be analyzed are already computed from
c the first run of the simulation (see chapter 2.4).
c They are stored in the files opened above.
c

      dmin = alog10(dmin)
      dmax = alog10(dmax)
      dden = (dmax-dmin)/float(256)
      deen = (emax-emin)/float(256)
      db3en= (b3max-b3min)/float(256)
      dv1en= (v1max-v1min)/float(256)
c
      jdim = 6*nx2z
      twonx2 = 2* nx2z
      fournx2 = 4* nx2z
      irecl = nx1z*6*nx2z*nterp*nterp
c
      do 10 j=je,js,-1
      do 10 i=is,ie
        ist=i-is+1
        jst=je-j
c+++++++++++++++++++++++++++++++++++++++++++++++++++++++++++++++++++++++
c  density (upper panel) vs toroidal field (lower panel)
```

```
         ico =  char(min(max(ifix(dim(alog10(d(i,j))-dmin,0.0)/dden)
     &  ,1),253))
         fech(jst*nx1z+ist) = ico
         fech((twonx2+jst)*nx1z+ist) =  ico
         fech((fournx2+jst)*nx1z+ist) =  ico
         fech((jdim-jst-1)*nx1z+ist) =  ico
c++++++++++++++++++++++++++++++++++++++++++++++++++++++++++++++++++++++++++++
c  density (upper panel) vs z-velocity (lower panel)
#ifdef MHD
         ico =  char(min(max(ifix(dim(b3(i,j)-b3min,0.0)/db3en)
     &   ,1),253))
         fech((twonx2-jst-1)*nx1z+ist) =  ico
#endif
c++++++++++++++++++++++++++++++++++++++++++++++++++++++++++++++++++++++++++++
c  density alone
         ico =  char(min(max(ifix(dim(v1(i,j)-v1min,0.0)/dv1en),1)
     &  ,253))
         fech((fournx2-jst-1)*nx1z+ist) =  ico
c++++++++++++++++++++++++++++++++++++++++++++++++++++++++++++++++++++++++++++
10     continue
       open(unit=4,file=filename,status='unknown',access='direct',
     &  form='unformatted',recl=irecl)
c//////////////////////////////////////////////////////////////////////
       if (nterp.gt.1) then  ! we expand the imgae by a factor nterp.
         call expand_image(fech,jdim,expand)
         write(4,rec=1) (expand(i),i=1,irecl)
       else
         write(4,rec=1) (fech(i),i=1,nx1z*6*nx2z)
       end if
       close(unit=4)
c//////////////////////////////////////////////////////////////////////
c We now call splitfile to split the image created
c into three different images (density/toroidal field;
c density/z-velocity and density/density) for easy
c display and analysis.
         call splitfile(filename,nterp*nx1z,nterp*6*nx2z)
         close(10)
         close(14)
         close(15)
       return
```

```
      end
```

2. Image Expansion

```
#include "zeus2d.def"
c=======================================================================
c//////////////////////////  SUBROUTINE MOVIE  \\\\\\\\\\\\\\\\\\\\\\\\
      subroutine expand_image(orig_im,jdim,exp_im)
c
c     EXPANDS USER DUMP FILE BY REPLICATION
c
c     written by: P. Monger
c
c     PURPOSE:  Called by ''movie.src'' to replicate pixels in the user dump fil
e
c    if the $iocon namelist variable nterp is greater than 1.  Expanded i
c   -mages
c    are then written to disk by movie()
c    Expansion is done by simple pixel replication (interpolation could be
c    added someday if justifiable)
c
c    LOCALS:
c-----------------------------------------------------------------------
      implicit NONE
#include "param.h"
#include "grid.h"
#include "field.h"
#include "root.h"
#include "scratch.h"
      character*1 orig_im(in*jdim),exp_im(in*nintp*nintp*jdim)
      integer i,j,i2,j2,iplace,jdim

      iplace=1

      do 10 j=1,jdim
      do 10 j2=1,nterp
      do 10 i=1,nx1z
      do 10 i2=1,nterp
        exp_im(iplace)=orig_im(nx1z*(j-1)+i)
        iplace=iplace+1
```

```
 10    continue
c      return
       end
```

3. Image Splitting

```
c=======================================================================
c//////////////////////////  SUBROUTINE SPLITFILE  \\\\\\\\\\\\\\\\\\\\
c=======================================================================
c
        subroutine splitfile(filename,isize,jsize)
c
c PURPOSE:
c
c       SPLITS THE GENERATED MOVIE FILES INTO THE THREE
c DIFFERENT COMPONENTS:
c
c Density/Toroidal Field
c Density/z-Velocity
c Density/Density
c
c
c
c       LOCALS:
c-----------------------------------------------------------------------
       subroutine splitfile(filename,isize,jsize)
       implicit NONE
       integer i,j,isize,jsize,jss,ivars
       parameter(ivars=3)
       character*8  filename,varfile*10
       character*1 fech(isize*jsize)
c
c We first read in the file to be split,
c
        read(filename,10)j
 10     format('usr',i3.3,'aa')

        open(unit=4,file=filename,status='unknown',access='direct',
     &  form='unformatted',recl=is*js)
```

```
        read(4,rec=1) (fech(i),i=1,is*js)
        close(unit=4,status='delete')
c
c and then generate the three frames.
c
        write(varfile,11)j
 11     format('b3',i3.3,'aa')
        jss=jsize/ivars
        open(unit=4,file=varfile,status='unknown',form='unformatted')
        write(4) (fech(i),i=1,isize*jss)
        close(unit=4)
        write(varfile,12)j
 12     format('v1',i3.3,'aa')
        open(unit=4,file=varfile,status='unknown',form='unformatted')
        write(4) (fech(i),i=isize*jss+1,isize*2*jss)
        close(unit=4)
        write(varfile,13)j
 13     format('den',i3.3,'aa')
        open(unit=4,file=varfile,status='unknown',form='unformatted')
        write(4) (fech(i),i=isize*2*jss+1,isize*3*jss)
        close(unit=4)
c
      return
      end
```

Bibliography

[] Achterberg, A., Blandford, R. D.& Goldreich, P. 1983, Nature, 304, 607

[] Adams, F. C., Lada, C. J. & Shu, F. H. 1987, Astrophys. J., 312, 788

[] André, P., Ward-Thompson, D. & Barsony, M. 1993, ApJ, 406, 122

[] Appl, S. & Camenzind, M. 1992, Astr. Astrophys., 256, 354

[] Baade, W. & Minkowski, R. 1954, ApJ, 119, 215

[] Balbus, S. A. & Hawley, J. F. 1991, ApJ, 376, 214

[] Balbus, S. A. & Hawley, J. F. 1992, ApJ, 400, 610 (BH)

[] Barral, J. F. & Cantó, J. 1981, RMAA, 5, 101

[] Beckwith, S.V.W., Sargent, A.I., Chini, R.S., & Güsten, R. 1990, AJ, 99, 924

[] Beckwith, S.V.W. in *Structure and Emission Properties of Accretion Disks.* 1991, eds. C. Bertout, S. Collin, J. P. Lasota & J. Tran Thanh Van, Editions Frontiéres, p.33

[] Beckwith, S.V.W., Sargent, A.I. 1993, In *Protostars and Planets III*, eds. E. Levy and J. Lunine, University of Arizona Press, p.521

[] Begelman, M. C. in *Accretion Disks and Magnetic fields in Astrophysics.* 1989, eds. G. Belvedere et al., (Kluwer), p.255

[] Bell, A. R. & Lucek, S. G. 1995, MNRAS, 277, 1327 (BL95)

[] Birkinshaw, M. in *Beams and Jets in Astrophysics* 1990, ed. P. A. Hughes, Cambridge University Press, p.278

[] Biretta, J. A., Owen, F. N. & Hardee, B. E. 1983, ApJL, 274, 274

[] Biretta, J. A. & Meisenheimer, K. 1993 in *Jets in Extragalactic Radio Sources*, eds. H. J. Rösser and K. Meisenheimer, Springer-Verlag, p.159

[] Blandford, R. D, Rees, M. J. 1974, MNRAS, 169, 395

[] Blandford, R. D and Payne, D. R 1982, MNRAS, 199, 883 (BP82)

[] Blandford, R. D. In SAAS Fée Lectures on Advanced Astrophysics, *Active Galactic Nuclei.* 1990, eds. R. D. Blandford, H. Netzer and L. Woltjer, Berlin:Springer, p. 161

[] Boksenberg A. et al. 1992, A&A, 261, 393

[] Bridle, A. H. 1985, Can. J. Phys., 64, 353

[] Brio, M. & Wu, C. C. 1988, JCP, 75, 400

[] Cabrit, S. 1990, PhD. thesis, Univ. Paris.

[] Cabrit, S., & André, P. 1991 , Astrophys. J., 379, L25

[] Calvet, N., Hartmann, L.& Kenyon J. S. 1993, ApJ, 402 623

[] Camenzid, M. 1987, A&A, 184, 341

[] Cantó, J. 1980, A&A, 86, 327

[] Cao, X. & Spruit, H. C. 1994, A&A, 287, 80C

[] Chandrasekhar, S. 1939, Introduction to the Study of Stellar Structure (University of Chicago Press)

[] Chernin, L. $ Masson, C. 1991, ApJ, 382, L93

[] Clarke, A. D., Norman, L. M. & Burns O. J. 1986, ApJ., 311, L63

[] Clarke, A. D. 1996, ApJ, 457, 291

[] Clayton, D. D. 1983, Principles of Stellar Evolution abd Nucleosynthesis, (University of Chicago Press)

[] Collela, P. & Woodward, P. R. 1984, JCP, 54, 174

[] Collin-Souffrin, S. 1992, In AIP Conf. No. 254, *Testing the AGN Paradigm*, eds. S. S. Holt, S. G. Neff and C. M. Urry , p.119

[] Courant, R. & Friedrichs. K. O. 1984, *Supersonic Flow and Shock Waves*, Springer-Verlag

[] Curry, C., & Pudritz, R.E. 1996, MNRAS, 281, 119

[] Dai, W. & Woodward, P. R. 194, JCP, 111, 354

[] Davis C. J., Mundt, R., Eislöffel, J.& Ray, T. P. 1995, AJ, 110, 766

[] DeCampli, W. M. 1981, ApJ, 244, 124

[] Dewar, R. L., 1970, Phys. Fluids, 13, 2710

[] Dopita, M. A. 1978, ApJS, 37, 117

[] Edwards, S., Ray, T. P. & Mundt R. 1993, In *Protostars and Planets III*, eds. E. Levy and J. Lunine, University of Arizona Press, p.567

[] Eislöffel, J. & Mundt, R. 1992, A&A, 263, 292

[] Eislöffel, J. & Mundt, R. 1994, ApJ, 284, 530

[] Esin, A. A., Narayan, R. & Ostriker, E., 1996, ApJ, 465, 312

[] Evans, C. & Hawley, J. F. 1988, ApJ, 33, 659

[] Ferreira, J. & Pelletier, G. 1995, A&A, 295, 807

[] Frank, J., King, R. A. & Raine, J. D. 1992, *Accretion Power in Astrophysics*, Cambridge University Press

[] Ghosh, P. & Lamb, F. K. 1978, ApJ, 223, 283

[] Gilfanov, M. et al. 1995, in NATO ASI Ser., The Lives of the Neutron Stars, ed. M. A. Alpar, U. Kiziloglu, & J. van Paradijs (Dordrecht: Kluwer), vol. 450, 331

[] Hartigan, P., 1989, ApJ, 339, 987

[] Hartigan, P., Raymond, J.& Meaburn, J. 1990, ApJ, 362, 624

[] Hartigan, P., Edwards, S. & Ghandouri, L. 1995, ApJ., 452, 736

[] Hartmann, L., Edwards, S. & Avrett, E. 1982, ApJ, 261, 279

[] Hartmann, L., Kenyon, S. & Hartigan, P. 1993, In *Protostars and Planets III*, eds. E. Levy and J. Lunine, University of Arizona Press, p.497

[] Hayashi, M. 1996, PhD Thesis, Chiba University, Japan

[] Hawley, J. F. & Balbus, S. A., ApJ., 376, 223 (1991)

[] Henriksen, R. N. & Rayburn, D. R. 1971, MNRAS, 152, 323

[] Heyvaerts, J. & Norman, C. 1989, ApJ, 347, 1055 (HN89)

[] Hjellming, R.M, & Rupen, M.P. 1995, Nature, 375, 464

[] Jackson, J. D. 1975. Classical Electrodynamics, New York:Wiley

[] Johnson, W. N., et al. 1994, in The Second Compton Symp., ed. C. E. Fichtel, N. Gehlers, & J. P. Norris (New York:AIP), 515

[] Kantrowitz, A. & Petsheck, H. E. 1966, plasma physics in theory and application, ed. W. B. Kunkel (McGraw-Hill, New York)

[] Kenyon, S. J. & Hartmann, L. 1987, ApJ, 323, 714

[] Kinzer, R. L., et al. 1994, in The Second Compton Symp., ed. C. E. Fichtel, N. Gehlers, & J. P. Norris (New York:AIP), 531

[] Königl, A. 1982, ApJ, 261, 115

[] Königl, A. 1986, Ann. NY Acad. Sci., 470, 88

[] Königl, A. 1989, ApJ, 342, 208

[] Königl, A. & Ruden, S. P. 1993, in *Protostars and Planets III*, eds. E. H. Levy and J. I. Lunine (Tucson: University Arizona Press), p.641

[] Kössl, D., Müller, E. & Hillebrandt, W. 1990, A&A, 229, 378

[] Krall, N. $ Trivelpiece, A. 173, Principle of Plasma Physics, (McGraw Hill, New York), P.78

[] Kuhi, L. V., 1964, ApJ, 140, 1409

[] Lada, C. J. 1985, ARA&A, 23, 267

[] Lada, J. C. & Fich, M., 1996, ApJ, 459, 638

[] Landau, L. D. & Lifshitz, E. M. 1960, Electrodynamics of continuous media, (pergamon Press New York)

[] Leahy, J. P. 1993 in *Jets in Extragalactic Radio Sources*, eds. H. J. Rösser and K. Meisenheimer, Springer-Verlag, p.1

[] Li, Z-H. 1995, ApJ, 444, 848

[] Liberman, M. A. & Velikovich, A. L. 1986, Physics of shock waves in gases and plasmas, (Springer Verlag)

[] Lind, R. K., Payne, G. D., Meier, L. D. & Blandford, D. R. 1989, ApJ, 344, 89

[] Lovelace, R. V. E., Wang, J. C. L., & Sulkanen, M. E. 1987, ApJ, 315, 504

[] Lubow, S. H., Papaloizou, J. C. B., & Pringle, J. E. 1994, MNRAS, 268, 1010

[] Lynden-Bell, D. 1969, Nature, 223, 690

[] Lynden-Bell, D. & Pringle, J. 1974, MNRAS, 168, 603

[] Masson, C. R. & Chernin, L. M. 1992, ApJ, 387, L47

[] McCaughran & O'Dell 1995, http://www.stsci.edu

[] McKee, C. F. & Zweibel, E. G. 1992, ApJ, 339, 551

[] McKee, C. F., Zweibel, E., Goodman, A. A. & Heiles, C. 1993, In *Protostars and Planets III*, eds. E. Levy and J. Lunine, University of Arizona Press, p. 327

[] Meier, D. L., Payne, D. G. & Lind, K. R. 1996, in *Extragalactic Radio Sources*, IAU Symposium No. 175, in press

[] Mestel, L. 1989, in *Accretion Disks and Magnetic Fields in Astrophysics*, ed. G. Belevedere, Kluwer Academic Publishers, p.151

[] Mouschovias, T. Ch. & Paleologou 1980, ApJ, 237, 877

[] Mundt, R. & Fried, J. W. 1983, ApJ, 274, L83

[] Muxlow, T. W. B. & Garrington, S. T. 1991, in *Beams and Jets in Astrophysics*, ed. P. A. Hughes, (Cambridge University Press), p.52

[] Netzer, H. in *Structure and Emission Properties of Accretion Disks.* 1991, eds. C. Bertout, S. Collin, J. P. Lasota & J. Tran Thanh Van, Editions Frontiéres. p.177

[] Norman, M. L., Smarr, L. & Winkler, K. H. A. 1985, in *Numerical Astrophysics*, ed. J. Centrella, J. LeBlanc, and R. Bowers (Boston: Jones and Bartlett), p.88

[] O'Dell, C. R. & Wen, Z. 194, ApJ, 436, 194

[] Osterloh, M. & Beckwith, S. V. W. 1995, Astrophys. J., 439, 2880

[] Ouyed, R. & Pudritz, R. E. 1994, ApJ, 419, 255 (OP94I)

[] Ouyed, R. & Pudritz, R. E. 1994, ApJ, 423, 753 (OP94II)

[] Ouyed, R., Pudritz, R. E. & Stone, M. J. 1997, Nature, in press

[] Ouyed, R. & Pudritz, R. E. 1997, ApJ, in press (OPI)

[] Ouyed, R. & Pudritz, R. E. 1997, ApJ, in press (OPII)

[] Owen, F. N., Hardee, P. E. & Cornwell, T. J. 1989, ApJ, 340, 698

[] Padman, R., Lasenby, A. N. & Green, D. A. 1991 in *Beams and Jets in Astrophysics*, ed. P. A. Hughes. (Cambridge University Press), p.484

[] Parker, N. D., Padman, R. & Scott, P. F. 1991, MNRAS, 252, 442

[] Pelletier, G. & Sol, H. 1992, MNRAS, 254, 635

[] Pelletier, G. & Pudritz, R. E. 1992, ApJ, 394, 117 (PP92)

[] Pudritz, R. E., 1985, ApJ, 293, 216

[] Pudritz, R. E., & Norman, C. A. 1986, ApJ, 301, 571

[] Pringle, J. E. 1981, ARA&A, 19, 137

[] Raga, A. C. & Kofman, L. 1992, ApJ, 386, 222

[] Ray, T. P. & Mundt, R. 1993, in *Astrophysical Jets*, eds. M. fall, C. O'dea, M. Livio and D. Burgarella (Cambridge University Press), p.145

[] Ray, T. P., Mundt, R., Dyson, J., Falle, S. A. F. G. & Raga, A. 1996, ApJ, in press

[] Rees, M. J. 1984, ARA&A, 22, 471

[] Reipurth, B. 1989, in *Low Mass Star Formation and Pre-Main-Sequence Objects*, ed. Bo Reipurth, Garching: ESO, 247

[] Reys-Ruis, M. & Stepinski, T. 1996, ApJ, 459, 653

[] Reipurth, B. 1989, Astr. Ap, 220, 249

[] Reipurth, B., Raga, A. C.& Heathcote, S. 1992, ApJ, 332, 145

[] Richer, J. S., Hills, R. E. & Padman 1992, Mon. Not. R. Astr. Soc., 254, 525

[] Richtmyer, R. D. & Morton, K. W. 1967, Difference Methods for Initial-Value Problems, (Wiley and Sons, New York)

[] Roache, P. J. 1972, Computational Fluid Dynamics, (Hermosa, Albuquerque)

[] Roberts, D. A., Crutcher, R. M., Troland, T. H. & Goss, W. M., 1993, ApJ, 412, 675

[] Sauty, C., & Tsinganos. K. 1994, A&A, 287, 893

[] Shakura, N. I. & Sunyaev, R. A. 1973, A&A, 24, 337

[] Shapiro, S. L. & Teukolsky, S. A. 1983, *Black Holes, White Dwarfs ans Neutron Stars-The physics of Compact Objects*, Wiley

[] Shibata, K. & Uchida, Y. 1986, PASJ, 38, 631 (SU86)

[] Shu, F. H., Lizano, S., Ruden, S. P. & Najita, J. 1988, ApJ, 328, L19

[] Shu, F. H., Najita, J., Wilkin, F., Ruden, S. P. & Lizano, S. 194, ApJ, 429, 781

[] Shulz, W. D. 1984, Methods in Computational Physics Vol. 3, (Academic, New York)

[] Sol, H., Pelletier, G., & Asseo, E. 1989, MNRAS, 237, 411

[] Spitzer, L. Jr. 1962, Physics of Fully ionized gases, 2nd ed., (New York Publish.)

[] Stahler, S. W. 1988, Astrophys. J., 332, 804

[] Stone, J. M., & Norman, M. L. 1992a, ApJS, 80, 753 (SN92a)

[] ———. 1992b, ApJS, 80, 791 (SN92b)

[] Stone, J. M., & Norman, M. L. 1994, ApJS, 420, 237

[] Stone, J. M., Hawley, J. F., Gammie, C. F. & Balbus, S. A., 1996 ApJ., 463, 656

[] Strom, S. E. & Strom, K. M. 1987 in *Star Forming Regions*, eds. M. Piembert and J. Jugaku, Dordrecht:Riedel, p255

[] Tajima, T. 1989, Computational Physics, (Addison-Wesley)

[] Taylor, G. B. Perley, R. A., Inoue, M., Kato, T., Tabara, H. and Aizu, K. 1990, ApJ, 360, 41

[] Uchida, Y., & Shibata, K. 1985. PASJ, 37, 515 (US85)

[] Ustyugova, G. V., Koldoba, A. V., Romanova, M. M., Chechetkin, V. M. & Lovelace, R. V. E. 1995, ApJL. 439, L39

[] van Leer, B. 1977, JCP, 23, 276

[] von Neumann, J. & Richtmyer, R. D. 1950, JAP, 21, 232

[] Wallinder, F. H. 1991, A&A, 249, 107

[] Wardle, J. F. C. & Potash, M. I. 1982 in IAU Symposium 97, Extragalactic Radio Sources, ed. D. S. Heeschen and C. M. Wade (Dordrecht: Reidel), p.131

[] Wardle, M.& Königl, A. 1993, ApJ, 410, 218

[] Whittet, D. C. B., Gerakines, P. A., Carkner, A. L., Hough, J. H., Martin, P. G., Prusti, P. A. & Kilkenny, D. 1994, ApJ, 268, 1

[] Zachary, A. L. & Collela, P. 192, JCP, 99, 341

[] Zweibel, E. G. & McKee, C. F. 1995, ApJ, 439, 779

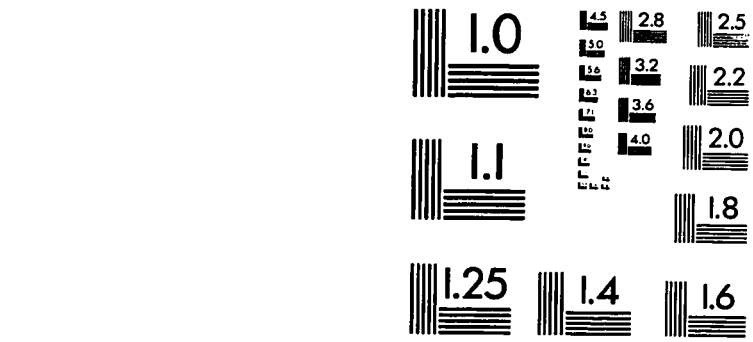

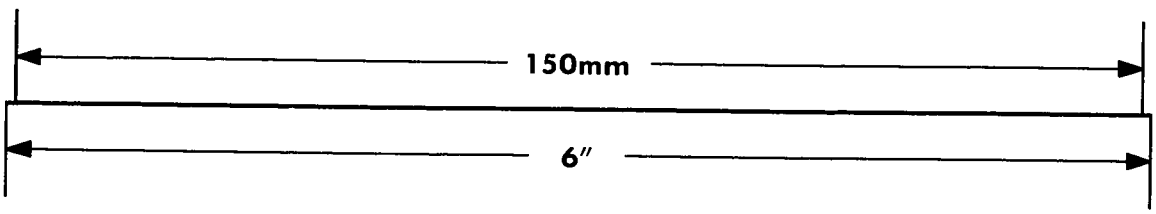

APPLIED IMAGE, Inc
1653 East Main Street
Rochester, NY 14609 USA
Phone: 716/482-0300
Fax: 716/288-5989